

Polycaprolactone and Poly(glycerol) sebacate polyHIPEs for regeneration of osteochondral defects



**Thesis submitted to the University of Sheffield for
the degree of Doctor of Philosophy**

María Fernanda Velázquez de la Paz

**Department of Materials Science
and Engineering**

June 2022

Acknowledgments

The journey of a researcher is passionate and exciting. However, it can also be frustrating and lonely. I could have not completed my studies if it was not for the amazing group of people around me.

First, I would like to thank the support and guidance of my supervisors. Professor Fred, your knowledge and passion made me the researcher I am today. Professor Gwen, thank you for being the wise advice through my project.

I would also like to recognise CONACYT Mexico and the Materials Science & Engineering Department at the University of Sheffield for funding my studies and making this possible.

To my dear mentor Betül, who introduced me to the fascinating world of HIPes and was always the voice in my head pushing me for better results. To my colleagues Nam, Boyang, Enes, and Mina. You are my family, and it has been a pleasure to share this journey with you.

To Sara, Alex, and Santiago. We have been together for so many years and I cannot ask for better and funnier friends.

To my mum and dad. Your discipline, encouragement and love are the pillars in my life. You are always with me, no matter distance and time. To my sister Sofia, who's complicity and friendship lightens my days. And to Andy, for loving me and being by my side through thick and thin.

Finally, I want to thank my grandad, who has always been my hero and my inspiration. Abuelo, this is to you.

Abstract

According to the Outerbridge grading system and the ICRS grading, osteochondral defects are described as a cartilage lesion that reaches down the subchondral bone and can penetrate across [1]. Physiologically, a decrease in the cartilage proteoglycans and an increase in degradative enzymes lead to loss of motor abilities, pain and over-mineralisation of joints.

Current preventive treatments include pharmacotherapies and cartilage enhancement procedures while corrective approaches mostly consist of major interventions (transplantations and invasive tissue engineering techniques). Materials proposed for tissue engineering (TE) and regenerative medicine (RM) show impressive advances in both production technologies and resilience responses after implantation [2], ameliorating the patient's mobility and lifestyle for years. However, there is still a huge gap between the number of academic proposals undergoing clinical trials and the product release to the market [3]. Finally, clinical interventions usually include site morbidity, immune rejection and tissue regeneration that does not exactly mimic the host environment.

Osteochondral (OC) defects and articular cartilage pathologies are part of the most common musculoskeletal (MSK) conditions in the UK [4]. They are known due to their low rate of healing and the concomitant pathologies around them. Almost 20 million people in the country have an MSK condition; osteoarthritis (OA), avascular necrosis (AVN), *osteochondritis dissecans* (OCD) and traumatic OC affects 3 out of 10 citizens over the age of 45. Surprisingly, OC affects mainly middle-aged high-performance athletes and women. Every year, the NHS develops partial or total one or two-sided replacements; around 102 000 hip, 109 000 knee replacements, and 7,000 shoulder replacements [5]. From these, over 90% of the patients are diagnosed with osteoarthritis [6].

With main symptoms as a decrease in the cartilage proteoglycans and an increase on the degradative enzymes, various treatments have been offered for the last two decades: (i) cartilage enhancement procedures & pharmacotherapies, (ii) transplantations (AOCT - Mosaicplasty), and (iii) TE techniques / cellular therapies (MACI – ACI). Despite their advantages in mobility restoration and symptom elimination, site morbidity, low availability of cell and tissue supply, fibrocartilage formation and allogeneic graft materials still limit their effectiveness.

The present work has as main objective to propose an alternative material or group of materials for the creation of porous structures that, when implanted, could support the formation of novel osteochondral tissue. For this;

- i) The first chapter explores the literature regarding the anatomy of the knee and its connections with OC defects. Additionally, an analysis of current treatments for OC defects is presented.
- ii) Materials and methods used through this work are mainly condensed in Chapter II.
- iii) The third chapter discusses polycaprolactone methacrylate (PCLMA) as a candidate for the formation of porous structures through emulsion templating (polyHIPEs), with a special focus on the chemical and mechanical characterisation of the material, as well as the study of their microstructure through scan electron microscopy (SEM) microscopy and micro-computed tomography (micro-CT).
- iv) The fourth chapter proposes poly(glycerol sebacate) methacrylate (PGSM) as a candidate for the formation of polyHIPEs through emulsion templating, with a special focus on the understanding and optimisation of the emulsification process, and the chemical and mechanical characterisation of the material, as well as the study of their microstructure through SEM, LightSheet microscopy and micro-CT.
- v) The fifth chapter explores blends of PCLMA and PGSM as biodegradable polymers and as HIPE material. A multi-layered scaffold is also displayed. The mechanical characterisation of the materials was explored through tensile and compressive tests, and the overall morphology was imaged through LightSheet microscopy and micro-CT.
- vi) The sixth chapter proposes a variety of techniques for the treatment of polyHIPEs to tune their wettability, bioactivity and biodegradability, as well as their attractiveness to cellular environments. The chapter also discusses the use of hydrogels as part of the internal phase of emulsions, and as carriers of molecules as sugars and cells for TE applications.
- vii) The seventh chapter collects cell experiments developed using materials previously discussed. The cellular lines (hES-MPs, BACs, Y201, MLO5) were selected due to their proximity to the tissues of interest (cartilage, osteochondral) and cell culture was done on 2D and 3D, using both qualitative and quantitative assays to measure cellular metabolic activity, extracellular matrix (ECM) production, and early differentiation.
- viii) The eighth chapter represents a final reflection on future work on both the biomaterial and TE approaches. Additionally, it also explores the feasibility of polyHIPEs for their commercial application as scaffolds for novel tissues, especially for the food industry.

It can be concluded that PCLMA and PGSM as individual or as a blend, are suitable polymers for TE applications. Additionally, that stable polyHIPEs can be formed from these materials, that can be functionalised and treated to increase their attractiveness to cellular environments in the macro and micro structural level and support metabolic activities that can lead to the production of ECM and new tissues.

List of abbreviations

μm	micrometre
AA	Ascorbic Acid
ACI	Autologous Chondrocyte Implantation
ARS	Alizarin Red Stain
BAC	Bovine Articular Chondrocytes
BGP	β -Glycerophosphate disodium salt hydrate
BM	Basal Media
BMS	Bone Marrow Stimulation
C+/-	Cell plus/minus
CEM	Chondrocyte Media
DAPI	4',6-diamidino-2-phenylindole
DCM	Dichloromethane
dH ₂ O	Distilled water
DMSO	Dimethyl sulfoxide
DOE	Design Of Experiments
ECM	Extracellular Matrix
EtOH	Ethanol
F212	Fibroblast cell line
FCF	Fast Green
FCS / FBS	Foetal Bovine / Calf Serum
FGF	Fibroblast Growth Factor
FITC	Fluorescein Isothiocyanate
GelMA	Gelatin Methacrylate
HA	Hydroxyapatite
HCl	Hydrochloric acid
hES-MP	Human ESC (Embryonic Stem Cells)-derived Mesodermal Progenitors
HEPES	4-(2-hydroxyethyl)-1-piperazineethanesulfonic acid
HIPE	High Internal Phase Emulsion
HM	High methacrylation
HMDS	Hexamethyldisilazane
LM	Low methacrylation

MAA	Methacrylic anhydride
MACI	Autologous Cultured Chondrocytes on Porcine Collagen Membrane
MEM	Minimum Essential Media
MXF	Microfracture
mm	millimetre
μ -CT	micro-Computed Tomography
NEAA	Non-Essential Amino Acids
nm	nanometre
OCS	Osteochondral Scaffolds
PBS	Phosphate-buffered Saline
PCL	Polycaprolactone
PCLMA	Polycaprolactone methacrylate
PGS	Poly(glycerol sebacate)
PGSM	Poly(glycerol sebacate) methacrylate
PS	Penicillin – Streptomycin
PSG	Penicillin – Streptomycin – Glutamate solution
PSM	Plasma Surface Modification
RFU	Relative Fluorescence Unit
RM	Response Medicine
ROP	Ring Opening Polymerisation
RR	Resazurin assay
S+/-	Scaffold plus/minus
SEM	Scanning Electron Microscopy
SM	Supplemented Media
TEA	Trimethylamine
TRITC	Tetramethylrhodamine isothiocyanate
UV	Ultraviolet light
TE	Tissue Engineering
VD	Vapour deposition
W/O and W/O/W	Water-in-Oil and Water-in-Oil-in-Water emulsions

Statement of originality

The work presented in this document is entirely my own work, unless otherwise stated.

The work of Master and Undergraduate students that is presented has been analysed by me.

Publications

- (1) Velazquez de la Paz MF*, Maksoud FJ*, Hann A, Thanarak J, Reilly G, Claeysens F, Green N, Zhang YS. "Porous Biomaterials for Tissue Engineering: A Review." *Journal of Materials Chemistry B*. Accepted Manuscript (2022). (*joined first author)
- (2) Velazquez de la Paz MF, Alemardaani M, Furnidge R, Pashneh-Tala S, Claeysens F. "Poly(glycerol) sebacate polyHIPE scaffolds for chondral tissue applications." Draft Manuscript (2022).

Conference Presentations

- (1) Biomaterials & Regenerative Medicine. Velazquez de la Paz MF¹. ¹The Kroto Research Institute, University of Sheffield, UK. **Engineering at Sheffield: Unifying Sciences. University of Sheffield, 2018 (Oral)**
- (2) PolyHIPEs for Osteochondral Regeneration. Velazquez de la Paz MF¹, Claeysens F¹, ¹The Kroto Research Institute, University of Sheffield, UK. **TCES, Nottingham, 2019 (Poster)**
- (3) PCL and PGS polyHIPEs for Osteochondral Regeneration. Velazquez de la Paz MF¹, Claeysens F¹, ¹The Kroto Research Institute, University of Sheffield, UK. **BiTEG York, 2019 (Poster)**
- (4) PCL and PGS polyHIPEs for Osteochondral Regeneration. Velazquez de la Paz MF¹, Claeysens F¹, ¹The Kroto Research Institute, University of Sheffield, UK. **Glasgow WBC, 2020 (Poster)**
- (5) PCL and PGS polyHIPEs for Osteochondral Regeneration. Velazquez de la Paz MF¹, Claeysens F¹, ¹The Kroto Research Institute, University of Sheffield, UK. **ABS University of Sheffield, 2021 (Poster)**
- (6) PCL and PGS polyHIPEs for Osteochondral Regeneration. Velazquez de la Paz MF¹. ¹The Kroto Research Institute, University of Sheffield, UK. **BioMedEng 2021, University of Sheffield, 2021 (Turbo Talk)**
- (7) PCLMA and PGSM polyHIPE scaffolds for Osteochondral Regeneration. Velazquez de la Paz MF¹. ¹The Kroto Research Institute, University of Sheffield, UK. **BRS Online, 2021 (Turbo Talk)**

- (8) PolyHIPE scaffolds for Osteochondral Regeneration. Velazquez de la Paz MF¹. ¹The Kroto Research Institute, University of Sheffield, UK. **CITER Cardiff, 2021 (Turbo Talk)**
- (9) PCLMA and PGSM polyHIPE scaffolds for Osteochondral Regeneration. Velazquez de la Paz MF¹. ¹The Kroto Research Institute, University of Sheffield, UK. **TCES, University of Sheffield, 2021 (Poster)**

Student Mentoring

- (1) INSIGNEO Summer programme, INSIGNEO, Sheffield, UK (2018) - Evangeline Hughes and Robin Watkins-New
- (2)
- (3) Exchange Summer students, The Kroto Research Institute, UK (2019) – Melissa Ligorio
- (4) Bioengineering Undergraduate Students (2019-2021) – Thomas M Mcdonagh, Chukwunonso J Efobi, Georgia S. Bickerton, Sam Kelly
- (5) Biomaterials & Regenerative Medicine MSc Students (2019-2021) – Sierra Kucko, Saida Musaeva, Ghazaleh Mazaheri Tehrani, Daniel Trinder-Hunt

Outreach

- (1) Volunteering at Primary School – STEM: Building Bridges (2019)
- (2) Course: Commercialisation of medical devices by Michael Murray Ltd. (2019)
- (3) Engineer You're Hired! Programme as facilitator for the topic on Knee Implant Prosthetics (2019-20, 2020-21, 2021-22)
- (4) Intent of Commercialisation Enquiry (ICE) at the University of Sheffield (2022)
Innovation to Market at the London Business School (2021-2022)
- (5) The Brilliant Club STEM Summer – *Biomaterials* (2021)
- (6) Mexico – USA Leaders Network – *Los materiales y su infinidad de aplicaciones* (2022)

Contents

Acknowledgments	2
Abstract	3
List of abbreviations	5
Statement of originality	7
List of Figures	13
List of Tables	22
List of Fabricated Materials	24
Chapter I: Literature review on osteochondral units and polymer emulsions	25
1.1. Background	25
1.1.1. The Knee	25
1.1.2. Macro and microstructure of the osteochondral unit	26
1.1.3. Articular cartilage (AC)	26
1.1.4. Tidemark	28
1.1.5. Subchondral bone	28
1.2. Mechanisms of osteochondral repair	30
1.2.1. Osteochondral defects	31
1.2.2. Osteoarthritis	32
1.3. Osteochondral regeneration	35
1.3.1. Current clinical treatments	35
1.4. Biomaterials for osteochondral regeneration	38
1.4.1. Hydrogels	38
1.4.2. Polymers	42
1.5. Current development and challenges: hydrogels and polymers for OC regeneration	56
1.6. Animal models for osteochondral repair	64
1.7. Project Aims and Objectives	66
Chapter II. Materials & Methods	67
2.1. Materials	67
2.2. Methods	67
2.2.1. Polymer Synthesis	67
2.2.2. Manufacturing	70
2.2.3. Scaffold washes and drying methods	71
2.2.4. Surface modification	71

2.2.5.	Characterisation	72
2.2.6.	Mechanical testing	73
2.2.7.	Imaging	74
2.2.8.	Degradation	75
2.2.9.	Hydrogels	75
2.2.10.	Cell lines	75
Chapter III: Polycaprolactone		80
3.2.	Introduction	80
3.3.	Aims and objectives	82
3.4.	Materials and Methods	83
3.4.1.	Internal Phase Volume	83
3.4.2.	Gel Fraction	83
3.4.3.	Degree of openness (DOO)	83
3.4.4.	Density	83
3.4.5.	Empirical porosity	84
3.4.6.	Pycnometry	84
3.4.7.	Interconnectivity	85
3.4.8.	Micro CT Imaging	85
3.5.	Results	86
3.5.1.	Polycaprolactone	86
3.6.	Discussion	106
3.6.1.	Synthesis and methacrylation	106
3.6.2.	PCL HIPEs	107
3.7.	Summary	113
Chapter IV: Poly(glycerol) sebacate synthesis and structuring		114
4.1.	Introduction	114
4.2.	Aims and objectives	115
4.3.	Materials and Methods	116
4.4.	Results	116
4.4.1.	Synthesis and methacrylation	116
4.4.2.	High Internal Phase Emulsions	119
4.4.3.	Optimisation of PGSM scaffolds	126
4.5.	Discussion	143
4.5.1.	Synthesis and methacrylation	143
4.5.2.	High Internal Phase Emulsions	143

4.6.	Conclusions	150
Chapter V: PCLMA - PGSM polyHIPEs		158
5.1.	Introduction	158
5.2.	Aims and objectives	159
5.3.	Materials and Methods	160
5.3.1.	Bulk PCL:PGS for mechanical testing	160
5.4.	Results	160
5.4.1.	PCL – PGS Blends	160
5.4.2.	PCLMA-PGSM polyHIPEs	161
5.4.3.	PCL – PGS Bilayer Scaffolds	168
5.5.	Discussion	172
5.6.	Conclusions	175
Chapter VI: PolyHIPE treatment and hydrogels		177
6.1.	Introduction	177
6.2.	Aims and objectives	178
6.3.	Materials and Methods	179
6.3.1.	Hydrogels	179
6.3.2.	Hydrogel-co-sugars	179
6.3.3.	Release experiments	180
6.4.	Results	181
6.4.1.	Emulsion optimisation	181
6.4.2.	Hydrogels	185
6.5.	Discussion	194
6.5.2.	Washing and drying scaffolds	194
6.5.3.	Hydrogels	196
6.6.	Conclusions	198
Chapter VII: Cell response to polyHIPEs for cartilage and bone regeneration		200
7.1.	Introduction	200
7.2.	Aims and objectives	202
7.3.	Materials and Methods	203
7.4.	Results	203
7.4.1.	Scaffolds in physiological environments: degradation assays	203
7.4.2.	Cells response to 2D polymer environments	207
7.4.3.	Cells response to 3D polymer environments	211
7.4.4.	Cell encapsulation	226

7.5.	Discussion	229
7.6.	Summary	235
7.7.	Annex	236
7.7.1.	The effect of space limitation on cell proliferation: Channelled scaffolds	236
Chapter VIII: Future Work		237
8.1.	Research & Development	237
8.1.1.	Scaffold optimisation	237
8.1.2.	Cell culture	237
8.2.	Commercialisation of PCLMA and PGSM polyHIPes	238
8.2.1.	Key Findings	238
References		251

List of Figures

- Fig. 1. Left: superficial medial region of the knee showing the different components [9]. Right: Transverse section of the knee [10].* 25
- Fig. 2. The 4 layers of the articular cartilage are represented herein. Histology cuts (left) show cells within the ECM. The orientation and organisation of collagen and elastin fibrils can be observed in the middle figure: the superficial zone is formed by fibrils aligned tangential to the surface; the middle zone is saturated with highly entangled, non-aligned fibrils; the deep layer followed by a calcified cartilage possess parallel oriented fibrils. A third diagram (right) displays cell density: a hypotrophic high flat-cell density in the superficial layer; low round cellular density on the middle layer; and an aligned round cell density on the deep and calcified zone. Source: Author.* 28
- Fig. 3. SEM micrographs of the bottom zones of the articular cartilage and the subchondral bone. cc: calcified cartilage, sbp: subchondral bone plate, tm: tidemark, rz: radial zone [26].* 30
- Fig. 4. Development of osteoarthritis in the knee joint [14].* 34
- Fig. 5. Alginate is formed by mannuronic and guluronic acid arranged in homopolymer blocks (MM, GG) alternated with regions with MG blocks (at different rations) [72].* 39
- Fig. 6. Typical gelatin structure formed by glycine, proline and 4-hydroxyproline residues: -Ala-Gly-Pro-Arg-Gly-Glu-4Hyp-Gly-Pro-.* 40
- Fig. 7. Gelatin structure derives from the extracellular matrix (collagen) of bone and skin tissues. Their statistical distribution can be observed at high temperatures (coils) and rigid chains at low temperatures [88].* 41
- Fig. 8. IPN and semi IPN networks with pure gelatin and gelatin/alginate blends [94].* 42
- Fig. 9. ϵ -caprolactone molecule (left) and poly- ϵ -caprolactone chain (right).* 43
- Fig. 10. Poly(glycerol)sebacate synthesis is obtained by a condensation reaction between glycerol and sebacic acid [119].* 44
- Fig. 11. Polycaprolactone PolyHIPes prepared with different solvent ratios. A. SEM images of C/T:60/40, C/T:80/20 and C/T:100/0; polymerized A. Right after preparation of HIPE, B. 5 days after preparation (scale bars: 100 μ m) [109].* 49
- Fig. 12. Silica-modified Pickering emulsions functionalised through MPtMS (3-(methacryloxy)propyltrimethoxysilane) as at two different rations [152].* 50
- Fig. 13. Synthesis of 4-arm PCL [89].* 67
- Fig. 14. Synthesis of PGS by a condensation reaction between glycerol and sebacic acid [90].* 69

Fig. 15. Cardboard structure to give extra support to assemble porous samples for tensile testing.73

However, PCL (LM, 50% and HM) showed methylene groups adjacent to hydroxyl end groups expressed in peak 3.6. When methacrylation took place, these peaks were reduced, and expressed in peaks 1.9, 5.5 and 6.1 ppm; such peaks were only visible on methacrylated polymers [89]. Fig. 16. Spectra of $n=3$ batches of 3-arm PCLMA 50% DM. Polycaprolactone peaks are found at 1.4, 1.6, 2.3 and 4.1 ppm. Methacrylic groups are found in 1.9, 5.5 and 6.1 ppm. The peak just before 1 ppm evidences its 3-arm structure. DM: degree of methacrylation. The two colours symbolise different batches. 87

Fig. 17. NMR spectra for PCL-HM, PCL-50% DM, PCL-LM and non-methacrylated PCL (NM). Peaks showing the chemical composition of polycaprolactone are on peaks 1.4, 1.6, 2.3 and 4.1 ppm, corresponding to a-c, whilst methacrylate groups can be observed on peaks 1.9, 5.5 and 6.1, illustrated as d-f. 88

Fig. 18. Solvent extraction was tracked over time through the total mass of the LM and 50% polymer solution during the rotavaporation process. 89

Fig. 19. Digital microscope images on PCLMA polyHIPEs prepared at 37 °C (A-B) and room temperature (15 °C – C-D). Magnification of images is 4x for A and C, and 10x for B and D. Scale bars are 500 μm . 91

Fig. 20. Water-in-oil emulsions with 2, 3 and 5 ml of water as water phase. Full adsorbance can be observed with 2 ml (water stained in blue to track its immersion). Phase inversion is observed when adding 3 ml of water, and emulsion coalescence with 5 ml. 92

Fig. 21. A & B. SEM images of a 50% PCLMA PolyHIPE. The big openings are referred to as windows and they have an average size of 35 μm . Such windows are the entrance to other pores. C. Big voids have an average size of 116 μm . Images were taken at high magnifications (>1000x), at 10 KV. 93

Fig. 22. (A,B) 50% PCLMA, with big windows (15 to 26 μm) containing small pores (2 to 9 μm). (C,D) LM PCLMA showing big windows (132 to 229 μm), less round but equally interconnected to small pores (30 to 57 μm). Images taken at Magnifications varying from 700 to 1000x, at 10 KV. 94

Fig. 23. The DOO of a cavity describes the degree in which the surface of a cavity (pore or window) is open. A structural diagram of the cavities in PCLMA scaffolds is observed on the left [280], and its application to SEM imaging on such scaffolds, on the right. Left diagram is obtained with permission from [280], and SEM images are product of this research. Magnification are 1000x and 6800x respectively. 95

Fig. 24. This polyHIPE scaffold was scanned whilst submerged in an aqueous solution. The bubbles around the grey solid construct (and high lightened in red) obstruct the correct reconstruction of the porous material. Top and bottom non-porous structures are pieces of metallic foil used to delimit the edges of the scaffold. 97

Fig. 25. Reproduction of LM PCLMA polyHIPE scaffolds scanned through $\mu\text{-CT}$, on yz (A), xz (B) and xy (C) planes. Scale bars are 1mm. 98

Fig. 26. Reproduction of 50% PCLMA polyHIPE scaffolds scanned through μ -CT, on yz (A), xz (B) and xy (C) planes. Scale bars are 1mm. 99

Fig. 27. Thresholding technique on 2D from the reconstructed scan of a LM PCLMA scaffold. A. The blue area shows the area occupied by the denser material, this is, the polymer; grey areas show the cavities (pores). B. Blue areas denote the polymer construct; black areas show pores and interestingly, some changes in density created by the windows within each pore, evidencing interconnection between pores. Scale bars are 500 μ m. 99

Fig. 28. Histograms showing the pore volume and diameter against its frequency for the LM and 50% PCLMA. Error bars are included. 104

Fig. 29. Highlights of the isolation of pores in 50% PCLMA on the edges of the scaffold. Some of this pores have been highlighted in red squares. Dark grey colour represents the background. 105

Fig. 30. PGSM NMR for non methacrylated PGS and 30%, 50% and 80% PGSM. Peaks at 3.7, 4.2 and 5.2 ppm were compared to the chemical composition of glycerol, shown as a-c; and 1.2, 1.6 and 2.3 ppm for sebacic acid, as d-f. Methacrylated groups on peaks 1.9, 5.6 and 6.2 ppm were labelled as g-j. Possible residues of DCM solvent and water are also shown in c. 117

Fig. 31. DCM solvent extraction for 50% and 80% PGSM. PGSM batches tested for a year show a similar behaviour, reported in the figure below, and indicate a reproducible process. 118

Fig. 32. Transversal cuts on PGSM scaffolds. A thick crosslinked layer is observed on the borders of the scaffold, whilst the middle areas take longer to crosslink, or do not crosslink at all. Arrows indicate crosslinked areas. Scales are 100 μ m. 121

Fig. 33. A PGSM scaffold (exhibit 13 from previous experiment), has been imaged on both the internal (left) and edge (right) areas, with no significative difference in pore sizes. Scale bar is 500 μ m. 121

Fig. 34. SEM images for PGSM scaffolds under conditions labelled as 2, 4, 6 and 8, according to Table 4, mixed at 850 rpm. Pore geometries are mimicked in the small black boxes (at scale). Despite of all images showing high interconnection among cavities, they are heterogeneous in most of the cases. Only number 8 shows round pores, proper from HIPEs. 123

Fig. 35. SEM images for PGSM scaffolds under conditions labelled as 14-17 according to Table 4, mixed at 350 rpm. Pore geometries are mimicked in the small black boxes. Images 14 and 17 show big round pores (>250 μ m), but with irregular and heterogeneous small windows (<100 μ m). On the contrary, image 14 shows homogeneous circular medium size pores with small and round windows, even on the surface. Finally, image 16 illustrates irregular cavities, and no pores nor windows can be fully differentiated. 124

Fig. 36. Differences in volumes between D0, 10 and 14 for PGSM-50% scaffolds manufactured with single solvents and under different solvent and polymer:DCM ratios. 130

Fig. 37. Difference in construct densities between days 7-14, organised by: A. PGSM:DCM ratio; B. solvent concentration (0.25-0.70 ml); C. Type of solvent. 131

- Fig. 38. LightSheet imaging for PGS-50%. Three different PGSM:DCM ratios were tested at 4 different solvent volumes (0.25 - 0.70 ml) for chloroform. Scale bars: 500 μm . Crosses: unsuccessful emulsions. 132
- Fig. 39. LightSheet imaging for PGS-50%. Three different PGSM:DCM ratios have been tested at 4 different solvent volumes (0.25 - 0.70 ml), for toluene, DCM and DCE solvents. All scale bars are 500 μm . The crosses show unsuccessful emulsions. 133
- Fig. 40. LightSheet imaging for PGS-50%. Three different PGSM:DCM ratios have been tested at 4 different solvent volumes (0.25 - 0.70 ml), for DCM. All scale bars are 500 μm . The crosses show unsuccessful emulsions. 134
- Fig. 41. LightSheet imaging for PGS-50%. Three different PGSM:DCM ratios have been tested at 4 different solvent volumes (0.25 - 0.70 ml), for DCE. All scale bars are 500 μm . The crosses show unsuccessful emulsions. 135
- Fig. 42. Scaffold shrinkage for D0, D1 and D7 on PGS-50% scaffolds and DCE : Toluene solvent. 136
- Fig. 43. Reproduction of PGS-50% scaffolds scanned through $\mu\text{-CT}$, on xy (A), xz (B) and yz (C) planes. Scale bars are 1 mm. 138
- Fig. 44. Reproduction of PGS-80% scaffolds scanned through $\mu\text{-CT}$, on yz (A), xz (B) and xy (C) planes. 139
- Fig. 45. Histograms showing the pore volume against its frequency for the 50% and 80% DM PGSM. Peaks related to the limits of the analysis are inside of the orange squares, the full explanation can be found on Chapter III. Fig. 28. 142
- Fig. 46. The theoretical refractive index is calculated using a refractometer as shown above: a thin beam of light is directed to the block of material (bulk PGS polymer) and the angle of refraction is measured against the scale. 152
- Fig. 47. Roulette of scaffolds exposed for 5 days to the reagents on Table 19. The effect on transparency of the scaffolds is reflected on the order of the labels (1 and top right being the less transparent). 157
- Fig. 48. Non-homogeneous PCLMA – PGSM blends for tensile testing. This is evidenced by the difference in photoinitiator mediated crosslinking (even if they were exposed to the same height and distance from UV light), and the uneven break of the dogbones (usually closer to the middle of the thin layer). 161
- Fig. 49. Mechanical testing (tensile tests) was performed on PCL-PGS methacrylated polymers. Results for pure PCL-HM, PCL-80%, PGS-50% and PGS-80% have been included as reference. 162
- Fig. 50. SEM images of cross sections of PCL-PGS scaffolds. Images are labelled as 1-12 according to their recipe (Table 20). Images 1-5 were taken at 605x and 6-12 at 1775x of

magnification. The change in magnification is for pore morphology and average size to easily appreciated. 166

Fig. 51. Micro-CT reconstruction of a 50PCL-PGS50 polyHIPE. A) 3D structure of the scaffold. B) Thresholding technique on 2D to identify pores and windows. C) Volume rendering of the threshold showing pores within the scaffold. 167

Fig. 52. 2D micro-CT scans of 50PCL-PGS50 polyHIPE. Each image represents a different slice of the reconstructed scaffold. Regions with different colours exemplify the connection between pores on the xy axis. Additionally, pore interconnectivity can be observed between both images by tracking the big pore on the top left side; changing slides show how interconnectivity varies (increases-decreases) over the y axis. 168

Fig. 53. Histogram and pie chart showing the pore width distribution for PCL:PGS blend (50:50). 168

Fig. 54. PGS – PCL bilayer scaffold imaged at naked eye, and digital microscope. 80% PGSM (top layer) has been dyed in blue to differentiate from the 50% PCLMA layer (bottom). Difference in porosities is easily observed. 169

Fig. 55. PCL-PGS bilayer scaffolds (C) sliced using a scalpel (B) and a vibratome (A) observed under the digital microscope. The top layer (red) is made of 80% PGSM and the bottom (blue) of 50% PCLMA. 170

Fig. 56. Digital microscope images on the interlayer between PCL-PGS bilayer scaffolds (A,B), 50% PCLMA layer (C), and 80% PGSM layer (D). Magnification used was 4x and scale bars are 200 μm . 171

Fig. 57. Compressive tests on PCL-PGS bilayer scaffolds. Compression was made using a 25 N load cell and at a rate of 0.1 mm/min. The red layer is 80% PGSM and the blue layer is 50% PCLMA. 171

Fig. 58. Microspheres created by phase inversion on PCL-PGS 75:25, creating a W/O/W double emulsion. 175

Fig. 59. PCLMA scaffolds before and after being dried in a dark space at room temperature. Almost no shrinkage can be observed as pores retain their size, and their form. Scale is 500 μm . 181

Fig. 60. PGSM scaffolds before and after being dried in a dark space at room temperature. For sample ID refer to experiment in Section 4.4.1.3.2 of Chapter IV. A) 90:10-0.55 Chloroform; B) 90:10-0.55 DCM; C) 90:10-0.25 Toluene; D) 90:10-0.55 DCE. Scale is 500 μm . 182

Fig. 61. PGSM scaffolds dried by freeze-drying after being washed with single or combined solvents (Water-methanol, methanol-water, PEG-water). Total collapse is observed in all cases with change of solvent, and partial collapse on PEG samples. 183

Fig. 62. PGS-50% scaffolds submerged in deionised water, methanol, and polyethylene glycol 99% were frozen by slowly reducing the temperature (freezer) and temperature shock (liquid nitrogen). Afterwards, they were freeze-dried overnight. 184

- Fig. 63. PGSM scaffold was dried overnight using a freeze-dryer. The scaffolds were covered with aluminium foil with holes pierced on it to control the drying speed. 185
- Fig. 64. Gelatin-co-sugar disks produced by moulding (A). The differences in colour between B and C are consequence of the ratio between Gel, Suc and water. B) Sucrose b1; C) Sucrose a1. 187
- Fig. 65. Gel:Gluc disks on degradation assays with PBS at 37 °C. Stacked lines show the relative change of weight for each group of samples at a given time. uv/n-uv: UV/non-UV light treated. Mean \pm S.D. 187
- Fig. 66. UV treated Gel:Gluc disks on degradation assays with PBS at 37 °C. Stacked lines show the relative change of weight for each group of samples at a given time. Mean \pm S.D. 188
- Fig. 67. Histogram representing the relative differences in weight from UV treated (UV) and non-treated 189
- Fig. 69. Patterns of gelatine release on Gel:Gluc disks treated and non-treated with UV light, over 20 days. Gelatin combinations that are not represented after certain days have completely dissolved. Mean \pm S.D. 190
- Fig. 68. Release behaviour of gelatin in UV-treated (UV) and non-treated (nUV) Gel:Suc disks over time. The hydrogels were completely dissolved after 90 minutes. The patters or release were similar between 2:1:2 and 4:1:2 combinations. Mean \pm S.D. 190
- Fig. 70. PCLMA scaffolds submerged in Gel:Gluc B2 solution are sliced using a vibratome. B) The initial penetration of the hydrogel is observed where gelatin has been coloured in blue. C) A 100 μ m slice of the scaffold is observed under the digital microscope. The red line marks the border where the gelatin penetrated. 191
- Fig. 71. PCLMA scaffold fully immersed in a Gel:Gluc B2 solution stained with blue dye. 191
- Fig. 72. PCLMA emulsion with gelatin as internal phase. Photocured polyHIPEs with 5% gelatin as internal phase using LM (D-E) and 50% PCLMA (B-C). The diameter of the scaffolds is 8.9 mm. 192
- Fig. 73. LM (B,D) and 50% PCLMA (A,C) polyHIPEs with gelatin as internal phase imaged under a digital microscope at 4 and 10x magnification. 193
- Fig. 74. Degradation assays for LM and 50% PCLMA, in bulk and porous forms, under an alkaline environment, over 60 days. The degradation is expressed as a loss in mass. Grey lines represent the measured samples, averaged in the green line. The line in red is the control sample (scaffolds submerged in PBS). Mean \pm S.D, n = 4. 204
- Fig. 75. Digital microscopy images on bulk and porous PCLMA scaffolds. 205
- Fig. 76. Degradation profile of PGSM 80% solid blocks under PBS and NaOH 0.8M. Mean \pm S.D, n = 5. 205

Fig. 77. Degradation profile of PGSM 50% solid blocks under PBS and NaOH 0.8M. Mean \pm S.D, n = 5. 206

Fig. 78. Degradation profile for porous PGSM-50% scaffolds in NaOH 0.1 M. Assessed through volume and weight loss, both percentages show similar behaviour. Mean \pm S.D, n = 5. 206

Fig. 79. Degradation profile of porous PCL:PGS scaffolds in NaOH 0.1M. Loss is measured in volume and weight. Mean \pm S.D, n = 5. 207

Fig. 80. Resazurin assays performed on PCL and PGS methacrylated films seeded with Y201 cells. (Blue) attachment at D1 and (grey) cell metabolic activity at D7. C-S-: media control, C+S-: cell control, PGS C+: seeded PGSM scaffolds, PCL C+: seeded PCLMA scaffolds. Mean \pm S.D, n = 5. 207

Fig. 81. Y201 cells seeded on polymeric films. A) Cells at day 1, successfully attaching to the films. B) Cells at day 7, attached and proliferated on the films, but with a round morphology, associated with apoptosis. C) Confluent Y201 cells on well plates. D) Cell non-attached to the films, growing between the well plate and the film. Scale bars are 400 μ m. 208

Fig. 82. The effect of air plasma on PCL and PGS methacrylated films was explored by seeding them with Y201 cells and tracking their attachment on day 1. C+: cells control, PCL C/NC: PCLMA coated/non coated films, PGS C/NC: PGSM coated/non coated films. Mean \pm S.D, n = 10. 209

Fig. 83. Y201 cells were seeded on Gel:Gluc B2, C1 and C2 films to assess their metabolic activity over 7 days. C+: control, cell seeded on tissue culture plastic. As a reference Gel:Glu:dH₂O composition of B2: 04:01:08, of C1: 02:01:16, and of C2: 04:01:16. Mean \pm S.D, n = 5. 210

Fig. 84. A) Cell films' unity help them migrate through the degrading Gel:Gluc surface. B) Gel:Gluc has folded over itself, trapping some cells within; however, some colonies are looking for some empty space and move into the surface of the well plate. Scale bar is 100 μ m. 210

Fig. 85. Front images of a water droplet injected on the surface of PCLMA scaffolds. Images are taken after 5 seconds. The water contact angle was registered from the above images and reported in Table 22. These are representative images of 5 samples per variable. Scale bars are 0.5 mm. 211

Fig. 86. Y201 cells seeded onto PCL LM & HM scaffolds, coated and non-coated with air plasma. Their proliferation has been tracked for 7 days using Resazurin metabolic assay. LM C/NC: low methacrylation coated/non-coated, HM C/NC: high methacrylation coated/non-coated. Mean \pm S.D, n = 5. 212

Fig. 87. hES-MP cells were seeded on PCL LM & HM and their metabolic behaviour tracked for 14 days. The green dotted line shows the cells that were not attached to the scaffolds and their viability over the time. S-C+: cells control. Mean \pm S.D, n = 10. 214

Fig. 88. This experiment tested three different times in-between seeding and adding media for BAC cells on PGS 50% scaffolds. The ideal time was explored to optimise the number of cells attached and how that affected cell numbers over 28 days of culture. Mean \pm S.D, n = 10. 215

- Fig. 89. BAC cells were seeded onto PGSM 50 and 80% scaffolds. Their metabolic activity was tracked over 28 days. C+: cells control. Mean \pm S.D, n = 10. 218
- Fig. 90. PGSM scaffolds were coated with a 50 μ g/ml solution of fibronectin and seeded with Y201 cell. Their metabolic activity was assessed by Resazurin assays over 7 days. Mean \pm S.D, n = 5. 217
- Fig. 91. Attachment and proliferation of BAC cells on Gel-coated and Gel-FBS-coated PGS 50% scaffolds were assessed through Resazurin assays. C+: cell control, NC: non-coated, Gel C: Gel-coated scaffolds, Gel C + FBS: Gel-FBS-coated scaffolds. Mean \pm S.D, n = 10. 218
- Fig. 92. Silicon (PDMS) rings were placed on the edges of PGS 50% scaffolds to improve cell attachment. C+: cells control, R: scaffolds with rings, NR: scaffolds without rings. Mean \pm S.D, n = 5. 218
- Fig. 93. ALP assay on LM and HM PCL scaffolds seeded with hES-MPs for 21 days. Mean \pm S.D, n = 5. 219
- Fig. 94. A. The alignment of red fibrils can be observed. This evidences the spindle like morphology of hES-MPs and their behaviour as a culture, as well as the fibrous structure of the released collagen (25k cell, 2D culture). B. SRS does not show a significant change over the 21 days of the experiment. n = 3. 220
- Fig. 95. Sirius Red assay performed on 2D and 3D cultures of hES-MP cells on day 21. Three different cell concentrations have been trialled to see the impact of cell concentration on production of ECM. Mean \pm S.D, n = 5. 220
- Fig. 96. Alizarin Red assays showed a visible difference on mineral deposition over the 21 days of the experiment; n = 3. 221
- Fig. 97. An Alizarin Red assay was performed at day 21 on PCL-LM scaffolds seeded with different hES-MP cell concentrations. Mean \pm S.D, n = 10. 221
- Fig. 98. A. Alizarin Red and B. Safranin O assays on 2D experiments of hES-MP cells over 21 days; n = 3. 222
- Fig. 99. Cell viability for BACs on PGS 50% scaffolds, fed with BM and CEM media for over 28 days. Mean \pm S.D, n = 10. 223
- Fig. 100. The effect of the initial cell concentration on collagen deposition was studied on BAC cells seeded on PGS 50% scaffolds on day 21. Mean \pm S.D, n = 10. 223
- Fig. 101. A) SRS Experiments for BAC cells on 2D. B) SRS on a PGS 50% scaffold on day 21; n = 3. 224
- Fig. 102. Sirius Red Assay for BAC cells seeded on PGS 50% scaffolds. The assay was run on day 21 and 28 for 3D and only on day 21 for 2D, as it was used as a reference. Mean \pm S.D, n = 10. 224
- Fig. 103. Alcian Blue assays on 2D experiments of BAC cells seeded with 75,000 cells; n = 3. 224

- Fig. 104. Alcian Blue assays for the detection of GAGs on PGS HIPes seeded with BAC cells. The measurements were performed on day 21 and 28. Mean \pm S.D, n = 10. 225*
- Fig. 105. A. Alizarin Red and B. Safranin O assays on 2D experiments of BAC cells over 21 days; n = 3. 225*
- Fig. 106. Cytotoxicity assay of hES-MP and MLO5 cells on sodium alginate (SA) and calcium chloride (CC) surfaces, to assess the response of cells to the individual components of calcium alginate. C+: cells control. Mean \pm S.D, n = 5. 227*
- Fig. 107. Optical images of hES-MP and MLO5 cells encapsulated in calcium alginate beads and their natural degradation over 14 days. N = 5. Scale bars are 200 μ m. 227*
- Fig. 108. hES-MP and MLO5 cells were encapsulated on calcium alginate beads and mechanically pushed into PCL-HM scaffolds. Their viability was tracked for 21 days. Mean \pm S.D, n = 5. 228*
- Fig. 109. Model of a channelled scaffold using a flat ended Ga 14 needle. 236*

List of Tables

<i>Table 1. Media formulations and conditions for cell growing on primary and derived cells.</i>	77
<i>Table 2. Theoretical and experimental degrees of methacrylation for 3-arm PCLMA, 4-arm PCL low methacrylated (LM), 50% methacrylated, and high methacrylated (HM).</i>	87
<i>Table 3. Average molecular weights, average molecular numbers, and polydispersity values for 3 and 4 arm PCLMA, obtained through GPC. NM: non methacrylated.</i>	88
<i>Table 4. Mechanical properties of dry porous / bulk LM & 50% PCLMA materials.</i>	90
<i>Table 5. Experiment developed to identify the optimal recipe for a stable PCL emulsion during and after mixing. Variables changed were temperature (T) and water intake (ml). The success of the emulsions was evaluated by the absence of division and phenomena during and after mixing. Stirring speed in rpm; solvent made by a chloroform: toluene 6:4 wt relation; all percentages are in relation to the polymer weight. Successful results are shown in green. Total mixing time was 10 minutes.</i>	90
<i>Table 6. Shrinkage under normal aqueous conditions on LM and 50% PCLMA</i>	92
<i>Table 7. Densities of water and oil phase involved in PCLMA HIPE emulsions. *Chloroform and toluene solvents are not considered for the calculation of the internal phase as they leave the emulsion through its formation and are washed away during the washing process.</i>	94
<i>Table 8. Thresholding strategies to identify pores and windows within the scaffolds starts on the correct segmentation of areas. An independent labelling technique was developed on the 3D reconstruction, where only 6 neighbouring points were considered for pores to be “connected”. Scale bars are 1mm.</i>	100
<i>Table 9. GPC results for non-methacrylated PGS, 50% and 80% degree of methacrylation. Results show the average molecular weight, the average molecular number, and the polydispersity.</i>	117
<i>Table 10. PGSM trials. Constant variables included photoinitiator being added at the same time as the other ingredients, a mixing time of 3 minutes before adding the water, and a mixing time afterwards of 3 min for a total mixing time of 10 minutes. Successful results are shown in green. Symbols: * In more than 50% of the batches prepared. ⁱ Scaffolds does not crosslink homogeneously: the outside is stiff, but the centre presents a gel-like composition indicating poor light curing because of scattering.</i>	119
<i>Table 11. PGSM scaffolds were produced by varying the polymer : solvent ratio, volume of photoinitiator and mixing speed. Boxes coloured in red show mixtures whose phases could not integrate to form an emulsion. Yellow boxes show semi stable emulsions which had minor to medium complications when crosslinked under UV light. Green boxes describe successful emulsions, but particular pore features: * scaffolds were cured for 20 minutes (10 on each side) unless otherwise stated.</i>	120

<i>Table 12. Densities of water and oil phase involved in PGSM HIPE emulsions. *Toluene solvent is not considered as it leaves the emulsion through its formation and is washed away.</i>	124
<i>Table 13. The density of solvent free emulsions is expressed as the sum of the partial densities of the reagents in the oily phase (polymer:solvent, surfactant and photoinitiator).</i>	127
<i>Table 14. Details of compositions on 50% PGSM PolyHIPEs prepared by using no solvent and single solvent of DCM, chloroform, toluene or DCE, and three polymer:solvent ratios (70:30, 80:20, 90:10 w/w). All volumes (V) are in ml. P/N: Porous/non-porous structure, N/Y: no/yes, NDP: non-defined pores.</i>	128
<i>Table 15. Densities of the polymer solution and oil phase for the study of emulsion stability with double solvents. The proportion of each component is stated in terms for the oil phase with and without solvents, for future considerations of theoretical porosity.</i>	135
<i>Table 16. PGS-50% emulsions were manufactured by varying the solvent composition (toluene and DCE). The table reports on the volumes per component, densities, their behaviour during and after mixing, and their porosity.</i>	136
<i>Table 17. Tensile and compressive tests results on PGSM 50% and 80% D_M. * Cannot be determined as the scaffold could resist loads higher than 250 N, which was the highest load available at the lab.</i>	137
<i>Table 18. Thresholding strategies to identify pores and windows within the scaffolds starts on the correct segmentation of areas. An independent labelling technique was developed on the 3D reconstruction, where only 6 neighbouring points were considered for pores to be “connected”. Scale bars are 1 mm.</i>	140
<i>Table 19. Porous PGSM scaffolds were submerged on the reagents below (organised in ascendent order). The ID column is related to Fig. 44, with random scaffolds selected for visual assessment on day 3.</i>	153
<i>Table 20. Successful (stable) emulsions and their viscosity observed with naked eye.</i>	163
<i>Table 21. Combinations of PCL:PGS at 25:75, 50:50 and 75:25 to identify stable emulsions and the impact of type and solvent ratio (chloroform, toluene and DCE). The quantities in brackets in the last column, represent the volume of water that could not be absorbed by the emulsion or that was released during the emulsion coalescence.</i>	164
<i>Table 22. Sucrose and glucose combinations used to produce Gelatin-co-sugar disks. All ratios are in grams. The state of matter was assessed 10 minutes after the mix was exposed to the temperature.</i>	186
<i>Table 23. The changes in wettability are registered below. Values between 0 ° and 90 ° indicate hydrophilic surfaces; whilst 90 ° to 180 ° angles indicate hydrophobic surfaces. All values are in degrees. *: sample compromised. ** < 5 degrees.</i>	212
<i>Table 24. Parameters considered to choose the ideal PCL scaffold.</i>	213

List of Fabricated Materials

Chapter	Material	Abbreviation (if applicable)
III	Polycaprolactone	PCL
	PCL methacrylate	PCLMA
	PCLMA polyHIPEs	
IV	Poly(glycerol sebacate)	PGS
	PGS methacrylate	PGSM
	PGSM polyHIPEs	
V	PCLMA and PGSM blends	PCLMA-PGSM blends
	PCLMA and PGSM blend polyHIPEs	PCLMA-PGSM HIPEs
	Bilayer HIPE (PCLMA and PGSM)	
VI	PCLMA with gelatin as internal phase	PCLMA-Gel
	Gelatin disks	Gel
	Gelatin and sucrose disks	Gel:Suc
	Gelatin and glucose disks	Gel:Gluc
VII	MLO5 and hES-MP cells in alginate beads	
	Cells encapsulated in alginate in PCLMA HIPEs	

Chapter I: Literature review on osteochondral units and polymer emulsions

1.1. Background

1.1.1. The Knee

1.1.1.1. Physiology and anatomy of the knee

The knee is a large and complex joint. Formed by the patellofemoral and the tibiofemoral articulations, it creates a hinge that supports general mobility and loading. Its stability is achieved through several ligaments, tendons, the synovial capsule, and complementary muscular components [7]. The osseous elements of the knee joint are the fibula, the femur, the tibia, and the patella. As defined by Hirschmann *et al* (2015), anatomy follows function [8]. The arrangement of parts allows the knee to extend, flex, rotate and glide. The meniscus, a semi-circular fibrocartilage tissue, is located between the femoral condyles and the tibial plateau for extra shock absorption. The anatomy of a normal knee can be found below.

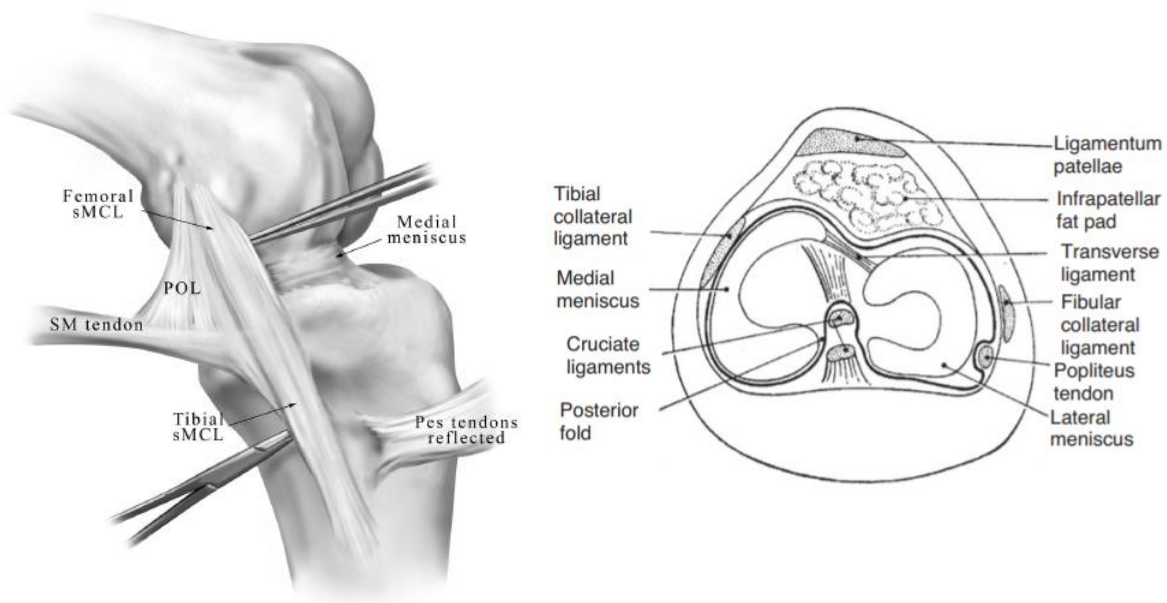


Fig. 1. Left: superficial medial region of the knee showing the different components [9]. Right: Transverse section of the knee [10].

The knee joint is formed by the medial and lateral tibiofemoral, the patellofemoral, and the proximal tibiofibular joint. Ligaments provide stability to the knee joint, through its 6 degrees of freedom: including rotation (flexion-extension, internal-external and varus-valgus), translation (anterior-

posterior and medial-lateral) and internal (compression-distraction) movements [8]. The movement of the knee is controlled by the ligaments and their coordinated functioning.

The menisci are a dynamic reservoir located in the anatomical incongruity of the femoral condyle and the tibial plateau. The medial and lateral meniscus support the gliding, rolling and rotation of the knee, and are connected to tendons and ligaments for dynamic movement, and signal communication [8].

The bones of the knee (femur, tibia, patella, and fibula) are interconnected by the ligaments into the joints of the knee. The patella is a semi-flat bone that protects the knee elements from trauma; it moves when bending and extending the knee, gliding between the femoral condyles and the patellofemoral groove. The femur is the longest bone of the body and is characterised by the condyles, round knobs at the end of the knee. The tibia runs in the opposite direction, terminating in the ankle, and is made of two plateaus (flat surfaces). The menisci are attached to each of them, and an extra protuberance located in the anterior part, called the tibial tubercle, attaches to the patellar ligament. The fibula is a long bone that runs thinly next to the tibia and carries a small proportion of its weight [11]. The surface of the osseous parts of the femur and the tibia are covered by articular cartilage which bears the load and cushions through movement. The articular cartilage is in contact with the menisci and acts as extra pad [12].

1.1.2. Macro and microstructure of the osteochondral unit

The subchondral unit is composed by articular cartilage (type II) surrounding the osteochondral bone. This arrangement allows the joint to balance through compressive, tensile and shear stresses. The osteochondral unit is formed by a top articular layer, a tidemark, and the subchondral bone (Fig. 2).

1.1.3. Articular cartilage (AC)

The biomechanical composition of this layer is a representation of the organisation of the extracellular matrix (ECM). This thin whitish layer [13] is formed by collagen (20% wet weight), proteoglycans (5-10% / especially aggrecan) and water (65-85%). The water residing within the articular cartilage is in free contact with the synovial fluid. Negatively charged aggrecan core proteins link to hyaluronic acid, to form proteoglycan aggregate. Crosslinked type II collagen strands, traps the proteoglycan aggregate, forming an organised network. The collagen network provides the tensile strength, whilst the proteoglycan aggregates provide the compressive resistance [14].

The collagen fibres are arranged in a pattern highlighted in Figure 1. The cellular density of the articular cartilage varies from layer to layer, and only comprises 1-2% of total cartilage volume, but can be as low as 1,000,000 cells per cm³. The anatomical-structural levels also have an impact on the

cell's morphology; cells show a flat morphology in the superficial layer and change into a round morphology in the central layers of the cartilage, closer to the subchondral bone. Additionally, near the surface the collagen fibrils align tangentially to the top layer, and bend in an anisotropic way. Fibrils in the other layers, respect a perpendicular arrangement (Fig. 1). The low cellular density and the anisotropic cell morphology affects the ability to repair wounded tissue and heal by itself. Finally, the graded mechanical properties vary throughout the cartilage, according to its structure and composition [15].

It has been found that the cartilage thickness varies from joint location and within the tissue. The range of thickness goes from 0.4 to 3.5 mm, with the thinnest AC located in the ankle and the thickest in the knees, followed by the hip [16]. It has also been shown that within the AC unit, thickness increases directly proportional with the load needed to be borne [17].

The orientation and alignment of the collagen fibres and cell composition depends on the depth of the chondral unit [13]:

- a. The superficial layer represents 10-20% of the total thickness and possesses collagen fibres aligned along the surface of the cartilage. Big flat and elongated cells, densely packed, produce lubricin that promote low-friction properties; there is a minimal concentration of glycosaminoglycans (GAGs), apart from these proteoglycan superficial zone proteins (SZPs). Chondrocytes in this layer are called “persistent chondrocytes” [18], and are good for dissipating shear forces.
- b. The intermediate zone has a major density of cells and collagen fibrils. It represents 40-60% of the chondral unit. Thick collagen fibrils are linked to each other by thinner fibres, creating an environment where roundish chondrocytes distribute and proliferate. The high concentration of GAGs increases the hydrophilicity hence being more sensitive to compression forces.
- c. The radial zone is formed by large fibrils and proteoglycan molecules. It accounts for 20-50% of the tissue's thickness. Elongated chondrocytes (hypertrophic) organise perpendicular to the subchondral bone, however this area has the lowest cell density. Due to its proximity to the subchondral bone, various types of collagen can be found here apart from II type, as Collagen X and Collagen I.
- d. Between the radial deep zone of the articular cartilage and the subchondral bone, two thin layers lie together, the tidemark and the calcified cartilage. The latter is the final basal layer, being rich in apatite and alkaline phosphatase.

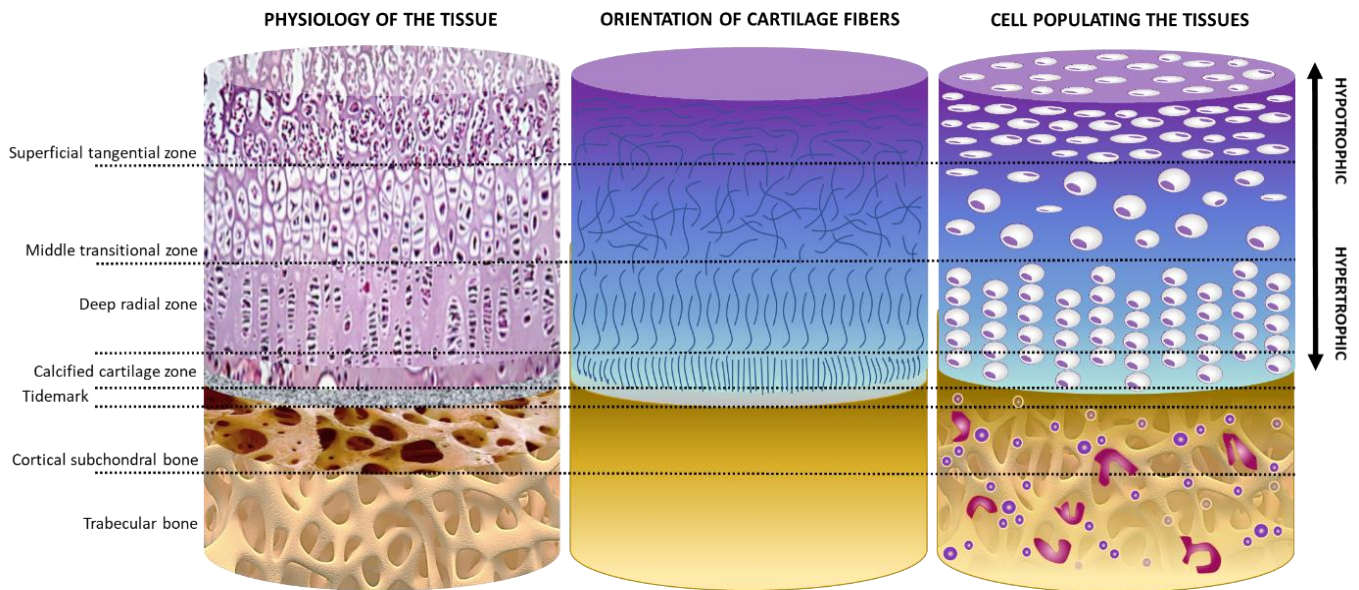


Fig. 2. The 4 layers of the articular cartilage are represented herein. Histology cuts (left) show cells within the ECM. The orientation and organisation of collagen and elastin fibrils can be observed in the middle figure: the superficial zone is formed by fibrils aligned tangential to the surface; the middle zone is saturated with highly entangled, non-aligned fibrils; the deep layer followed by a calcified cartilage possess parallel oriented fibrils. A third diagram (right) displays cell density: a hypertrophic high flat-cell density in the superficial layer; low round cellular density on the middle layer; and an aligned round cell density on the deep and calcified zone. Source: Author.

1.1.4. Tidemark

Set as the border between the deep zone of the hyaline tissue and the calcified cartilage, its role has not been fully defined. The trilaminar microanatomy of this layer serves as the anchor to the subchondral bone, and aids the force transmission in the joint, even supports the underlying bone nutrition [19]. It is also believed to contribute to the release of pro-angiogenic factors to the basal layers of wounded cartilage (hypertrophic or cracked). It has shown to thicken when the AC layer gets thinner in osteoarthritic (OA) patients [20]. The calcium-rich layer is able to bear compression and lateral shear forces, providing a stable matrix for the calcified cartilage and a communication channel (responsive) with the bone [21].

1.1.5. Subchondral bone

The subchondral bone lays distal to the calcified layer of the articular cartilage, the subarticular spongiosa. The definition of the subchondral bone is ambiguous, but it can be agreed that it comprises

the area between the calcified zone of the articular cartilage, and the subchondral trabecular bone [22]. The subchondral bone plate, or subchondral zone, is richly innervated and vascularised with a strong interaction with the articular cartilage. The cortical tissue of the bone plate has shown to be saturated with nerves and vessels, localised in channels in the areas of more stress [23]. Accordingly, the porous trabecular bone supports the plateau and provides nutrients to upper layers, metabolically active.

The calcified cartilage extends to the bone marrow cavity in various thicknesses, where it is remodelled and replaced by lamellar bone (bone sheets), similar in composition to the underlying trabeculae bone. The porosity of this layer is oriented to the direction of the lamellar sheets, with plates of 0.2-0.4 mm and pores of 0.4-0.6 mm [22].

The trabeculae in the spongy bone are oriented differently depending on the bone location and mechanical stimuli. This respects Wolff's hypothesis, which describes the dependence of internal architecture and external conformation of the bone, to the direction and magnitude of the mechanical load it sustains locally [24]. The anatomy of the subchondral unit is highly variable, the pores of the subchondral bone plate are connected to the marrow cavity of the subarticular spongiosa and vary from a round sack to a channel-like structure depending on its location; and as mentioned before, tend to accumulate on areas of greatest stress. This can be directly linked to a denser vascularization (15-25% more), and these channels are the ones used by the bone marrow in some surgical techniques. The advantage of having such well-connected channels, is that the nutrient supply can also reach the cartilage layers easily [25].

Bones are populated by three types of cells, osteoblasts, osteoclasts, and osteocytes. Osteoclasts, which have a macrophage origin, are involved in bone remodelling, since they resorb bone matrix. This is balanced by pluripotent mesenchymal cells known as osteoblasts and osteocytes, which mediate bone formation. The remodelling process responds to natural skeletal turnover mechanisms, and to external stimuli. Finally, osteocytes allow the formation of an interconnected network with the osseous area and are responsible for responding to the biomechanical and chemical signals in the extracellular matrix, regulating cell-cell interactions with osteoblasts and osteoclasts (Fig. 3).

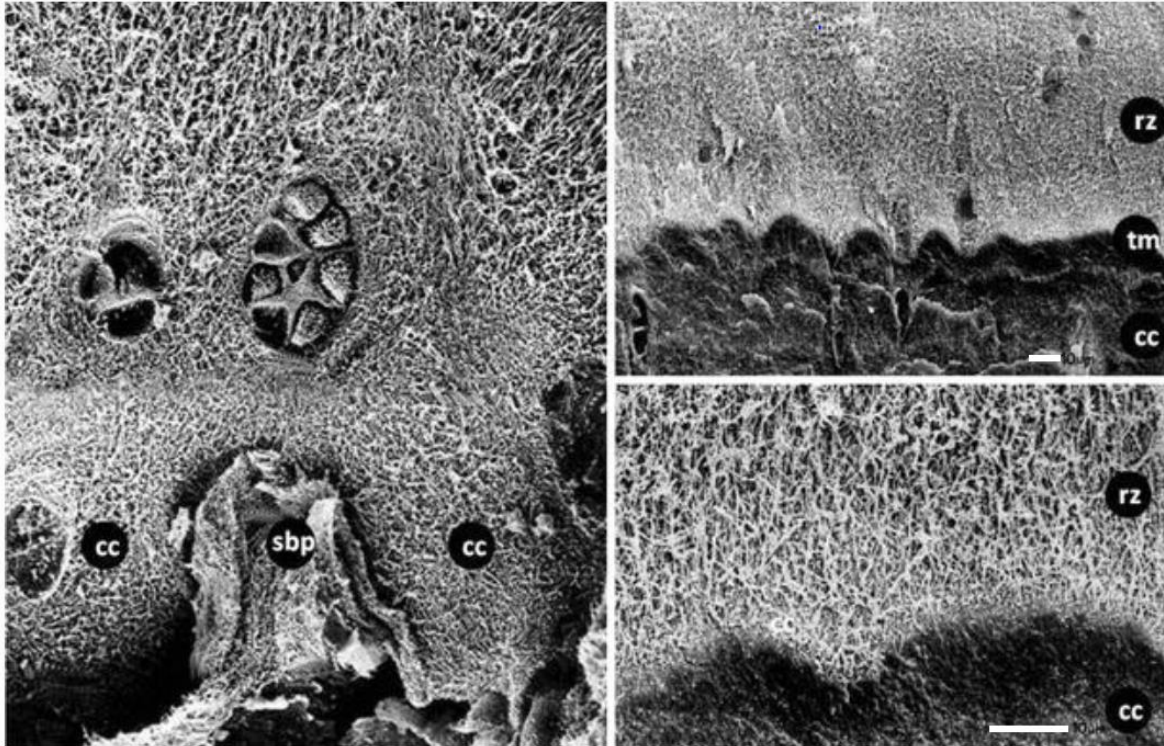


Fig. 3. SEM micrographs of the bottom zones of the articular cartilage and the subchondral bone. cc: calcified cartilage, sbp: subchondral bone plate, tm: tidemark, rz: radial zone [26].

1.2. Mechanisms of osteochondral repair

Depending on the skeletal location, mesodermal or ectodermal progenitor cells differentiate into skeletogenic mesenchymal cells. Among the most relevant molecules coordinating this process are fibroblast growth factors (FGF), bone morphogenetic proteins (BMP), sonic hedgehog homolog (SHH) and its related ligands. Their signalling regulates the condensation of skeletogenic mesenchymal progenitor cells which express transcription factors, determining the differentiation into chondrogenic and osteogenic [27]. These proteins are additionally up or downregulated by the growth factors (BMP, FGF and SHH) and ligands. Bones can be formed through endochondral or intramembranous ossification. The first process is the most common; chondrocytes produce a cartilaginous template that mineralises, whilst intramembranous ossification involves the production of bone directly by osteoblasts (bone forming cells) [28].

Osteoblasts come from pluripotent mesenchymal cells which can differentiate into adipose, myocyte, chondral and bone tissues. During the bone formation, osteoblasts produce collagen type I. Additionally, they support the mineralisation process where phosphates from the osteoblast matrix

vesicles join molecules of calcium (ECM liquid), forming hydroxyapatite crystals (inorganic mineral part of the bone). On the other hand, chondrocytes create a homogeneous complex network of proteins, glycoproteins and collagen type II (hyaline cartilage), where both the composition of the ECM and the fibrils orientation/organisation define the physical and chemical properties of articular cartilage.

1.2.1. Osteochondral defects

Osteochondral defects (OCD) can either be diagnosed after traumatic and non-traumatic aetiologies. The most relevant ones are osteoarthritis (OA) and *osteochondritis dissecans*.

Depending on a wide variety of factors, as age, gender, lifestyle, and genetics, these aetiologies can lead to joint degeneration. OCD defects classification has allowed researchers to differentiate the severity of the injury and therefore the treatments available. Cartilage damage has also been linked directly to OC injuries and usually to secondary OA diagnosis [29]. It has been reported that injuries to elements in the knee such as ligaments, menisci, joint capsule and the synovial fluid, are associated with cartilage damage [30].

As previously mentioned, OA is mainly related to aged people whilst other OC defects and early OA diagnosis' rates keep increasing in both high-performance athletes and the general female populations. Reasons for this are usually entailed to the women's knee anatomy and the distribution of load per surface area [31], and high loads on articulations in contact and impact sports.

Normal cartilage is able of bearing 2.5-5 times the load generated by walking. However, when assembled in the osteochondral unit, the subchondral bone absorbs about 30% of the load and only 1-3% is distributed onto the articular cartilage [22]. It has been reported that when a small injury in the osteochondral unit occurs (less than 3 mm diameter and low grades in the Outerbridge classification), an immediate recruitment of mesenchymal cells leads to the formation of an early cartilage-like tissue next to the damaged chondral area. Later, the morphology of chondrocytes changes from round to large and become hypertrophic [32]. Secretion of collagen type X and angiogenic factors promote vascularisation of ECM, enriched with apoptotic chondrocytes that left behind a useful matrix for the subsequent formation of the subchondral bone [33].

After high (25 MPa) and / or chronic impact loading, cartilage ECM has shown a loss in proteoglycans (PGs), which can be caused by the inability of the tissue for synthesising it, or to a degradation of the tissue itself [30]; even with an intact subchondral bone.

Osteochondral defects have a different mechanism of action as they progress and/or an injury happens [34]:

- A. During a trauma, haemorrhage follows immediately after the injury. Otherwise, the process will happen slowly. Chondrocytes go catabolic in response to mechanical stress. Inflammatory molecules like cytokines and necrosis factors lead to the degradation of the ECM.
- B. As a counterattack, anabolic chondrocytes seek for regeneration of the ECM through an over-production of collagen and proteoglycans; regulated by growth factors, including transforming growth factor (TGF- β) and platelet derived growth factor (PDGF).
- C. After two weeks, chondrocytes have gone hypertrophic and round. They start to express collagen type X and undergo apoptosis. This generates osteophytes (bone spurs) and the destruction of the articular cartilage.
- D. Dedifferentiated fibroblastic-like chondrocytes produce collagen type I, II, and III. This is, a fibrillar tissue.
- E. Ossification of the remaining cartilage matrix (bottom layers) happens through endochondral ossification.

However, the fibrillar / hyaline-like healed cartilage and the remodelled subchondral bone unit rarely perform as it used to.

1.2.2. Osteoarthritis

Osteoarthritis is a slow progressive, chronic, and degenerative disorder that affects both the articular cartilage and the subchondral bone (Fig. 4).

Characterised by chronic pain, joint instability, and degenerative lesions on the components of the joint, OA is the most relevant OC defect in the UK. This multifactorial pathology corroborates age, gender, and trauma risk factors, but also include genetic predisposition, inflammation, metabolic and hormone syndromes. OA commits both cartilage and bone mechanisms simultaneously; on one side the formation of osteophytes and alterations to bone remodelling, and the changes in menisci and synovium capsules matrices [20].

The evolution of osteoarthritis can be observed in the figure below, as can be broken down into the following stages [14]:

- A. On the cellular level, chondrocytes are altered from their non-stressed state where collagen type II and the sulphated proteoglycans share an anabolic environment. As the water increases,

biomechanical forces, growth factors and the presence of cytokines switch chondrocytes to a catabolic phenotype that also activate factors that complement the degeneration process. For example, disintegrins, matrix metalloproteinases (MMPs) and thrombospondin motifs [35] [36]. The cortical porosity increases as well as an acceleration on bone remodelling.

- B. As the organisation of the extracellular matrix is altered, chondrocytes release free radicals and the proteoglycan and collagen network breaks down. This is the moment where a loss of cartilage can be perceived. On the subchondral bone, the thickness of the cortical phase increases, but the bone mass decreases, as its architecture thins.
- C. Fissuring and disintegration of the cartilage layer is followed by the formation of osteophytes and bone cysts.
- D. A late OA is characteristic of an extension of the calcified cartilage into the fragmented articular cartilage, still populated by now apoptotic chondrocytes. The tidemark has thickened, and the abnormal head bone is full on cysts.

Even though the involvement of both aspects can be visible in synergy, it has been shown that changes in the subchondral bone can trigger and impact the development of OA. A study assessing mineralisation of subchondral bone blocks found that osteoarthritic both weight-bearing and non-weight-bearing, had a lower degree of mineralisation, than normal ones in young and aged bone blocks [37]. Additionally, it was thought that possibly the loss of mechanical properties of the bone could affect the stability provided to the articular cartilage; a subchondral bone was replaced with cement (2.6 times stiffer than cancellous bone). However, the deformation of the articular layer was uniform in both arthritic and cement joints. It was later demonstrated that the OA subchondral bone increases its mineral activity (remodelling) by increasing the thickness of the cortical bone, although in an under-mineralised tissue [38]. Contrary, it doubles the area per volume of the subchondral trabecular bone (low density), complemented by the appearance of osteoid. This shift to lower density is mainly found on the surface of the subchondral bone, this is, the heads of the femur and tibial.

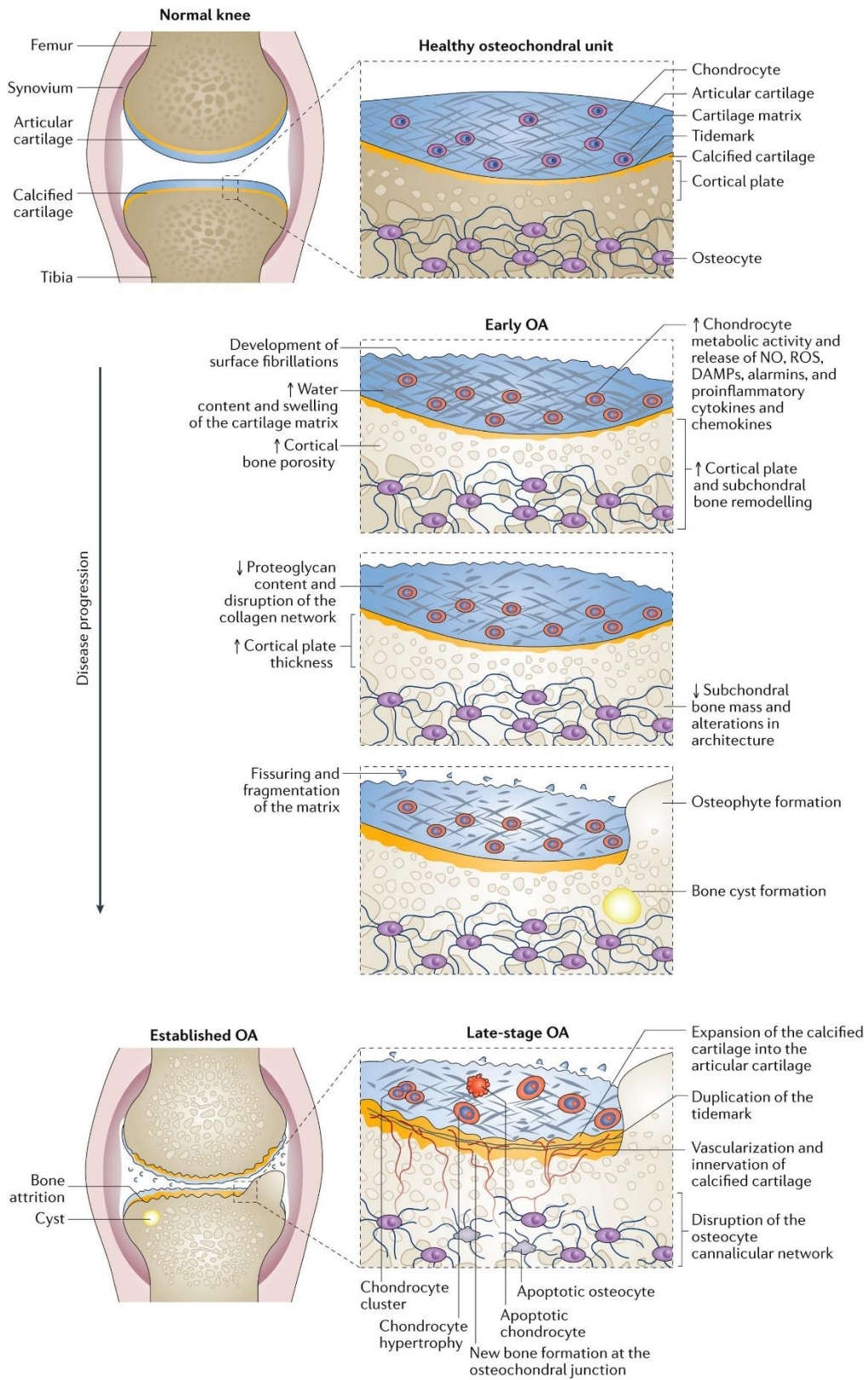


Fig. 4. Development of osteoarthritis in the knee joint [14].

1.3. Osteochondral regeneration

1.3.1. Current clinical treatments

In the early 1980's transplantation was seen as the promise for large organ and tissue defects. However, scientists and physicians recognised the complexity, and risk, of these procedures. Paul Russel, in 1985, published a review on cell transplantation and emphasised that if there was a way to transplant only the essential cell components, it could be more advantageous for both the surgeon and the patient. He called this, selective transplantation [39]. It was thought one of the promising areas would be cartilage regeneration, due to the tissue consisting of a single cell type and being free of nervature and blood vessels. However, soon it was discovered the challenge of replicating the complex internal structure of the cartilage, as well as the layers of contact with the subchondral bone (the interlayer) and the ECM.

Initially, pharmacotherapies were proposed as a corrective measure to offer immediate improvement of motor skills and pain symptoms. As they are a temporal solution, new proposals seek to inhibit molecules such as MMPs, pyrophosphates (linked to osteoporosis), and neurovascular growth [35]. However, challenges in adverse effects, molecule targeting, and durability still need to be addressed.

Clinical management of early OA patients includes a first phase of life-style modification and a second surgical treatment. Despite their success in restoring joint mobility, increasing the articulation function and delaying further degeneration [40] [41], they still represent invasive-incision techniques with no warranty on the immune response of the host body. Surgical treatments to address cartilage and subchondral bone repair include arthroscopic debridement, microfracturing, mosaicplasty, partial or total replacements, and TE approaches [42].

The main objective of the bone marrow stimulating (BMS) techniques is to condense mesenchymal cells from the bone marrow and activate the healing system through natural means. Both subchondral drilling (Kirschner wire) and microfracturing are BMS techniques. Usually for smaller lesions (< 4cm²) microfracturing is used as it is less invasive. Bigger lesions and related to OCD are treated with drilling, so deep holes can ensure enough bleeding and cell supply [43].

Various studies have shown cancellous bone after 4 weeks and fibrocartilage cover after 8-12 weeks. However, excessive bleeding in donor tunnels have raised problems as patients require debridement to prevent septic complications, and even sometimes a second surgical intervention. Additionally, even though fibrocartilage tissue can work for load-bearing areas, it increases the risk of failure post-intervention. Some early proposals included filling up the empty tunnels with biocompatible and

biodegradable materials as polyglyconate-B [44]. For example, this procedure has been well received in talus applications, partially linked to the anatomical design of the joints and the distribution of forces whilst moving. Clinical researchers have found that in osteoarthritic patients reported with Grade 4 in the knee, only a grade 2-3 was visible in the ankle joints [45]. Pain and functional assessment scores were lower in mosaicplasty than in micro-fracture, and recovery was faster. These results were improved, when adding supplements as platelet-rich-plasma [46, 47].

Autologous Osteochondral Transplantation (OAT) or mosaicplasty, is a technique that allows implanting autologous hyaline cartilage-bone plugs for OCD. OAT is used in cases where debridement or BMS is not responsive (bigger than 150 m²) and with cystic components, and areas of vascular insufficiency, especially in the talus [48]. However, as with many of the autologous techniques, frequent infections and comorbidities have sometimes even led to avascular necrosis. Additionally, there is little evidence of chondral integration [49].

Tissue engineering proposals use of a variety of natural and synthetic materials in combination with different sources of cells to restore the balance in the host tissue. Early autologous chondrocyte implantation (ACI) set the first seeds on cell transplantation techniques, whilst encountering problems with defect size and donor site morbidity [50]. Later improvements resulted in matrix guided autologous chondrocyte implantation (MACI) and gel-type ACI (GACI), the third-generation implants. Both MACI and GACI keep the advantages of ACI procedures, simplifying the surgical technique. Better re-differentiation of seeded chondrocytes has been shown after 5 years post-treatment [51] with a low failure rate (1-8%). A clinical study was developed comparing microfracture (MFX) and MACI treatments, 28 months after the intervention. There was no significant difference between appearance of subchondral oedema, cysts, and granulation tissue, despite their presence in most cases. Cartilage repair was slightly better in MACI patients, with the big advantage of differentiated chondrocytes to form more hyaline-like tissues. Additionally, MACI is considered a better option on large size defects (up to 10cm²) [52]. Regardless of the good news, rigorous selectivity of patients (young ages, limited injury location & state of gravity), the condition of their osseous joint bed, and painful post-surgical symptoms, limit its implementation [53].

GACI is a fibrin gelatinous scaffold with implanted chondrocytes. The gel solidifies in contact with the body, adapting to the volume and form of the defect. It has been reported to form hyaline-like cartilage [54], even though existing doubts between fibrin glue and transplanted chondrocytes. Whilst improving the postoperative scores for mobility and pain at 2- and 5-years post implantation [55]. Only few peer reviewed papers have been published and they mention a delayed cartilage repair, and almost 40% of the patients have required a second intervention due to pain [56].

Additionally, the nature of the procedure makes it difficult for further histology tracking systems to be implemented and regeneration to be quantified. For example, the new tissue engineering procedures, due to their novelty, are implemented in surgeries as freehand procedures, which can be linked to replication error. Koulalis *et al*, compared knees of cadaveric bodies where either freehand or opto-electronically navigated procedures for osteochondral transplantation have been performed, and found improved accuracy on the navigated ones [57]. However, as exemplified here, the limitation of imaging systems and the ability of taking samples from the treated patients, limit the depth of study post-surgery.

Small osteochondral defects have been treated in research using mono and poly-phasic scaffolds, with promising results [58, 59]. Trying to mimic the host body, these structures are composed of either a single layer that resembles the cartilage structure and invites blood vessels/nerves to grow in the basal layer (as subchondral bone), or multi-layered scaffolds. However, only a few novel cell-free products have renewed approval for clinical implementation, MaioRegen®, TruFit® Plug, and Agili-C®. Independent from the preliminary results, follow-up data is yet not significant and show failures and complications after years of implantation [60] [61] [62] [63, 64].

A clinical trial developed by the University of Helsinki compared BSA techniques versus coll-HA MaioRegen® scaffold, tracking for 2 years, imaging (MRI-MOCART), pain (VAS index), KOOS (Knee Injury and Osteoarthritis Score), IKDC (Knee Examination form) and Tegner scores. The results showed that BMS are more optimal treatments for cartilage-only lesions, and coll-HA, suited for OCD [43]. Nonetheless, they did not find significant differences in any of the aforementioned values. It was also identified that the cartilage tissue formed during the healing process was fibrous, congruent with other research groups. Semi-qualitative subchondral measures found a slow bone healing, but enhanced osteoconduction [65, 66].

TruFit® plugs are three dimensional matrices made of poly-lactide-co-glycolide copolymers, incorporated in two porous layers, supplemented by calcium sulphate (in the bone part) and a surfactant (in the cartilage layer). They have not been as successful as their neighbours. With a slower and sometimes unusual incorporation rate (up to 24 months) [66], and a small clinical improvement on IKDC scores, they have a failure rate of almost 20% [67, 68]. Additionally, there is no evidence of osteoconductive bone ingrowth [67].

In both commercial scaffolds, cysts, granulation tissue and oedema have been observed. Even if this has not been reported as affecting the overall outcome of the treatment, its presence has been noticed in most of the referenced studies.

The latest product launch was developed in Israel and consists of an aragonite-based porous scaffold. Agili-C® aragonite's structure is formed by calcium carbonate in the stiffer part, and hyaluronic acid in the superficial cartilage phase. Even though it has shown pre-clinical advantages to recruit cells on both layers, only one report in literature exists for post-surgery examination (18 months), and only mentions promising restoration of the articular layer [68].

Imaging of progression and improvement of cartilage treatments has not been fully developed. Current techniques are evaluated through magnetic resonance imaging (MRI), using an evaluation system called MOCART (Magnetic Resonance Observation of Cartilage Repair Tissue), and are effective for chondral tissues. Some research groups have modified the techniques to apply on osteochondral trials, yet with some sensitivity limitations [69]. Expensive alternatives include single photo emission computerised tomography/computerised tomography (SPECT/CT).

It is important to notice that no effective therapy has shown to prevent or reverse the progression of OA.

1.4. Biomaterials for osteochondral regeneration

For the last decades, there has been an increase in the surgical interventions on OCD. As described above, some of them have found the way of keeping low to no immunity reactions, whilst providing a frame for host cells to populate; unluckily they have only shown encouraging short-term results. On the contrary, early tissue engineering techniques involving bioactive and biocompatible materials have not yet fulfilled the biological and mechanical requirements to ensure neo-tissue formation. One of the most important elements for a successful tissue regeneration technique is the choice of material. Herein, some of the most promising biomaterials for osteochondral regeneration are introduced.

1.4.1. Hydrogels

Hydrogels in their wet state allow the exchange of water, glucose, and oxygen molecules, which diffuse depending on the gelation techniques and the solution concentration. A variety of hydrogels from natural and synthetic sources have been proposed for clinical and research applications [70, 71].

1.4.1.1. Alginate

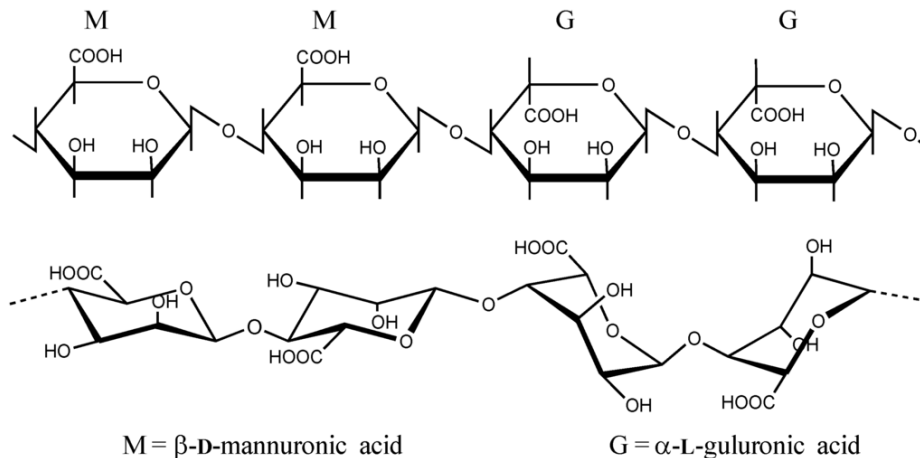


Fig. 5. Alginate is formed by mannuronic and guluronic acid arranged in homopolymer blocks (MM, GG) alternated with regions with MG blocks (at different ratios) [72].

Alginate is a natural polysaccharide obtained from brown seaweed, although some novel research proposed bacteria as an alternative source [73]. Its linear formation alternates guluronic and mannuronic acid in different ratios, affecting the physicochemical and rheological properties (Fig. 5). Alginates possess low toxicity, medium degradability, and a chemical versatility, useful for drug / molecule delivery and cell transportation [74]. By being crosslinked through ionic or covalent means, it can form stable gels in aqueous media and undergo chemical functionalisation, the reason why it is used as wound dressings, for molecule diffusion and as secondary materials (due to poor mechanical properties) [75, 76].

Alginate has an advantage for bone and cartilage regeneration, as it can be introduced to the body in a low invasive way (injected), with versatility of shapes and chemical properties (crosslinking, swelling and degradability). The treatment of bone injuries has been enriched using alginates to primarily deliver growth and osteoinductive factors [77, 78, 79] or to support bone regeneration processes [80] [81].

Similarly, alginate has proved useful to transport chondrocyte and stem cells to restore damaged or degraded chondral tissue. The manufacturing of constructs mimicking host collagen has been developed to the point of minimal surgery intervention, where a lyophilised or dehydrated version of the alginate is injected, following further *in situ* hydration and gelation. Results from long experiments (30 week) with chondrocytes suspended in a sodium alginate / calcium sulphate solution showed high levels of proteoglycans and collagen formation [76]. Additionally, encapsulation of stem

cells seems to regulate chondral cell differentiation (alginate promotes round cell morphologies) [82]. Finally, some experiments using alginate as mono-layer of bi-phasic scaffolds to treat osteochondral defects; showed viability and differentiation after 3 weeks [83].

1.4.1.2. Gelatin

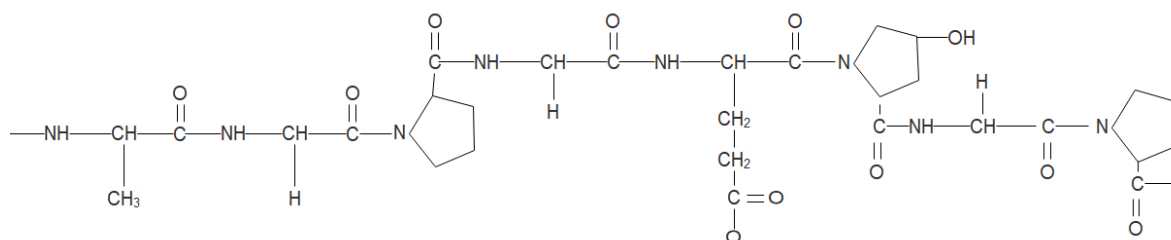


Fig. 6. Typical gelatin structure formed by glycine, proline and 4-hydroxyproline residues: -Ala-Gly-Pro-Arg-Gly-Glu-4Hyp-Gly-Pro-.

Gelatin is a natural hydro soluble biopolymer, irreversibly denatured from collagen. The source of gelatin has mainly been from animal raw materials, porcine and bovine being the most common ones, but including fish skins and bones [84]. Their origin defines its specific amino acid composition hence their material properties, as the amino acid components differ, specially for alanine, proline, arginine and serine. The typical structure of gelatin can be found in Fig. 6. At room temperature, rigid-chains of gelatin exhibit the properties of some common polymeric substances. However, at elevated temperatures and aqueous solutions, gelatin shows a statistical coil conformation, this is, a random distribution of monomer subunits oriented in a “statistical distribution” [85], as shown in Fig. 7.

Gelatin is mostly used as an IPN (interpenetrating polymer network). However, it can also promote the formation of semi-IPN hydrogels, when mixed with other hydrogels and/or polymeric solutions. Fig. 8 illustrates the two types of networks, using alginate as the co-hydrogel. As an IPN, gelatin is formed by at least two networks partially interlaced, separated only by breaking its chemical bonds. Conversely, semi-IPNs gelatin polymers blend together in a non-covalent interaction and can be split without breaking their chemical bonds. As a result of the thermal treatment and denaturalisation process, gelatin has a low intrinsic viscosity (gels below 37°C) and high-water volume (80-85%) [86], an advantage for cell encapsulation techniques.

Gelatin crosslinking can be done through physical and chemical means. Physical crosslinking includes dehydrothermal (DHT), plasma and ultraviolet (UV) treatments (for surface modification); chemical crosslinking makes use of agents like carbodiimide chlorides and aldehydes [87].

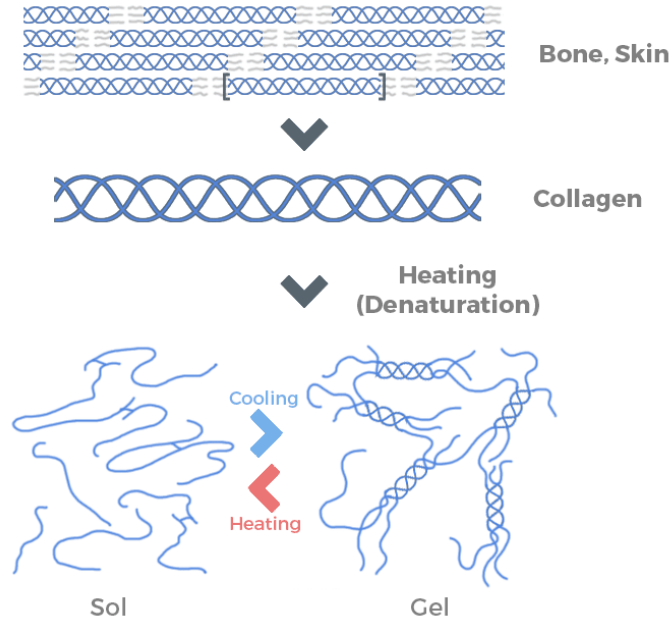


Fig. 7. Gelatin structure derives from the extracellular matrix (collagen) of bone and skin tissues. Their statistical distribution can be observed at high temperatures (coils) and rigid chains at low temperatures [88].

Nonetheless, gelatin crosslinking and gelation processes still pose a few challenges. On one hand, these procedures are promising for tissue engineering applications; it has been found that at high levels of crosslinking, the degradation and swelling ratios decrease.

On the other hand, physical crosslinking produces unstable materials whilst chemical crosslinking protocols are complicated and expensive. Innovative proposals like sugar crosslinking [88] and methacrylated gelatin (Gel-MA) [89, 90] offer interesting alternatives. Taking advantage of the thermal stability that UV light confers to collagen systems, gelatin has been crosslinked with glucose, obtaining pore sizes suitable for tissue engineering [91, 92]. Similarly, Gel-MA hydrogels have been enriched with heparin to enhance the mechanical properties of the hydrogel, with the cellular bioactivity of heparin. They found it to enhance cell viability and chondrocyte morphology [93].

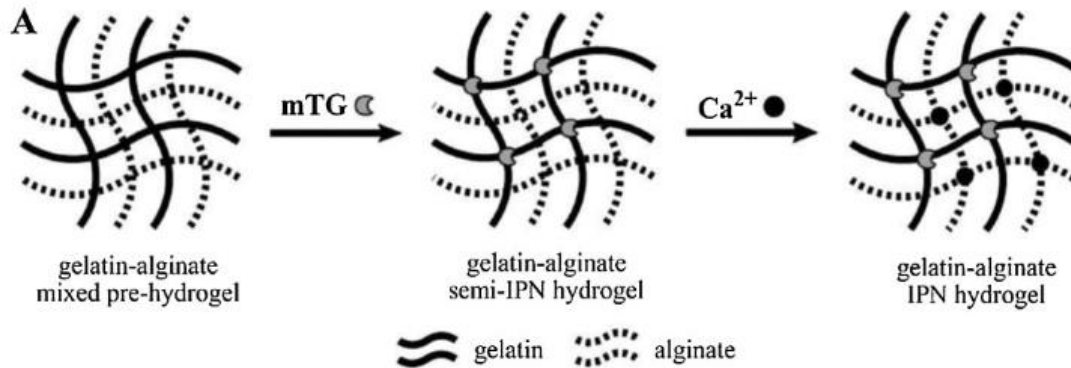


Fig. 8. IPN and semi IPN networks with pure gelatin and gelatin/alginate blends [94].

Additionally, photo and thermo responsive hydrogels have been developed, increasing their versatility by being controlled by external stimuli. Photocrosslinkable hydrogels have been tested for curing whilst containing cells, showing an even distribution of cells and viability after 7 days [94]. Similarly, Kim *et al* have developed a hydrogel-based perspiration membrane that deforms as a response to thermal changes in the skin [95].

Early applications of gelatin in bone TE were either as a guide for bone regeneration (remodelling), or to transport molecules in non-invasive treatments [96, 97]. Mixed polymeric (synthetic & natural) scaffolds between PCL-Ge have shown osteogenic advantages for both autologous and mesenchymal stem cells [98]. However, novel experiments offer both scaffold and controlled release methods for both bone and cartilage applications [99, 100]. On the cartilage field, PLLA-Ge matrices have shown good proliferation and differentiation results using stem cells, with production of hyaline-like collagen [97, 101].

1.4.2. Polymers

Polymers, metals, glasses, colloids, and composites have been proposed to work as a temporal or definite structure, to either support, guide, and transport cells, biomolecules, or drugs. Polymers are considered suitable materials due to their organic nature. They can be tailored in their conformational properties (monomeric / polymeric, porosity, interconnectivity), chemical properties (thermo-plasticity, degradation rate), surface features (hydrophobicity, polarity) and internal mechanical properties (rheology, Young Modulus (YS), Ultimate Tensile Strength (UTS) and elasticity) [102]. Their application has been both in basic research and therapeutics [103].

Polymers have shown positive attachment, proliferation, and migration results in a variety of cell lines, enhancing the production of new tissue matrices [104, 105]. For applications in tissue

engineering and regenerative medicine, porous materials have been selected since the void/pore relation and degrees of interconnectivity simulate pockets where cells can lay, proliferate and produce ECM [106, 107]. Two polymeric materials with promising applications in osteochondral tissue engineering are introduced herein, including their manufacturing techniques and suitable characteristics for TE applications.

1.4.2.1. Polycaprolactone

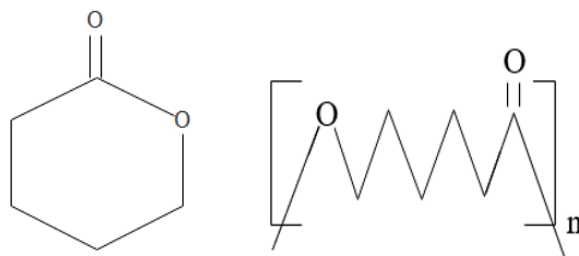


Fig. 9. ϵ -caprolactone molecule (left) and poly- ϵ -caprolactone chain (right).

Polycaprolactone (PCL) is one of the most common polyesters used for the synthesis of polyurethane (PU). It is hydrophobic and semi-crystalline, and it has been extensively used due to its low melting point (plus good solubility), and blend compatibility. It can be synthesised through a ring opening reaction (ROP) using initiators (ionic) and catalysts (metal alkoxides and metal carboxylates) [74]. Pure polycaprolactone exists as polycaprolactone polyols, polycaprolactone diol and polycaprolactone triol. Their main variation is their functionality (1, 2 and 3 arms) which confer them different molecular weights and properties as melting points, glass transition temperatures, degradation rates, miscibility, and compatibility [108]. The recent synthesis of a 4-arm PCL has also shown an increase yield of functionalisation protocols, as methacrylation [109, 110].

PCL is soluble in diverse solvents at room temperature, such as benzene, carbon tetrachloride, cyclohexanone, dichloromethane (DCM), dimethyl carbonate (DMC), dioxane, 2-nitropropane, and tetrahydrofuran (THF); and only partially soluble in acetone, ethyl acetate, 2-butanone. It is a highly hydrophobic substance, and immiscible with alcohols and ethers [111]. DCM has been used for the synthesis of polyesters as it is a cost effective solvent that can be easily handled during the polymer synthesis, and easily extracted during the purification.

PCL usually degrades within 2 years, which is considered a slow degradation process, compared to other synthetic materials like lactic acids (LA) and glycolide (GA); copolymers with these materials have been created to overcome this drawback [111]. Additionally, its degradation can be manipulated

through PCL's molecular weight and the chain groups' order (chemical structure). A modification of the polymer molecular weight or the immersion of external particles, as well as hydrolytic, aminolytic and surface treatments can enhance or trigger material decay [112]. Non-enzymatic random chain scission is the main cause of degradation of PCL, although internal (end-groups, free radicals, and reaction residues) and external (enzymatic environment) variables play an equally important role [113].

Remaining challenges of the material are being explored, like their hydrophobic nature and low level of interaction with biological fluids [114]. The use of polycaprolactone constructs for cell culture was first reported in 1993 although the mechanical properties were too low to sustain a 3D structure, which collapsed impeding the growth of a cell line [115]. PCL has been used by itself or copolymerised for regenerative medicine applications [116]; promising results have been found on fully biodegradable and biocompatible grafts on bone, pelvic, cardiac and corneal applications, among others [117, 118].

1.4.2.2. Poly(glycerol sebacate)

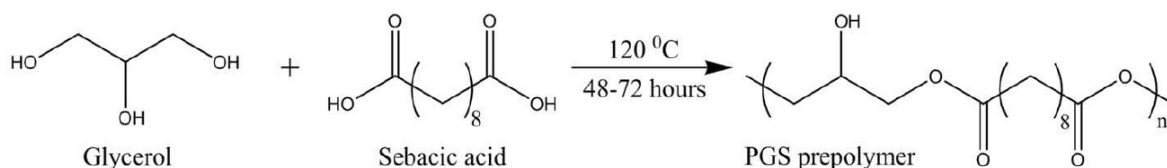


Fig. 10. Poly(glycerol)sebacate synthesis is obtained by a condensation reaction between glycerol and sebacic acid [119].

Synthesised through an equimolar condensation reaction between glycerol and sebacic acid, PGS has been used for almost two decades in soft tissue engineering. It is a soft, still robust and flexible elastomer that degrades through controlled hydrolysis, whilst maintaining over time its mechanical properties better than poly(lactic acid) (PLLA), PCL and poly(3-hydroxybutyrate) [120]. It has found its way in myocardial, nerve and blood vessel reconstruction [121], with only recent approaches to bone and cartilage applications [122, 123].

PGS is highly hydrophobic and poorly bioactive. Additionally, it has reported to release acidic by-products when degrading, which could make it cytotoxic [124]. In this matter, research groups have tried to encapsulate these reactive groups with nanoparticles as Bioglass® and silica for bone regeneration applications [124] (whilst improving PGS biocompatibility); nonetheless, inclusion of particles in the structure might affect the uniformity of the structure and result in a heterogeneous stability.

PGS has been used as a blend and a composite. Hydrogels like PGS-Gelatin hybrids were proposed by *Kharaziha et al* to ameliorate PGS's bioactivity [125]. Similarly, bioactive glass-PGS matrices have been used for bone applications [126], with an *in vivo* degradation of 6 weeks. PLLA-PGS in different ratios have stopped PGS from collapsing or flowing to undesired areas through curing [120]. Congruently, PGS/PCL electrospun fibres manufactured for corneal applications were mixed with the objective of summing up both materials' mechanical properties; when blended, even though PGS provides extra support (stiffness), it decreased the elastic properties of the mix [127]. PGS/PCL electrospun scaffolds have also been studied for cardiac tissue engineering, with mechanical properties close to the native tissue and best cell viability, compared to independent material experiments [118].

From all academic papers retrieved, PGS scaffolds and blends have used PGS as a bulk material or structured via electrospinning [128, 129], 3D printing [130]) or salt leaching [131, 132], but not as a porous structure or as a result of an emulsion (e.g. HIPE). Regarding cartilage regeneration, few have been explored. The same research group first explored the compatibility of PGS with chondrocytes, and then confirmed the preference of these cells to produce aggrecan and collagen 2 : collagen 1 ratio on PGS scaffolds, compared to PCL ones [133, 134]. However, similar experiments have also shown contradictory cell phenotypes, gene expression linked to cartilage destruction, and ossification [135].

1.4.2.3. Material characterisation

1.4.2.3.1. Structure: Emulsions

With the objective of mimicking the microenvironment of human tissues, biomaterial-based porous constructs have been proposed. The porosity of these constructs can be found in either 2D or 3D and can be supported by both structural and topographical features. Desired porous structures can be obtained through porogen leaching, thermodynamic processes (gas foaming, phase separation, freeze drying), microsphere sintering and emulsions [136]. However, some of the techniques release residues that can be cytotoxic or affect the material behaviour over time; the options for biomaterials are limited.

Emulsions and dispersions are non-spontaneous fine droplet dispersion of one liquid into another, immiscible or partially miscible between each other. It is formed by a dispersed phase (droplets) suspended in a continuous phase (liquid). Due to this distribution, emulsions/dispersions have large surface areas and high surface energy, which make them unstable to heat and energy changes. Emulsions are a two phase (liquid/liquid or semiliquid/semiliquid) system that form droplets of few

microns due to the addition of energy, contrary to dispersions which droplets are in the range of dozens to hundreds of microns. Dispersions will split into two separate layers as soon as the energy ceases. Emulsions, on the other hand, are able to maintain their structure for long enough (even months) to be processed; surfactants (emulsifiers) aid to keep this stability [137]. Surfactants are molecules or polymers that possess one hydrophilic and one lipophilic head. Seeking to fulfil both attractions, they stay in the interface between the water and the oil phase (in a process called adsorption), stabilising the emulsion. Surfactants are classified according to their hydrophilic-lipophilic balance (HLB) as it is directly related to their performance in the emulsion. The range of values goes from 0 to 40, being the ones within the range of 0-20 the most relevant for chemical industry, and the ones between 0-6 the focus of polymer material sciences. A lower value of HLB describes a lipophilic surfactant (likely to form O/W emulsions), whilst values above 11 HLB describe highly hydrophilic surfactants [138]. Common surfactants include silicas and mineral-derived molecules, lattices, detergents (soaps), proteins and block copolymers [139].

Emulsions can be classified depending on their morphology (water-in-oil (W/O), oil-in-water (O/W), water-in-oil-in-water (W/O/W), and oil-in-water-in-oil (O/W/O)); their degree (first and second degree), and their state of matter (liquid/liquid, semi-solid and solid). Emulsions can also be characterised according to their volumetric composition (drop size and drop distribution), rheology (Newtonian and non-Newtonian fluids), and stability against forces (that affect flocculation and coalescence, and determine size, shape, porosity and strength of openings). Reactions in emulsions happen in microseconds, hence the importance of keeping times tight and enhance reproducibility.

Emulsions are formed when a fluid (oil or water) is added to a stirring continuous phase (external phase); the phases are miscible to each other. In the case of a W/O emulsion, an oil phase is usually being stirred with a surfactant, a catalyst and some additional solvents, and the future internal phase (water in this case) is dropwise added to the mix. Plateau-Rayleigh instability describes the mechanism by which the falling liquid breaks into smaller droplets with the same volume, but a higher surface area (more, smaller droplets). This breaking effect is linked to the surface tension dominating the stirring continuous phase, and that pushes the incoming aqueous phase to minimise its surface area [142].

Therefore, the size of the new droplets will be consequence of the energy required; big droplets require less energy and these emulsions can easily be created using a high-speed stirrer [140]. This can be explained through considering the difference in pressure between the inside and outside environment of the droplet, described by Laplace's pressure Δp . Droplet sizes is also linked to the interaction between droplet break and coalescence. Coalescence is an emulsion and dispersion

phenomenon in which the two miscible phases involved (oil and water) reject each other and form partial or totally separated phases, the phase with less density will also be pushed to the top of the container [144]. Coalescence is caused by the excessive closeness of droplets and the consequential thinning of the film dividing them (hence the lower concentration of surfactant / stabiliser molecules around to support the repulsion between layers). When the layer breaks, the two droplets merge into one, adopting a spherical-like morphology as it distributes better internal/external pressures (Laplace's pressure) [145].

Viscosity is the visible property of rheology. As such, understanding the variables that affect viscosity, will increase the control over the emulsion. These factors include internal phase, viscosity of external phase, size of droplet and forces acting on the fluid (shear force, temperature, pressure). The internal phase Viscosity increases with decreasing particle size. Viscous (frictional) forces that create droplets create a shear stress between the droplets and the continuous phase. This force is affected by the viscosity of the oil phase (external phase); the higher the viscosity the longer it will take to deform a droplet (hence create other / smaller ones). Whilst the viscosity of the internal phase has little effect on this, the gap between both viscosities is the one that will affect the emulsification rate (droplet deformation time). Additionally, the viscosity of both phases can be affected by the stirring rate. The efficiency of emulsion extraction increases as the mixing speed does, decreasing the size of droplets (higher mass transfer area). Additionally, a high stirring rate can also make droplets unstable (increased shear stress), leaking the internal phase, thus affecting resulting topologies.

Finally, the volume ratio of the emulsion will increase as the emulsion is formed, with a slower rate as it approaches the point where there is not enough solvent nor oil phase to support the creation of bigger or more droplets [141].

What forms interconnectivity? When droplets with a defined radius R get closer to each other, each being surrounded by a layer of adsorbed surfactant, their walls interact, either overlapping with each other and/or compressing the droplet (making it change its form). This phenomenon does not come naturally, and a counter force repels this interaction, through an osmotic repulsion [140]. As the internal phase volume ratio gets closer to its maximum, the wall / film (oil phase) thickness decreases, as well as the surfactant concentration, promoting the formation of interconnected windows, stabilised through further polymerisation. It has been observed that the appearance of first windows coincides with the gelation point present through polymerisation [142]. There is no bulk shrinkage on emulsions, but an internal shrinkage between emulsion droplets due to the described proximity and wall thickness.

1.4.2.3.1.1. PolyHIPEs and Pickering HIPES

High Internal Phase Emulsions (HIPEs) are emulsions with highly packed fractions of non deformable droplets. HIPEs allow the polymerisation of viscous foams that retain their shape and that possess an internal volume fraction higher than 74% [143]. PolyHIPEs were first reported by D. Barby and Z. Haq in a patent owned by Unilever in 1982 [144]. A polyHIPE is obtained by crosslinking a polymeric solution A (usually dissolved and with terminal OH groups) which represents the continuous phase, and a liquid solution B (commonly hydrochloric acid (HCl) or water), in the presence of a surfactant (emulsifier) and an optional crosslinker. Crosslinkers and initiators activate the crosslinking process, enhancing gelation processes and the structural stability of the final product. To increase their efficiency, they should be close to their water affinity (hydrophobic to the liquid phase for both W/O and O/W) [145].

The composition and concentration of each material plays an important role in the stability and structure of the resulting HIPE. The structure of the HIPE will replicate the emulsion at the gel point thus is highly dependent on the stability and homogeneity of the emulsion, therefore a stable polymer eases the gelation process. For example, the attraction and exclusion (polarity) of both the continuous and the liquid phase plays an important role and is supported by solvents (in the continuous phase – observed in Fig. 11), and by emulsifiers. As mentioned before, emulsifiers have a dual role in lowering the surface tension energy, and migrating to the oil-water interface, reducing the work required for droplet formation. The ideal concentration of an emulsifier depends on the inherent features of the surfactant, and the interaction with the rest of components. Emulsifiers have been created using as little as 5% w/w (relative to monomer phase) but are usually added up to 40% w/t [146], hence making the external immediate environment of droplets more water or oil-like [138].

Incorporation of the liquid phase can be done either at the beginning of the mixing process, or slowly through the emulsification process, enhancing viscosity gradients. Depending on the desired pore features, the liquid phase volume is selected, however some polyHIPEs are able to incorporate an internal water phase of 99% wt. Subsequent to the polymerisation of the continuous phase, the liquid phase can leave the structure through the pores created. Big spherical cavities are left, and are referred to as voids, whilst the small interconnected pores are called windows [142].

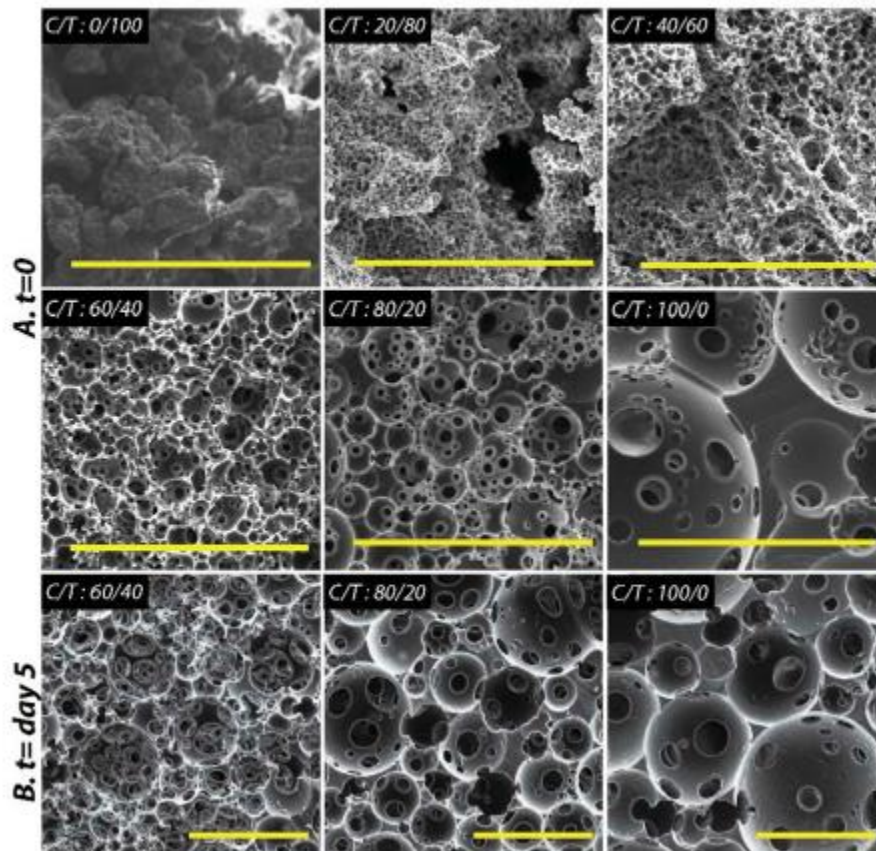


Fig. 11. Polycaprolactone PolyHIPEs prepared with different solvent ratios. A. SEM images of C/T:60/40, C/T:80/20 and C/T:100/0; polymerized A. Right after preparation of HIPE, B. 5 days after preparation (scale bars: 100 μm) [109].

Pickering emulsions are emulsions that use solid particles to achieve a long static, and in most recent cases, dynamic stability. These emulsions are characterised by the lack of coalescence over time, even if going through temperature changes. This is attributed to the fact that Pickering emulsions are irreversible; the solid particles act as a physical barrier between the oil and the continuous phase. Some of the most common solid particles used, called colloidal stabilisers, are inorganic nanoparticles (silica/silanes [147], Fe_3O_4 [148] and calcium based materials [149]), ester based polymers (polyurethanes [150]) and bio-inspired materials (hydroxyapatite [151]).

As the stabilisation of Pickering emulsions depend on the maintenance of the aforementioned particles between the two liquids, it is extremely important to enhance the migration of these solids to the interface [152]. This ability can be measure by a three-phase contact angle θ , that describes the location of the particle in the oil-water (or vice versa) interface; the closer is θ to 90° the highest the stability, going slightly higher or slightly lower depending on the type of emulsion seeking to obtain

(O/W or W/O) [153]. For example, silica nanoparticles can be extremely hydrophobic and even if supporting the oil-interface, are unable to successfully stabilise O/W emulsions. Therefore, these particles were functionalised using glymo (3-Glycidyoxypropyl)trimethoxysilane), which helped to improve the amphiphilic character, whilst also preventing the agglomeration of the nanoparticles [147]. These modifications not only show an increased stability versus the original emulsion but allow emulsions to increase their internal phase volume above 90%.

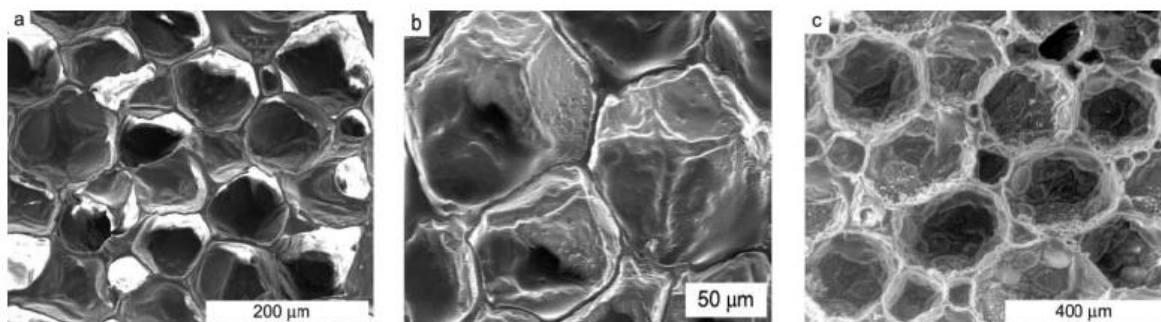


Fig. 12. Silica-modified Pickering emulsions functionalised through MPtMS (3-(methacryloxy)propyltrimethoxysilane) as at two different rations [152].

Although Pickering HIPEs are easily recognized due to their polyhedral pore structure, Fig. 12 shows both semi round and hexagonal forms, with varying sizes. This can be caused by the concentration of the particles in the solution, and by temperature. The effect of heating the HIPE produces a simultaneous polymerisation and destabilisation. An emulsion with small droplets will achieve gelation faster and stabilise less, thus keeping a polyhedral frame. On the contrary, big round pores will be observed on highly destabilised systems. Even though in most cases the droplets have an homogeneous size, bi and multi sized droplets can be observed when small droplets are not covered by the stabilising particles and either coalesce with others or stain in the interstitial space between two big droplets [153]. By increasing the concentration of stabilisers, the viscosity of the external phase increases, decreasing the pore size, but also the risk of coalescence. This is the same effect that has an increased concentration on the continuous phase. Contrary, by increasing the internal phase volume, bigger droplets could be observed [154].

One of the drawbacks of the so-stable Pickering emulsions is their applicability to biomedical research. Some of the colloidal stabilisers used could show cytotoxic or counteracting effects when in contact with cell lines and body tissues.

1.4.2.3.2. Crosslinking: functionalisation and photocurable polyHIPEs

Emulsion polymerisation allows the production of low and high molecular weight polymers through controlled reaction rates, which are usually higher than bulk polymerisation. Polymerisation can be performed in batches, semi continuous and continuous reactions. As explained by Harkins in 1946, in a conventional emulsion polymerization 4 actors interact [155]:

- i) A water phase containing the catalyst / chain initiator is believed to promote the creation of free radicals. Depending on the origin of the initiator (preferring O/W or W/O interfaces), the droplet morphology can be affected (polyhedral or spherical) [156].
- ii) Suspended in this water phase, monomer droplets supply other polymerisation phases with monomer.
- iii) Dissolved monomer micelles (also called monomer-swollen micelles) “generate” polymer particles until fully absorbed on the polymer-water interface.
- iv) After the initiation of polymerisation, small polymer particles swollen with monomer play a role of “loci” of polymerisation.

According to this, the rate of polymerization is determined by the rate of formation of free radicals, the rate of escape of those radicals to the “loci”, and the individual rate of polymerization per radical in the locus. Even though the size of the polymer particles does not determine the polymerization rate, their total volume does [157]. If the rate of formation of free radicals is low, the water phase will dictate the time of the reaction, affecting thus the next steps, therefore the polymerization rate. In a second case where the number of free radicals per reaction locus is around one half, high rates of polymerization and high molecular weights can be obtained as it simplifies the chain propagation. A third case can also be considered; when the number of free radicals per reaction locus is much higher than a half, the rate is regulated by the oil phase [158].

Most polyHIPEs use conventional free radical polymerisation (FRP), although some novel emulsions have been obtained through inverse emulsion polymerisations; which describe the emulsification of a water-miscible monomer (in presence of an aqueous solution) in an oil medium with a W/O or O/W initiator. The product is a colloidal emulsion of water-swollen polymer particles [159].

The crosslinking density is based on a hypothetical primary polymer molecule created during polymerisation and describes the number of crosslinked units within the total number of units bound in the polymeric chain [160]. Crosslinking density might be weak at the beginning of the process but will get stronger as the number of available monomeric units increases.

To enhance both the polymerisation rate and the crosslinking density, pre-polymer solutions can be developed through adding “reactive handles” or functional groups, leveraging the monomer functionality [109]. Amines [161], phenyls [162] and polyols [109] have been used for this purpose.

Methacrylation is one of the most used ways of polymer functionalisation as it allows to couple more points of functionalisation on already interesting polymers, under free radical conditions [163]. Methacrylic anhydride is a carboxylic anhydride famous to polymerise through free-radical initiation. Polyacrylic anhydrides are always unsaturated [164], responsible for further gelation, hence an opportunity of being used for crosslinking optimisation [165].

One of the applications of acrylic functionalisation, is photo crosslinking due to the fast-crosslinking rates of acrylates and methacrylates [166]. The degree of methacrylation of the original polymer will control the number of chemical bonds “to form crosslinks”, which also has an effect on the degradation properties of the material [167].

A photoreaction is induced when a multifunctional monomer (a molecular structure with various applications), meets a telechelic polymer (a polymer capable of polymerisation via its end groups) [168]. Under its simplest version, this monomer is transformed into a crosslinked polymer through a chain reaction induced by free radicals or ions. The source of these ions can have various sources of irradiation, including UV light. Under this intense illumination, high rates of polymerisation can be obtained in low time frames, as small chain reactions last only a fraction of seconds, but behaving similarly as thermal polymerisation. Photocurable alternatives are suitable for emulsions and specifically for HIPEs as they are highly unstable.

A photoinitiator with large absorption in the emission range (of the light source) will give high yields of polymerisation. The rate of curing and the viscosity of the prepolymer define the product fidelity (non-Newtonian fluids tend to shrink during or after the process) [169, 143]. When polymers as caprolactone and glycerol-sebacate are methacrylated, photocuring occurs through a free-radical mechanism; acrylates are considered one of the most reactive monomers, with further applications in silicones [166], hydrogels (gelatin [170] and chitosan [171]), and other polymers (poly(ethyl) methacrylate/tetrahydrofurfuryl methacrylate (PEMA/THFMA) [172]).

1.2.3.4.3. Pore size and porosity

Crosslinked emulsions are usually three-dimensional structures; the voids and windows left by the continuous phase are now pores. Porous materials have been used for purification in the chemical industry as substances are able to travel through, retaining targeted molecules (i.e. toxins, residues).

Biomedical and tissue engineering areas have found in porous materials a niche since the form and size of voids resemble body tissues, therefore, simulating macro and micro biological environments. Whilst surface porous materials enhance cell attachment, a highly interconnected porous structure allows for migration of molecules and cells within the construct. Additionally, they perform as a 3D guide for *de novo* tissue formation.

As described in the emulsification process, the size and form of droplets (pores) is the result of the interaction amongst the oily and the watery interface pressures (dictated by their viscosity), the mixing speed, and the properties of the emulsifier. Aforementioned variables will also define the number of droplets per surface volume (porosity), their packing (closeness to each other) and their interconnectivity. For example, small and few pores could become interesting for reactive functional groups to attach. As the porosity increases, various sizes of pores could arrive to a packing situation in which they could interconnect with each other, providing pathways for the transfer and migration of both molecules and cells. However, it is important to consider that by increasing the internal surface volume (this is, the space of total void), the overall integrity of the construct can be compromised. For example, bigger pores up to saturation would mean that the films of the monomer are thinner, increasing the interconnection level, but risking a decrease in the mechanical properties.

Porous structures used as biomaterials have been classified into macro ($>100\ \mu\text{m}$), micro ($10\text{-}100\ \mu\text{m}$) and mesopores ($<100\ \text{nm}$); the latter usually referred to as nanopores [173]. For a pore to be considered as such, should have a depth larger than its width [174]. Macroporous scaffolds with pores usually ranging between 150 and $800\ \mu\text{m}$, are used to provide a solid frame, to mimic extracellular matrices [175], to investigate the development of cells and tissues in biochemical spatiotemporal scenarios [176], and in conjunction with electronic biosystems [177].

Micropores are widely used in tissue engineering applications since the smallest human cells are sperms and have an average volume of $30\ \mu\text{m}^3$ (φ (body length diameter) $\cong 4\ \mu\text{m}$) and the bigger cells are fat cells and oocytes, with $600,000\ \mu\text{m}^3$ ($\varphi \cong 50\text{-}69\ \mu\text{m}$) and $4,000,000\ \mu\text{m}^3$ ($\varphi \cong 100\ \mu\text{m}$) respectively; pores for TE applications range between 50 and $800\ \mu\text{m}$ in diameter [178]. Cells use pores as physical cues to attach, build extracellular matrix, proliferate, and differentiate. Although some types of cells share morphologies and behaviours at specific maturation and/or differentiation times, they go through dynamic changes that need to be considered when designing them a porous “home”. Even though macro and micropores may fulfil this requirement, nanoporous biomaterials have been explored as they possess high surface areas, high porosities and their small pores give a special topography, roughness, and energy to their surfaces, attractive to cells [179]. They are currently used in artificial kidney systems (biofiltration) [180] and for drug delivery, but more

importantly on hybrid macro/nano or micro/nano constructs to enhance osteogenic differentiation in adipose and bone marrow cells [181] and hydroxyapatite formation [182].

The osteochondral unit is home of mainly two cell types: chondrocytes and osteoblasts. Chondrocytes change their morphology depending on their maturation stage but also their location within the articular cartilage; chondrocytes have an average size of 20 μm and seldom go over 60 μm . For this reason, pores comprising between 50 and 150 μm have been proposed to mimic the articular cartilage environment [58] [183], with high porosities [184]. Several studies have shown porosity to have a less important effect than pore size in cell matters, whilst affecting significantly the mechanical properties [185]. Contrastingly, the subchondral bone porous structure should not only provide a home for bone cells, but also enhance angiogenic and nervature processes. Proposed scaffolds have pores sizes ranging between 150 and 800 μm [186, 187] where results have found bigger pores (>300 μm) Several studies have shown porosity to have a less important effect than pore size in cell matters, whilst affecting significantly the mechanical properties [185], are better for cell attachment and cell migration, but smaller for proliferation. In terms of porosity, the cortical bone has an overall porosity of 10%, compared to 50-80% in the trabecular bone. Porosities ranging from 50 to 90% have been combined with different pore sizes, finding a positive trend (cell behaviour) on medium to high porosities and large pores, whilst there is no reported directly proportional relation [188].

1.2.3.5. Surface treatments

The surface of a biomaterial is the first interaction between the implant and the host body. Surface parameters as chemical composition, electrical charge, wettability, crystallinity, and roughness determine the immediate and consequent biological reactions. The availability of molecules and atoms forming the surface of the biomaterial interact with the ones in the host environment, extending the arrangement between both of them, ideally immersing into one shared space. Surfaces are able to modify their structures by segregating and reconstructing looking for the state with the lowest surface energy (equilibrium) [189]. Through segregation, the most common effect that biomaterials take advantage of, molecules and cells can be adsorbed at specific “functional” domains. Cells interact in the tissue in a spatiotemporal way by their surface receptors.

The surface of a biomaterial can be modified, when: i) the surface is creating an undesired initial reaction with the living tissues; ii) the surface possesses good features, but not good enough for the intended purpose, iii) additional features as embedded materials, drug delivery, tailored degradation

want to be added (product differentiation). Surface modifications include crosslinking, blocking surface states, incorporating self-assembled monolayers (SAM), and coatings, are some of the solutions.

Wettability is another property directly linked to cell attachment. Studies have shown that hydrophilic surfaces tend to attract more cells than hydrophobic ones. Some experiments have also shown that higher protein adsorption levels are observed in hydrophobic-like surfaces. These contradictory experiments show that it depends on the material, the coating and the environment exposed, the surface characteristics to be tailored. For polymers and hydrogels, the maximal cell adhesion was observed on polymeric surfaces with a water contact angle close to 70° , while decreased in cases where wettability was too high or too low [190].

Surfaces can also have a two-fold objective, to attract cells to the surface of the implant, and to slowly release the molecules from the surface into the cellular environment. The entrapment of biomolecules can be done with or without chemically bonding it to the bulk surface, which makes this initiative really versatile. Hydrogels are suitable for this job; collagen coatings have been investigated as they can mimic native matrix conditions, as well as interact with signals and growth factors during tissue regeneration. Among the most successful adsorbed proteins, fibronectin has shown significant improvement for fibroblast cell adhesion [190].

Bioactivity of surfaces can also be improved by plasma surface modification (PSM). Plasma is ionised gas with variable temperature and pressure that is ejected in a confined space. Plasma is generated through the segregation of a parent atom into ionised electrons; usually achieved through applying an electric field (commonly in the range of microwave radio frequency) to the source of gas. The charged particles easily react with a substrate, altering its composition [191]. The gas precursor (oxygen, CO_2 , CH_4 and NH_3 being the most common ones) needs to be chosen according to the functional groups present in the surface, which will attract the proteins or cells. Plasma techniques include plasma sputtering, etching, implantation, deposition, polymerization, spraying and laser plasma.

When a polymer is exposed to plasma, the hydrogen from the surface polymeric chains is abstracted, creating free radicals that interact with oxygen or nitrogen from the plasma source, and generally affecting the material's wettability [192]. A direct way of modifying the chemistry of a surface is through plasma coatings. For example, calcium phosphate coatings have been extensively used as they simulate early layers of mineral deposition for osteogenesis. From the same family, hydroxyapatite, and carbon apatites have also been used, showing an increase in high reactivity (good for first interactions) and high solubility (easy degradation). Application of these coatings can be

through electrophoretic or cathodic deposition, biomimetic and ion precipitation, and plasma spraying. The latter also promotes higher surface roughness, which improves the attractiveness to cells. For example, calcium phosphates and chitosan have been used to coat polyetheretherketone (PEEK) implants for regenerative medicine and orthopaedic surgery [193]. And polymers such as PLLA and PGA are commonly coated with ammonia plasma to provide regulatory endothelialisation mechanisms to vascular implants. Finally, even soft surfaces such as silicone sometimes require coatings to increase their wettability and reduce biofouling; ion plasma deposition is used on silicones for ophthalmic applications [192].

1.5. Current development and challenges: hydrogels and polymers for OC regeneration

Taking aside the materials' difficulties while manufacturing scaffolds, there are persistent hurdles in developing strategies for osteochondral repair. The chondral and bone tissue coexist in a complex environment, restrained from each other. For instance, the cartilage lays in a synovial bath free from nerves and blood vessels, whilst the bone is strongly saturated by the two latter elements. To correctly mimic the native system, both environments should be favoured. Matrix-free treatments and scaffolds have been proposed for OC repair. The latter ones can be further classified into mono, bi and tri layered. Prior to implantation, scaffolds can be seeded with cell lines, or implanted cell-free. Seeded scaffolds have tried various combinations for cartilage-bone layers: all chondrocytes, all MSCs, chondrocytes : MSCs, and MSCs: MSCs.

a. Cell lines

Independently of the decision of implanting cell-free or pre-seeded scaffolds, *in vitro* studies require the “future cast” (or a similar one), to test the frame, the environment, and the features of the tissue-to-be. Chondrocytes and osteoblasts are the original inhabitants of the subchondral units (among osteocytes and osteoclasts); it is natural to use them to simulate how things could be working *in vivo*. Seeding independent well-defined cell lines can avoid the problem of mixed differentiation and changes in morphology linked to proliferation in external environments. However, harvesting native cells can cause site morbidity, transmission of diseases, and is expensive [194].

Scaffolds seeded with only chondrocytes have been tested to promote a controlled chondral differentiation and an endogenous ossification in the bottom layer. Although it has been proved that mesenchymal cells differentiated into chondrocytes can undergo further endogenous ossification [195], controlled parameters such as over-expression of proteins, oxygen and weight loading have been studied aiming to stop them before or after [196]. Similarly, osteogenic differentiation has been obtained through the addition of osteoinductive and osteoconductive factors, vascularization, and infiltration channels [197]. Current problems remain in the selection, supply and distribution of factors and supplements to enhance cell differentiation altogether but independent by tissue, whilst coexisting in a proposed scaffold. Relevant studies on efforts of regenerating both articular cartilage and subchondral bone are reviewed herein.

Stem cells are a rich and viable source of reprogrammable cells, which can be oriented towards the experiment's objective, including low immune response from the host body. From the available pool of stem cells, adult stem cells are relatively easy to grow, less likely to be rejected by the body, and with less ethical concerns. MSCs are multipotent, non-hematopoietic stromal cells of easy isolation and proliferation. MSCs from the mesoderm layer are able to differentiate into cartilage, fat and bone cells, and can be isolated and expanded from human and animal sources, or cocultured with chondrogenesis-promoting cells that encourage them to differentiate into chondrocytes or induced by osteoinductive cues to form new bone [198, 199, 200, 201]. Differentiation of MSCs into their mesodermal lineages is commonly done by supplemented media. Osteoblasts are first differentiated into pre-osteocytes, and finally arriving to mature osteoblasts, when supplemented with ascorbic acid, β -glycerol phosphate, and dexamethasone. This process induces activity of alkaline phosphatase and mineralisation. On the other hand, the differentiation of MSCs into pre-chondrocytes and mature chondrocytes include a wide range of supplements (platelet rich plasma (PRP [202]), insulin transferrin selenium, linoleic acid, selenious acid, pyruvate, ascorbate-2-phosphate, dexamethasone, bone morphogenetic protein-2 (BMP-2)), growth factors (transforming growth factor- β III (TGF- β III), insulin like growth factor-I (IGF-I)), and hormones (parathyroid hormone-related peptide (PTHrp) and triiodothyronine (T3)) that allow cells to express cascade signals to induce chondrogenesis [201].

Bone-marrow mesenchymal cells (BMSCs) have been preferred due to their osteo origin; their use simulates what is intended in surgical techniques like microfracture. BMSCs have shown to differentiate into both bone and cartilage tissues, preserving cells' natural morphology and secreting t-cell suppressive cytokines, important for allogeneic transplantation [203]. Fibrin/methacrylated HA

porous scaffolds were used to induce articular cartilage regeneration, with successful suppression of the production of collagen type I [203]. Promising results were also achieved in a bi-layer Ch-HA/Ch-Alg-HAp scaffold co-seeded with BMSCs/osteosarcoma cells or chondrocyte-like/osteosarcoma cells to study the interaction between cell lines, observing better chondrogenic expression (type II collagen) on BMSCs than chondrocyte like cells, and an equal positive osteocalcin expression on both tests [204].

Adipose-derived stem cells (ASCs) have also been investigated due to their ubiquity [205] and resemblance to BMSCs for osteogenesis. Additionally, 1 g of adipose tissue can yield 500 times more stem cells than 1g of bone marrow [206]. Despite their high proliferations, there is not a big understanding on how the ECM guides and induces differentiation in ASCs [207].

BMSCs and ASCs share high availability and successful differentiation *in vitro*, although challenges related to the number of cells available after increasing subculturing and working passages [208]. Additionally, dedifferentiation and differentiation protocols have not been yet standardised.

Synovium-derived MSCs (SMSCs) have also been considered for bone and cartilage tissue engineering. SMSCs can be isolated from joints (limiting their availability) but obtaining the best differentiation results among the researched stem cells [74]. Other varieties of stem cells like induced pluripotent stem cells (iPSCs), embryonic stem cells (ESM) and infrapatellar fat pad derived stem cells (IFP-) have been studied mainly for chondrogenic differentiation. Even though results are promising, there are few clinical studies to prove their harvest and efficiency for osteochondral regeneration [209]. Vascular Smooth Muscle cells (VSMCs) are smooth muscle cells that when stressed or damaged, inhibit their original function (dedifferentiate), and redifferentiate into chondrocyte and osteogenic properties, and showing mineralisation and calcification of their ECM [210]. Few insights have been done on how this could be applied on osteochondral regeneration but could support its enhancement of both osteogenesis and angiogenesis.

b. Mimicking topographical features and spatial environment

Orientation and organisation of pores influence cell behaviour (attachment, migration, proliferation, and differentiation). The optimisation of the spatial environment aims to support chondral cells to migrate into their respective layers, and facilitate the formation of neo-tissue, close to the native one. PLGA scaffolds with radially oriented pores ($\cong 40 \mu\text{m}$) were fabricated through freeze-drying. Cells populated the microtubules and showed an elongated morphology, homogeneously distributed, and

deeper migrated against random pores used as control. Even though a hyaline-like cartilage tissue was noticed, a natural interlayer was formed, dividing both tissues [211]. Randomly aligned, axially oriented and radially oriented pores have been studied in terms of mechanical properties and cell affinity. Axially oriented pores were found to increase the elastic modulus, while vertical aligned channels were more propense to collapse under compressive forces.

Surface features can be isotropic (changes in organisation) or anisotropic (grooves and ridges). Isotropic multidirectional zonal (MZ) scaffolds supplemented with hyaluronic acid and carbonated hydroxyapatite were seeded with bone marrow stromal cells (BMSCs)-GFP (green fluorescent protein) as a reporter. They were able to differentiate to early stages both chondrocytes and osteoblasts; the pore size and geometry helped cells to respect their layer morphology, and media / soluble factors could mediate cellular phenotype. Additionally, both had a big impact on ECM composition and structure [212]. Tubular structures have also been explored. A calcium phosphate-collagen bilayer scaffold with aligned channels was proposed for osteochondral regeneration. Cells migrated quickly through the channels (dependent on channel diameter), enhancing cell attachment and proliferation in both areas. However, bone regeneration was so fast that it overran chondrogenesis, suggesting that a control of the subchondral regeneration (more associated with random pores) was required, but maintaining the benefits of channels on chondral layers [213]. Bilayer scaffolds (half tubular and half porous) found that their tubules would mimic articular cartilage fibre organisation [214]; multi-layered collagen scaffolds seeded with ASCs showed cellular aggregations on the swollen networks, forming rod like cellular conglomerations both only showing chondrogenesis when induced through growth factors [215]. These results are supported by radially oriented PLGA scaffolds [211, 216] and a monolayer silk fibroin-collagen [217] that tested the differences between axial, radial and random pore alignment, where radial pores were preferred for OC regeneration, followed by axial and random ones.

Biomaterials have intrinsic physico-chemical properties. Among them, surface energy stands out as it determines the anchor points for cell and molecule attachment, influencing cell behaviour and fate. PCL, PLA and PEO:PBT were 3D printed in a mesoporous scaffold and their chondrogenic and osteogenic capacities were measured in stiffness (SG) and wettability gradients (WG). They discovered that for both SG and WG, a higher ALP expression was registered on the softer material (PEO:PBT), whilst GAG amount has higher in PLA (for WG) and no significance difference with SG for chondral expression. This remarks the importance of gradient mechanical properties and wettability *in vitro* [218]. Surface energy can also be achieved through porous prepolymer solutions

that form porous scaffolds. PCL/DCM micro struts (ca. 60 μm) with nano pores of 0.2–2.4 μm had an increased 10 fold surface energy versus non porous struts, supporting protein hence cell adhesion; additionally, MSCs on chondral media exhibited long bodies and filopodia, whilst denoted round cellular behaviour on non-porous surfaces. However, osteogenic differentiation worked the other way around, evidencing the interrelation between surface topography and the biochemical environment [219].

c. Mimicking ECM environments

Hydrogels are soft and malleable by nature. Even though they were initially discarded due to their low mechanical properties, novel proposals take advantage of their high-water content, chemical resemblance to the ECM, biocompatibility, and biodegradability, to engineer functional materials.

Alginate, chitosan, and agarose have all shown to be able to support growth and proliferation of encapsulated chondrocytes and MSCs over time, whilst maintaining their cell morphology [220, 221, 222]. Even though all these materials are from easily available sources and are highly biocompatible, they are not known by their bioactivity nor their desirable mechanical properties. However, physical and chemical crosslinks have been used to functionalize their reactive groups [223], and to include peptide patterns [224] and nanomaterials (ceramics [225], calcium phosphate [226], apatites [227]) in the core of the hydrogel solution, increasing their attractiveness to cells, and mechanical properties. As the hydrogel degrades, the immersed particles get available for cells which can use for either build desired ECM, or support differentiation processes like chondrogenesis and osteogenesis (some cases only osteoconductivity and some others osteoinductivity [228]). Microparticles as Wollastonite and Laponite have shown to improve the mechanical properties of hydrogels, whilst influencing mineral deposition [229, 230]. Pre-osteoblasts and osteoblasts have been studied to regenerate subchondral bone. Pre-osteoblasts are able to differentiate into osteoblasts *in vitro*, and osteoblasts embedded in HA-PEG-clay hydrogels have shown production of ECM and matrix mineralisation (apatite deposition) [231].

Collagen multi-layered scaffolds have been proposed due to their similarity with the host tissue. A three-layer scaffold (top: type II collagen and HA, middle: type I and II collagen and HA, bottom: type I collagen and HAp) was freeze dried and showed promising biocompatibility on MSCs, supported by the high porosity and interconnectivity of yet independent layers [232]. These results are contrary to the ones reported for silk materials. Bilayer silk-fibrin scaffolds seeded with

chondrocytes were implanted in rat knees for over 36 weeks. Even though the material integration and degradation were achieved within that time, only chondral regeneration was observed, whilst ossification was merely perceived in bottom layers of the scaffold [233].

When cocultured, cell lines used for subchondral regeneration might go through endochondral ossification. Whilst this is desired for the bone layer and partially desired for the chondral one, biggest challenges are to maintain cell morphology (hence differentiation), and to either inhibit or control endochondral ossification and related chondrocyte hypertrophy. A bilayer porous collagen scaffold seeded with differentiated chondrocytes showed an increase in type II collagen and GAG production, although they underwent fibroblastic phenotype. Osteoblasts, on their hand, evidenced early mineralisation signals and ALP activity [234]. Accordingly, chondrocytes and MSCs were seeded in a bilayer agarose scaffold. Chondrocytes were able to keep viable (even if not proliferated), maintaining their phenotype, whilst MSCs showed mineralization in a hypertrophic medium through endochondral ossification [235].

Even if not fully understood, the role of the calcified intermediate layer has been associated with delimiting cartilage and bone layers. This barrier has been mimicked as a physical layer or in a difference in chemical and biological components. For instance, agarose-alginate-HAp/BG (bioglass) composites were used to create a hypertrophic calcified interface for OC applications [236]. In a similar experiment, the importance of a third layer proved important to create a calcified layer between bone and cartilage. Additionally, the media supplement played an important role. Tri-layer collagen scaffolds seeded with MSCs showed that, under normal media co culturing conditions, cells could keep their phenotype, but remained undifferentiated, mainly close to the middle layer of the scaffold. On the contrary, under chondrogenic media, chondrogenesis was achieved, and hypertrophic behaviour (type X collagen) was observed on interfacial cells. Divergently, co cultured cells in osteogenic media calcified all layers, even if expressing collagen and GAGs in the cartilage layer [237]. This confirms the strong effect of media supplements to influence ossification signals transferred from bottom to top layers (bone microenvironment).

Polymers have also been proposed for osteochondral applications, and commonly mixed with hydrogels. Multi layered PCL-HA-atelocollagen constructs were 3D printed to simulate chondral (atelocollagen) and subchondral bone structures (HA). In vivo analysis on knee rabbits showed a complete integration of the material with the surrounding native tissue. Similar results were obtained in PCL-HAp multilayer scaffolds, where HAp promoted the integration between native and new bone

[238]. Chondral morphology was kept for up to 8 weeks without mineralization from the bottom layers, with observed new bone formation, even if not significant mineralisation [239].

In terms of angiogenesis, native bone tissue cells are usually not far than 200 μm from the nearest capillary (diffusion distance). Alginate and fibrin hydrogels have shown to facilitate vascularization, against chitosan which has helped cells to produce significant quantities of aggrecan and cartilage ECM. GelMA was used to create bulk and micro-channelled scaffolds to research bone regeneration and angiogenesis. Even though vascularisation of the scaffolds was increased with channelled scaffolds ($\sim 365 \mu\text{m}$), bone mass was not significantly higher, remarking the importance of developing designs that address both requirements [240].

d. Mimicking mechanical properties

The native osteochondral unit is a dynamic one. Both the articular cartilage and the subchondral bone are exposed to constant compressive, tensile and shear forces. The ECM and the cells within it are influenced by this. Stem cells have a direct interaction to their extracellular frame, and can respond to mechanical stimuli within a range of 0.020-0.080 MPa for cartilage and 0.110-0.190 MPa for osteoblasts [241]. Osteochondral defects on bovine explants were placed in a bioreactor (ceramic ball) to create compressive and shear loading. Chondrocytes-seeded fibrin-PU scaffolds were placed in the tunnel and tracked over 10 days. Cell viability and morphology was positive and equal through the experiment, except from areas on the edges of the defect, possibly due to tissue trauma. However, fibrin-PU scaffolds showed low cell migration rates, even when supplemented with fibrin [242].

The aim of biomaterials is to closely mimic the mechanical properties of the native tissue, but not to overpass it as it can drive damage to the host tissue. The articular cartilage has a low compressive stiffness (0.1-2.0 MPa), an elastic modulus of 0.3-1.5 MPa and a Poisson's ratio of $\nu = 0.2$ (stability during elongation process). It has been reported that the minimum stiffness to promote chondrogenesis on MSCs is 5.4-11.8 kPa. On the other hand, the subchondral bone has an elastic modulus of 1-15 GPa; a stiffness of 25-40 kPa is required to promote osteogenesis.

This has been attempted through various manufacturing techniques, being microfluidics and 3D bioprinting the most successful ones [245, 241]. 3D printed polymer/hydrogel scaffolds allow macro and micro-structures to be printed in detail; the combination of inks, and the introduction of cells and molecules within the polymer / hydrogel structures. 3D printed hydrogel-based scaffolds still show low mechanical properties (mainly after implantation), take a long time to be printed (hence risking

cell viability), and the low resolution of constructs does not allow them to reach micro/nano scales [243]. However, mechanical testing on prototypes where ceramics and hydrogels were mixed resulted in the features of soft ceramics: low modulus and low compressive strength, which is significant for their use in soft and hard tissues.

Natural polymers reported good mechanical properties, plus the benefit of a quick degradation. Soybean-derived polyesters scaffolded through salt leaching reported a Young's modulus, UTS and elongation at break of 0.66-2.03, 0.19-0.21 and 62-184% respectively, varying monomer ratio. Degradation rates were also tested and observed bulk degradation, complete within one month *in vitro*. Although increased mechanical properties are closer to native bone ones, embryonic cells attached and proliferated better on mid soft constructs over time, and early mineralisation was observed [244].

Synthetic polymers, pure or blended with micro/nano molecules reported ideal mechanical properties to enhance cell interaction. PCL-Hap scaffolds had 8.7 and 4.6 MPa of compressive modulus and compressive strength [238]. Biphasic porous PCL-coated-PGA and PCL-HAp scaffolds were 3D printed and obtained a compressive modulus of 5.1 ± 1 MPa and 80 ± 30 MPa respectively, both in range with native tissues. Regeneration after 6 weeks denoted articular cartilage, a thin interface, and mineralisation & vascularisation of the subchondral area [245]. PLGA, another polymer highly used due to its exceptional biocompatibility and tailored degradation, was used to produce triphasic porous (200-400 μm) scaffolds with a tubular structure for cartilage regeneration, and a random porous one for bone. The chondral and bone (reinforced with nano HAp) areas had a compressive modulus of \cong 0.85 and 1.95 MPa respectively [215].

Pore size has shown to have a minor effect on overall compressive modulus and yield stress [246]. On the contrary, overall porosity and pore geometry greatly affect these mechanical properties. Pore geometries have been altered to understand how the mechanical properties change and possible effects on cell behaviour. PCL-HAp scaffolds with different angle conformation showed that an increase in porosity was linked to a decrease in Young Modulus, and a similar inversely proportional relation was present between compressive forces and the angle between pore walls (varying according to the axis in which the force was ejected). This is a similar behaviour to the trabecular bone in the body [247].

1.6. Animal models for osteochondral repair

Implanted pieces should be as close as possible to the clinical environment. Small animals for OCD include rats and rabbits, and big animals, dogs, pigs, sheep, goats, and horses [251]. Other elements to be considered are the size and location of the joint, the age of the tissue, its mechanical properties, and its availability. In most cases, the critical size of OCD is created to ensure a less but still significant invasive procedure, as in related to the mean weight of the species. The table below illustrates the most common animals used in OC research and their characteristics [248].

Specie	Skeletal maturity	Cartilage	Bone	OC defects	Disadvantages	Applications
Rats	7 months	Thin (0.1 mm)	Small	2 x 2 mm tunnels are commonly used	Joints are too small for results to be tracked.	Preliminary biocompatibility, toxicity, bioactivity, and materials' interaction [249, 250]
Rabbits	9 months	Thin (0.3 mm)	Small and thin	3-5 x 2-5 mm OC defects	Joint sizes and thickness are not comparable with humans	
Dogs	12-24 months	Thin (0.95 mm)		Propense to develop OCD (OA and osteochondritis) and their tissues do not repair themselves	Big ethical considerations	Articular cartilage regeneration [251, 252]
Pig	18 months	1.5 mm	Close to human	Defects of 6-8 mm and variable depths	Expensive purchase and maintenance	
Sheep	2-3 years	Thin (0.45 mm)	Close to human	Critical size defect is 7 mm	Cartilage is to thin	Orthopaedic research (trabecular metals TM) [33]
Goat	2-3 years	1.1 mm	Similar joint forces	Prone to OC bone defects	Expensive purchase and maintenance;	Degradation rates and safety profile

				Defects used are 6 mm	small size of lesions	of biomaterials [253, 254]
Horse	2 -4 years	1.75 mm	Closest to human anatomy	Prone to OCD Defects used 10 x 5-10 mm	Expensive purchase and post-surgical care	Osteochondral unit repairs under load bearing conditions [255]
Monkey	10 years	0.5-0.7 mm		3.2 x 4 mm defects	Healing behaviours different to other animal models and human	Cartilage regeneration [248]
Human	18-22 years	2.35 mm	Prone to OCD			

From all proposed species, horses are considered the most ideal model due to two main reasons: on one side, their extremities' anatomy (specifically their OC units) is similar to the human body, and they are prone to develop OCD. On the other hand, their active lifestyle resembles the one of humans, where the behaviour of the joints bearing load and shear stress can be used as a reference for human clinical models. Despite of all the advantages, the availability of horses as samples, and the tracking time limit their use.

1.7. Project Aims and Objectives

The aim of this project was to investigate and determine the ideal material properties to design and manufacture a bilayer porous scaffold that could behave as an osteochondral plug in bone and cartilage tissue engineering applications.

This could be accomplished by:

1. The synthesis of PGS and PCL prepolymer solution, and their further functionalisation through methacrylation processes.
2. The design and manufacture of monolayer scaffolds of PCLMA and PGSM through emulsion templating that possessed mechanical properties within the range of the host tissues.
2. The test of above-mentioned scaffolds in biocompatibility and material-cell interactions with cell lines related to their application.
3. The optimisation of both the material and the cell culturing techniques to support cell attachment, proliferation, migration (and optional differentiation) under the described variables.
4. The design and test of bilayer scaffolds under the same parameters.

Chapter II. Materials & Methods

The experimental work took place in the Kroto Research Institute S18 and the Pam Liversidge C+ Laboratory. This section contains materials and methods where protocols are often used in the following chapters. Specific protocols relevant to chapters can be found in such chapters.

2.1. Materials

All reagents were purchased from Sigma-Aldrich (UK) unless otherwise stated.

2.2. Methods

2.2.1. Polymer Synthesis

2.2.1.1. Polycaprolactone (PCL)

2.2.1.1.1. Synthesis of 4-Arm Polycaprolactone [34]

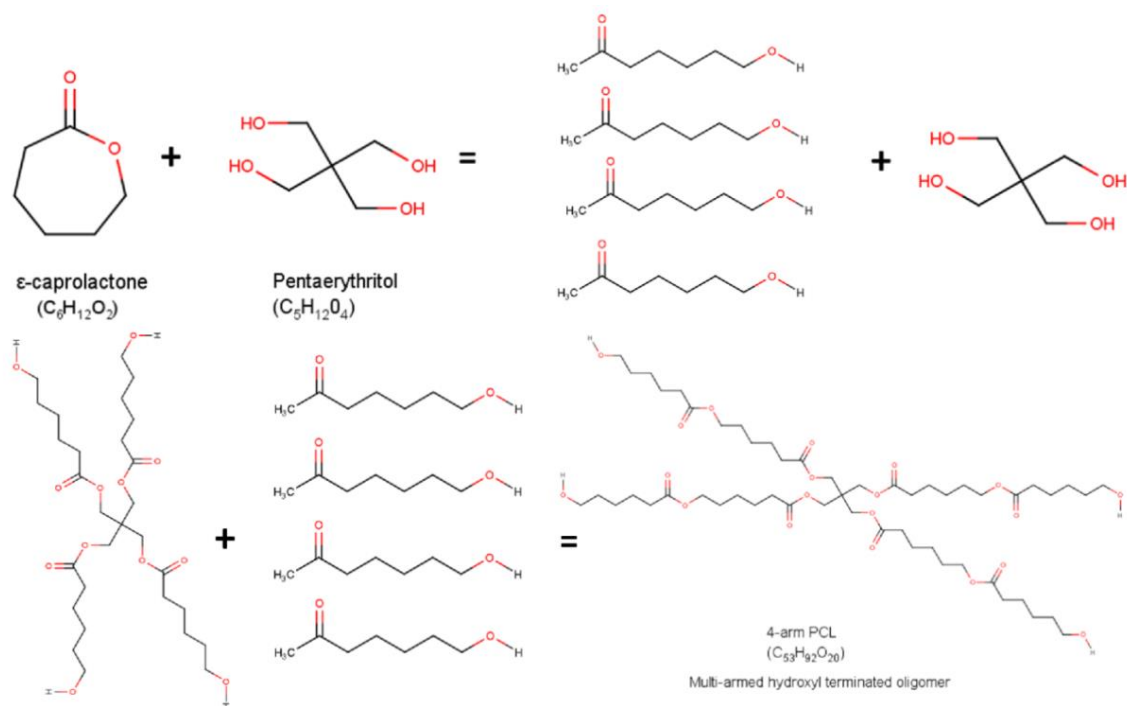


Fig. 13. Synthesis of 4-arm PCL [89].

A ring-opening polymerisation was promoted under a nitrogen-rich atmosphere (1-1.5 LPM, 14 psi). ϵ -caprolactone and pentaerythritol were added to a three-neck flask, plus an 50% excess. The system was set in an oil bath system and warmed up to 160°C at 200 rpm. The left neck was covered with

foil paper, the middle with a cap and the right one with the nitrogen source. When the pentaerythritol had completely dissolved, a drop of Tin 2-ethylhexanoate was added and the system was covered with foil paper and left for 24 hours. The system was then removed from the bath and cooled down. Fig. 13. Illustrates the synthesis process.

2.2.1.1.2. Methacrylation of 3 and 4-arm PCL

The functionalisation of PCL oligomers was done by adding photo-crosslinkable methacrylate groups to the polymer terminal ends. Dichloromethane (DCM, $\geq 99.8\%$) was used to dissolve the PCL before transferring it to a 3-neck round flask. 6:1 molar proportion of Triethylamine (TEA, $\geq 99.5\%$) was added and the reagents were stirred with extra volume of DCM. The flask was immersed in an ice bath and set to 350 rpm. Methacrylic acid (MAA, 99%) was weighed in a 6:1 molar proportion and mixed with 100 ml of DCM. This was transferred to a dropping funnel and included in the ice bath system, at the speed of one drop per second. When the MAA had been poured, the system was left overnight at room temperature, in dark conditions and at 350 rpm.

2.2.1.1.3. Polymer purification

A litre of HCl (12 M) solution was prepared with deionised water. The prepolymer solution was added to a separation funnel and the acid solution was poured in. The container was then shaken in cycles to remove remaining pressure. The system was left to decant, and the polymer/DCM layer was poured out. This was repeated 3-4 times. The mixture was then washed with deionised water. Subsequently, the mixture was transferred to a rotary evaporator system, covered in foil paper and placed in a water bath. The solvent was removed over time and the PCL methacrylate was transferred to a large bottle with 8-12 \times volume of methanol. The solution was placed in a -80°C freezer overnight and the next day the methanol was replaced. After repeating this process for 2 days, the extra solvent was removed in the rotary evaporator and the PCLMA was stored in a vessel in the freezer.

2.2.1.2. Poly(glycerol sebacate) (PGS)

2.2.1.2.1. Synthesis

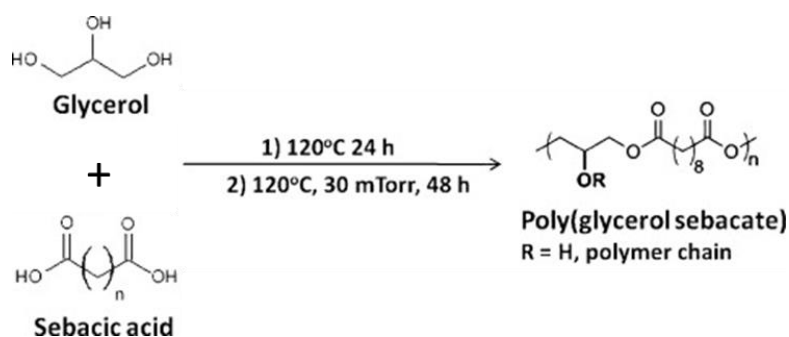


Fig. 14. Synthesis of PGS by a condensation reaction between glycerol and sebacic acid [90].

The desired weight of sebacic acid (usually 120 g) was placed in a three-neck flask. An equimolar weight of glycerol was poured from the middle neck. The flask was placed in a nitrogen system; the left neck was connected to the nitrogen source, the middle one was open for gas recirculation and the third one supported a thermometer. The system was warmed up to 120°C and left for 24 hours in an oil bath at 150 rpm. The nitrogen source was then replaced with the vacuum and the middle neck was covered. The system was left for 24 hours (Fig. 14).

2.2.1.2.2. Methacrylation

A gram of prepolymer PGS possesses around 0.00387 moles of OH [34]. 30%, 50% and 80% PGSM was produced. After 24 hours of vacuuming, the system was removed from the oil bath and left to cool at room temperature. DCM (1:4 w/v) was added until completely dissolved using agitation. When homogeneous, the system was set into an ice bath. Triethylamine (TEA) was added on the middle neck according to the amount of moles of OH intended to be methacrylated (1g of PGS prepolymer solution has approximately 0.00387 mol of OH). Subsequently, Methoxyphenol (MeHQ) was added by 1 mg MeHQ per g of prepolymer PGS to prevent undesired crosslinking. When the solution had been well mixed, Methacrylate anhydride (MEA) was incorporated using a dropping funnel at a rate of one drop / second. The system was covered with foil paper and left at 150 rpm for 24 hours. The next day, an extra 0.5 mg of MeHQ/ g of PGS prepolymer was added to stop crosslinking.

2.2.1.2.3. Purification and solvent extraction

Washes were performed using a litre solution of 30mM hydrochloric acid (HCL) as explained in PCLMA steps. The system was placed in an ice bath in the rotary evaporator and the solvent was removed until the PGSM reached a honey-like viscosity. The PGSM was transferred to a glass bottle and stored in the freezer under dark conditions.

2.2.2. Manufacturing

PCLMA, PGSM and PCLMA:PGSM bulk polymerisation

Polymer solution was warmed up to room temperature and 5% of photoinitiator (diphenyl (2,4,6 trimethylbenzoyl)) was added to a glass vial. The mix was stirred at 850 rpm for 5 minutes and poured into the silicon or printed moulds. To remove big bubbles, the mix was placed in the vacuum oven at room temperature until no signs of bubbles were present.

2.2.2.1. PCLMA PolyHIPEs

0. 4 g of PCLMA and 10% wt of Hypermer surfactant were added to a glass vial and heated to 40°C until completely dissolved. This step can be removed if the PCLMA solution is in a liquid form rather than powder. A Chloroform: Toluene solvent solution 60%:40% wt was prepared and 1.5x volume was added from PCLMA weight (0.6 g); and 5% PCLMA wt of photoinitiator. The mixture was placed in a 37°C water bath and mixed at 350 rpm using a small oval magnetic stirrer and a 20 ml glass vial. When homogeneous, a known volume of water was added dropwise (2 to 3 ml), and the mixture was left for a total mixing time of 10 minutes. The emulsion was transferred to a plastic syringe or PDMS silicon moulds and placed under UV light using an OmniCure Series 1000 curing system (100W, Lumen Dynamics, Canada) for 5 minutes each side.

2.2.2.2. PGSM PolyHIPEs

0. 5 g of PGSM, 0.05 g of Hypermer surfactant, 0.5 g of Toluene solvent and 0.2 g of photo-initiator (diphenyl (2,4,6 trimethylbenzoyl)) was added to a glass vial and mixed at room temperature and 350 rpm, using a small oval magnetic stirrer. When the mix was homogeneous, a known volume of water was added dropwise (2 to 3 ml), and the mixture was left for a total mixing time of 10 minutes. Curing steps were as reported in PCLMA.

2.2.2.3. PCLMA:PGSM PolyHIPEs

PCLMA and PGSM polymer solution was mixed at 350 rpm, according to the desired ratio for at least 1 hour at room temperature, using an amber vial and a small magnetic stirrer. Posteriorly, 0.5g of the PCLMA:PGSM, 0.05 g of Hypermer surfactant, 0.2 g of photo-initiator and 0.5g of a Toluene:DCE solvent solution 60%:40% wt was added to a glass vial. The mix was allowed to become homogenous for 3 minutes; a known volume of water (2-3 ml) was added dropwise, and the mixture was left for a total mixing time of 10 minutes. Curing steps are as we reported for PCLMA.

2.2.3. Scaffold washes and drying methods

2.2.3.1. Methanol and water washes

Scaffolds were washed in methanol solutions for 4 days (100%, 80%, 50%, 30%) and then placed into deionized water for mechanical testing or PBS for cell seeding.

2.2.3.2. Drying method: Air conditions

Scaffolds were placed in separate wells in a 24-well plate. The lid is left half open, and they remained in dark, dry conditions overnight.

2.2.3.3. Drying method: Freeze drying

Scaffolds were placed in separate wells of a 24-well plate. An extra volume of water was left on each well. Afterwards, they were placed inside of the freezer at -80°C for at least 2 hours. Scaffolds were then placed inside of the cold chamber of an EC Modulyo Freeze Dryer at -60°C and vacuum pressure. They were left under such conditions, overnight.

2.2.4. Surface modification

2.2.4.1. Plasma coating

Scaffolds were either dried overnight or in a 30-45°C environment before being coated. Scaffolds were placed in a foil paper bed and a Zepto Plasma Surface Machine (Diener Technologies) was used for the time and power depending on the hydrophobicity desired. Scaffolds were then placed into PBS or deionised water and were used within 3 days.

2.2.4.2. Fibronectin

Scaffolds were moved from their deionised containers and placed in a 50 µg/ml solution of human fibronectin (Yo Proteins AB). The vials were left in fresh conditions, overnight.

2.2.5. Characterisation

2.2.5.1. Hydrophobicity: Water contact angle

A Kruss DSA 100 machine was used to test hydrophobicity of porous scaffolds. Scaffolds, both plasma-coated and non-coated, had previously dried at room temperature. The sample was placed in the platform and 5 ml of deionised water was dropped from a 1 ml syringe with Gauge 23 needle size. The angle was recorded and a picture from the position was taken immediately after.

2.2.5.2. ^1H Nuclear Magnetic Resonance (NMR)

Bruker BioSpin AVANCE III 400 NMR (5mm solution state BBFO - ^1H / ^{19}F - ^{15}N dual resonance, z-gradient) System GH000507 was used to identify peaks related to chemical compounds in polymer solutions. A fresh vial of polymer was kept in dark conditions and low temperatures beforehand. A sample of 10 μl was tested, and readings were repeated in triplet. Specific NMR spectra peaks were associated to corresponding functional groups (or chemicals remaining).

2.2.5.3. Gel Permeation Chromatography (GPC)

A Viscotek GPCmax VE200 system with differential refractive index detector (Waters 410), was used to determine the molecular weight of non-methacrylated and methacrylated polymer solutions (10-20 mg), dissolved in tetrahydrofuran (THF). A flow rate of 1 ml/min at 40 $^{\circ}\text{C}$, and polystyrene calibration standards were used.

2.2.5.4. Scanning Electron Microscopy (SEM)

PCLMA scaffolds were dried beforehand at room temperature and covered in foil paper. PGSM and PCLMA:PGSM scaffolds were firstly frozen at -80°C for at least two hours and then dried overnight in a freeze-dryer under dark conditions, -60°C and a vacuum system. Polymeric samples were moulded into metallic stands with conductive carbon stickers. Next, they were exposed to gold coating using a Quorum Q150T-ES with a layer of 8-10 nm. To ensure full conductivity in thick samples, dots of silver ink were placed between the coating and the sticker. An Inspect FEI F50 SEM was used with magnifications from 40x-2000x to record images of the surface and internal porosity of scaffolds, coated and non-coated, before and after they were seeded with cells. The accelerating voltage used varied between 5 to 10 kV.

2.2.6. Mechanical testing

2.2.6.1. Tensile strength

Bulk monoliths were created by mixing the polymer solution with 5% of photoinitiator as described in *Section 2.2.2.1*. Porous samples were created by using the PolyHIPE formulas as mentioned above. The mix was then injected into PDMS moulds designed in accordance with ASTM D638-10 but reduced by a factor of 3.83 to fit the maximum sample size of the testing machine. The final dimensions of the exposed part of the dogbone (testing part shown as red in Fig. 15). Bulk and porous polymers were cured under a UV lamp for 5 minutes on each side.

Bulk samples were clamped into a Mecmesin OmniTest single-column materials tester using a 25 N load cell for porous samples, and a 250 N load cell for bulk samples. Porous samples were fragile; therefore, a cardboard support was created to ease the clamping and removed for the testing Fig. 15. Samples were tested at a speed of 6mm/min and the test was left until the point of break. Young's modulus was determined using the linear region of the load-displacement curve.

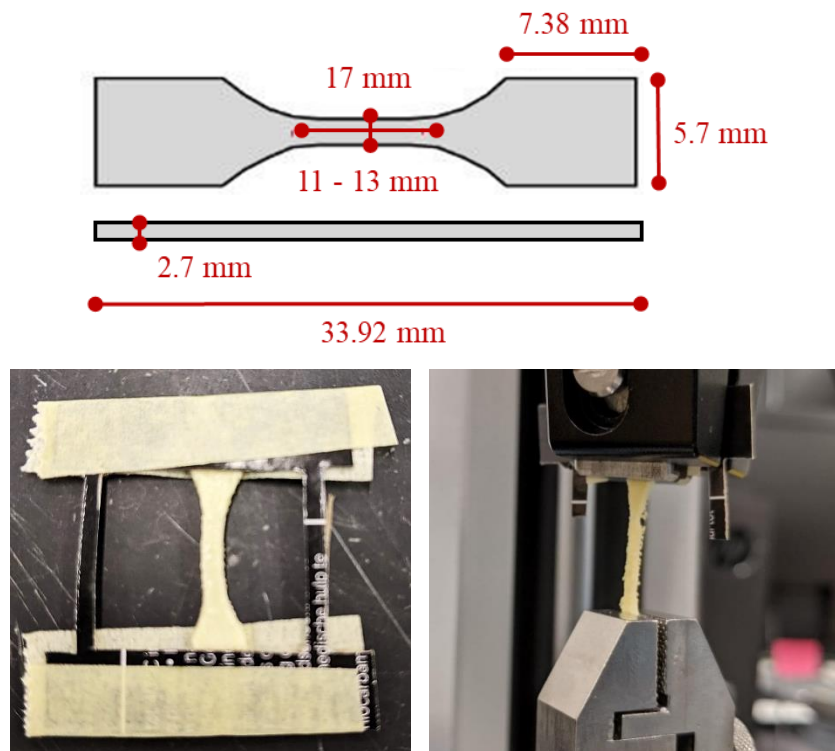


Fig. 15. Cardboard structure to give extra support to assemble porous samples for tensile testing.

2.2.6.2. Compressive Strength

Bulk monoliths were created by mixing the polymer solution with 5% of photoinitiator as described in *Section 2.2.2.1*. Porous samples were prepared as PolyHIPE formulas mentioned above. The polymer mix was poured into cylindrical moulds [256]; samples were cured under UV light for 10 minutes on each side.

Samples were placed in plates of a Mecmesin OmniTest single-column materials tester using a 25 N load cell for porous samples, and a 250 N load cell for bulk samples. Samples were tested at a speed of 1 mm/min and the test was left until total collapse. Compressive Young's modulus was determined using the linear region of the load-displacement curve.

2.2.7. Imaging

2.2.7.1. Vibratome

PolyHIPE and bulk scaffolds were sliced using a *Ci* Campden Instruments 5100 Mz Vibratome with a range of thickness of 25 to 500 μm , at a speed of 0.15 m/s and 80 MHz. The slicing environment was kept cold and wet using a bed of deionised water and ice. PGSM and hydrogel samples were frozen at -80°C overnight before being mounted. Slices were kept submerged in PBS with 0.1% sodium azide to prevent the growth of pathogens.

2.2.7.2. Digital Microscopy

A Motic BA210 Binocular Compound Microscope was used to image slices from porous polymer and hydrogel scaffolds. Slices were kept in a wet environment whilst imaging to reduce blurriness on the edges. Lens with magnifications of 4x, 10x, 20x and 40x were used, as indicated in the legend of the figures.

2.2.7.3. Lightsheet Microscopy

Lightsheet microscopy was used to obtain 3-dimensional images of PCLMA and PGSM scaffolds using a Z.1 lightsheet microscope (Carl Zeiss AG, Germany) and ZEN imaging software (Zen 9.2.8.54, Carl Zeiss, Germany). Wet scaffolds were cut into 2 mm diameter cylinders using a hole puncher and arranged inside of a glass capillary, aided by a 1% agar solution. Samples were localised and positioned in front of the objective (Zeiss W Plan-Apochromat 10 x / N.A. 0.5 for detection and Zeiss W Plan-Apochromat 10 x / N.A. 0.1 for illumination). Alexa Fluor 488 and Alexa Fluor 546 were used as excitation and emission wavelengths, taking advantage of the scaffold's own

fluorescence. Images were processed using Zen software and Image J. A Z-stack was used to create three dimensional images of the scaffolds, made up of 150 – 400 stacked images.

2.2.7.4. Epifluorescent Microscopy

Sliced scaffolds between 30 and 80 μm were kept in an aqueous environment and imaged using the Brightfield setting of an Inverted Olympus Fluorescent Microscope. Lenses with magnifications of 4x, 10x, 20x and 40x were used, as indicated in the legend of the figures.

2.2.8. Degradation

Polymeric scaffolds were placed in different solutions to track their degradability over time: i) PBS buffer solution (as a neutral environment) and ii) Sodium hydroxide 0.1 and 0.8 M (used as alkaline solution to simulate an aggressive environment like the one scaffolds could face *in situ*). Scaffold degradation was measured at t_0 and every week for 3 months. For doing that, bulk scaffolds were dried in an oven for 1 hour before being weighed, and porous scaffolds were dried with a soft white cloth. Disturbances in the solution were observed using a digital microscope and the naked eye as delamination and cracking of the scaffolds can be easily identified in the macrostructural level.

2.2.9. Hydrogels

2.2.9.1. Alginate matrices

Sodium alginate and calcium chloride solutions were prepared by dissolving the desired amount (1-2%) of each material in deionised water. Solutions were filter sterilised and autoclaved prior to cell studies. Drops, slurries or moulds of sodium alginate were submerged in a beaker with calcium chloride and then removed prior to storage in water at 4°C or in media at 37°C.

2.2.9.2. Gelatin matrices

Gelatin solutions from bovine skin were prepared by dissolving the desired amount (1-2%) in boiling water and left stirring for at least 3 hours in a boiling water bath. Vials of the solution were stored at 4°C.

2.2.10. Cell lines

2.2.10.1. For tissue regeneration purposes

2.2.10.1.1. Osteoblast cell line

Human embryonic stem-cell derived mesenchymal progenitors (hES-MPs) were used for osteogenic growth and further differentiation. They possess a mesenchymal phenotype and a fibroblast

morphology, which is spindle-like when cultured in static conditions [257]. They are able to express markers present in adult MSCs [258]. The passages ranged between 9 – 11.

2.2.10.1.2. Chondrocyte cell line

Bovine articular chondrocytes (BACs) were used for chondral research. In high densities, they produce matrices rich in type II collagen and proteoglycans. They have a spherical morphology when cultured in solution / hydrogels and a flattened one in monolayered cultures [259]. Passages used were between 3 – 6.

2.2.10.1.3. Immortalised cell line

The clonal line Y201 was initially isolated from human bone marrow and has been shown to maintain adipogenic, chondrogenic and osteogenic potential. They have been immortalised with the human telomerase gene (“hTERT MSCs”) to help overcome challenges in limited lifespan and variability of other MSCs [260].

2.2.10.2. For control

Human Dermal Fibroblasts (HDF) and Murine Osteocyte-like (MLO5) cell lines were used as controls on early cytotoxic and attachment experiments. The culture and seeding techniques were equal to the ones they were paired to (HDF as hES-MPs control, and MLO5 as BACs control).

2.2.10.3. Culture media preparation

BACs, MLO5, HDF and hES-MP cell lines were used a Basal Media (BM) which is the simplest formulation of medium plus foetal bovine serum (FBS), antibiotics and glutamine. The Expansion Media (EM) was used to enhance growing during culturing and includes BM and human fibroblast growth factor (hFGF). The EM was used only on day 1 when culturing BACs and in every media change for hES-MPs if the passage was higher than 11. Finally, a specialised media to promote differentiation was prepared. This Supplemented Media (SM): Osteochondral Media and Chondral Media (OCM / CEM respectively) was distributed according to Table 1.

Table 1. Media formulations and conditions for cell growing on primary and derived cells.

Cell line	hES-MPs	BACs
BM	α -MEM (Lonza) + 10% FBS + 2mM L-glutamine + 100 U/mL penicillin + 100 mg/mL streptomycin	DMEM (Sigma) + 10% FBS + 2mM L-glutamine + 100 U/mL penicillin + 100 mg/mL streptomycin
EM	BM + 4 nM hFGF	
SM	OCM: BM + 5 mM β GP + 50 μ g/mL AA-2P + 100 nM Dex	CM: BM + 1% NEAA + 1% HEPES + 1.67% Glucose
Conditions	37°C and 4-10% CO ₂	
Culturing time	8 – 10 days	4 – 5 days

Y201 cell line used an alternative serum-free media (SFM) from STEMACS which was supplemented with its own supplement and antibiotics. The expansion and differentiation media used was identical to the OCM.

2.2.10.4. Expansion, growing, culturing, and subculturing

Cell lines were expanded in T75 flasks. hES-MP culturing requires a previous coating with gelatine 1%. EM is added to all flasks from day 0.

Media change was performed on day 1 after thawing / subculturing and every 2-3 days, except on Y201 cells with a media change every 4-5 days. Cells were subcultured / frozen / used when they arrived at 80% confluency.

When cells were confluent, they were washed with a volume of 3 ml of PBS. 3 ml of trypsin (Trypsin-EDTA) was added to each flask and incubated at standard conditions for 5 minutes. The flask was then mechanically stimulated to enhance correct cell de-attachment, confirmed under the digital microscope. 2:1 BM media volume was added to the flask and then transferred to a Universal tube to be centrifuged at 1000 rpm for 5 minutes.

A small vial of 20 ml was sampled for cell counting (Cell sample: Trypan Blue solution at 1:1) and pelleted into a haemocytometer. When the cell tube was ready, the supernatant was removed in a single move; the pellet was resuspended in the desired volume of media.

If cells were required to be preserved, they were frozen under liquid nitrogen at -196°C , in a similar process as subculturing. After cells were centrifuged, they were suspended in Freezing Solution (FS), 90% FBS and 10% liquid DMSO. Cells were then pelleted into 1 ml cryovials, labelled, and placed in a Mr Frosty at -80°C overnight. The next day they were transferred to the nitrogen environment.

If cells were required to be thawed, they were warmed up for 20 seconds in a water bath and immediately transferred to a calculated BM volume and a flask. Media change was done on day 1 to remove residual DMSO.

2.2.10.5. Seeding

After being coated, scaffolds were stored in a PBS solution. The night before seeding, they were transferred to FBS and stored at 4°C . Early morning, scaffolds were placed in a 24 well plate with a FBS mirror layer on each well to prevent them from drying out. Cells were detached from the flasks and centrifuged as previously described whilst a sample was used to count them. The pellet was then resuspended in a known volume of media. All experiments followed the next concentration except otherwise stated: 25,000 cells per side (if two sides seeded) or 50,000 cells per side (once seeded) and 20 ml of cell volume was pipetted on the surface of each scaffold. After seeding, cells lay for 1 hour in-between seedings and afterwards, 1 ml of BM was added and stored in the incubator. Resazurin viability test was performed on day 1, 3, and then weekly. Media is changed every 2-3 days and post-Resazurin test washes.

2.2.10.6. Cell viability test:

2.2.10.6.1. Resazurin reduction assay

This protocol was developed on both 2D and 3D experiments (both seeded scaffolds and cells that fell into wells). First, a Resazurin solution was prepared from filtered Resazurin stock (1% in deionised water) at 10% with BM. Media was removed from the wells and 1 ml of the Resazurin solution was added to each well. Plates were covered with foil paper and incubated for at least 2 hours. Subsequently, each well was sampled in triplet with 200 μl and placed into a 96 well plate, in a non-parallel pattern. Four control wells were included: Resazurin solution, media solution (S-C-), seeded cells in media (S-C+), and scaffolds in PBS (S+C-). A Tecan Infinite F200 Pro plate reader was used for reading fluorescence values from 540 - 590 nm. Scaffolds and wells were washed with PBS three times before media was added.

2.2.10.6.2. MTT assay

A solution of 0.5 mg/ml of MTT in PBS was prepared in a controlled environment. Each well was added with 1 ml of the solution and incubated for 40 minutes. In the meantime, acidified isopropanol was prepared by adding 80 ml of 10M HCl to 10 ml of 99.5% propan-2-ol. MTT solution was removed from the wells and gently washed with PBS; repeat this step another 2 times. 1 ml of acidified isopropanol was added to each well. Subsequently, each well was sampled in triplet with 200 µl and placed into a 96 well plate, in a non-parallel pattern. Absorbance was determined using a plate reader at 562 nm and a reference of 630 nm.

2.2.10.7. Migration: histology and cryo-dissection

2.2.10.7.1. Cell fixation

The media was removed from the wells and a 3.7% formaldehyde solution was added to cover the surface of each well (2D) or the scaffolds (3D); plates were left at room temperature from 15-20 minutes. Wells / scaffolds were washed in PBS 3 times for 5 minutes and the procedure was repeated using a 0.1% v/v Triton X200/PBS solution. Scaffolds/wells were left in PBS in the fridge.

2.2.10.7.2. Cryo-dissection

Samples immersed in PBS were dried using tissue paper. The samples were placed in a plastic mould in the desired orientation (direction of cut). Freezing media was added and bubbles were removed using the vacuum chamber. Freezing media was solidified using liquid nitrogen and samples were dismantled from moulds and kept inside of cryo-dissector Leica Reichert Jung Cryocut Cryostat. Slices or 8-10 mm were cut and arranged on labelled objective glasses. If samples were not to be stained, microscope mounting media was used to stick coverslip to objective glass. Otherwise, samples were left to dry before staining.

2.2.10.7.2.1. H & E staining

Objectives were assembled in the staining dishes on the same orientation. The rack was immersed in the following steps: 1) Distilled water for 1 minute, 2) Harris Haematoxylin solution for 1.5 minutes, 3) Running water for 4 minutes, 4) Eosin-phloxine solution for 5 minutes, 5) Dunk in tap water, 6) Dunk in deionised water, 7) Dunk in 70% ethanol, 8) 100% ethanol for 30 seconds, 9) Dunk in xylene. Objective glasses were dehydrated under the hood before being dismantled and covered with microscope mounting media and coverslips as previously mentioned.

Chapter III: Polycaprolactone

A successful biomaterial provides a stable platform for the regeneration of neo-tissue, whilst encouraging the necessary biological mechanisms for this to happen. In this resides the importance of tailoring the material's properties to mimic the tissue where it will be implanted. This chapter is focused on the production (synthesis and functionalisation) of polycaprolactone (PCL) as a biomaterial for osteochondral applications, specifically for the mineralised cartilage and trabecular bone area. Additionally, it discusses the construction of 3D scaffolds through photo-crosslinking water-in-oil emulsions. Mechanical and chemical characterisation of PCLMA scaffolds is included, as well as a thorough analysis on the effect of the several manufacturing variables in the macro and micro features of the resulting scaffold.

3.2. Introduction

Synthetic biomaterials like metals, ceramics, glass, hydrogels, and polymers are widely used for biological applications. By synthesising them, chemical and physical properties can be tailored to the required detail. Human tissues and organs have macro, micro and nano conformations that can be mimicked by these biomaterials. Within the wide range of possible features, ceramics, hydrogels, and polymers have been the most promising, specifically in relation to osteochondral applications; a solid structure is required on the bone part, whilst a softer still structured layer can support cartilage regeneration.

The synthesis of PCL has been extensively studied, as it is a component for production of polyurethanes [111, 265]. Among other organic chemistry procedures, this is an easy and practical reaction, as well as being cost efficient. Additionally, it allows for the use of optimisation techniques like blending, functionalisation, and copolymerisation [266]. The synthesis of PCL through a ring opening reaction is compatible with the functionalisation of important biomolecules like carbohydrates and proteins [267, 116].

Functionalisation of polymers can be achieved through diverse ways. The chemical family of methacrylates was first used in the late 1880's [166]. Methacrylates polymerise easily, conferring beneficial features to their products or when added to other materials. The acquired chemical and physical stability influences final mechanical properties and degradability. PCL prepolymer solution has been methacrylated to different degrees using methyl methacrylate. The addition of methyl acrylates to available reactive end groups facilitates the creation of crosslinkable structures. These

structures were designed using a water-in-oil (W/O) emulsion, which allowed the development of porous and interconnected scaffolds. W/O emulsions are tailored through internal and external variables. Internal variables concern the nature of the ingredients used: polymer, solvents, surfactants, photoinitiators, and the difference/similarity among each other's properties. External elements include mixing speed, phase densities and applied pressures and temperatures. The interconnected relation among these factors influences the pore morphology, pore and window size, porosity, internal phase volume (which ultimately affect the mechanical properties of the structure), and the cellular response. According to the literature, the resulting 3D constructs can be categorised as HPIEs (more than 74% internal phase volume), whose mechanical properties are suitable for hard tissue applications (bone and cartilage).

3.3. Aims and objectives

- i) To synthesize prepolymer solutions of PCL useful for biomaterials applications.
- ii) To methacrylate PCL prepolymer solution to degrees where their functionalisation supports optimal mechanical properties for cartilage and bone applications.
- iii) To create stable PCLMA emulsions with a defined porosity higher than 70%, phase internal volume higher than 70% and pore sizes in ranges of 100-300 μm .

3.4. Materials and Methods

Despite the main materials and methods being outlined in Section 2, the following were used in this chapter.

3.4.1. Internal Phase Volume

To calculate the internal phase volume of porous materials, **Erreur! Source du renvoi introuvable.** Where the oil phase is made by the polymer solution, surfactant, and photoinitiator. The water phase is made by the adsorbed deionised water. All values are in volume.

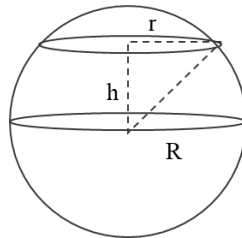
3.4.2. Gel Fraction

The determination of the gel fraction was used to measure the level of crosslinking of the polymers. For this, polymer solution was mixed with 5% w/w photoinitiator and photocured with UV light for 5 minutes on both sides. Samples were immersed in 10 ml of DCM to dissolve uncrosslinked polymer. Samples were then dried and vacuumed overnight. The weight was recorded at t_0 (W_0) and the next morning (W_i). Gel fraction is calculated using below [109]:

$$\% \text{ Gel Fraction} = \frac{W_i}{W_0} \quad \text{Eq. 1}$$

3.4.3. Degree of openness (DOO)

When scaffolds are sliced or moulded, the fracture or tearing occur at the weakest areas around the pore and not in the largest diameter. Therefore, a correction factor was used to account for this. Measured pores were multiplied by $\frac{2}{\sqrt{3}}$; when dissected pores are sliced on random (h) distances from their centre, their radius (R) can be calculated from h rather than the hypothetical radius (r), as $\frac{R}{r} = \frac{2}{\sqrt{3}}$ [261]:



3.4.4. Density

The density of both the bulk polymer and HIPEs was calculated in triplet through the mass and volume of the cylindrical scaffolds. The average dimensions of the constructs were 6 mm diameter and 4 mm height.

3.4.5. Empirical porosity

The porosity of the HIPEs was calculated through Eq. 2 [262]:

$$\% \text{ porosity} = \left(1 - \frac{\rho \text{ polyHIPE}}{\rho \text{ wall}} \right) \times 100 \quad \text{Eq. 2}$$

Where $\rho \text{ polyHIPE}$ is the density of the HIPE, and $\rho \text{ wall}$ is the density of the HIPE's wall. The density of the HIPE was calculated using Eq. 3:

$$\rho \text{ polyHIPE}_{\text{theoretical}} = \rho_{\text{polymer}} \times (1 - \theta) \times \text{Gel Fraction} \quad \text{Eq. 3}$$

Where ρ_{polymer} is the density of the bulk polymer, θ is the internal phase volume, and the gel fractions were calculated as explained in Section 3.3.2. The density of the HIPE's wall was calculated using the density of the bulk polymer.

3.4.6. Pycnometry

Pycnometry is a non-destructive technique based on either Archimedes' principle of body displacement (if liquid) or Boyle's Law of volume-pressure (if testing solids using helium gas). The tests were used to determine the density of bulk polymers. Additionally, it was used to determine the density of polyHIPEs and verify the porosity of the 3D scaffolds. Measurements were run on an AccuPyc 1340 gas pycnometer (Micromeritics, GA, USA) at room temperature (15°C) and a constant pressure of 19 psi. The samples were firstly weighed by triplet and each sample was measured in a cycle of 5 runs and 5 purges in a 1cm³ chamber.

The total porosity of the materials studied ($P^{(\text{He})}$, %) was calculated as the fraction of space accessible to the gas (He) in the chamber, according to Eq. 4 [263]:

$$P^{(\text{He})} = 100 \left(\frac{V_{\text{empty}}}{V_{\text{u.cell}}} \right) = 100 \left(1 - \left(\frac{d_{\text{calc}}}{d^{(\text{He})}} \right) \right) \quad \text{Eq. 4}$$

Where,

V_{empty} = volume of unit cell accessible to He

$V_{\text{u.cell}}$ = volume of the unit cell

d_{calc} = density calculated from XRD data (room temperature)

$d^{(He)}$ = density from He pycnometry measurement (skeletal density)

3.4.7. Interconnectivity

The interconnectivity between pores was calculated from the average void diameter (pore size, D) and the average interconnect diameter (window size, d), following Eq. 5 [109, 261].

$$\frac{d}{D} = \frac{\text{window size}}{\text{pore size}} \quad \text{Eq. 5}$$

3.4.8. Micro CT Imaging

A Zeiss Xradia Versa 530 (Pleasanton, CA, USA) was used to carry out high-resolution non-destructive imaging; this was achieved using a CCD (charge coupled device) detector system with scintillator-coupled visible light optics and a tungsten transmission target. Initial scans of the barnacle region block were achieved with an X-ray tube voltage of 70 - 80kV, a tube current of 120-125 μA , and an exposure time of 4-7 seconds. A total of 1601 projections were collected. A filter (LE4) was used to filter out lower energy X-rays, and an objective lens giving an optical magnification of 0.4 and 4x was selected with binning set to 2, producing an isotropic voxel (three-dimensional (3D) pixel) size of 2.02, 8.92 or 13.01 μm . The tomograms were reconstructed from 2D projections using Zeiss Microscopy commercial software package (XMReconstructor) and an automatically generated cone-beam reconstruction algorithm based on filtered back-projection. The scout and zoom methodology were used to create high-resolution regions of interest (ROIs) within the sutures. Samples were scanned at the X-ray CT Facility at the University of Sheffield, UK. 3D volume information was segmented and visualised in the specialised tomographic software Avizo (Thermo Fisher Scientific, Hillsboro, USA).

3.5. Results

3.5.1. Polycaprolactone

As mentioned above, polycaprolactone is a biocompatible and FDA-approved material, currently used for tissue ingrowth and drug delivery. Additionally, this polymer is commonly synthesised due to its low melting point and low temperature glass transition. PCL is a malleable product, soluble in a variety of organic solvents and available for blending [264].

3.5.1.1. Synthesis and methacrylation

3-arm PCL can be purchased directly from Sigma Aldrich, On the other hand, 4-arm PCL was firstly synthesised through a ring opening reaction (ROP) between ϵ -caprolactone (Mw: 114.14 g/mol) and pentaerythritol (Mw: 136.15 g/mol) in an equimolar relation 8:1. The system was catalysed through Tin (II) 2- ethylhexanoate and the system was left to react under a nitrogen environment. The resulting prepolymer solution was methacrylated as highlighted in the next paragraph. The resulting polymer has its spectra illustrated in Fig. 17.

PCL pre-polymers were methacrylated as explained in *Section 2*. Briefly, PCL triol (Mn: 900 g/mol) was dissolved in dichloromethane (DCM). Triethylamine (TEA / Mw: 101 g/mol) and methacrylic anhydride (MAA / Mw: 154 g/mol) were added in 1:1 molar ratio and the system was left in a nitrogen environment for 20 hours to reach a degree of methacrylation close to 50%. Reproducibility of the batches is observable in *Fig. 16*.

PCL was methacrylated for 10, 20 and 36 hours and the resultant products were labelled as low (PCL-LM), 50% (PCL-50%) and high (PCL-HM) methacrylation. PCL methacrylation was controlled through the reacting OH groups of the polymer chain.

The ¹HNMR analysis on both 3 and 4-arm PCL confirmed the chemical composition of caprolactone at peaks 1.4, 1.6, 2.3 and 4.1 ppm. The small peak at 1ppm denotes the presence of methyl protons of the 3-arm PCL (the central -OH group has 3 hydroxyl groups instead of 4, as the 4th -OH group is substituted by -CH₃) [267].

However, PCL (LM, 50% and HM) showed methylene groups adjacent to hydroxyl end groups expressed in peak 3.6. When methacrylation took place, these peaks were reduced, and expressed in peaks 1.9, 5.5 and 6.1 ppm; such peaks were only visible on methacrylated polymers [89].

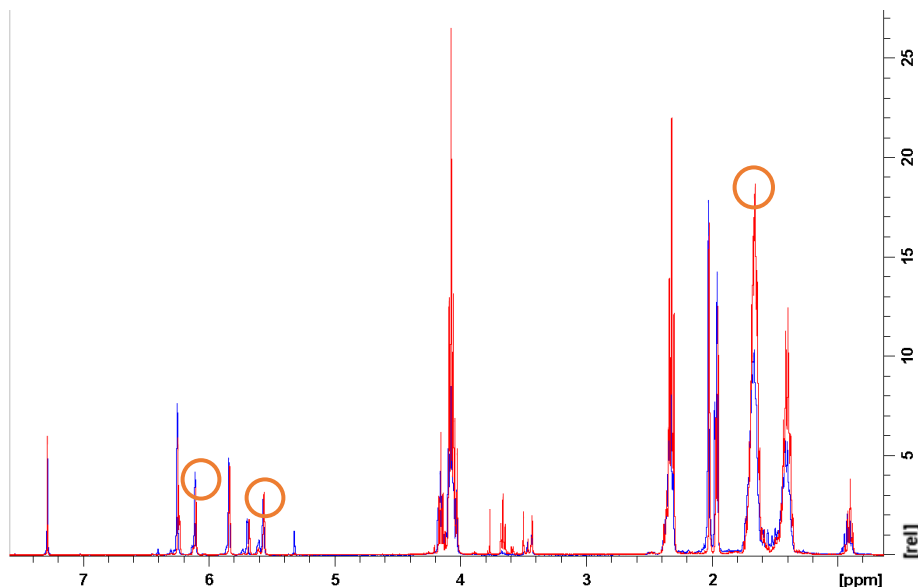


Fig. 16. Spectra of $n=3$ batches of 3-arm PCLMA 50% DM. Polycaprolactone peaks are found at 1.4, 1.6, 2.3 and 4.1 ppm. Methacrylic groups are found in 1.9, 5.5 and 6.1 ppm. The peak just before 1 ppm evidences its 3-arm structure. DM: degree of methacrylation. The two colours symbolise different batches.

Messori *et al*, proposed the following formula to verify the degree of methacrylation (D_M), by using the area below the peaks 3.5 and 3.64 ppm, related to methylene groups adjacent to unreacted hydroxyl groups, and methylene groups adjacent to nitrogen on reacted groups [266]:

$$D_M = \frac{I_{3.5}}{I_{3.5} + I_{3.64}} \times 100 \quad \text{Eq. 6}$$

According to this, the degrees of methacrylation were as shown in Table 2.

Table 2. Theoretical and experimental degrees of methacrylation for 3-arm PCLMA, 4-arm PCL low methacrylated (LM), 50% methacrylated, and high methacrylated (HM).

Sample	Theoretical D_M	Experimental D_M
3 arm PCL 50%	50%	48.3%
4 arm PCL LM	20%	17.9%
4 arm PCL 50%	50%	48.8%
4 arm PCL HM	70%	72.0%

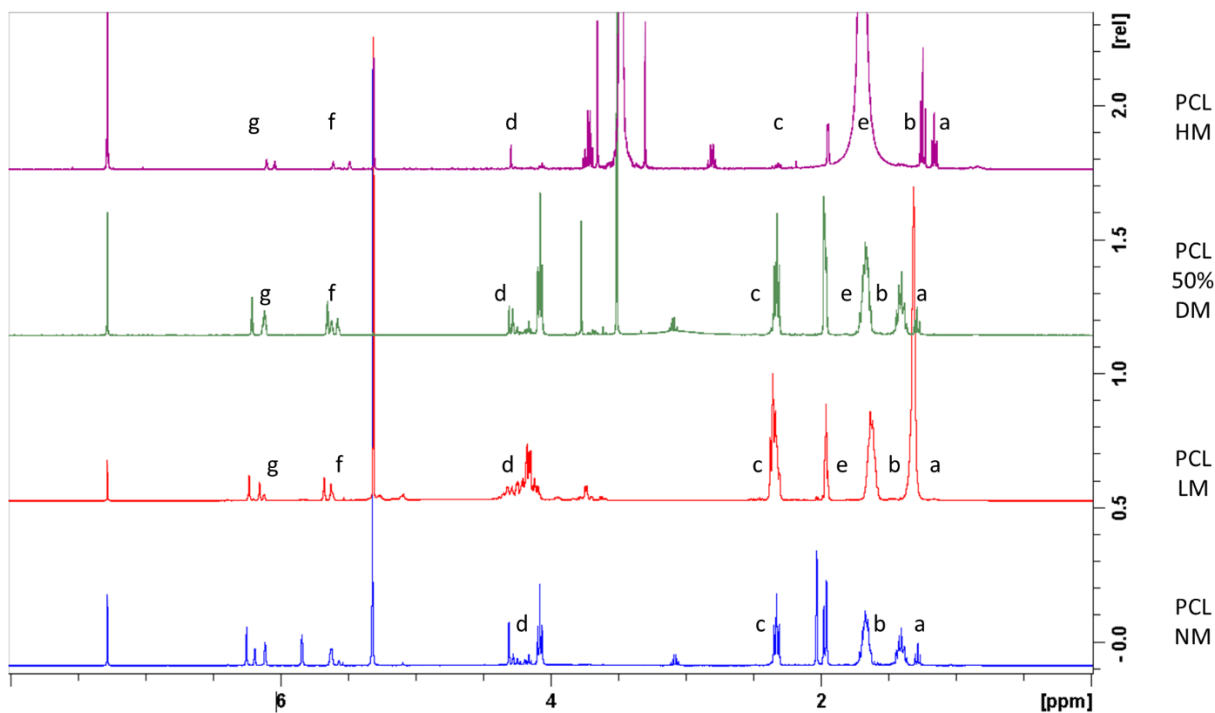


Fig. 17. NMR spectra for PCL-HM, PCL-50% DM, PCL-LM and non-methacrylated PCL (NM). Peaks showing the chemical composition of polycaprolactone are on peaks 1.4, 1.6, 2.3 and 4.1 ppm, corresponding to a-c, whilst methacrylate groups can be observed on peaks 1.9, 5.5 and 6.1, illustrated as d-f.

Resulting polymer solutions were characterised using GPC tests. The molecular weight, molecular number, and polydispersity (PD) are reported in Table 3, for 3 arm PCL and 4 arm PCL low (LM) and high methacrylated (HM).

Table 3. Average molecular weights, average molecular numbers, and polydispersity values for 3 and 4 arm PCLMA, obtained through GPC. NM: non methacrylated.

PCLMA	Avg. Mw	Avg. Mn	PD
3 arm PCL LM	2 276	1 759	1.29
3 arm PCL 50%	2 272	1 782	1.39
4 arm PCL NM	2 167	1 616	1.34
4 arm PCL LM	3 460	2 300	1.5
4 arm PCL 50%	2 773	2 210	1.25

As 4-arm PCLMA has shown advantages for the manufacturing process of HIPEs in terms of the stability of the emulsion and crosslinking capacity [109], from this point on, only 4-arm PCLMA in

LM, 50% and HM has been used. Therefore, all PCLMA that has been referred to, corresponds to the 4-arm composition.

3.5.1.1.1. Purity and reproducibility of chemical processes

Methacrylated polymer solutions were washed with an acid solution to remove impurities in the organic phase. The residual solution was rotary evaporated to ease the extraction of DCM solvent. As the presence of undesired volumes of solvent affect the stability and crosslinking of HIPEs, the solvent extraction of 4 arm PCL LM and 50% was tracked over batches. As it is shown in Fig. 18, batches of PCL took approximately 2 hours to become stable in mass and show a honey-like viscosity.

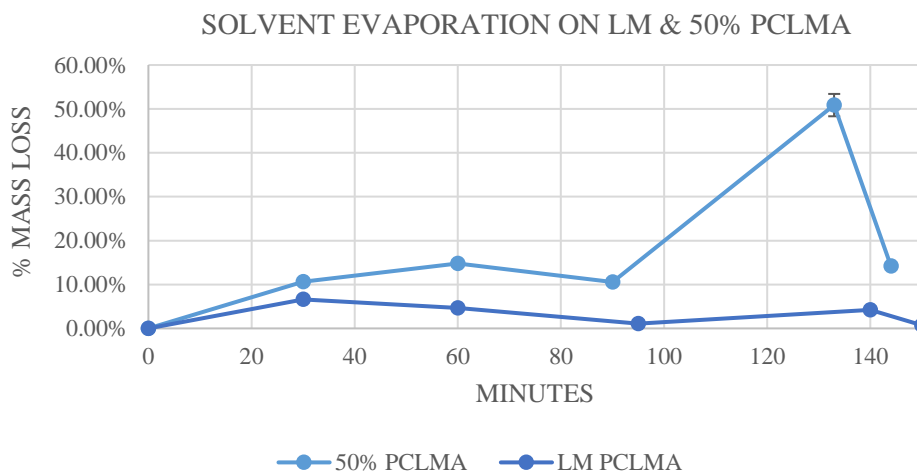


Fig. 18. Solvent extraction was tracked over time through the total mass of the LM and 50% polymer solution during the rotavaporation process.

Further solvent extraction was completed through methanol washes.

3.5.1.1.2. Mechanical properties of PCLMA scaffolds

For the following experiments, 4 arm PCLMA was chosen due to their high number of functional groups, which also impacted its crosslinking density. The functionalisation degrees of interest were 20 and 50% D_M and they are referred to as LM and 50% from this section.

The mechanical properties of these materials were determined for successful PCLMA emulsions. Compression and tensile strength (UTS) tests were performed under dry conditions, using non-porous structures as control Table 4.

Table 4. Mechanical properties of dry porous / bulk LM & 50% PCLMA materials.

Conditions		Material	ϵ (MPa)	Compressive Strength (MPa)
Dry	Bulk	50% PCLMA	5.643	5.091
		LM PCLMA	1.644	27.916
	Porous	50% PCLMA	0.014	0.633
		LM PCLMA	0.013	0.569

3.5.1.2. High Internal Phase Emulsions

3.5.1.2.1. Emulsion Stability

Water-in-oil emulsions (W/O) were developed using 4 arm LM and 50% PCLMA solutions. The stability of the emulsions was evaluated during and after mixing, according to the successful water intake, and the absence of phenomena like coalescence, Ostwald ripening and phase inversion. The volume of water intake, and the temperature of mixing was varied in combination, for both 50% and LM PCLMA. Results shown in Table 5 evidence that the optimal temperature for LM PCLMA is at 37°C and either room temperature (~ 15 °C), or 37 °C for 50% PCLMA. Additionally, the optimal water intake is 3 ml for both polymer solutions.

Table 5. Experiment developed to identify the optimal recipe for a stable PCL emulsion during and after mixing. Variables changed were temperature (T) and water intake (ml). The success of the emulsions was evaluated by the absence of division and phenomena during and after mixing. Stirring speed in rpm; solvent made by a chloroform: toluene 6:4 wt relation; all percentages are in relation to the polymer weight. Successful results are shown in green. Total mixing time was 10 minutes.

PCLMA										
Reactive					Conditions			Divided during (DM) or after mixing (AM)	Resolution	
Polymer	Surfactant	Solvent (6C:4T)	Photo initiator	Stirring	T	Water intake	UV lamp treatment			
LM PCLMA	0.4 g	10%	150%	5%	350 rpm	T _{room}	3 ml	5 min p/side	-	Pores too small
LM PCLMA						37°C	3 ml		-	Successful
LM PCLMA						T _{room}	4 ml		AM	Too aqueous
LM PCLMA						37°C	4 ml		AM	Too aqueous
50% PCLMA						T _{room}	3 ml		-	Successful
50% PCLMA						37°C	3 ml		-	Successful
50% PCLMA						T _{room}	4 ml		DM/AM	Coalescence
50% PCLMA						37°C	4 ml		DM/AM	Coalescence

3.5.1.2.1.1. The effect of temperature

Emulsions created under room temperature conditions showed average big pores of $81.25 \mu\text{m} \pm 2.75$ SD and small pores of $18.24 \mu\text{m} \pm 2.73$ SD. On the contrary, as expected, emulsions mixed at 37°C showed higher pore sizes, with big pores of $158.54 \mu\text{m} \pm 16.63$ SD and small pores of $32.23 \mu\text{m} \pm 5.52$ SD (Fig. 19).

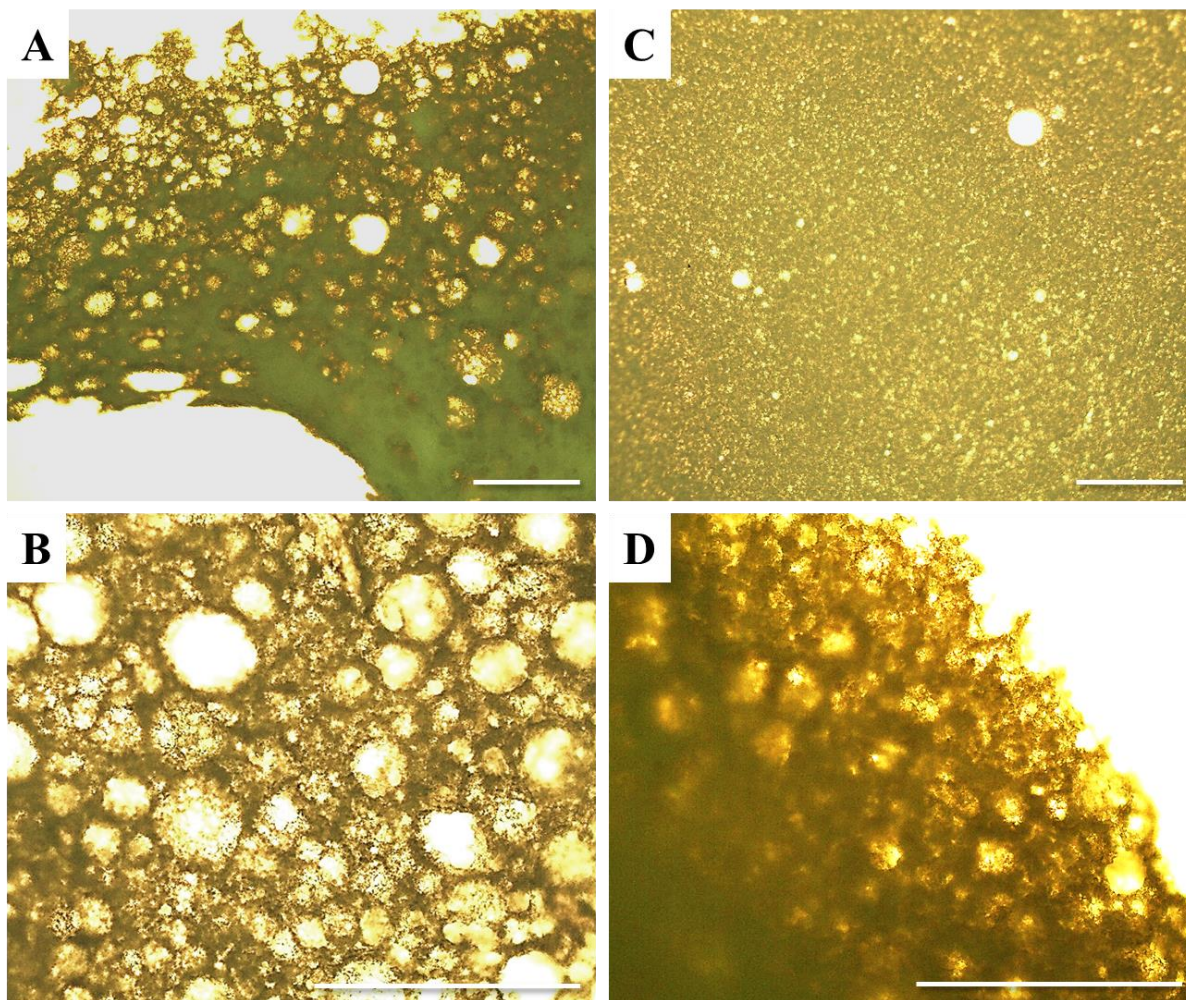


Fig. 19. Digital microscope images on PCLMA polyHIPEs prepared at 37°C (A-B) and room temperature (15°C – C-D). Magnification of images is 4x for A and C, and 10x for B and D. Scale bars are $500 \mu\text{m}$.

3.5.1.2.1.2. Limits of water intake

The balance between the continuous and the water phase in an emulsion dictates the pore size, impacting the wall thickness, hence the material stability. Volumes between 2 and 4 ml of water. Full adsorption occurred at 2 and 2.5 ml. As the volume increased, the water did not mix with the emulsion, causing water coalescence and phase inversion, as evidenced in Fig. 20.

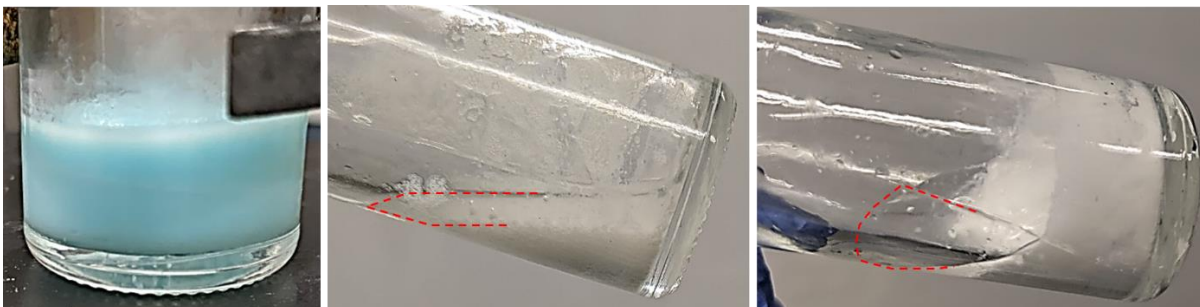


Fig. 20. Water-in-oil emulsions with 2, 3 and 5 ml of water as water phase. Full adsorbance can be observed with 2 ml (water stained in blue to track its immersion). Phase inversion is observed when adding 3 ml of water, and emulsion coalescence with 5 ml.

The summary of successful (stable photocurable scaffolds) is:

Polymer		Surfactant (Hypermer)	Solvent (6C:4T)	Photo initiator	Stirring	T	Water intake	UV lamp treatment
LM PCLMA	0.4 g	10%	150%	5%	350 rpm	37°C	3 ml	5 min p/side
50% PCLMA	0.4 g	10%	150%	5%	350 rpm	T _{room}	3 ml	5 min p/side
50% PCLMA	0.4 g	10%	150%	5%	350 rpm	37°C	3 ml	5 min p/side

Disk-like scaffolds were produced, 4 mm in height and 6 mm wide using PDMS moulds. Bulk scaffolds showed an increase in weight (but not in volume) between day 0 and day 1 (of around 3.65%), and a minimum shrinkage for the following weeks (Table 6). On the contrary, porous scaffolds shrank between 15.58 and % between day 0 and 1, and a consecutive shrinkage that only stabilised after three weeks. Scaffolds were submerged only in deionised water.

Table 6. Shrinkage under normal aqueous conditions on LM and 50% PCLMA

Polymer solution	D0-1 – Shrinkage (Horizontal Axis)	D0-1 – Shrinkage (Vertical Axis)	D0-1 – Total Volume Shrinkage	D2-9 – Total Volume Shrinkage
Bulk LM PCLMA	NA	NA	4.15%	10.87%
Porous LM PCLMA	4.45%	9.99%	15.58%	40.42%
Bulk 50% PCLMA	NA	NA	0.45%	3.41%
Porous 50% PCLMA	3.86%	3.52%	12.82%	5.94%

3.5.1.2.2. Geometries of PCL HIPEs

The structure of PCL HIPEs is illustrated in Fig. 21 where the size and geometry of the pores and windows is observed at different magnifications. Images A and B evidence the spherical structure of PCL for both windows and pores, and their connectivity across the three-dimensional structure. Fig. 21 shows the distribution of such pore morphologies among pores and windows through the surface of a PCL HIPE.

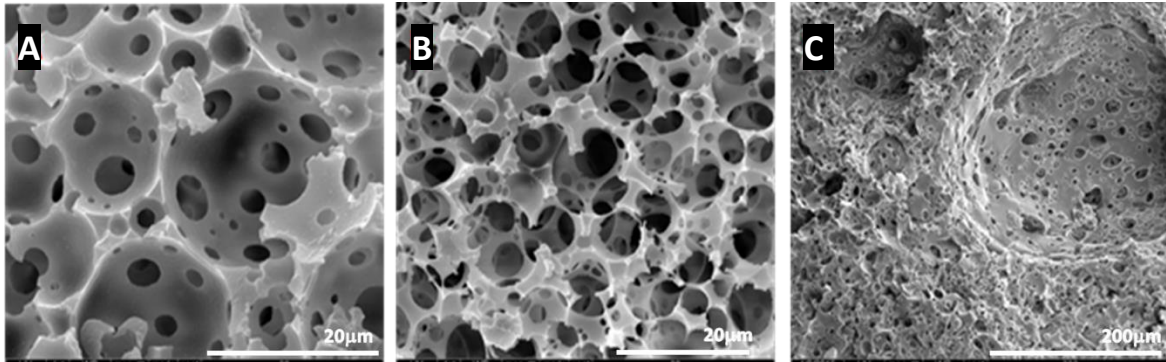
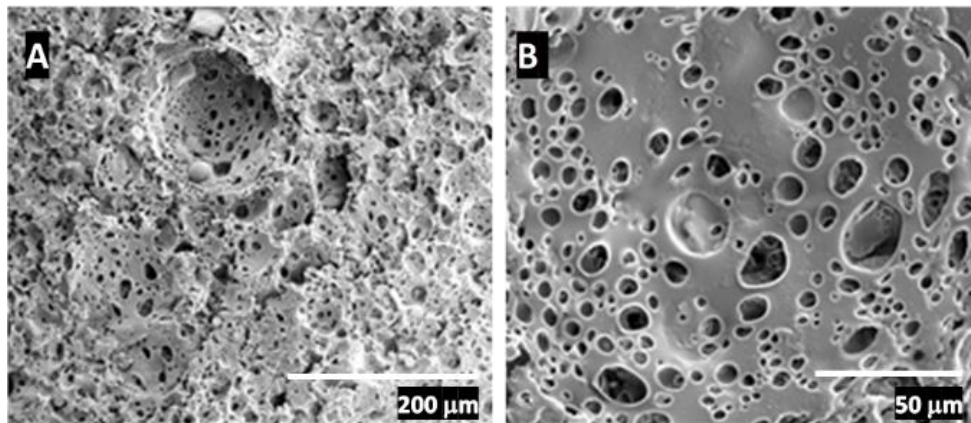


Fig. 21. A & B. SEM images of a 50% PCLMA PolyHIPE. The big openings are referred to as windows and they have an average size of 35 μm . Such windows are the entrance to other pores. C. Big voids have an average size of 116 μm . Images were taken at high magnifications ($>1000\times$), at 10 KV.

A comparison between methacrylated PCL scaffolds is shown in Fig. 22. In the case of high methacrylated scaffolds, the round HIPE structure is always visible, with big round windows composed of small pores interconnected to each other. On the contrary, low methacrylated scaffolds show a less homogeneous round structure, with bigger windows. The pore size keeps the same as the high methacrylated scaffolds, but their interconnectivity appears higher.



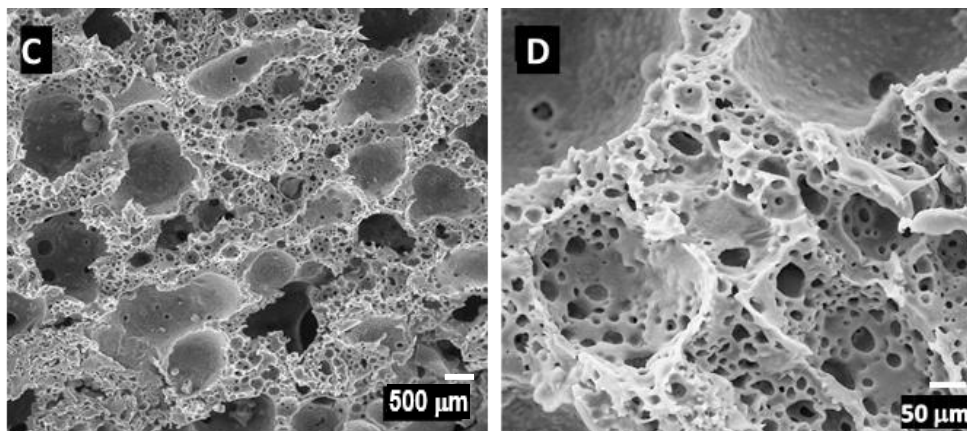


Fig. 22. (A,B) 50% PCLMA, with big windows (15 to 26 μm) containing small pores (2 to 9 μm) . (C,D) LM PCLMA showing big windows (132 to 229 μm), less round but equally interconnected to small pores (30 to 57 μm). Images taken at Magnifications varying from 700 to 1000x, at 10 KV.

3.5.1.2.2. Internal Phase Volume

To understand how the manufacturing process impacts on the porosity and interconnectivity of the constructs, it is important to calculate the space covered by the oil and the continuous (removed) phase. The oil phase is formed by the polymer solution, the surfactant, solvents, and the photoinitiator. For the following calculations, the solvent values are removed as they leave the emulsion during its formation. Finally, the densities reported in Table 7 have been considered.

Table 7. Densities of water and oil phase involved in PCLMA HIPE emulsions. *Chloroform and toluene solvents are not considered for the calculation of the internal phase as they leave the emulsion through its formation and are washed away during the washing process.

Reactive	Density (g/mol)	Weight (g)	Volume (ml)
Hypermer Surfactant	0.94	0.04	0.0376
Polymer solution	1.1	0.4	0.44
Toluene*	0.866	(0.4)*(0.6)	0.2078
Chloroform*	1.128	(0.6)*(0.6)	0.4061
Photoinitiator	1.12	0.150	0.168
		Total	0.6456 ml

Therefore, the internal phase volume of the HIPEs is 82.29%:

$$\text{Internal phase} = \frac{\text{water phase}}{\text{oil} + \text{water phase}} = \frac{3 \text{ ml}}{3 \text{ ml} + 0.6456 \text{ ml}} * 100 = 82.29\%$$

For a porous structure to be considered a HIPE, an internal phase volume of at least 74% is required. The PCLMA emulsions fit this criteria and therefore can be referred to as polyHIPEs.

3.5.1.2.3. Degree of Openness

The internal phase volume is associated with the degree of openness (DOO) as the latter describes the total surface of the cavities, which is crudely equal to the total diameter of the internal phase droplet (Fig. 23). To calculate this, a total of 100 random pores (not windows) were measured using ImageJ and the average measurement was multiplied by the statistical correction factor. The DOO was found to be 0.3274 for 50% PCLMA and 0.1196 for LM PCLMA.

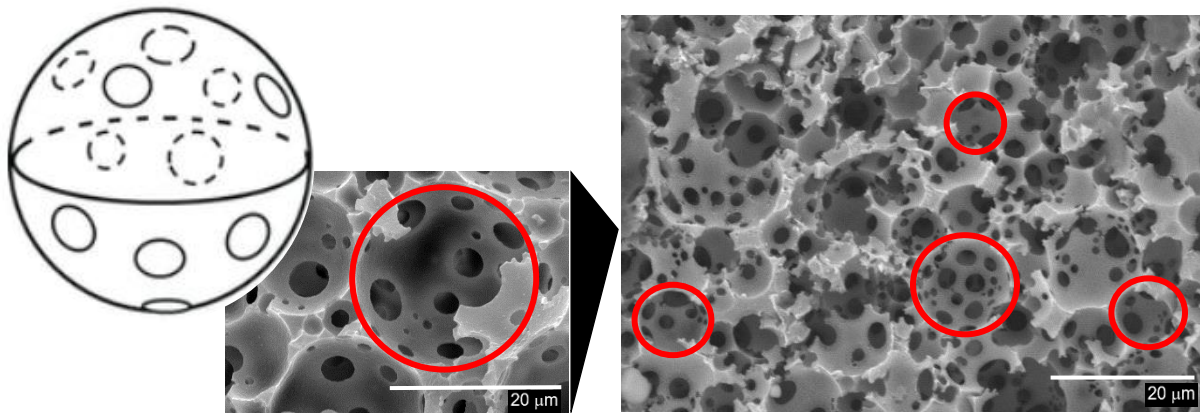


Fig. 23. The DOO of a cavity describes the degree in which the surface of a cavity (pore or window) is open. A structural diagram of the cavities in PCLMA scaffolds is observed on the left [280], and its application to SEM imaging on such scaffolds, on the right. Left diagram is obtained with permission from [280], and SEM images are product of this research. Magnification are 1000x and 6800x respectively.

3.5.1.2.4. Density and Porosity of PCL HIPEs

The DOO is directly related to the porosity as they both focus on the hollow part of the scaffold, being the DOO the internal surface area of the cavities, and the porosity, the volume that this area occupies.

The density of bulk PCLMA was calculated by weighing and measuring polymer solution, to be $1.0915 \frac{g}{cm^3}$. The density of PCLMA polyHIPEs was calculated both theoretically and experimentally. Theoretically it was calculated through the formula before, where the gel fraction was 97.01%. The polyHIPE density is then $0.1875 \frac{g}{cm^3}$.

The experimental density of the polyHIPE was obtained using a pycnometer and was reported to be $1.2718 \frac{g}{cm^3}$ for 50% PCLMA and $1.3416 \frac{g}{cm^3}$ for LM PCLMA. The difference between the theoretical and the experimental densities can be due to the heterogenicity of the manufacturing process, and a possible partial collapse due to drying scaffolds [262].

The theoretical porosity of the PCLMA emulsion was calculated through the empirical Eq. 2 and Eq. 3. The density of the wall was calculated using the polymer solution, the surfactant and the photoinitiator; it was calculated as $1.0915 \frac{g}{cm^3}$. Therefore, the theoretical porosity of LH and 50% polyHIPE is 82.82%. The total porosity of the materials studied ($P^{(te)}$, %) was calculated through Eq. 4 as $0.7121 \frac{g}{cm^3}$.

3.5.1.2.5. Interconnectivity of PCL HIPEs

Finally, the interconnectivity of the scaffolds can be determined by either the relation between the windows and pore sizes (as shown on Eq. 5), that is, the relation between the cavity surface and open surface area. The interconnectivity of PCL polyHIPEs was reported to be 27.5% for 50% PCLMA and 24.1% for LM PCLMA.

3.5.1.3. Micro Computed Tomography for the study of polyHIPEs

Some of the main challenges of studying 3D constructs are: i) calculations are based in theoretical approaches or, ii) imaging and/or analysis is performed in a two-dimensional plane. In both cases, it is difficult to visualise the three-dimensional structure of the polyHIPEs, and it can only be speculated that the overall volume will behave and look the same as what we are observing at a given time or plane.

On this matter, micro computed tomography (μ -CT) has been used as a non-destructive technique to characterise and quantitatively analyse the pore and window structure, distribution, and interconnection [273].

Initial polyHIPE scaffolds were scanned whilst being submerged in an aqueous solution. This was done to reduce the risk of shrinkage observed when drying scaffolds. However, the liquid (deionised water) surrounding the scaffold proved to be an obstacle for the successful reconstruction of the constructs, as it added noise. Bubbles of water can be observed around the scanned polyHIPE on Fig. 24.

To correct this, dry PCLMA (LM and 50%) polyHIPE scaffolds were scanned and reconstructed as mentioned in *Section 3.3.8*. The resulting digital structures were processed using Avizo software and rendered in two and three dimensions, as observed in Fig. 25 and Fig. 26.

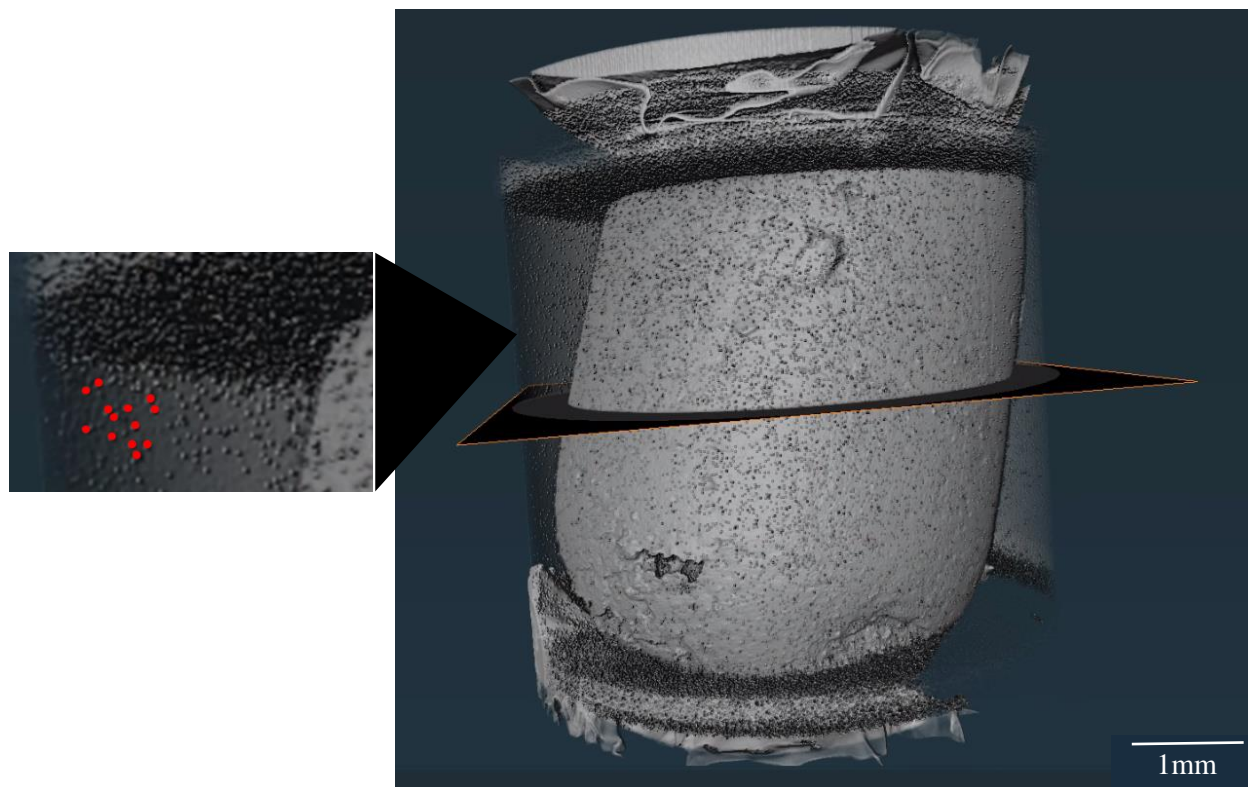


Fig. 24. This polyHIPE scaffold was scanned whilst submerged in an aqueous solution. The bubbles around the grey solid construct (and high lightened in red) obstruct the correct reconstruction of the porous material. Top and bottom non-porous structures are pieces of metallic foil used to delimit the

The scaffolds submerged in a povidone-iodine (PVP-I; Sigma Aldrich) solution didn't prove to be as effective with inert materials as the PCL HIPEs. This could have been caused by the low concentration of titratable iodine in the solution; the solution was prepared by mixing 10% of PVP-I which originally contains only 1% of iodine. However, the experiment did not show any significant difference.

Due to the difference in densities between the solid and vacant areas in the scaffold, it was possible to examine the segment between the empty spaces around the scaffold. A thresholding technique was used to identify the pores and windows within the scaffold, and to label them (Fig. 27). Interconnectivity between most pores can be observed in Table 8 for LM and 50% PCLMA.

Pores were identified using the thresholding technique. As the interconnectivity between pores was already proven to be evident, the technique was also used in a more rigorous manner to identify pores in a single manner, being able to quantify their diameter and speculative volume.

Fig. 28 are histology diagrams on the pore distribution in terms of diameter and volume for both LM and 50% PCLMA. The range in pore diameters is between 15 and 70 μm for LM PCLMA (with a peak on pores 15-30 μm), and between 15 and 500 μm for 50% PCLMA (with a peak on pores 15-40 μm and at 150 μm). Pore volumes were more frequent 1,000 and 5,000 μm^3 for both LM and 50% PCLMA, with an extra peak for the 50% PCLMA bigger pores at 50,000 to 250,000 μm^3 .

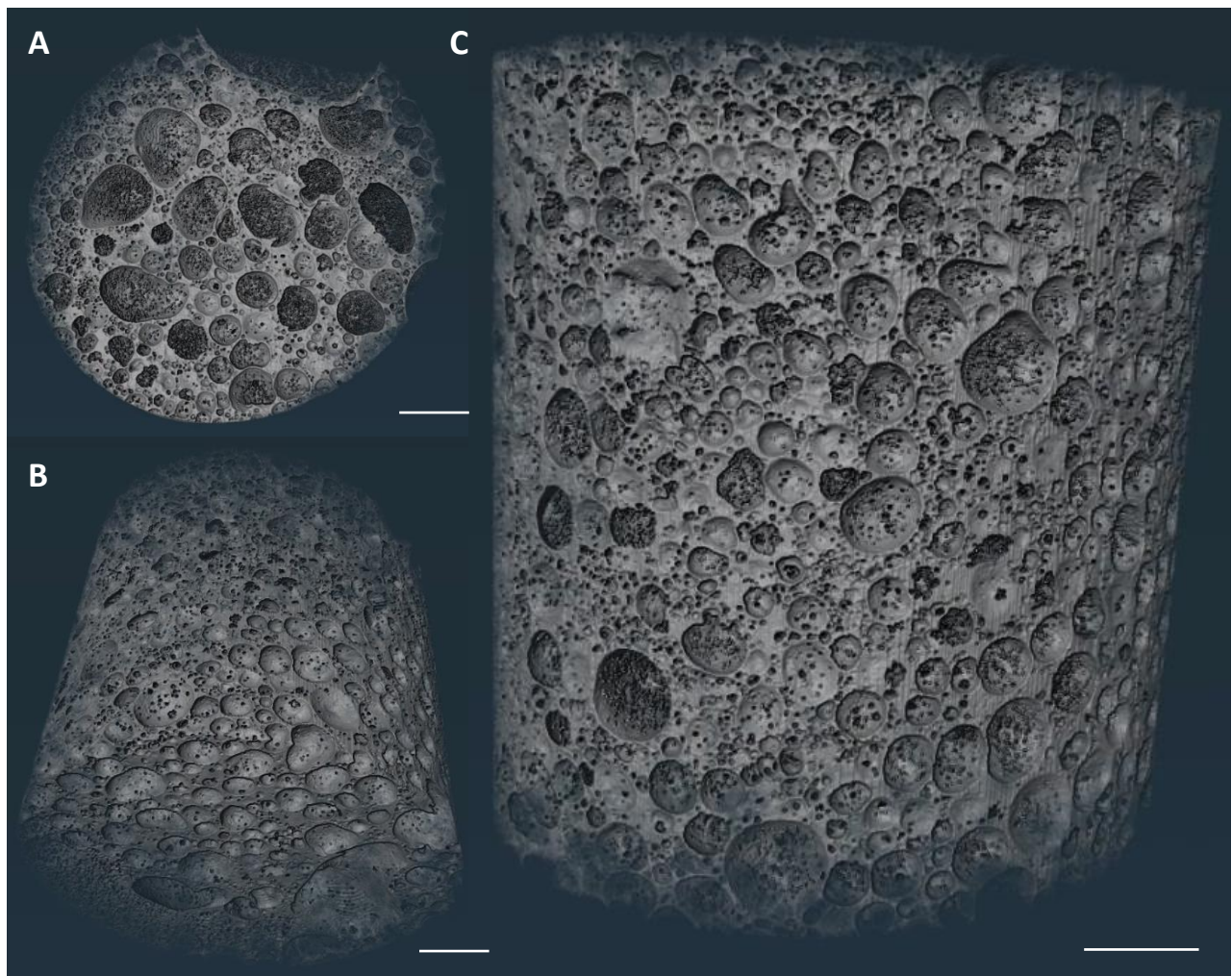


Fig. 25. Reproduction of LM PCLMA polyHIPE scaffolds scanned through $\mu\text{-CT}$, on yz (A), xz (B) and xy (C) planes. Scale bars are 1mm.

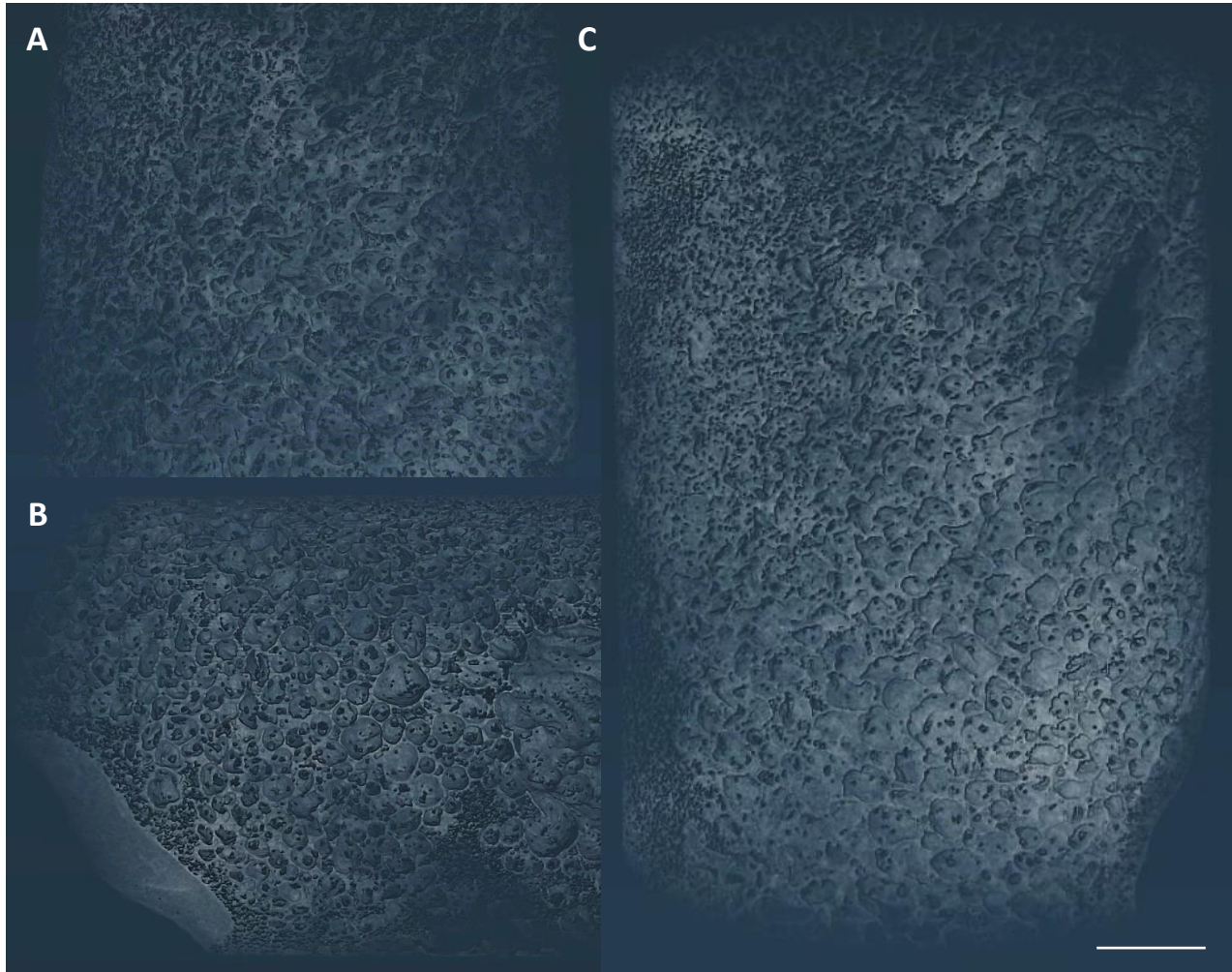


Fig. 26. Reproduction of 50% PCLMA polyHIPE scaffolds scanned through μ -CT, on yz (A), xz (B) and xy (C) planes. Scale bars are 1mm.

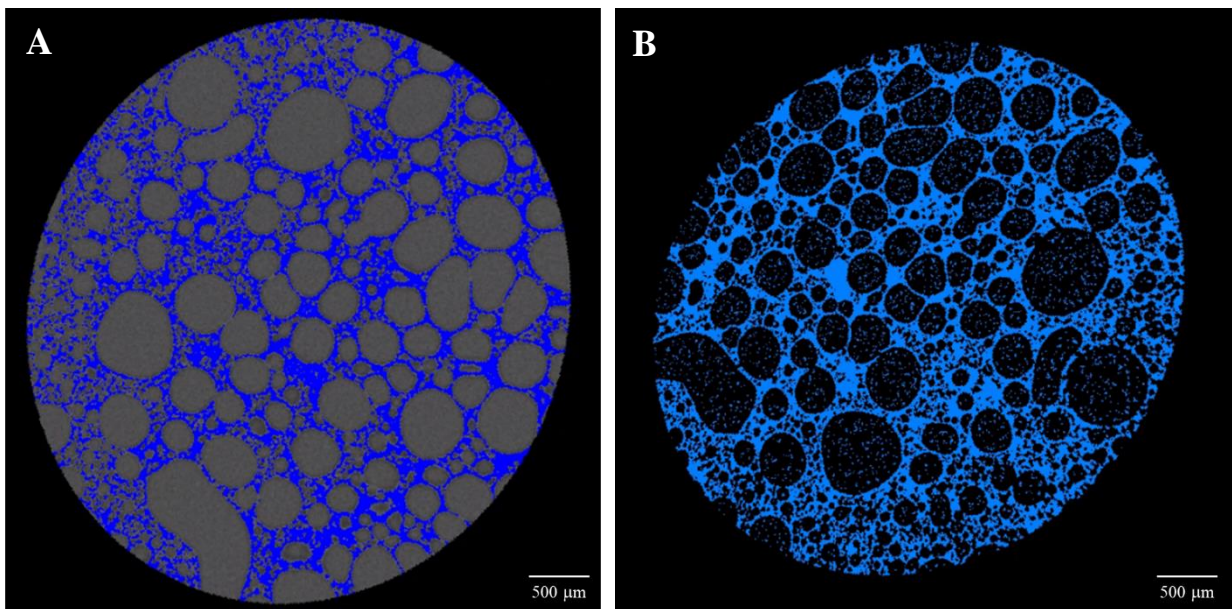
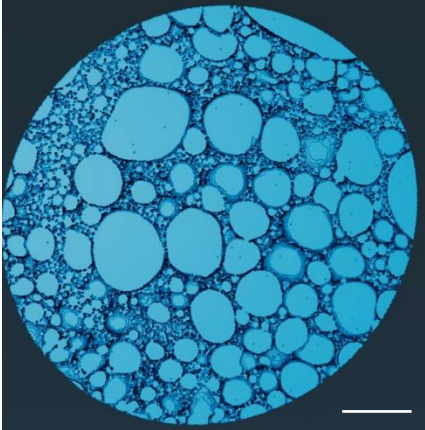
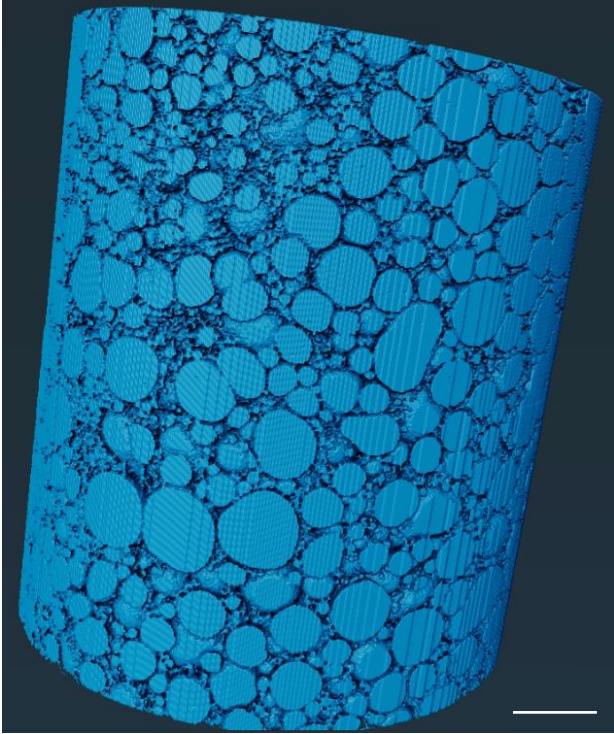
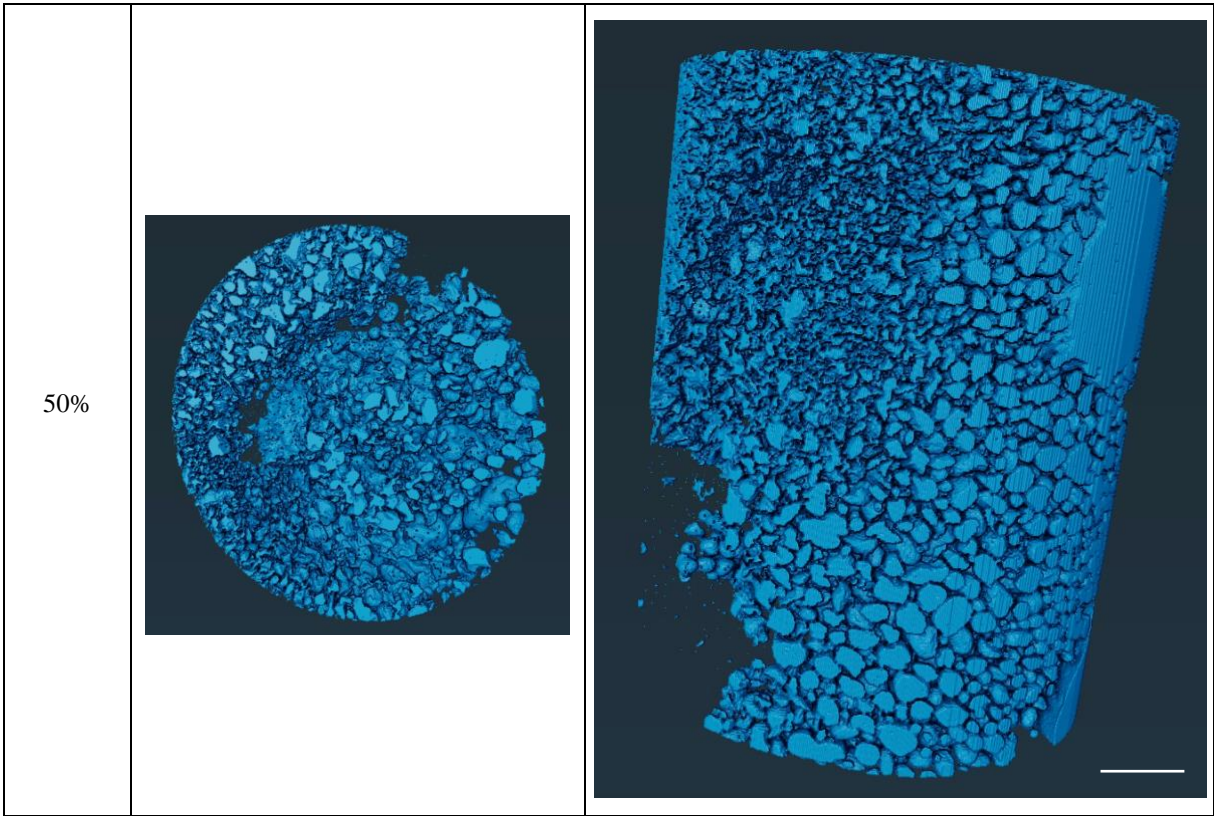
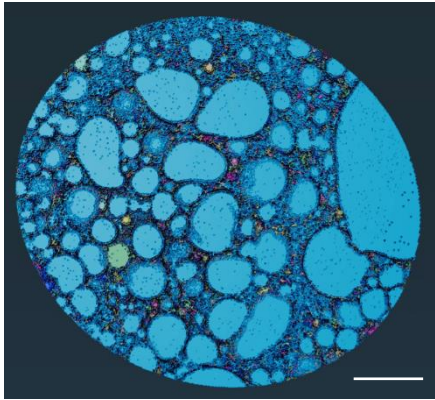
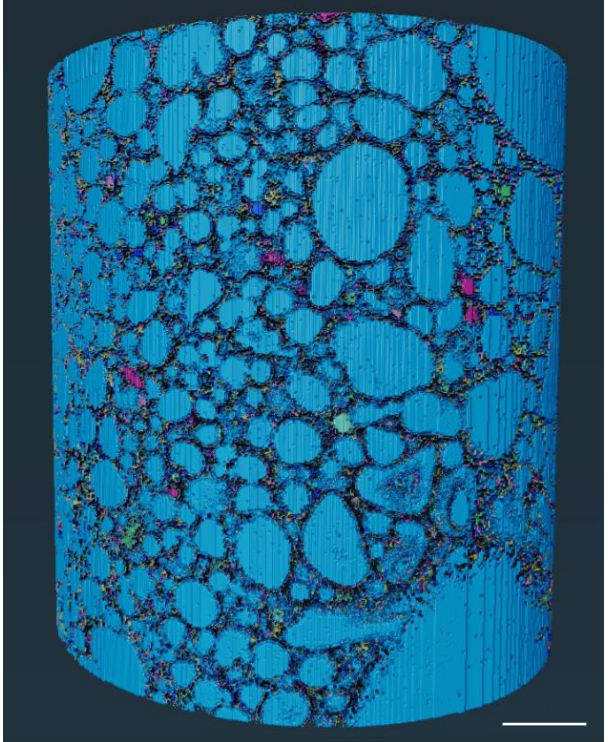


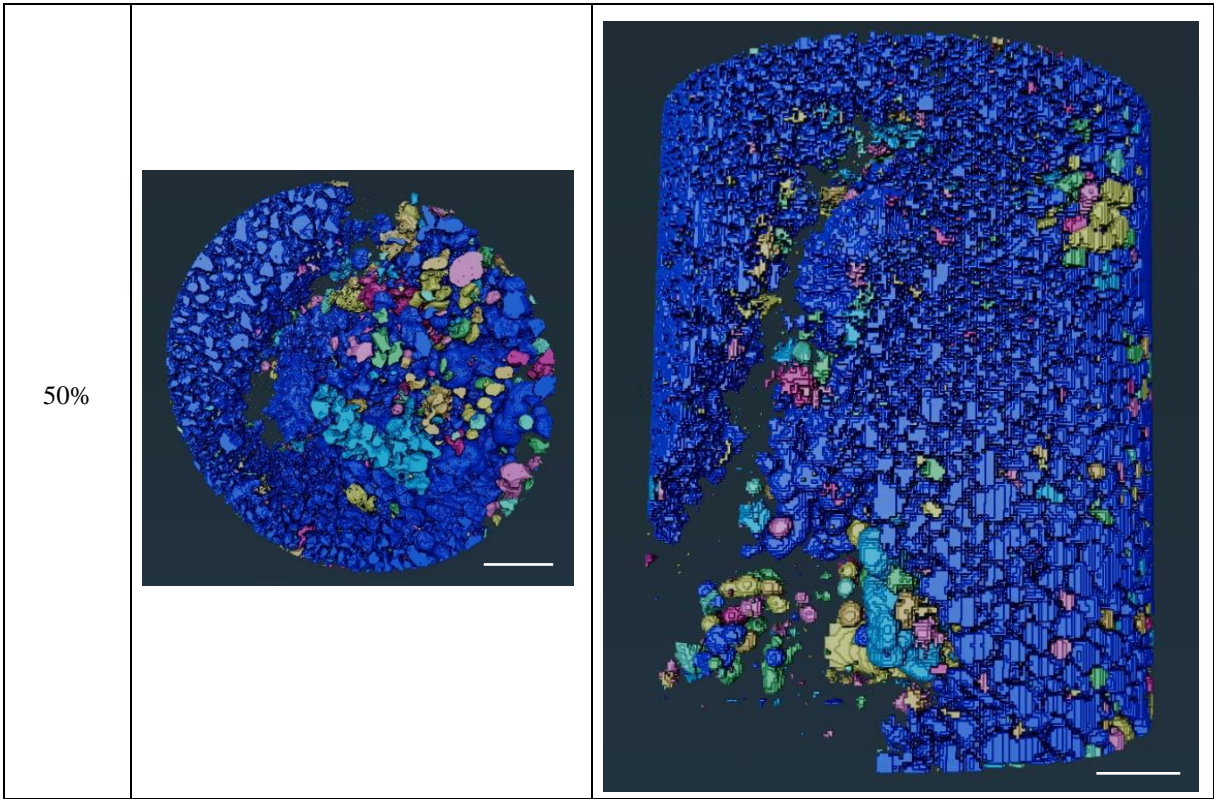
Fig. 27. Thresholding technique on 2D from the reconstructed scan of a LM PCLMA scaffold. A. The blue area shows the area occupied by the denser material, this is, the polymer; grey areas show the cavities (pores). B. Blue areas denote the polymer construct; black areas show pores and interestingly, some changes in density created by the windows within each pore, evidencing interconnection between pores. Scale bars are 500 μ m.

Table 8. Thresholding strategies to identify pores and windows within the scaffolds starts on the correct segmentation of areas. An independent labelling technique was developed on the 3D reconstruction, where only 6 neighbouring points were considered for pores to be “connected”. Scale bares are 1mm.

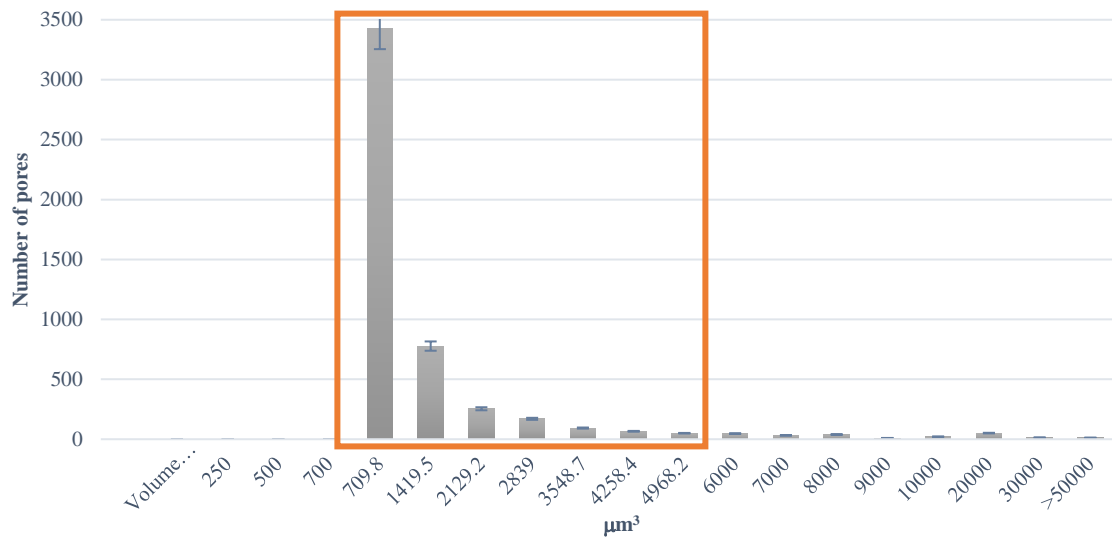
Thresholding		
PCLMA	2D	3D
LM		



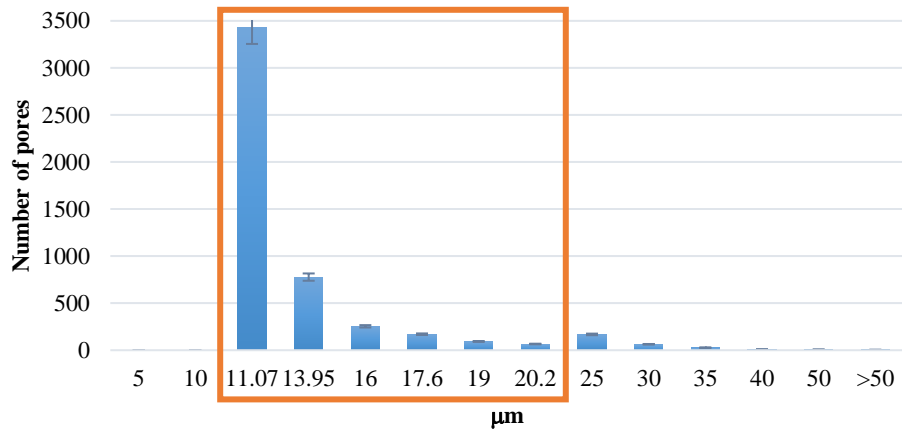
Labelling		
PCLMA	2D	3D
LM		



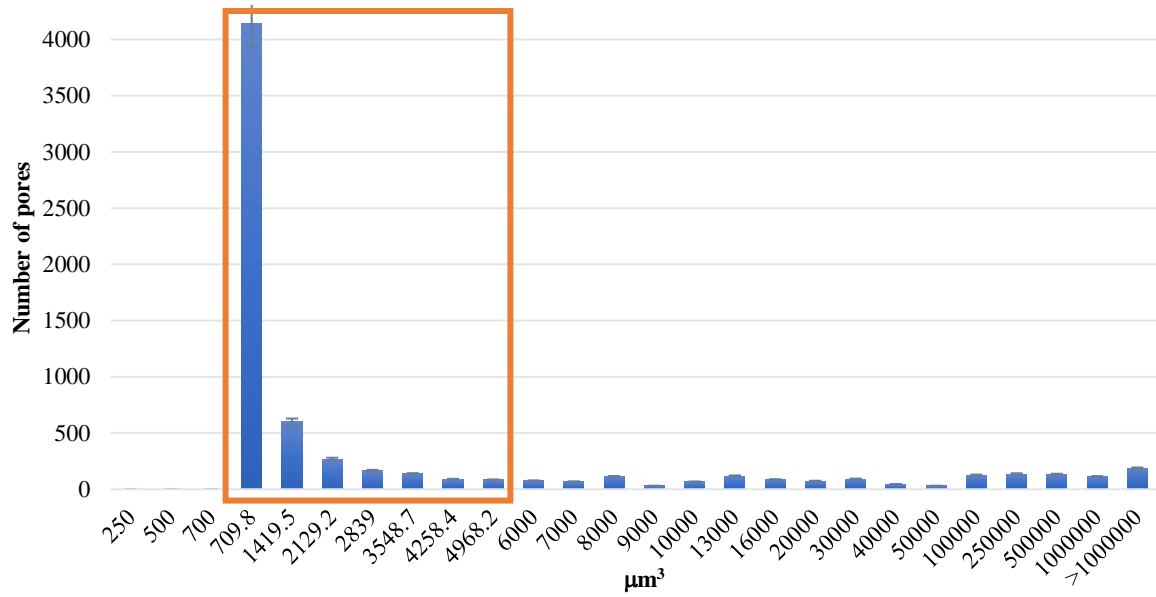
DISTRIBUTION OF PORE VOLUME ON PCL-LM



DISTRIBUTION OF PORE DIAMETERS ON PCL-LM



DISTRIBUTION OF PORE VOLUME ON PCL-HM



DISTRIBUTION OF PORE DIAMETERS ON PCL-HM

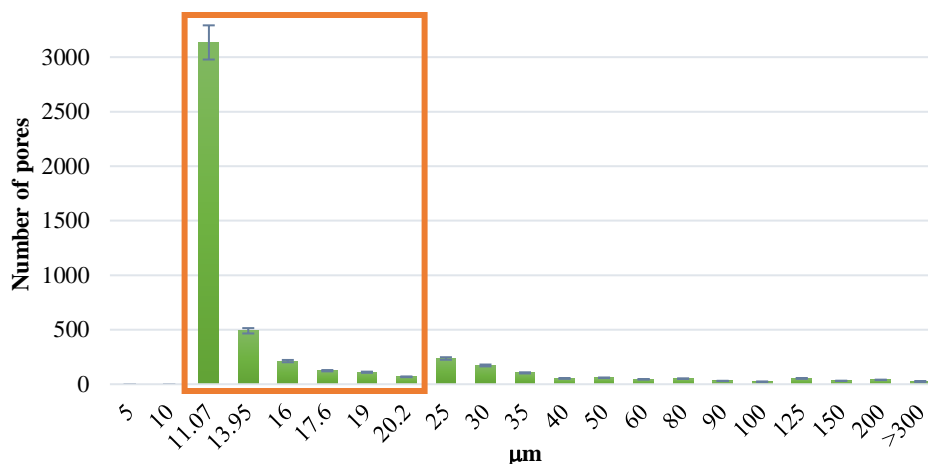


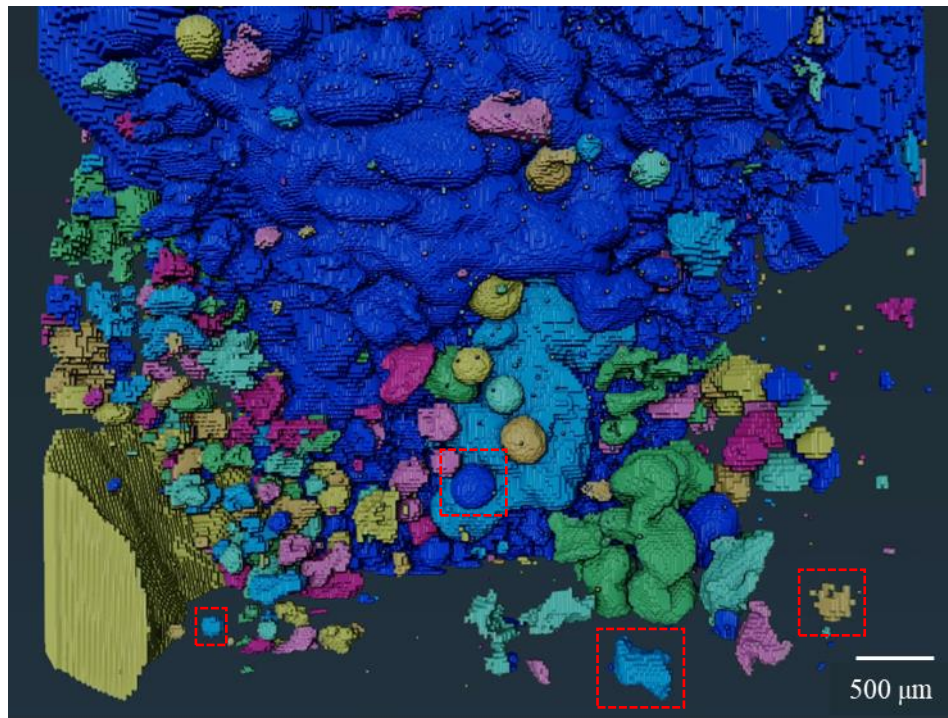
Fig. 28. Histograms showing the pore volume and diameter against its frequency for the LM and 50% PCLMA. Error bars are included.

50% PCLMA curiously showed more interconnection in the central areas of the scaffold. At the bottom and edges of the scaffold, more isolated pores were identified, which were geometrically spherical but in less communication to adjacent pores, as illustrated in Fig. 29. This is in good correspondence with the pycnometer density results that a small percentage of pores are not interconnected.

The limits of the thresholding and labelling analysis are dictated by a machine and a human component. The scanning parameters like voxel size, X-ray power, exposure time, among others are set up after initial trials and have an overall impact on the final resolution of the scan. Additionally, the researcher uses the analysis software (e.g., Amira, Avizo) to manipulate the parameters that analyse pore edge, interconnection and separation between phases using the visualization tools in the software. The software then takes these parameters and analyses the whole structure (2D and 3D) accordingly, reporting then pore diameters, pore volumes, sphericity, neighbouring (interconnection), among others. In the measurement of pore diameters and volumes a normal distribution of values was expected. However, peaks in number of pores were noted at 11.07, 13.95, 16.0, 17.6, 19.0 and 20.2 μm , with no pore diameters registered between such values. However, a homogeneous distribution between pores was observed on values higher than 20.2 μm . This can be explained by the abovementioned “limits” imposed by the user and the software, or by the sensitivity (resolution) of the scans, making it difficult to measure below certain values (like the voxel size). This could also be observed in pore volumes, with peaks at 709.8, 1419.5, 2129.2, 2839, 3548.7, 4258.4 and 4968.2

μm^3 . The same hypothesis can be drawn here. Finally, the same peaks were observed on both PCL LM and 50%, which shows that: i) the hypothesis stands, ii) and that the user method is somewhat reproducible as what is consider a standard for pore limit and similar parameters was the same in both analysis.

Fig. 29. Highlights of the isolation of pores in 50% PCLMA on the edges of the scaffold. Some of this pores have been highlighted in red squares. Dark grey colour represents the background.



3.6. Discussion

3.6.1. Synthesis and methacrylation

The work developed in this chapter primarily aimed to synthesise a prepolymer solution that could be functionalised into a variety of solutions useful for emulsion templating and ultimately generate 3D structures with a pore size, morphology, and interconnectivity useful to soft and semi-hard tissue engineering. To achieve this, 3- and 4-arm PCL were synthesised and methacrylated to several degrees. Afterwards, they were characterised to determine the most practical material to work with, as well as the one that could be tailored to aforementioned features. Emulsions were created, imaged and mechanically tested to understand their behaviour in body-like conditions. Finally, a more thorough study on the emulsion crosslinking and its homogeneity was performed using micro-CT scanning.

In its natural form, the chemical structure of polycaprolactone contains a hydroxyl (OH) end group. This OH group can be further functionalised via (meth)acrylation and used as a precursor for free-radical polymerisation. When ϵ -caprolactone is mixed with pentaerythritol (tetra-ol) or Tris(hydroxymethyl)propane (triol) in the appropriate ratios of small 4-arm or 3-arm PCL prepolymers can be synthesised via an addition reaction. As discussed by Lang et al, multi-armed PCL presents an opportunity to use these materials as building blocks for further polymers via functionalising the end-groups by (meth)acrylation and then further polymerisation [267]. Therefore, the amount of free hydroxyl groups is high enough to promote a high yield methacrylation via methacrylic anhydride (MA), to develop photo- and thermo-responsive polymers, as shown for PCL [109] and other polymers, in particular natural polymers [171, 90]. Three different levels of methacrylation (amount of non-free OH ends) were obtained for PCL.

Both the PCL synthesis and methacrylation are reported to be reproducible processes. This is in particular relevant since pre-polymeric fragments with a high level of methacrylation enables a high yield in photoinitiation and thus rapid curing. It was observed that the pre-polymer synthesis was completed under the current reaction conditions and resulted in a composition that was dictated by the molar ratios of the reactants, while the methacrylation, even with a 1 to 8 excess of methacrylate to pre-polymer did not complete in 36 hours.

However, by keeping a strict control on the addition of reactants and the extraction of solvents/reaction residues, a reproducible process was achieved. Additionally, the NMR spectra reported for 3-arm and 4-arm PCL corresponds to the one reported in literature [109, 265, 266]. On

the same line, the projected and calculated D_M 's were within the experimental error (Table 2) as the variation falls into the 2.6% for the 50% 3-arm PCLMA, and both LM and 50% 4-arm PCL. The difference between the predicted methacrylation and the calculated was less than 2.5%. After methacrylation, the polymers are washed, and the remaining solvent is extracted. This last process has also been explored in detail to ensure reproducibility; most solvent is extracted after 2.5 hours. Overall, from our set of experiments we can confirm that the pre-polymer production and methacrylation processes provided excellent control over the manufacturing of PCL-based photocurable resins with tuneable properties.

The molecular weight distributions and dispersion of the produced polymers was also measured to assess the quality of the pre-polymer. As expected, methacrylation increased the molecular weight of the polymer and higher degrees of methacrylation recorded a proportional increase in both weight and number average molecular weight. Additionally, 4-arm PCL showed significantly higher molecular weights than 3-arm PCL, due to the longer chain lengths and the higher amount of branching in the 4-arm PCL. The dispersity values denoted the ratio between the weight average to number average molecular weight. In practical terms, it explains the non-uniformity of the distribution of polymer chains in the polymer solution. Reported values range between 1.25 and 1.5, which is in line with expectations for a step growth polymerisation process. These results were congruent with literature, where PCLMA has reported a molecular weight of 3581 g/mol and PD of 1.33 [109].

The mechanical properties of the native cartilage have been reported as 1.2 MPa for tensile stress, and 0.15 MPa for compressive stress, given that the articular surface in the human knee can experience peak loads of 10–12 MPa [268]. The mechanical properties of bulk LM and 50% PCLMA are higher than those reported for the native cartilage tissue by a factor of 4, however, those from the porous scaffolds are below the range for a magnitude of 10 and above the range for the compressive stress. The low values on tensile strength can be associated with the fragility of the dogbone moulds used for testing, which also do not resemble the design that the scaffolds would have if implanted in the human body.

3.6.2. PCL HIPES

The dimension of the scaffolds was selected based on the microfracturing technique, where plugs of 2-3 cm² are implanted within the osteochondral tissue of joints, specifically the knee. Allograft

transplant from 2-8 cm². ACI up to 10 cm² [269]. Arthrex is a common single-use OATS as it is versatile as it allows for a graft harvest of 6, 8 and 10 mm, and a thickness of up to 10 mm [270]. Equally, commercial scaffolds like Trufit® offer a range of scaffolds with diameters from 5-11 mm and 18 mm tall [271]. Similar researchers using PCL 3D printed scaffolds have used similar dimensions for their OC constructs [264]. This projects has developed PCLMA constructs with 6-8 mm diameter and 5 mm height (5-10 cm²).

The ideal pore size and morphology, porosity and interconnectivity of PCL HIPEs can be tailored by the emulsion conditions and the components used. Pore size is impacted by parameters like internal shear forces, phase densities and overall emulsification viscosity. Pore morphology is impacted by the pore size, pore packing and the polymerisation conditions.

Water-in-oil (W/O) emulsions from both LM and 50% were developed through emulsion templating. Emulsions are considered reversible, which can cause them to be somewhat unstable (they lack thermodynamic equilibrium). As shown in the results, the drop size of the dispersed (water) phase, the spatial distribution of the phases and the emulsification (stirring) and curing conditions, impact structural and mechanical properties of the cured scaffold.

From a broad variety of combinations, it was found that LM PCLMA created optimal scaffolds at high temperatures (37°C) and lower volumes of water. Emulsion droplet (therefore cell diameter) has an inverse relation with the stability of the emulsion [272]. At 37°C, the emulsion can become more unstable but also allowing all components, and mainly the surfactant, to dissolve completely. Additionally, as the water intake is controlled, the size of the droplets can be maximised, as desired for PCL scaffolds. Experiments developed on *Section 3.4.1.2.1.1.* and *3.4.1.2.1.2.* evidence such effects on pore sizes and general emulsion stability.

For 50% PCLMA, stable emulsions could be created with 3 ml of water and low or high temperatures. The difference between LM and 50% ideal conditions relies on the relation between their viscosities and the viscosity of the aqueous phase. An optimal viscosity leads to higher emulsion stability but also to a higher kinetic barrier to emulsion phenomena, such as coalescence. However, higher viscosities can also limit the addition of the droplet phase, as observed on coalescent emulsions resulting from the adsorption of 4 ml of water. Further work on the increase of the pore sizes can be achieved by using high temperatures.

After the emulsions have been exposed to the UV lamp, most of the crosslinking has been completed as they are photocurable, with only a non-significant post-curing crosslinking. The scaffolds are then immersed into methanol and water solutions to remove non-crosslinked polymer, solvent and photoinitiator residues, evidenced by the turbidity of the methanol solution after washes. Additionally, the monomer can present a shrinkage due to the surface tension of the solution it's immersed, and the changes between washing solutions. Bulk scaffolds did not show a significant shrinkage for 9 days but did increase their weight on day 1 by 10.87% and 3.41% on LM and 50% PCLMA respectively. This can be explained by the absorbance of water due to the non-finalised crosslinking process (the gelation fraction is lower than 100%). Porous scaffolds showed an initial shrinkage of 15.58 and 32.33% for LM and 50% PCLMA but then stabilised on the following days (day 2 to day 9) and decreased on the following weeks. As it will be explained below, LM PLCMA is associated with higher porosities, therefore it is logical for their shrinkage to be higher.

This does not affect the pore morphology or the size as the measurements are developed on already washed emulsions. *Dikici et.al.* has reported a shrinkage of 15-20% on her PCL scaffolds, similar to the obtained results. Although it has been reported that this can be minimised by freeze drying and using low surface tension washing solvents.

Pore morphologies are observed to be round and widely interconnected; as reported by diverse PCL works [108, 273, 146]. Additionally, the internal morphology of the HIPE is kept at the glass/polymer boundary which is attractive for future cell work as cells have reported to profit from round-like surfaces [274]. The difference in pore morphology between LM and 50% PCLMA is observed where LM has bigger pores and smaller windows (average sizes of 209 vs 23 μm) that were created both in the surface area of the pore and in the intersection between the pores. This indicates LM emulsions are less stable than 50% emulsions and are hence more likely to coalesce.

50% PCLMA scaffolds have defined pores with internal "medium-size" windows (average sizes of 132 vs 30 μm). Such variations can be due to the viscosity of the polymer and its contrast with the droplet phase, impacting the emulsification process.

The internal phase volume of 50% PCLMA was defined as 82.29% and did not consider the solvent nor the photoinitiator volumes, the solvent will evaporate after photocuring and the remnant photoinitiator after photocuring will be removed during the washing steps. This high internal phase volume HIPEs have been previously reported by *Dikici et al.* in her 4-arm PCL particulate-free HIPEs [109, 184], and are most common on particle-stabilised emulsions (Pickering emulsions) as they

prevent the emulsions from inverting phases as the internal phase increases [275]. By keeping high internal phase volumes, the W/O interface surface increases, and the polymer layers between windows thin [154]. An increase in the packing of water droplet layers lead to an increase in the pore (interconnects) as well. These interconnects are formed during the curing process, when the cross-linking increases the density of the oil phase. Because of the density increase, the thin polymer films around the droplets rupture and form interconnects [276]. The internal phase is closely linked to the degree of openness as it describes the internal surface of the pores. Similarly, the type (HLB number) and volume of surfactant have a role on the DOO. The reported value is 11.96% for PCL-LM and 32.74% for 50% DM. The literature has reported values between 2.8 and 11.7% for HIPEs created with 10% of surfactant wt% [277, 278]. And values between 6 and 15% were reported by a previous research group working with EHA HIPEs [279].

This of course supposes that both the pores and the interconnecting windows are primarily circular [280]. The surfactant plays an important role here as at higher amounts of surfactants, the layer oil between the droplets thins to the point where droplets touch each other, leading to bigger and/or more often openings in the cell wall after curing (this behaviour is also impacted by the surfactant's HLB). Additionally, the volume of water adsorbed by the emulsion is highly dependent on the ability to stabilise the water droplets in the oil phase. Larger water droplets present a lower water-oil interfacial area for the same volume than smaller droplets. This will result in a lower interfacial energy for the same volume, which means larger droplets indicate a less stable emulsion.

There is a direct relation between the DOO and the porosity of HIPEs as the DOO refers to the internal surface area of the cavities, whilst the porosity represents the volume that such areas occupy. The theoretical and experimental porosities were determined and found to be different from each other (17 vs 80%). This was associated with the partial collapse of the scaffolds during measurements with the pycnometer. As reported in tissue engineering, porosities above 50% retained their mechanical strength during tensile and compressive tests, whilst still providing an adequate porosity that enabled cell and molecule migration for soft tissue engineering applications [273], and even vascularisation of the neo tissues, in HIPEs for bone applications [279].

The interconnectivity of the scaffolds was found to be 24.1 and 27.5% for LM and 50% PCLMA. There are a few theories in the literature that talk about the origin of the interconnects (or windows). One theory, proposed by Silverstein's group, explains that polyHIPEs interconnect during gelation as the monomer contracts through the transition process from a liquid to a solid phase (polymerisation)

[281]. As the region between droplets is the thinnest, the contraction process leads to the opening of new windows. An alternative theory proposed by the Bismarck group highlights that windows are actually created by a mechanical effect during the post processing conditions (washing or drying) [282]. Photo-crosslinked scaffolds imaged under SEM reported interconnectivity that was not significantly different from washed (single solvent) and unwashed scaffolds, which leans to supporting Silverstein's theory. Additionally, continuous, and double-solvent washing did result in the shrinkage of scaffolds, which would not result in an increment of interconnectivity.

As previously stated, most calculations on porosities, pore size, morphology, and interconnectivity are developed on 2D images of the HIPEs and complemented by equations with correction factors that aim to approximate calculated values to the real ones. Such techniques (e.g., SEM microscopy) usually require the material to be dried which leads to a partial shrinkage of the construct and a modification on the initial pore morphology and distribution. Non-invasive techniques like micro-CT scanning allow materials to be analysed whilst preserving their integrity [283, 284]. Initially, the scaffolds were scanned whilst submerged in an aqueous solution. As the accuracy on the identification of pores and grains is based on the differences in densities between the bulk material (polymer) and the voids (pores and windows), a different approach was needed. Iodine is commonly used to scan biological material to create more contrast between the solid and the liquid matter. A study on the pore-scale analysis in sandstone recommended the use of sodium iodine brine (with minimum, of 6% iodine) to increase the x-ray contrast to a significant level [285], however the experiment did not prove effective to differentiate both phases (polyHIPE and iodine aqueous solution).

Finally, partially dried scaffolds were scanned, and the results have shown the most accurate representation on the pore geometry, size, and distribution on such porous constructs. Even though the study of biomaterials with computed tomography has been previously reported [284, 283, 286], to our knowledge, no literature includes the study of polyHIPEs with this technique.

A thresholding technique was used to identify the pores within the scaffold and to enable their labelling and analysis in both the qualitative and quantitative way. This process might be biased, as the limits between thresholding (edges within pores and appearance of windows) can be varied depending on individual user's criteria and preference. However, to introduce reproducibility within these the experiments, all tomographies were measured with the same thresholding values, determined by matching the porosity to independent measurements (picnometry and SEM). Similarly, the selection of neighbourhoods, that is, the number or connecting points to adjacent voxels, was kept

to 6 as it was considered that interconnectivity between pores could happen if at least these voxels were connected to other pores. The scans were performed at 7.82 voxel size; therefore, it was assumed that if an “empty voxel” was identified, it could be considered as an interconnect.

It has been previously highlighted that porosity value estimated by m-CT measurements are generally lower than the ones calculated with density measurements, which is caused by the variation in the resolution of the computed scan, and the voxel size [287]; smaller voxel sizes increase resolution which facilitates segmentation, although it increases the reconstruction time and can show not significant change if data is not noise free [288]. A few isolated pores were identified at the bottom of the scaffolds and did not seem to be interconnected with any other pores.

Finally, pore diameters and pore volumes were analysed using the thresholding tool. With most pores between 15 and 35 μm for both LM and 50% PCLMA, the pore volume distribution between low and high methacrylated emulsions varied significantly. The pore median was kept around 1000 μm^3 , whilst LM PCLMA reported few big pores with volumes at 2 000, 3 000 and 50 000 μm^3 . This coincides with what is reported in the literature for PCL [279, 109, 273] and co-PCL [272] HIPE structures. Other polymer HIPE structures have reported smaller pore sizes between 2 and 20 μm , similar to the ones found in 50% PCLMA.

PCL porous structures have been manufactured through a variety of techniques, mainly to produce larger pore diameters. This is because such structures are intended for biological purposes where diverse cell lines (with a unit size of at least 30 μm) are to populate, migrate and differentiate within such spaces. The relevance of pore diameter will be reviewed in following chapters.

Some of such techniques include stereolithography, particulate-polymer leaching, 3D-printing, foaming with supercritical carbon dioxide, and freeze drying, where average pore sizes have been reported around 465 μm [289], 378-435 μm [290], 323 μm [291], 180-360 μm [292], and 100 μm [293] respectively.

Emulsion templating of PCLMA is indeed a promising fabrication route for 3D constructs with interconnected pore sizes and morphologies that are attractive to tissue engineering applications, as it offers a balance between robustness and tunability.

3.7. Summary

This chapter initially focused on the synthesis of methacrylated polycaprolactone and its characterisation. Subsequently, it described the optimisation procedures for the manufacture of 3D structures through emulsion templating.

LM and 50% PCLMA polymer solutions were successfully synthesised, and the process proved reproducible. The produced materials were characterised, and their chemical and mechanical properties were explored. The polymer solution was photo-crosslinked via addition of photoinitiator and the exposure to UV light.

Emulsions are unstable and hydrophobic by nature [294]. However, by the right mixture of parameters, PCLMA polyHIPEs were successfully manufactured through W/O emulsions. The determining parameters in HIPE stability were the volume of water addition and the mixing speed. Both PCL LM and 50% worked better when the volume of water was the lowest and at low rpms. The HIPE porosity and interconnectivity agrees with what has been reported in the literature. The study of such features was achieved partially through physical characterisation and corroborated through micro computed tomography which allowed a deeper analysis on the 3D features of the construct.

PCL polyHIPEs could have advantageous properties as tissue engineering scaffolds since they can combine a fully highly interconnected porosity structure, a low bulk density, a high permeability, and a large surface area with moduli similar to those of soft tissue [295].

Chapter IV: Poly(glycerol) sebacate synthesis and structuring

4.1. Introduction

Poly(glycerol) sebacate (PGS) is a tough and flexible elastomer, which is the result of an equimolar condensation reaction between glycerol and sebacic acid. This same mechanism enables the creation of important biomolecules like carbohydrates and proteins in nature. PGS was first proposed as a biodegradable and biocompatible elastomer by *Wang et al.* in 2002, with mechanical properties higher than most hydrogels but lower than other biodegradable polymers e.g., polycaprolactone or polylactide [296].

PGS is an emerging biomaterial and the body of research has grown in the last two decades as a promising biomaterial for soft tissue engineering due to its ease of blending with both natural and synthetic polymers [297], and its quick degradability [119]. Additionally, it has an inexpensive manufacturing process, and both glycerol and sebacic acid have been approved by the US Food and Drug Administration (FDA) as a safe material for medical application, although the polymer has not been FDA approved.

The PGS backbone is formed by a random coil network with hydroxyl groups that enables PGS to be further functionalised. PGS has undergone such modifications through acrylation [298] and methacrylation [119, 299, 300], making it photocurable. Some research groups have also tried to photo, thermo and double cure PGS to create a tough structure that offers controlled swelling/deswelling, and a tailored biodegradability [300].

PGS has been used to produce both bulk and porous materials through diverse techniques, including electrospinning [127, 128], 3D printing [129] and salt leaching [130, 131]. For example, Pashneh-Tala et. al. manufactured 3D structures from methacrylated PGS with two levels of porosity (macro and micro) through 2-photon polymerisation, providing robustness to the product as well as being attractive to biological environments.

Up to now, there is no published work that concerns both emulsion templating and PGS. Therefore, this chapter explores the feasibility of producing PGS polyHIPEs as potential 3D structures for soft tissue engineering, specifically for cartilage applications.

4.2. Aims and objectives

The aim of this chapter is to synthesise a photocurable PGS solution that can be used for the manufacture of PGS polyHIPEs with tailored meso- and micro-structures of potential interest to cartilage tissue engineering. For such, the following steps are required:

- i) Synthesis and methacrylation of poly(glycerol) sebacate, including its chemical and mechanical properties.
- ii) Developing PGS polyHIPEs using toluene as a reference solvent.
- iii) Optimising the emulsification formula and process.
- iv) Optimising washing and drying methodologies for the better study of HIPEs.
- v) Analysing the PGS HIPE morphology using digital imaging and scanning.

4.3. Materials and Methods

Main materials and methods have been outlined in Section 2; specific methodologies for both polycaprolactone and poly(glycerol) sebacate are contained in Section 3.3 of Chapter 3.

4.4. Results

4.4.1. Synthesis and methacrylation

Briefly, PGS was synthesised using equimolar volumes of glycerol ($92.09 \frac{g}{mol}$) and sebacic acid ($202.25 \frac{g}{mol}$), under a nitrogen system for 24 hours. The nitrogen facilitates non-reacted molecules to leave and enhances the condensation reaction. The prepolymer was then vacuumed for another 24 hours to remove the water by-product from the condensation reaction. PGS prepolymer solution uses DCM as a solvent and is methacrylated by the addition of methacrylic groups from MAA ($154 \frac{g}{mol}$); the degree of methacrylation is controlled through stoichiometry.

The free hydroxyl groups of the prepolymer solution were methacrylated to the desired ratio as it was assumed that two thirds of the hydroxyl groups present in the glycerol reacted with the sebacic acid, leaving one group free. According to this, 3.9 mmol of hydroxyl groups per gram of PGS prepolymer solution are available for methacrylation [119]. PGS was methacrylated at 30%, 50% and 80% and labelled as PGSM-30%, PGSM-50% and PGSM-80% respectively. MeHQ was used to control the post-crosslinking effects and it was added during the methacrylation reaction, and right after stopping the reaction.

The PGS NMR H⁺ spectra (Fig. 30) evidence peaks related to the chemical composition of glycerol at 3.7, 4.2 and 5.2 ppm, and of sebacic acid at 1.2, 1.6 and 2.3 ppm, as reported by S. Pashneh-Tala [121]. The result of the incorporation of methacrylate groups (methacrylation) can be observed on peaks 1.9, 5.6 and 6.2 ppm, also confirmed by Singh et al [11]. Methacrylation peaks increase as the methacrylation degree increases. The peak located in 7.3 ppm is associated to CDCl₃ (chloroform), the solvent used to test the samples. The molecular weight of PGSM 30%, 50% and 80% were determined by GPC analysis, as shown in Table 9.

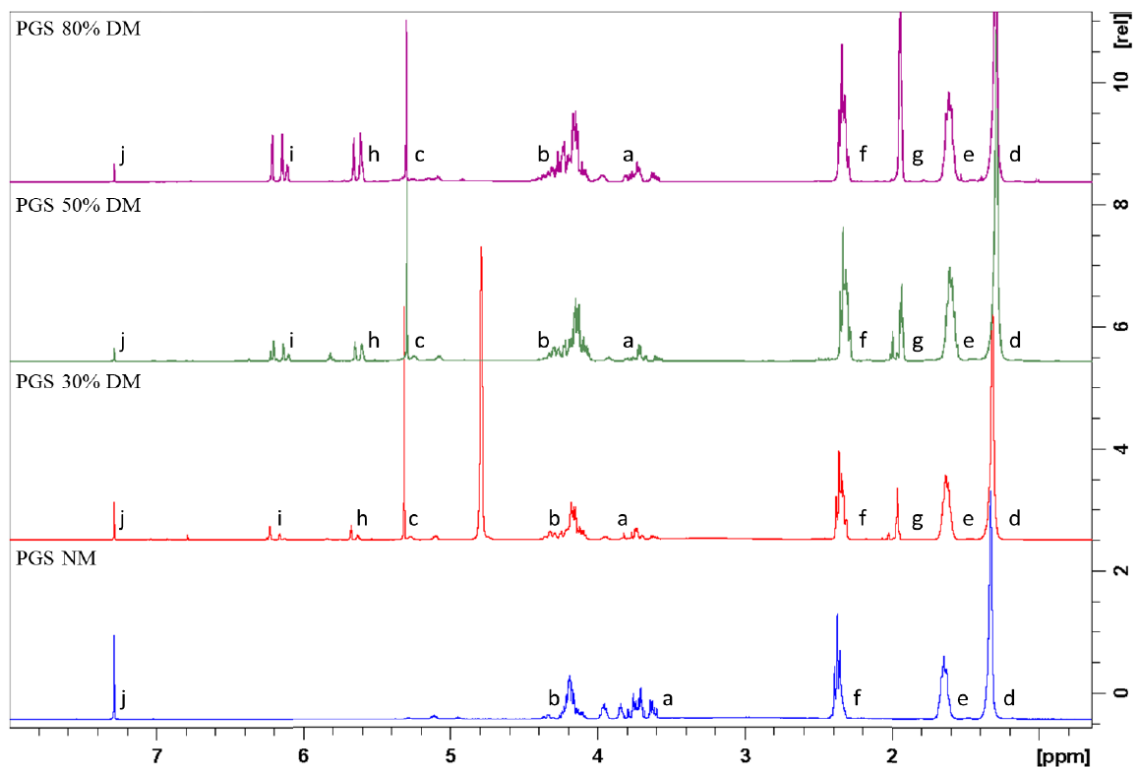


Fig. 30. PGSM NMR for non methacrylated PGS and 30%, 50% and 80% PGSM. Peaks at 3.7, 4.2 and 5.2 ppm were compared to the chemical composition of glycerol, shown as a-c; and 1.2, 1.6 and 2.3 ppm for sebacic acid, as d-f. Methacrylated groups on peaks 1.9, 5.6 and 6.2 ppm were labelled as g-j. Possible residues of DCM solvent and water are also shown in c.

Resulting polymer solutions were characterised using GPC chromatography. The molecular weight, molecular number, and polydispersity (PD) are reported in the table below, for non methacrylated, 50% and 80% methacrylated PGS (Table 9).

Table 9. GPC results for non-methacrylated PGS, 50% and 80% degree of methacrylation. Results show the average molecular weight, the average molecular number, and the polydispersity.

Sample	Avg. M_w	Avg. M_n	PD
PGS	1637	769	2.12
PGSM 50% DM	7394	2200	3.36
PGSM 80% DM	2065	1238	1.66

Molecular weights for PGS are in the range of what has been reported in literature ($5,420 \pm 430$ to $17,340 \text{ g/mol} \pm 760$) [302]. The three different formulation were prepared from 3 different batches of PGS, although the 80% PGSM is similar in M_w as the un-methacrylated PGS the 50% PGSM has clearly as higher M_w and PD compared to the other two formulations. High values of M_w were also reported by *Pashneh-Tala* between $5,420 \text{ g/mol} \pm 430$ and $17,340 \text{ g/mol} \pm 760$ for reaction lengths between 48 and 72 hours (our process is 24 hours). Dispersity values for PGS are also consistent with literature, as they range between 2 and 5, as reported by *Wang et al* in his photo-thermal functionalised PGS using 2-isocyanatoethyl methacrylate [121].

4.4.1.1. The effect of solvent residues

As observed in the NMR spectra, an increased peak in 5.3 ppm on *Fig. 30* is result of sporadic solvent and water residues in the polymer solution [303].

To better control the synthesis and manufacturing of emulsions, a study on PGSM 50% and 80% batches was further investigated. To remove the residual unknown volume of DCM, syringes with open lids were vacuum for intervals of 30 to 60 minutes and their weight was tracked over time. According to non-published studies by Samand Pashnela-Tala and Jonathan Field, when the weight change is less than 1% most of the DCM has been extracted (and only small portions of water are left). This has an effect in the reproducibility of the synthesis process and could have a later effect in emulsion stability. Differences between solvent evaporation can be observed in *Fig. 31* for various batches of PGSM run over the years, for both PGSM-50% and 80%. Even though both polymer methacrylations have different time frames to arrive at optimal conditions, the observed pattern is similar.

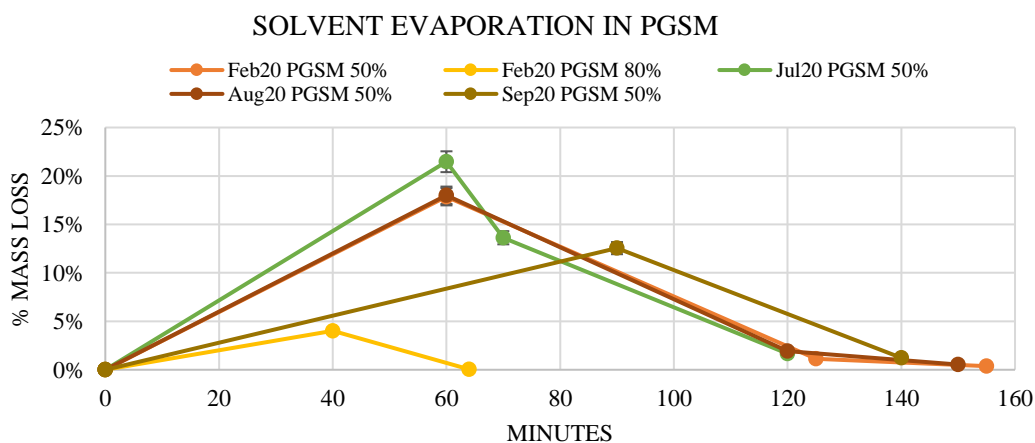


Fig. 31. DCM solvent extraction for 50% and 80% PGSM. PGSM batches tested for a year show a similar behaviour, reported in the figure below, and indicate a reproducible process.

4.4.2. High Internal Phase Emulsions

4.4.2.1. Emulsion stability

The success of an emulsification process depends on both internal factors of the two phases (oil and water), and the external parameters. Internal variables like the volume of photoinitiator and polymer:solvent ratios were studied at two different mixing speeds (350 and 850 rpm). Mixing time and other manufacturing parameters were kept the same. The amount of surfactant, solvent and water intake volume were also kept constant.

Scaffolds were developed in triplet for each of the combinations. Emulsion results are reported in *Table 10*. It was intended for all emulsions to absorb 4 ml of water, but the addition of water was stopped at the first sign of coalescence (a thin layer of water formed in the middle or top of the glass vial). Regardless, some emulsions were unstable and coalesced right after the mixing stopped.

*Table 10. PGSM trials. Constant variables included photoinitiator being added at the same time as the other ingredients, a mixing time of 3 minutes before adding the water, and a mixing time afterwards of 3 min for a total mixing time of 10 minutes. Successful results are shown in green. Symbols: * In more than 50% of the batches prepared. ⁱ Scaffolds does not crosslink homogeneously: the outside is stiff, but the centre presents a gel-like composition indicating poor light curing because of scattering.*

PGSM								Resolution	
Reactive				Conditions					
Polymer		Surfactant (Hypermer)	Solvent (Tol)	Photo initiator	Stirring	T	Water intake		UV lamp treatment
PGS 50%	0.5 g	10%	100%	40%	350 rpm	T _{room}	3 ml	5 min p/side	Emulsion unstable
					350 rpm		4 ml		Emulsion unstable
					350 rpm		3 ml		Pores ~100 μm
					850 rpm		4 ml		Emulsion unstable*
					850 rpm		3 ml		Pores ≤100 μm
PGS 80%	0.5 g	10%	100%	40%	350 rpm	T _{room}	4 ml	5 min p/side	Emulsion unstable
					350 rpm		3 ml	5 min p/side	Pores ~100 μm ⁱ
					850 rpm		3 ml	5 min p/side	Pores <100 μm ⁱ
					850 rpm		3 ml	10 min p/side	Pores ≤100 μm ⁱ
					850 rpm		3 ml	20 min p/side	Pores ≤100 μm
					850 rpm		4 ml	5 min p/side	Emulsion unstable*

From all possible combinations, those that proved to be successful were:

Polymer		Surfactant (Hypermer)	Solvent (Tol)	Photo initiator	Stirring	T	Water intake	UV lamp treatment
PGS 50%	0.5 g	10%	100%	40%	350 rpm	T _{room}	3 ml	5 min p/side
PGS 50%	0.5 g	10%	100%	40%	850 rpm	T _{room}	3 ml	5 min p/side
PGS 80%	0.5 g	10%	100%	40%	850 rpm	T _{room}	3 ml	20 min p/side

The variation in results highlighted a lack of understanding on how the internal conditions of the emulsion could affect the emulsion stability and the resulting scaffolds. Therefore, the role of the polymer : solvent ratio, the nature of the solvent and the volume of photoinitiator were explored at two different mixing speeds: 350 and 850 rpm, as shown in *Table 11*. For such experiments, 50% PGSM was used as it is a more stable polymer (higher degrees of methacrylation are associated with undesired crosslinking).

*Table 11. PGSM scaffolds were produced by varying the polymer : solvent ratio, volume of photoinitiator and mixing speed. Boxes coloured in red show mixtures whose phases could not integrate to form an emulsion. Yellow boxes show semi stable emulsions which had minor to medium complications when crosslinked under UV light. Green boxes describe successful emulsions, but particular pore features: * scaffolds were cured for 20 minutes (10 on each side) unless otherwise stated.*

Mixing speed: 850 rpm				
		PGS-M:DCM ratio (g)		
		70:30 (0.35:0.15)	80:20 (0.4:0.1)	90:10 (0.45:0.05)
PI (g)	0.125	(1) Emulsion unstable	(2)* Semi stable emulsion	(3) Did not crosslink
	0.2	(4) Successful emulsion	(5) Emulsion obtained, took 30 minutes to crosslink	(6) Very viscous Not cured in the middle after 30 minutes
	0.35	(7) Emulsion obtained, took 30 minutes to crosslink	(8)* Better consistency than samples 4-6	(9) Emulsion unstable

Mixing speed: 350 rpm				
		PGS-M:DCM ratio (g)		
		70:30 (0.35:0.15)	80:20 (0.4:0.1)	90:10 (0.45:0.05)
PI (g)	0.125	(10) Emulsion unstable	(11) Emulsion unstable	(12) Emulsion unstable
	0.2	(13) Aqueous emulsion, did not cure completely	(14)* Stable emulsion	(15) Stable emulsion
	0.35	(16)* Stable emulsion	(17)* Stable emulsion	(18)* Less viscous than previous Stable emulsion

A factor that was identified as critical was the homogeneity of the crosslinking process. It was observed that the surface of the scaffolds would crosslink first and that the highly scattering emulsions would obstruct the middle layers from being cured at the same speed and quality. This was evidenced through digital microscopy (*Fig. 32*). Direct consequences of this incomplete crosslinking are scaffold shrinkage and partial or full scaffold collapse.

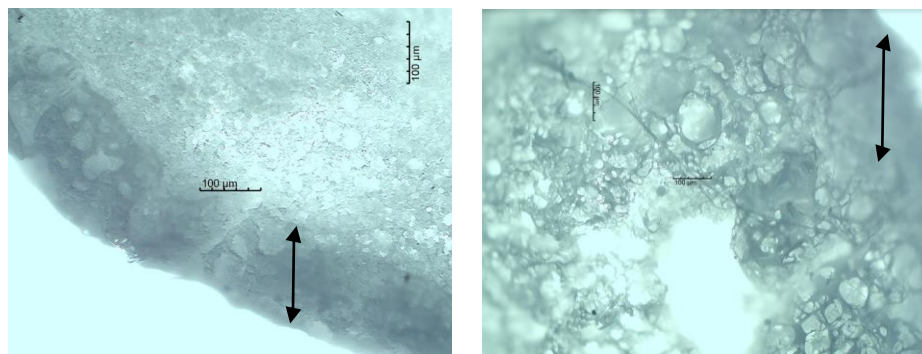


Fig. 32. Transversal cuts on PGSM scaffolds. A thick crosslinked layer is observed on the borders of the scaffold, whilst the middle areas take longer to crosslink, or do not crosslink at all. Arrows indicate crosslinked areas. Scales are 100 μm .

It is important to note that no dependence was found between the pore size and their distribution (edges or central areas) in the scaffold, as evidenced in *Fig. 33*.

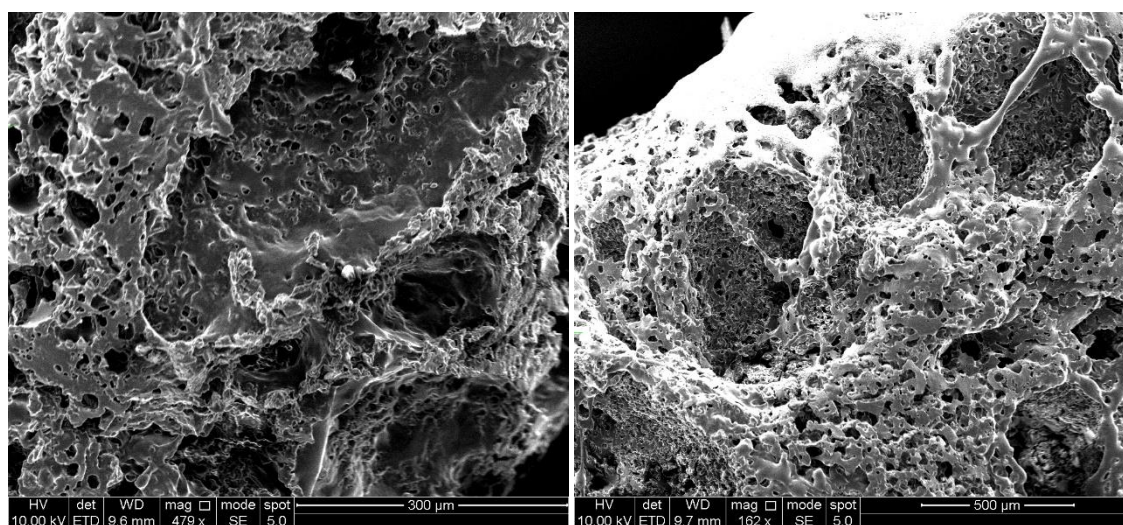


Fig. 33. A PGSM scaffold (exhibit 13 from previous experiment), has been imaged on both the internal (left) and edge (right) areas, with no significant difference in pore sizes. Scale bar is 500 μm .

It was hypothesised that this effect could be caused due to the scattering of the UV light by both the uncured and cured emulsion during exposure to the medium intensity UV light. The light would cure the outer areas of the scaffold, but the power would not be enough to penetrate to the emulsion's inner part. By increasing the time of curing, the porous nature of the cured scaffold (as observed by the

white colour) would scatter the light and slow down the crosslinking process of the inner part of the scaffold. In such cases, it was required to leave the scaffolds under the UV light for almost 40 minutes. To solve this problem, the source of light was changed and a higher power, from the Onmicure S1000 (100 W and $\sim 10\text{-}20\text{ W/cm}^2$) to a GEW Engineering UV conveyor belt (80 W/cm^2) was used.

4.4.2.2. Geometries of PGSM HIPEs

SEM imaging was used to identify pore geometry. Fig. 33 and Fig. 35 show the emulsions that could be successfully crosslinked from Table 11. As previously mentioned, scaffolds manufactured at higher rpms, showed big pores ($>300\text{ }\mu\text{m}$) on the surface (exposed to both glass and air through crosslinking). Smaller windows and, in some cases, interconnectivity between windows (Fig. 33) can be observed.

At 350 rpm, most of the scaffolds show homogeneous round pores (ranging from $250\text{-}500\text{ }\mu\text{m}$) at the surface and middle layers, and a visible high interconnection between pores and windows. In images 14, 15 and 17, really small windows can be appreciated, and not necessarily respecting the round geometry expected on HIPEs (Fig. 35).

Despite the results being successful in terms of porosity, the pores and windows found in these samples rarely resemble the ones related to HIPEs from PCL [111], EHA-TMPTA [304] or HA [305]. Only the last image (8) of Fig. 34 shows round pore geometries associated with HIPEs. This can be due to the effect of internal forces in the emulsification process, and on collapse and swelling-shrinking mechanisms during the washing and drying techniques. This was explored later on.

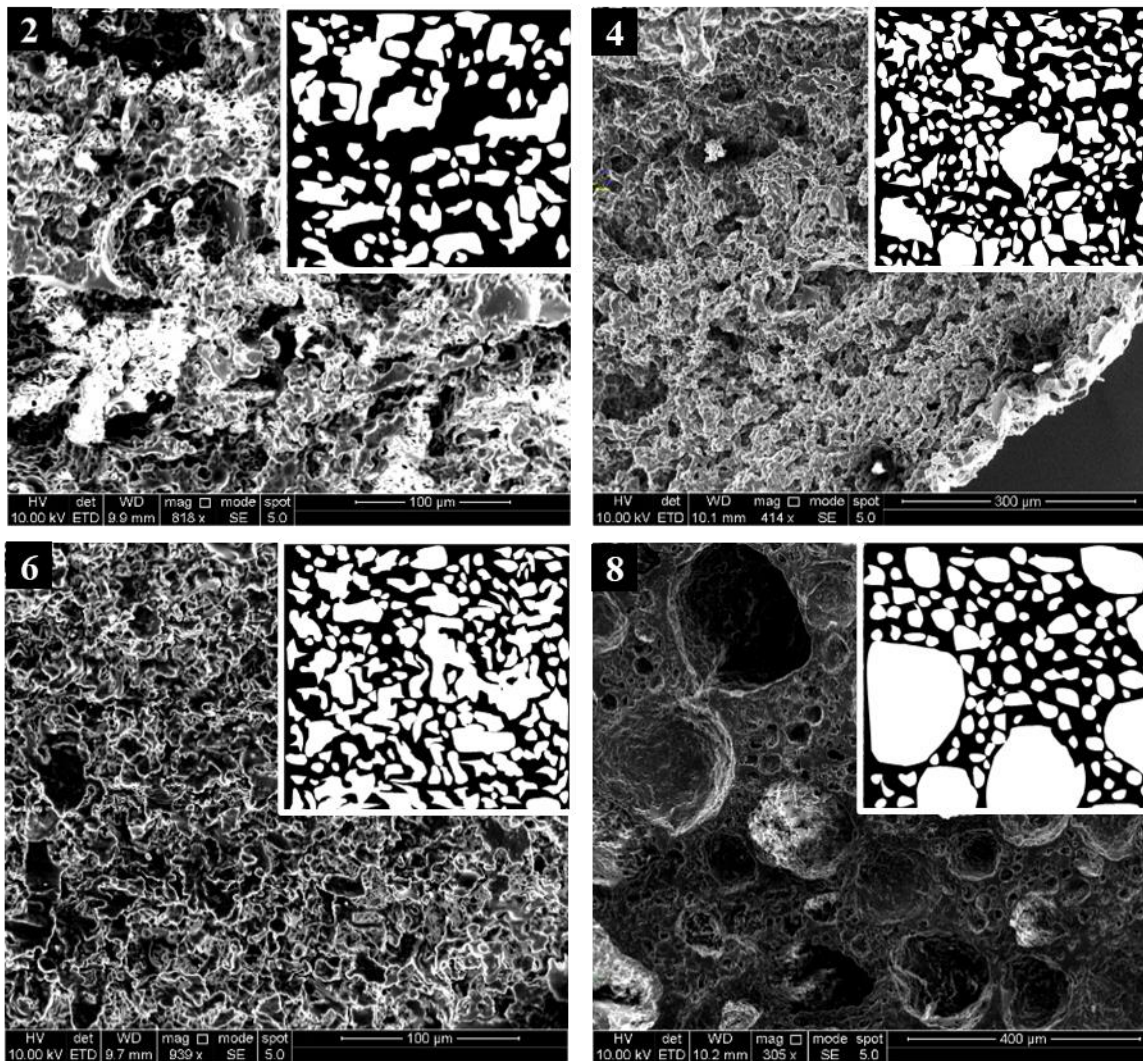


Fig. 34. SEM images for PGSM scaffolds under conditions labelled as 2, 4, 6 and 8, according to Table 4, mixed at 850 rpm. Pore geometries are mimicked in the small black boxes (at scale). Despite of all images showing high interconnection among cavities, they are heterogeneous in most of the cases. Only number 8 shows round pores, proper from HIPEs.

4.4.2.3. Internal Phase Volume

As with PCL emulsions, the oil phase is formed by the polymer solution, the surfactant, solvents, and the photoinitiator. The densities reported in Table 12 have been considered.

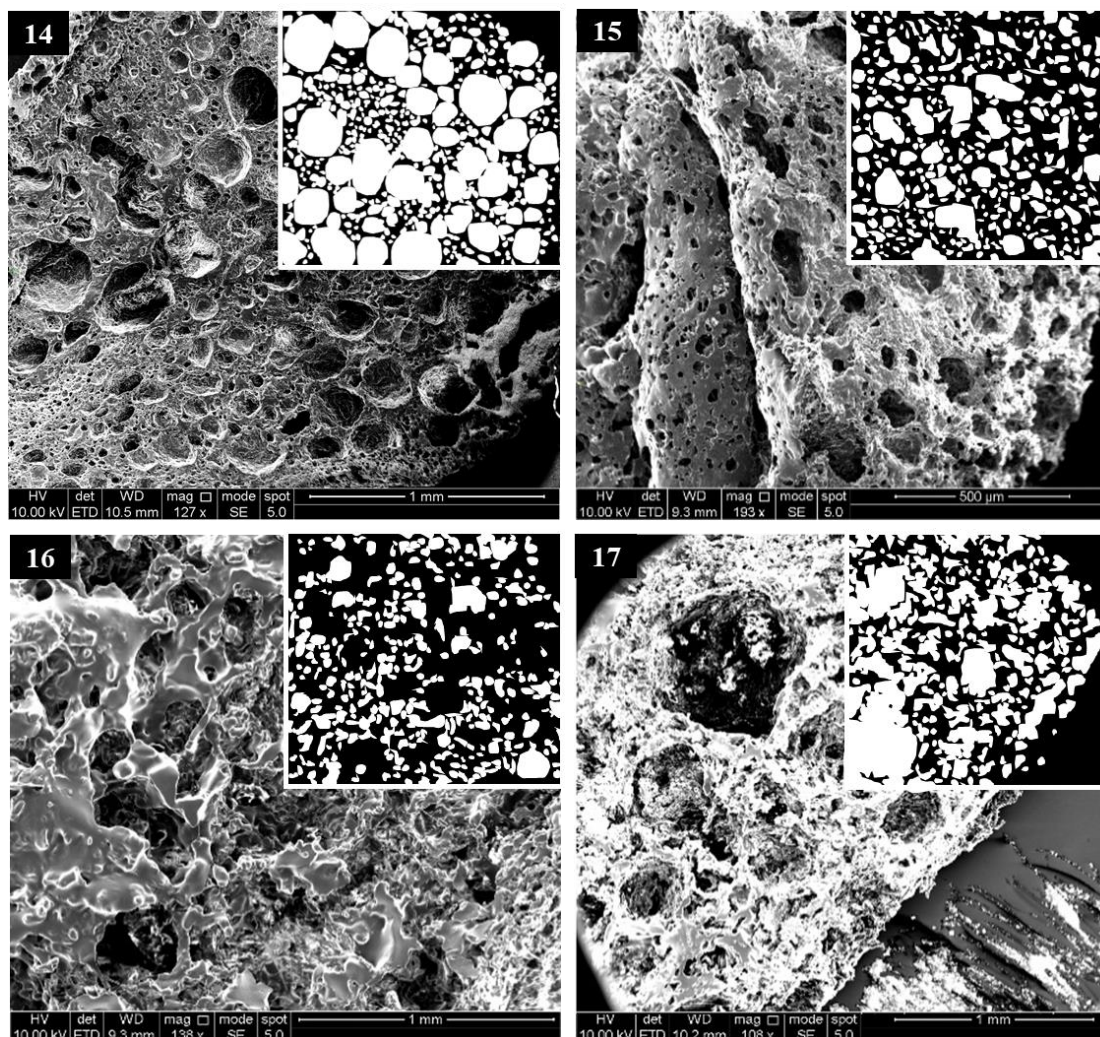


Fig. 35. SEM images for PGSM scaffolds under conditions labelled as 14-17 according to Table 4, mixed at 350 rpm. Pore geometries are mimicked in the small black boxes. Images 14 and 17 show big round pores ($>250\ \mu\text{m}$), but with irregular and heterogeneous small windows ($<100\ \mu\text{m}$). On the contrary, image 14 shows homogeneous circular medium size pores with small and round windows, even on the surface. Finally, image 16 illustrates irregular cavities, and no pores nor windows can be fully differentiated.

Table 12. Densities of water and oil phase involved in PGSM HIPE emulsions. *Toluene solvent is not considered as it leaves the emulsion through its formation and is washed away.

Reactive	Density (g/mol)	Weight (g)	Volume (ml)
Hypermer Surfactant	0.94	0.05	0.053
Polymer solution	1.32	0.5	0.3788
Toluene*	0.866	0.5	0.5773
Photoinitiator	1.12	0.2	0.178
		Total	0.6098 ml

Density values for PGSM have not been reported in literature but other polymer materials have reported them between 1 and 2 $\frac{g}{mol}$ [303].

The calculation of the internal phase volume for the uncured emulsion includes the solvents as they are within the mix. The internal phase volume is 71.64%, and temporarily classified as a MIPE (Medium Internal Phase Emulsions).

$$Internal\ phase = \frac{water\ phase}{oil + water\ phase} = \frac{3\ ml}{3ml + 1.1871\ ml} * 100 = 71.64\%$$

For the cured emulsion, we can assume that the solvents have left the emulsion, and their internal phase volume is 83.11%, therefore being classified as a polyHIPE.

$$Internal\ phase = \frac{water\ phase}{oil + water\ phase} = \frac{3\ ml}{3ml + 0.6098\ ml} * 100 = 83.11\%$$

It is important to note that 3.5 ml of water phase results in 85.16% of internal phase volume and 4 ml, in 86.77%. However, at higher volumes of water, the PGSM emulsions are more inclined to destabilise via coalescence and Ostwald ripening. For a porous structure to be considered a HIPE, an internal phase volume of at least 74% is required [311]. The PGSM emulsions fit this criteria and therefore can be referred to as polyHIPEs.

4.4.2.4. Degree of Openness

The methodology has been described in *Section 3.4.1.2.4* of Chapter 3. The internal phase volume is associated to the degree of openness (DOO) as the latter describes the total surface of the cavities, which is crudely equal to the total diameter of the internal phase droplet. To calculate such, a total of 100 random pores were measured using ImageJ and the average measurement was multiplied by the statistical correction factor. The DOO was found to be 0.4653 for PGSM-50%.

4.4.2.5. Porosity of PGSM HIPEs

The DOO is directly related to the porosity as they both focus on the hollow part of the scaffold, the DOO describes the internal surface area of the cavities, and the porosity, the volume that this area occupies.

The theoretical porosity of the PGSM emulsion was calculated through the empirical *Eq. 3* and *Eq.4* in *Section 3.3 of Chapter 3*. The experimental density of the polyHIPE was reported to be $1.1469 \frac{g}{cm^3}$ and $1.2053 \frac{g}{cm^3}$ for 50% and 80% PGSM as measured through pycnometry.

The gel fraction was calculated to measure the extent of crosslinking. It was determined to be 83.91% and 90.55% for 50% and 80% PGSM respectively. Therefore, the theoretical porosity of the polyHIPE is:

$$\rho_{polyHIPE_{theoretical}} = \rho_{polymer} \times (1 - \theta) \times Gel\ Fraction$$

$$\rho_{polyHIPE_{theoretical}} = 0.1644$$

Therefore, the average experimental porosity of the polyHIPEs is:

$$\% porosity = \left(1 - \frac{\rho_{polyHIPE}}{\rho_{wall}}\right) \times 100 = \left(1 - \frac{0.16437}{1.32}\right) \times 100 = 87.55\%$$

4.4.2.6. Interconnectivity of PGSM HIPEs

Finally, the interconnectivity of the scaffolds can be determined by either the relation between the windows and pore sizes, that is, the relation between the cavity surface and open surface area. The interconnectivity of PGS polyHIPEs was reported as 16.39%. This will be contrasted with the results from the nano-CT later on.

4.4.3. Optimisation of PGSM scaffolds

4.4.3.1. Emulsion stability with single solvents

As a more comprehensive understanding of the role of each element in the formation of a successful emulsion, a study on single solvents was developed, using solvents commonly found in water-in-oil emulsions. The volume of stability for four different solvents (toluene, chloroform, DCE and DCM) were studied independently, using the feedback from previous experiments (375 rpm and 0.2 g of photoinitiator) and analysing three different polymer : DCM ratios (70:30, 80:20 and 90:10), as reported in *Table 14*. For solvent free (SF) emulsions, their density is expressed as the sum of the partial densities of the polymer solution, the surfactant and the photoinitiator, as shown in *Table 13*.

Table 13. The density of solvent free emulsions is expressed as the sum of the partial densities of the reagents in the oily phase (polymer:solvent, surfactant and photoinitiator).

Sample ID	Ratio	ρ polymer:solvent ($\frac{g}{ml}$)	ρ oil phase ($\frac{g}{ml}$)
SF7030	70:30	1.3265	1.2454
SF8020	80:20	1.326	1.2451
SF9010	90:10	1.3255	1.2447

Three main elements have been explored using these graphs: separation during mixing, separation after mixing and presence of defined pores. Separation of the emulsion during mixing has not happened frequently, but with a higher incidence in 70:30 and 80:20 ratios, and mostly for scaffolds which use DCM as a solvent. Separation after mixing has been frequent, and higher for 90:10 emulsions with all solvents except toluene. Solvents that more frequently cause division in emulsions are DCM and chloroform. Most of the emulsions at 90:10 have reported porosity (13/16 or 81.25%), with only some exceptions in samples with toluene. However, for scaffolds at 80:20, only half reported defined pores; non-porous scaffolds were present at higher concentrations of DCM and chloroform. Finally, higher solvent volumes tend to produce division in scaffolds, mainly after mixing, specifically on DCM and chloroform. Patterns can be addressed from these results.

4.4.3.2. Changes in densities

Scaffolds were weighted and measured at day 1, 7 and 14 after being manufactured, and the differences in volume per solvent concentration (0.25–0.70 ml per emulsion batch), polymer:DCM ratio (70:30, 80:20, 90:10 w/w) and type of solvent (toluene, chloroform, DCM, DCE) is reported in *Fig. 36*. Additionally, the difference in densities between day 1-7 and day 7-14 was graphed and reported in *Fig. 37*. Values close to 0 are reported as null changes; the experiment was run in triplicate.

Table 14. Details of compositions on 50% PGSM PolyHIPEs prepared by using no solvent and single solvent of DCM, chloroform, toluene or DCE, and three polymer:solvent ratios (70:30, 80:20, 90:10 w/w). All volumes (V) are in ml. P/N: Porous/non-porous structure, N/Y: no/yes, NDP: non-defined pores.

Polymer : solvent ratio - 90:10	Solvent	Sample ID	V solvent	V polymer 90:10	V surfactant	V PI	V _{oil} phase	ρ _{oil} phase (g/ml)	Separation during mixing	Separation right after mixing	Porous structure
	None	SF	0	0.3772	0.0532	0.1786	0.6090	1.2319	N	Y	N
	DCM	DCM0.25	0.25	0.3772	0.0532	0.1786	0.8590	1.2604	N*	Y	P
		DCM0.4	0.4	0.3772	0.0532	0.1786	1.0090	1.2708	N*	Y	P
		DCM0.55	0.55	0.3772	0.0532	0.1786	1.1590	1.2784	N*	Y	P
		DCM0.7	0.7	0.3772	0.0532	0.1786	1.3090	1.2844	Y	Y	N
	N*: division after adding 1.5-2 ml of water										
	Chloroform	C0.25	0.25	0.3772	0.0532	0.1786	0.8590	1.2016	Y	Y	P
		C0.4	0.4	0.3772	0.0532	0.1786	1.0090	1.1907	Y	Y	P
		C0.55	0.55	0.3772	0.0532	0.1786	1.1590	1.1826	N'	Y	P
		C0.7	0.7	0.3772	0.0532	0.1786	1.3090	1.1763	N	N	P
N': absorbed 2.5 ml of water only											
Toluene	T0.25	0.25	0.3772	0.0532	0.1786	0.8590	1.1254	N	Y	P	
	T0.4	0.4	0.3772	0.0532	0.1786	1.0090	1.0868	N	N	P	
	T0.55	0.55	0.3772	0.0532	0.1786	1.1590	1.0582	N	N	NDP	
	T0.7	0.7	0.3772	0.0532	0.1786	1.3090	1.0362	N	N	NDP	
NDP: not defined pores											
DCE	DCE0.25	0.25	0.3772	0.0532	0.1786	0.8590	1.2372	N'	Y	P	
	DCE0.4	0.4	0.3772	0.0532	0.1786	1.0090	1.2391	N'	Y	P	
	DCE0.55	0.55	0.3772	0.0532	0.1786	1.1590	1.2405	N'	N	P	
	DCE0.7	0.7	0.3772	0.0532	0.1786	1.3090	1.2416	N	Y	P	

Polymer : solvent ratio - 80:20	Solvent	Sample ID	V solvent (ml)	V polymer 80:20	V surfactant	V PI	V _{oil} phase	ρ _{oil} phase (g/ml)	Separation during mixing	Separation right after mixing	Porous structure
	None	SF	0	0.3771	0.0532	0.1786	0.6088	1.2319	N**	Y	N
									N**: watery homogeneous phase		
	DCM	DCM0.25	0.25	0.3771	0.0532	0.1786	0.8588	1.2604	Y	Y	N
		DCM0.4	0.4	0.3771	0.0532	0.1786	1.0088	1.2708	N	Y	P
		DCM0.55	0.55	0.3771	0.0532	0.1786	1.1588	1.2784	N	Y	P
		DCM0.7	0.7	0.3771	0.0532	0.1786	1.3088	1.2843	Y	Y	N
	Chloroform	C0.25	0.25	0.3771	0.0532	0.1786	0.8588	1.2016	Y	Y	P
		C0.4	0.4	0.3771	0.0532	0.1786	1.0088	1.1907	Y	Y	P
		C0.55	0.55	0.3771	0.0532	0.1786	1.1588	1.1826	Y	Y	P
		C0.7	0.7	0.3771	0.0532	0.1786	1.3088	1.1763	N'	Y	P
								N': absorbed 2.5 ml of water only			
Toluene	T0.25	0.25	0.3771	0.0532	0.1786	0.8588	1.1254	Y	N	P	
	T0.4	0.4	0.3771	0.0532	0.1786	1.0088	1.0868	N	N	P	
	T0.55	0.55	0.3771	0.0532	0.1786	1.1588	1.0582	Y	Y	N	
	T0.7	0.7	0.3771	0.0532	0.1786	1.3088	1.0362	N	N	N	
DCE	DCE0.25	0.25	0.3771	0.0532	0.1786	0.8588	1.2371	N	N	P	
	DCE0.4	0.4	0.3771	0.0532	0.1786	1.0088	1.2391	N	N	P	
	DCE0.55	0.55	0.3771	0.0532	0.1786	1.1588	1.2405	N	N	P	
	DCE0.7	0.7	0.3771	0.0532	0.1786	1.3088	1.2416	N**	N	P	

Polymer : solvent ratio - 70:30	Solvent	Sample ID	V solvent (ml)	V polymer 70:30	V surfactant	V PI	V _{oil} phase	ρ _{oil} phase (g/ml)	Separation during mixing	Separation right after mixing	Porous structure
	None	NS	0	0.3769	0.0532	0.1786	0.6087	1.2318	N**	N	N
	DCM	DCM0.25	0.25	0.3769	0.0532	0.1786	0.8587	1.2604	N	Y	P
		DCM0.4	0.4	0.3769	0.0532	0.1786	1.0087	1.2708	N**	N	P
		DCM0.55	0.55	0.3769	0.0532	0.1786	1.1587	1.2784	N**	N	N
		DCM0.7	0.7	0.3769	0.0532	0.1786	1.3087	1.2843	N**	N	N
	Chloroform	C0.25	0.25	0.3769	0.0532	0.1786	0.8587	1.2016	Y	Y	P
		C0.4	0.4	0.3769	0.0532	0.1786	1.0087	1.1907	N	Y	P
		C0.55	0.55	0.3769	0.0532	0.1786	1.1587	1.1825	Y	Y	N
		C0.7	0.7	0.3769	0.0532	0.1786	1.3087	1.1763	Y	Y	N
	Toluene	T0.25	0.25	0.3769	0.0532	0.1786	0.8587	1.1253	N	Y	P
T0.4		0.4	0.3769	0.0532	0.1786	1.0087	1.0868	N	N	P	
T0.55		0.55	0.3769	0.0532	0.1786	1.1587	1.0582	N**	N	N	
T0.7		0.7	0.3769	0.0532	0.1786	1.3087	1.0362	N**	N	N	
DCE	DCE0.25	0.25	0.3769	0.0532	0.1786	0.8587	1.2371	N	N	P	
	DCE0.4	0.4	0.3769	0.0532	0.1786	1.0087	1.2390	Y	Y	P	
	DCE0.55	0.55	0.3769	0.0532	0.1786	1.1587	1.2405	N**	N	P	
	DCE0.7	0.7	0.3769	0.0532	0.1786	1.3087	1.2416	N**	N	P	

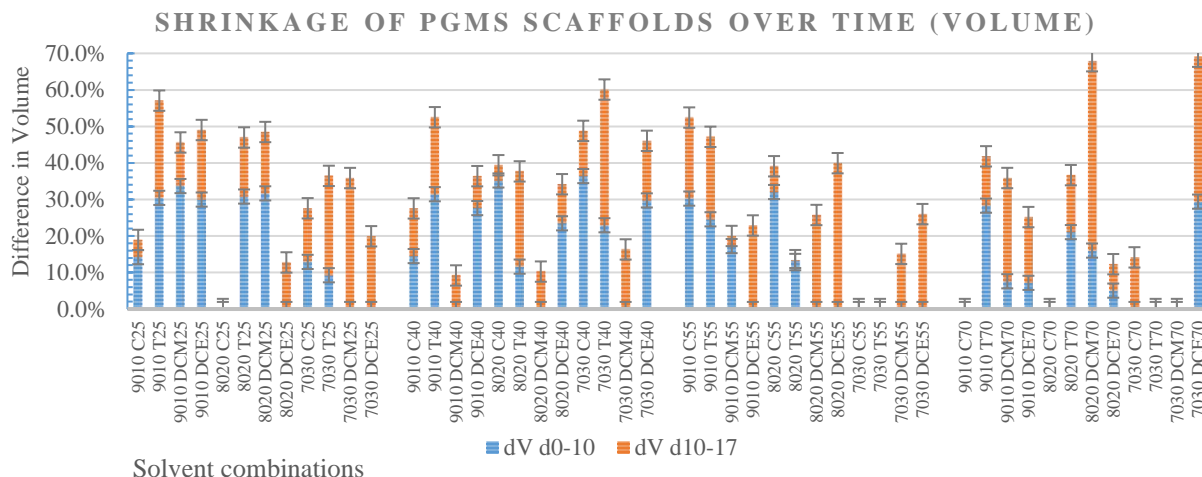


Fig. 36. . Differences in volumes between D0, 10 and 14 for PGSM-50% scaffolds manufactured with single solvents and under different solvent and polymer:DCM ratios.

The differences in volume were higher between days 1-7 than days 7-14, which is consistent with the differences in densities. Results also show that in most cases, volume, and weight decreased, but the volume decrease was more significant.

As a second point of analysis, the type of solvent has been explored. The major volume and density changes were reported by DCE and toluene (boiling points: 88 and 110 °C), whilst DCM and chloroform (boiling points: 39 and 66 °C) seem to have a milder effect. The solvent concentration is also closely related, reporting higher differences in densities and volumes for scaffolds with 0.25 and 0.40 ml of solvent, with an inconsistent pattern between volume/density change for the 0.55- and 0.70-ml samples. Finally, changes in volume and densities were reported as higher for 90:10 polymer:solvent ratios.

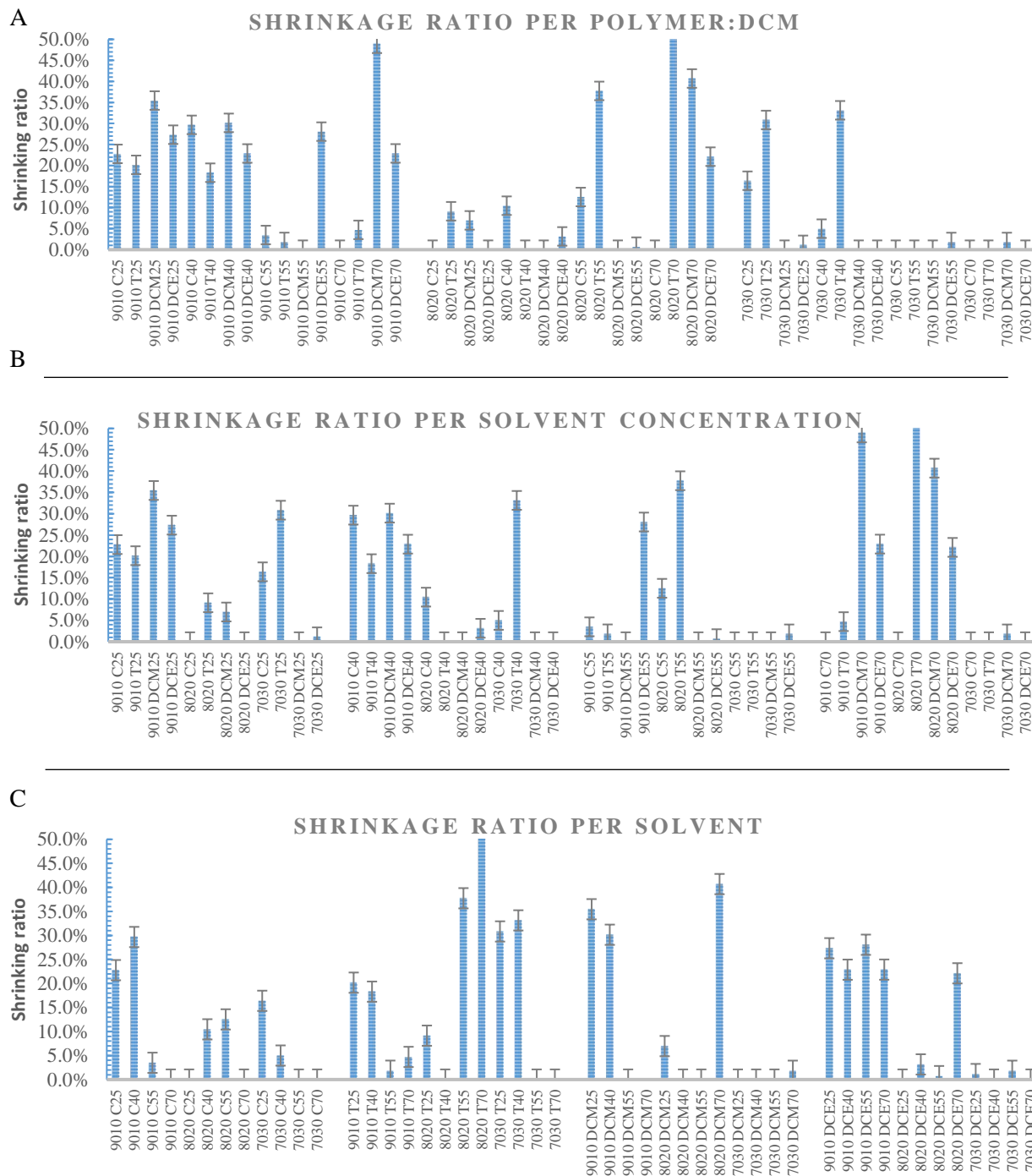


Fig. 37. Difference in construct densities between days 7-14, organised by: A. PGSM:DCM ratio; B. solvent concentration (0.25-0.70 ml); C. Type of solvent.

4.4.3.2.1. 3D imaging of single solvent scaffolds

4.4.3.2.1.1. LightSheet Imaging

Scaffolds successfully manufactured for all variables previously described (Table 14) were imaged using a LightSheet microscope. Samples were kept in a wet environment and suspended in a 1% agar solution. The structure of the emulsion, pore geometries and pore : window ratio can be appreciated from Fig. 39 to Fig. 41. Pores appear round in most cases, which somehow evidenced how scaffolds partially collapse through conventional drying processes.

Chloroform supported the creation of big pores and an increase in the continuous phase viscosity. At lower polymer:solvent ratios and higher solvent concentrations, bigger pores are found, with a size that may attempt the emulsion's stability as shown in 80:20 and 70:30 emulsions (Fig. 38).

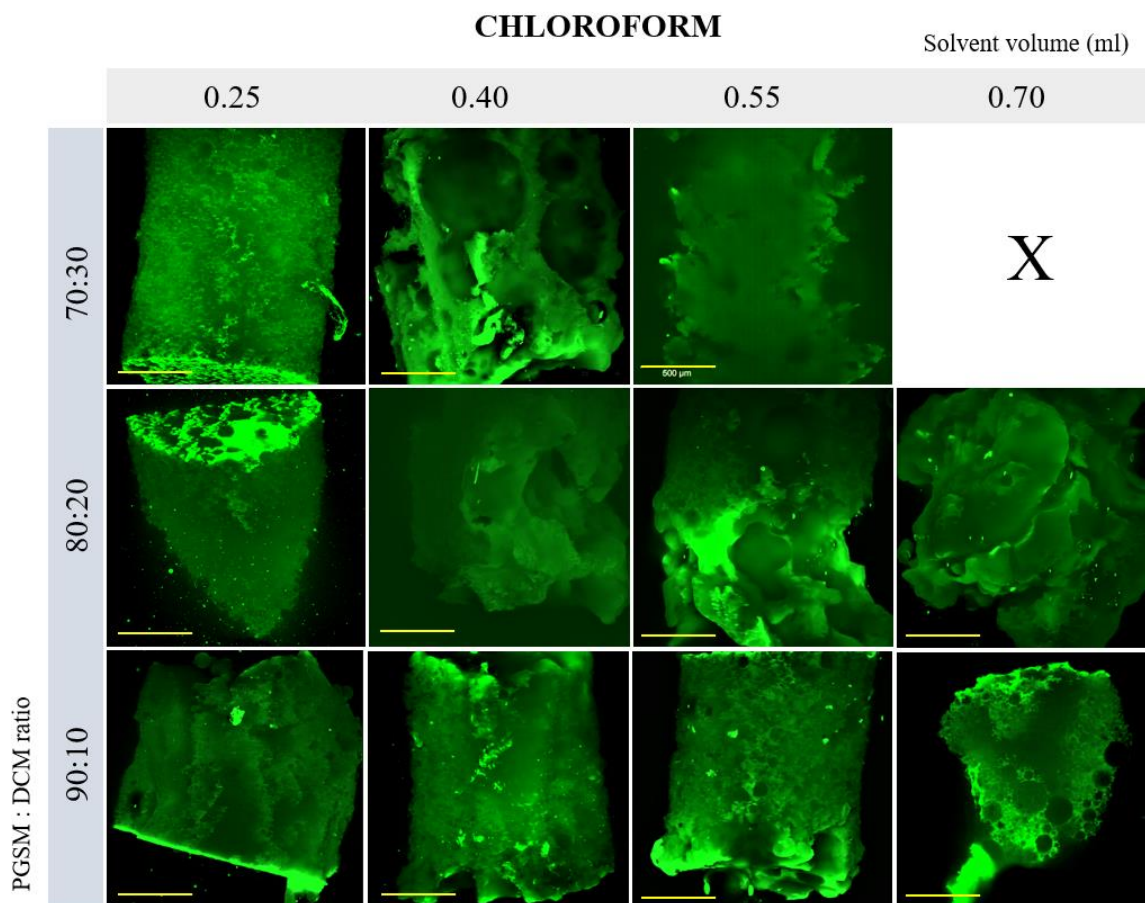


Fig. 38. LightSheet imaging for PGS-50%. Three different PGSM:DCM ratios were tested at 4 different solvent volumes (0.25 - 0.70 ml) for chloroform. Scale bars: 500 μ m. Crosses: unsuccessful emulsions.

Toluene was the only solvent that absorbed all 3 ml of water without dividing during nor after mixing. Pore morphology was not consistent nor exhibited round well-defined pores at higher solvent concentrations. It can be noticed that at lower concentrations of solvent the size of the pores and windows is quite small (there is not a significant difference between one or the other). See Fig. 39.

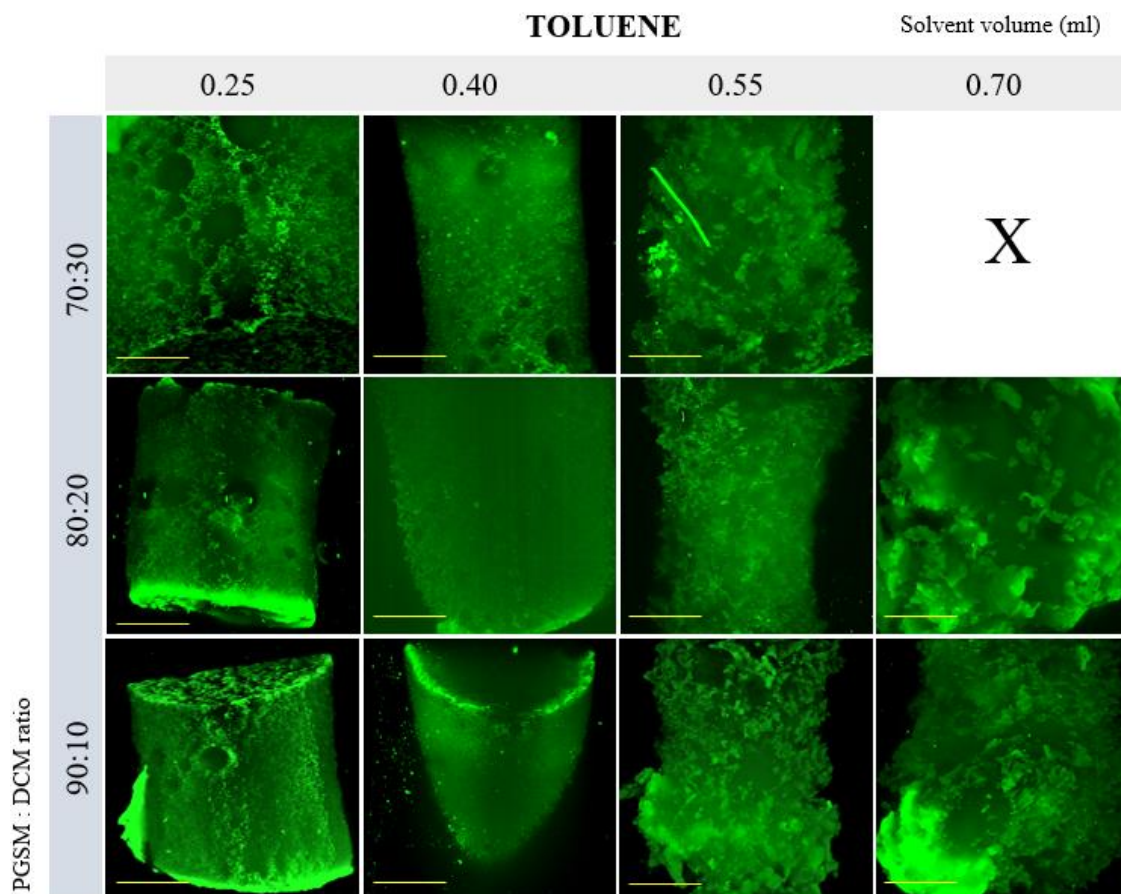


Fig. 39. LightSheet imaging for PGS-50%. Three different PGSM:DCM ratios have been tested at 4 different solvent volumes (0.25 - 0.70 ml), for toluene, DCM and DCE solvents. All scale bars are 500 μm . The crosses show unsuccessful emulsions.

Dichloromethane (DCM) is the solvent commonly used to dissolve and process PGS [121]. As observed in most cases, after adding a certain amount of water (2 to 2.5 ml), the emulsion broke down. This breakdown occurs in the internal phase of the emulsion, as evidenced at higher solvent concentrations (Fig. 40).

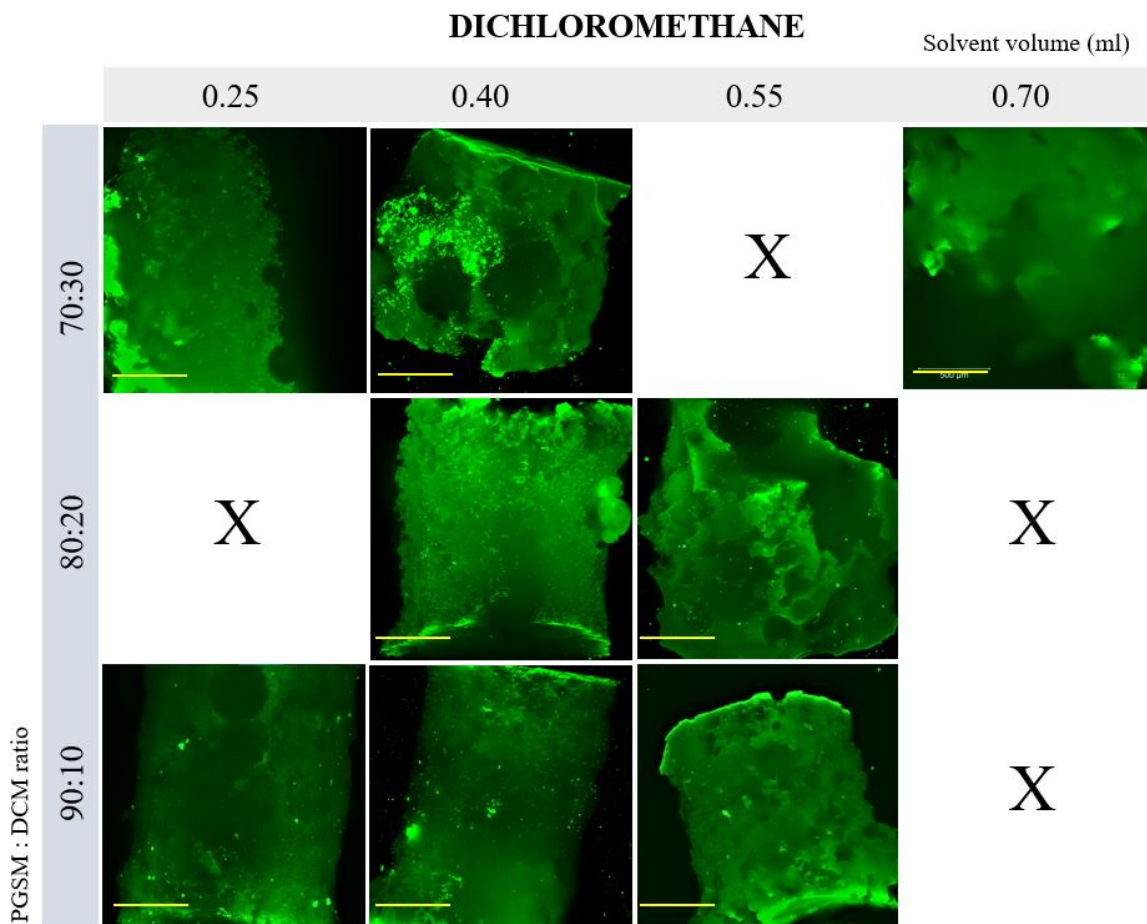


Fig. 40. LightSheet imaging for PGS-50%. Three different PGSM:DCM ratios have been tested at 4 different solvent volumes (0.25 - 0.70 ml), for DCM. All scale bars are 500 μm . The crosses show unsuccessful emulsions.

Out of each of the four solvents, dichloroethane (DCE) was the one with more consistent results. Water absorption was optimal for most scaffolds and for all, 2.5 ml was optimal, which resulted in an increased emulsion viscosity. In all cases, DCE scaffolds showed round pores and windows, being both of them easily distinguishable from each other in size and location. Finally, they seem to be highly interconnected (Fig. 41).

As a result, toluene and DCE were selected as good solvents for the manufacturing of successful PGS polyHIPes. The stability point with double solvents was thereafter explored. Because DCM as a solvent did not facilitate the formation of desired emulsions, from now on all emulsions are 100:0 polymer:DCM ratio.

DICHLOROETHANE

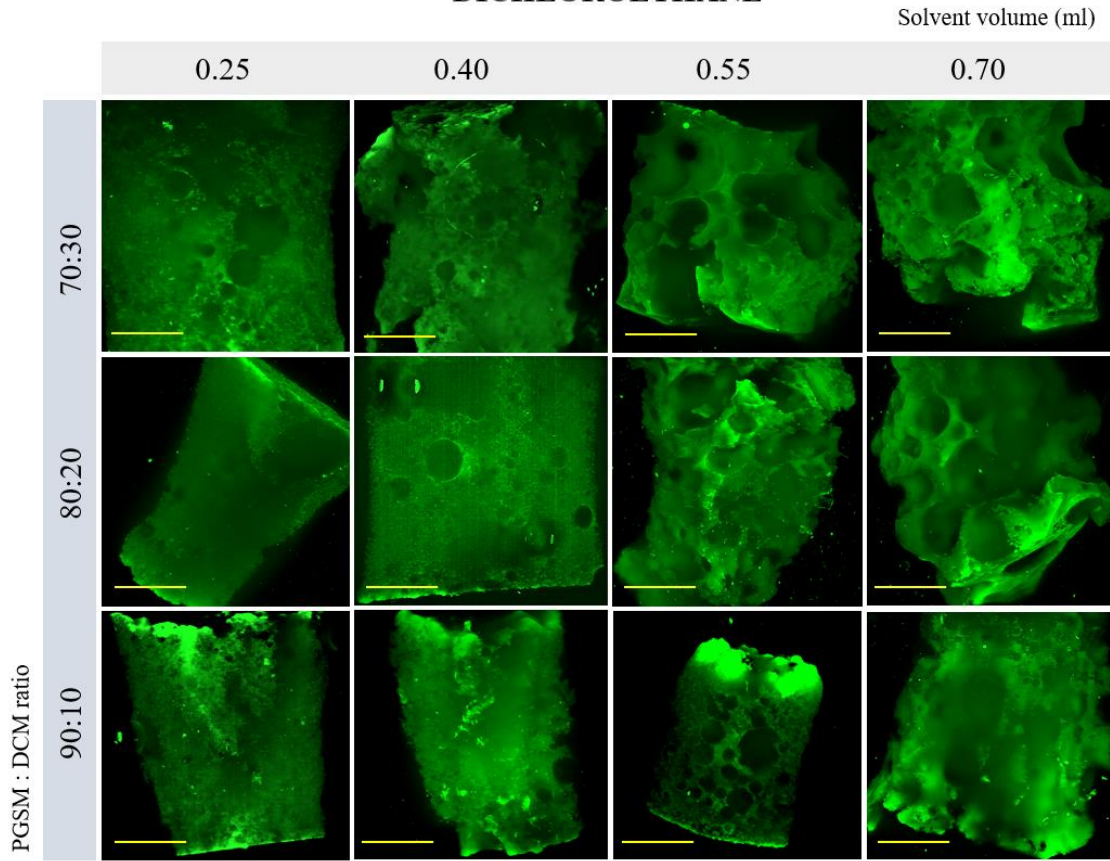


Fig. 41. LightSheet imaging for PGS-50%. Three different PGSM:DCM ratios have been tested at 4 different solvent volumes (0.25 - 0.70 ml), for DCE. All scale bars are 500 μm . The crosses show unsuccessful emulsions.

4.4.3.2.2. Emulsion stability with double solvents

As the single solvent experiment allowed identification of the impact of the four solvents on PGSM HIPEs, it was considered that a blend of solvents would bring the best of each and support the stability of the emulsion, and desired pore morphology. For such, dichloromethane and toluene were chosen.

The characteristics of the polymer solution and the oil phase for PGS emulsions were as reported in Table 15.

Table 15. Densities of the polymer solution and oil phase for the study of emulsion stability with double solvents. The proportion of each component is stated in terms for the oil phase with and without solvents, for future considerations of theoretical porosity.

Sample ID	ρ polymer ($\frac{g}{ml}$)	ρ oil phase ($\frac{g}{ml}$)	V oil phase (ml)
100:0	1.325	1.2313	0.6091

	$\rho \left[\frac{g}{ml} \right]$	w (g)	V (ml)	% (v/v) w/o solvent	% (v/v)
ρ PGSM 50%	1.325	0.5	0.3774	62%	34%
ρ DCE*	1.25	0.25	0.2000	No solvent	18%
ρ toluene*	0.866	0.25	0.2887	No solvent	26%
ρ photoinitiator	1.12	0.2	0.1786	29%	16%
ρ surfactant	0.94	0.05	0.0532	9%	5%
Total V_{oil} phase		1.25	1.0978	100%	100%

To find the ideal composition of the solvent (toluene and DCE) to create stable emulsions with pore morphologies and sizes of interest, the combinations in *Table 16* were developed.

Table 16. PGS-50% emulsions were manufactured by varying the solvent composition (toluene and DCE). The table reports on the volumes per component, densities, their behaviour during and after mixing, and their porosity.

PGSM:DCEM (100:0)	Solvent 1	Solvent 2	V solvent (ml)	V polymer (ml)	V surfactant	V PI	V _{oil} phase	ρ_{oil} phase $\left(\frac{g}{ml} \right)$	Separation during mixing	Separation right after mixing	Porous structure
	None	NS	0	0.3774	0.0532	0.1786	0.6091	1.2313	N	Y	N
	DCE0.25	T0.75	0.53303	0.3774	0.0532	0.1786	1.1421	1.0944	N	N	Y
	DCE0.50	T0.50	0.48868	0.3774	0.0532	0.1786	1.0978	1.1386	N	Y	Y
	DCE0.75	T0.25	0.44434	0.3774	0.0532	0.1786	1.0535	1.1866	N	Y*	Y

It was observed that, as in single solvent emulsions, the batches with higher volume of toluene could absorb all 3 ml of water, but that the other batches would reject the last 0.5 to 1 ml of water, as a consequence of the coalescence of the emulsion.

From above experiments, emulsions with DCE : toluene 25:75 were the ones that resulted in stable and porous scaffolds. These were the scaffolds that were used in the mechanical testing and the structure determination by micro-CT. The shrinkage of the scaffolds over time is illustrated on *Fig. 42*.

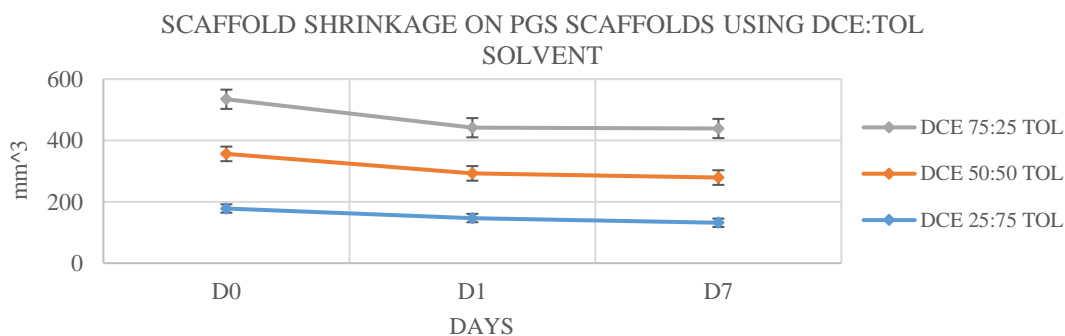


Fig. 42. Scaffold shrinkage for D0, D1 and D7 on PGS-50% scaffolds and DCE : Toluene solvent.

4.4.3.3. Mechanical properties of PGSM scaffolds

The mechanical properties of the materials were determined for successful emulsions of PGS-50%. The tests were also performed on PGS-80% as a reference point. As described in the methods section, dog bone shaped tensile samples were produced and scaled down to fit the mechanical testing machine. The compressive tests were developed using cylindrical samples that respected the 2:1 proportion. Compression and tensile strength (UTS) tests were developed in bulk and porous structures, the latter under dry conditions. Results are found in Table 17.

*Table 17. Tensile and compressive tests results on PGSM 50% and 80% DM. * Cannot be determined as the scaffold could resist loads higher than 250 N, which was the highest load available at the lab.*

Conditions	Conditions	Material	UTS (MPa)	Compressive Strength (MPa)
Dry	Bulk	PGSM 50% DM	3.1715	5.0910
		PGSM 80% DM	6.8402	*
	Porous	PGSM 50% DM	0.7943	0.6515
		PGSM 80% DM	0.2596	1.4670

4.4.3.4. Micro Computed Tomography for the study of polyHIPES

Even though LightSheet microscopy allowed for the overall study of the three dimension of the scaffolds, micro computed tomography (μ -CT) was used to characterise and quantitatively analyse the pore and window structure, distribution, and interconnection of PGS-50% and 80% scaffolds.

Reconstruction of the scaffolds are found in *Fig. 43* and *Fig. 44*.

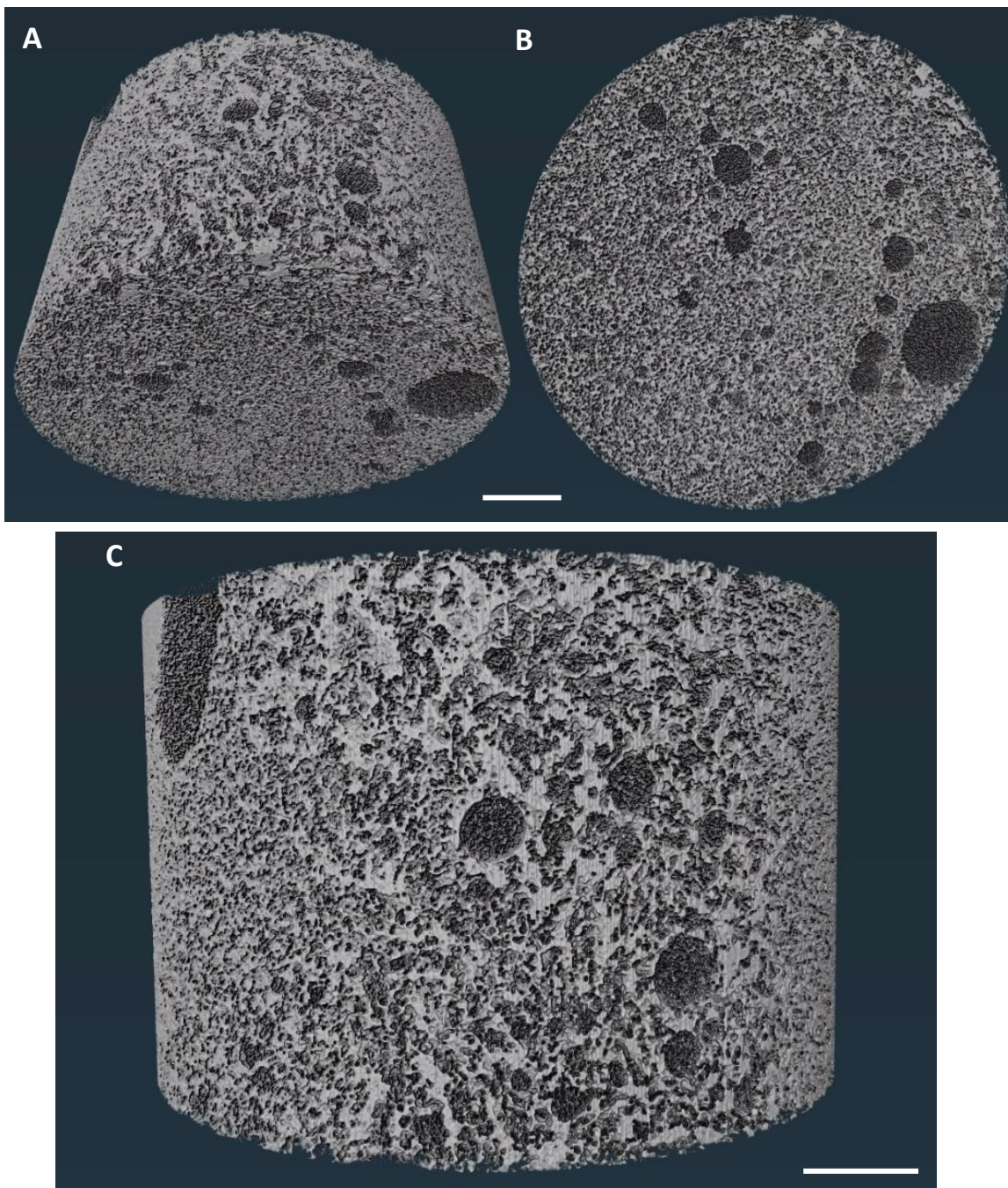


Fig. 43. Reproduction of PGS-50% scaffolds scanned through μ -CT, on xy (A), xz (B) and yz (C) planes. Scale bars are 1 mm.

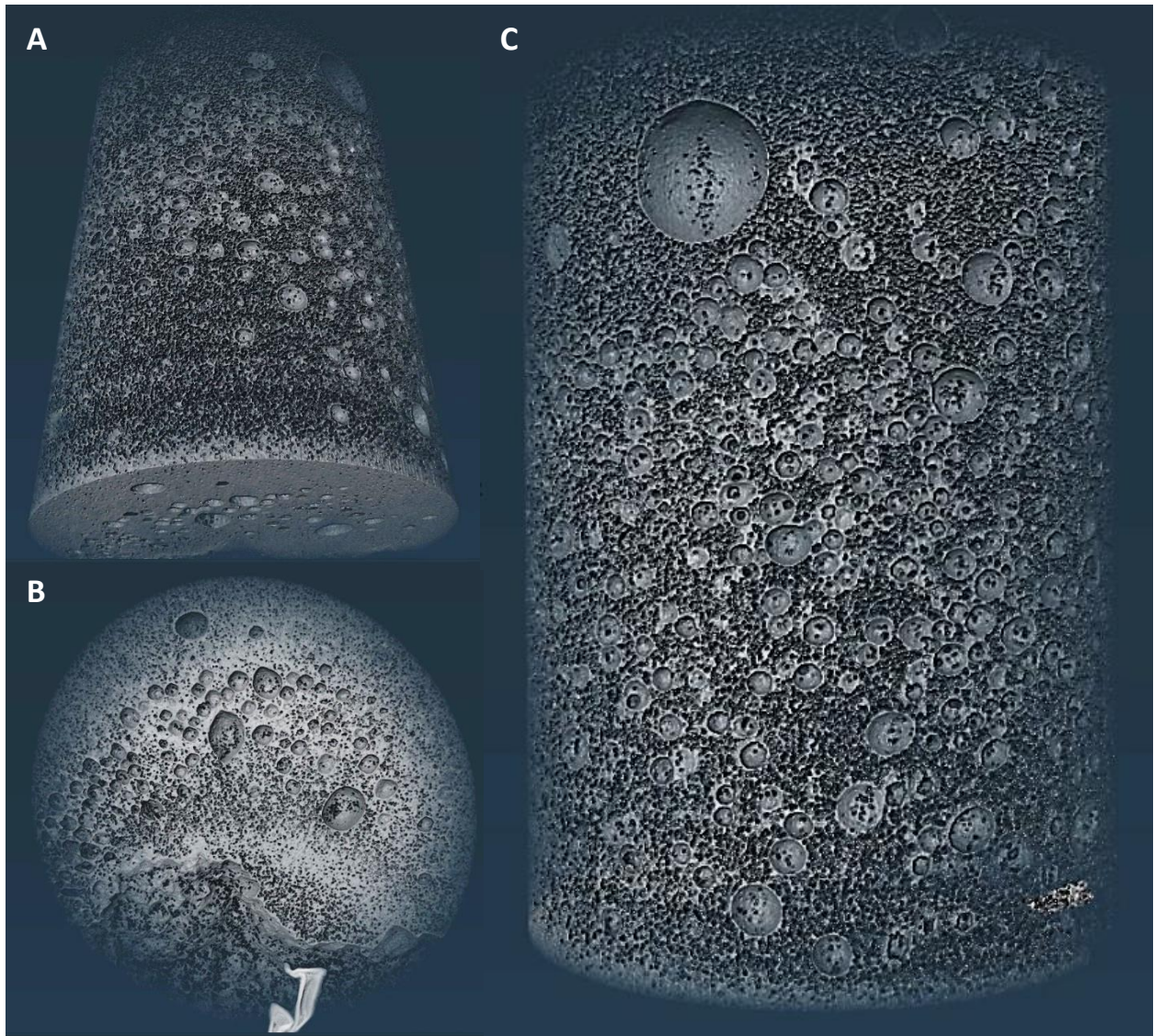
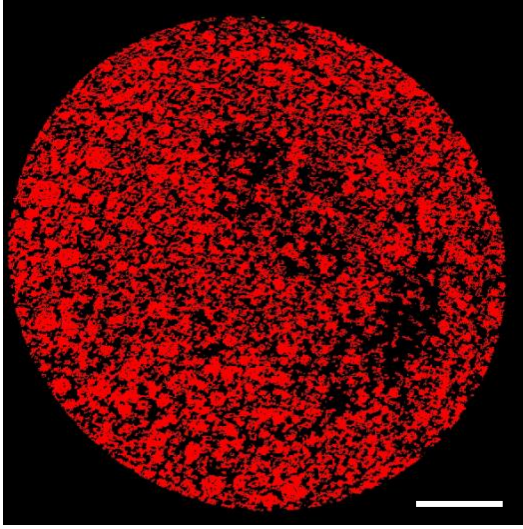
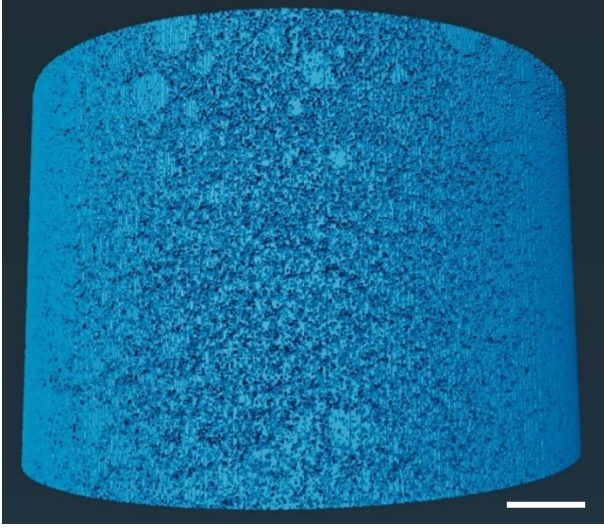
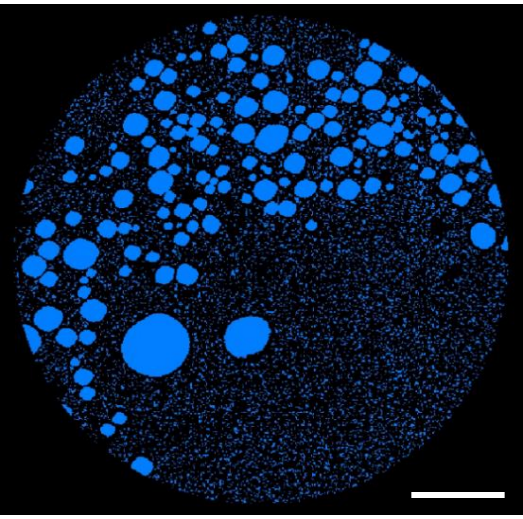
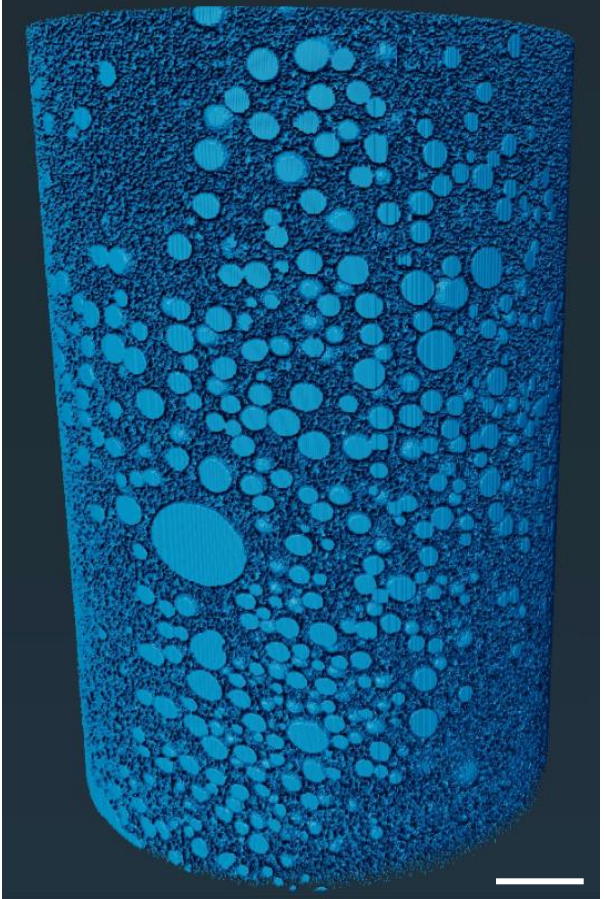


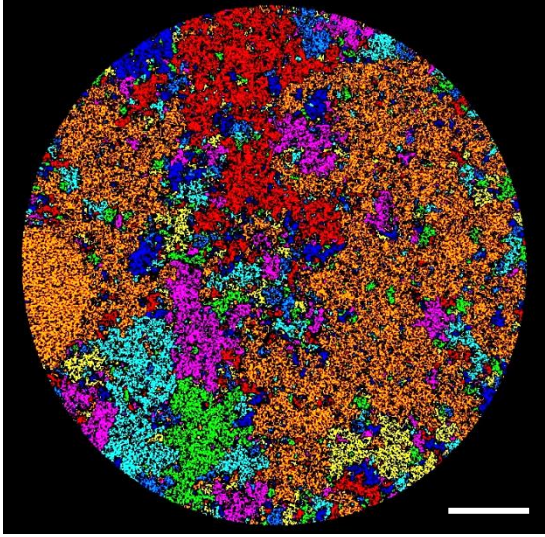
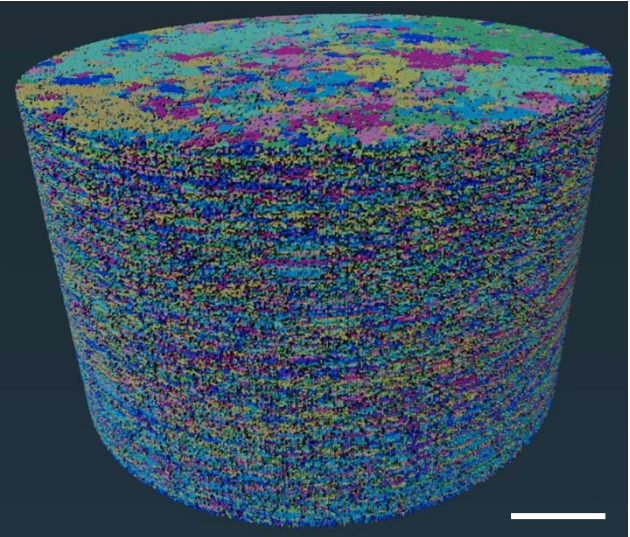
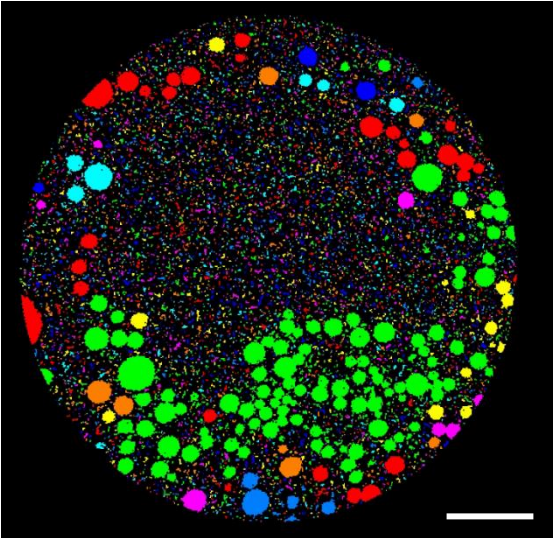
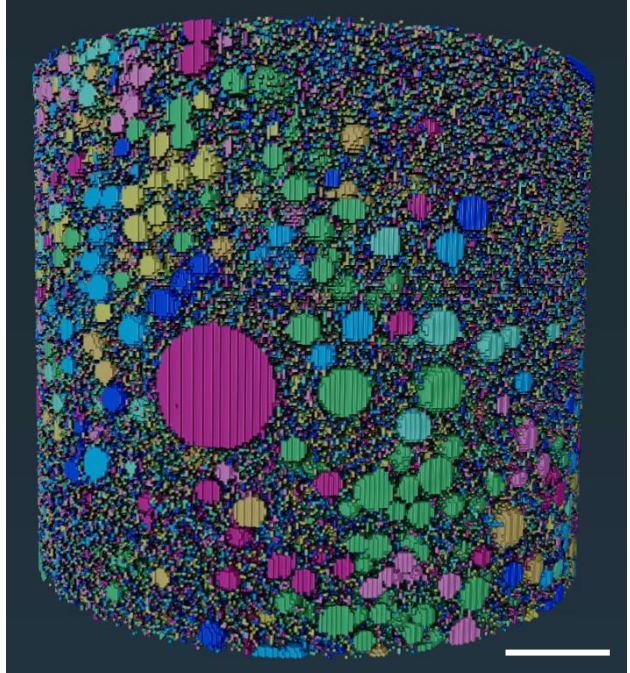
Fig. 44. Reproduction of PGS-80% scaffolds scanned through μ -CT, on yz (A), xz (B) and xy (C) planes.

A thresholding technique was used to identify the pores and windows within the scaffold, and to label them (Table 18).

Additionally, histograms with the distribution and frequency of pore diameters can be found in **Erreur ! Source du renvoi introuvable.**

Table 18. Thresholding strategies to identify pores and windows within the scaffolds starts on the correct segmentation of areas. An independent labelling technique was developed on the 3D reconstruction, where only 6 neighbouring points were considered for pores to be “connected”. Scale bars are 1 mm.

Thresholding		
PGSM	2D	3D
50%		
80%		

Labelling		
PGSM	2D	3D
50%		
80%		

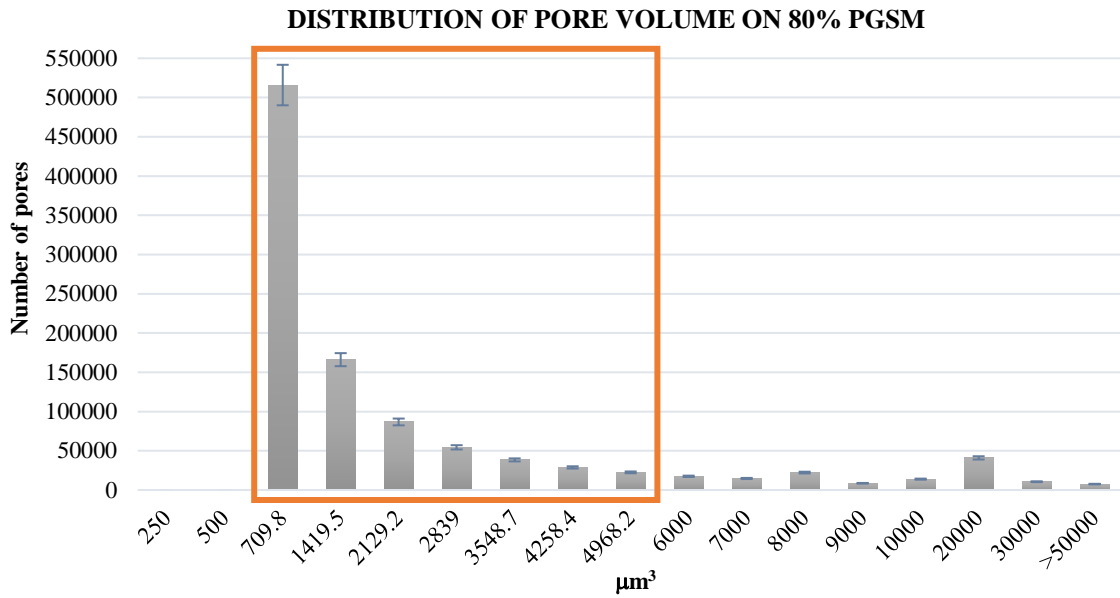
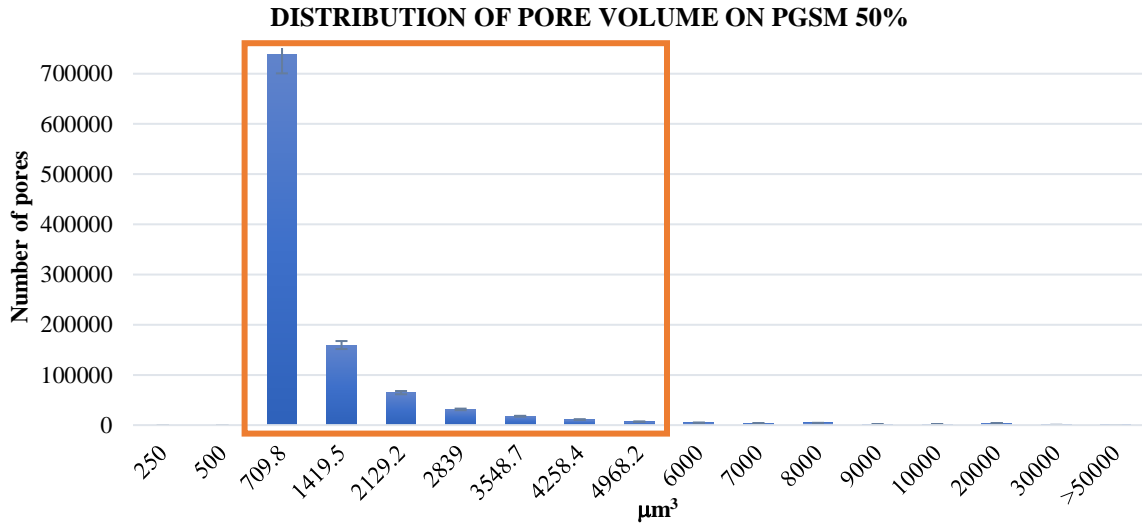


Fig. 45. Histograms showing the pore volume against its frequency for the 50% and 80% DM PGSM. Peaks related to the limits of the analysis are inside of the orange squares, the full explanation can be found on Chapter III. Fig. 28.

4.5. Discussion

4.5.1. Synthesis and methacrylation

Poly(glycerol) sebacate (PGS) synthesis and methacrylation is controlled by molar ratios, which can be seen as an advantage in maintaining reproducibility and scalability in the process [300]. During the synthesis, it is assumed that two thirds of the hydroxyl groups react with the glycerol/sebacic acid, leaving one hydroxyl group free [119]. Through the methacrylation, free hydroxyls react with the acrylate and methacrylate groups, functionalising the polymer chains of PGS [300, 299].

Photocurable polymers represent an advantage versus thermally cured polymers as the latter usually requires high temperatures, high vacuum, and long duration treatments [312]. Photocurable polymers are able to achieve cross-linking with a single source of light, and at reduced times [304]. As the side chains of the polymer are relatively long, the crosslinking process is facilitated. Additionally, such features allow photocurable elastomers to be cured whilst being in contact with biological material (*in vitro* and *in situ*) [299].

PGS was methacrylated at three different degrees (30, 50 and 80%) and characterised through proton H⁺ NMR and GPC. The NMR spectra showed the relevant peaks associated to glycerol, sebacic acid, and methacrylate groups for all three D_M, to a different extent. The calculated areas under the peaks demonstrated the proximity of the theoretical and the experimental degree of methacrylation. Number averaged molecular weights and polydispersity values of 1200-2800 $\frac{g}{ml}$ and 1.5-3.0 respectively coincide with the ones reported in the literature; as observed, higher molecular weights are also associated with higher levels of polydispersity [119, 299, 124].

According to the methodology, DCM is used to facilitate the polymer to dissolve into other reagents during the synthesis and methacrylation. It is also used to clean the crystalware of otherwise leftover polymer, increasing the yield of the process. Even small concentrations of solvent might also change the mechanical properties and in particular to increase the elasticity of the polymers, by acting as a plasticizer [283]. However, solvents can also obstruct the crosslinking process if they are left in excess [305]. The controlled extraction of solvent ensures the reproducibility of the methacrylated polymer solution, and the consistency of results down the line.

4.5.2. High Internal Phase Emulsions

As reported by *M.G. Pérez-García et.al*, polyHIPEs are attractive to a diverse range of applications due to their tuneable morphologies and mechanical properties [277]. This is achieved by modifying

the solvent and surfactant composition, the concentration of the external phase, and the polymerisation conditions. PCL polyHIPEs have been extensively studied by our research group [109, 301, 265] and therefore the manufacturing process was adapted for the production of PGS polyHIPEs. The internal composition of and external parameters for the W/O emulsions were varied to understand how they affected the stability and morphology of the emulsion. The proposed combinations were tried on both PGS 50% and 80% as the D_M will impact on the viscosity of the polymer solution, therefore making the emulsion more stable/unstable. Accordingly, the availability of methacrylic groups to be crosslinked increases as the D_M does, as reported for thermal and photocurable PGSM [119, 300].

Most of the emulsions with the lowest polymer ratio (and thus, higher water intake) were unsuccessful and divided during the emulsification process. This can be because the proportion of polymer was not high enough to create an optimal oil phase (ruled by viscosity). The viscosity is only ideal if the continuous and the droplet phase's miscibility encourages the formation of droplets (as internal phase), as mentioned in previous experiments with HIPEs [27]. In other words, the density of both the oil and water phase should be different enough to encourage the miscibility between layers, but low enough to promote the formation of droplets [21].

It was also found that the effect of photoinitiator was related to the mixing speed for a successful crosslinking. At low mixing speeds (350 rpm), all reagents are able to mix correctly, and emulsions were more stable during and after mixing (as well as their pore morphologies, as evidenced later on) [306]. Although the photoinitiator has no direct effect in the formation of droplets, away than on their contribution to the viscosity of the continuous phase (1.12 vs $1.3 \frac{g}{cm^3}$), it needs to be homogeneously distributed within the emulsion, to ensure a correct crosslinking [168]. On the line of the mixing speed, it was observed that smaller pores are created when the mixing speed is higher. This relies on the creation of droplets through the emulsification process; at higher mixing speeds, the dropwise-added water droplet will break into smaller droplets due to the shear force and the internal force of the oily phase [155]. Even if the stability of the emulsion is increased in this way, the pore size and pore packing will be compromised.

As mentioned above, the leftover solvent affected the stability of the emulsions. To explore this on a deeper level, different amounts of photoinitiator and mixing speeds were used to manufacture emulsions with three different polymer:DCM ratios. As expected, emulsions with lower volumes of photoinitiator did not crosslink. When UV light is irradiated over a solution containing photoinitiator,

the monomer is crosslinked by a chain reaction. The yield and rate of polymerisation is affected by the type of photoinitiator, but also by its availability, therefore a minimum volume of photoinitiator is required [168]. An optimum was found at 0.2g of photoinitiator for both 850 and 350 rpms, and for higher PGS:DCM ratios. However, high amounts of photoinitiator can also obstruct the crosslinking process [307]. Increasing amounts of photoinitiator will consequently increase the photoabsorption of the resin which will reduce the penetration depth of the light, and it will reduce the photocuring efficiency overall. Finally, it was found curing was depth dependent. It has been found by *Ligon-Auer et al.*, that light scattering of composites limits the depth of curing [308]; PGS HIPEs change their colour to white-yellowish when emulsifying, which will scatter to UV light reducing the curing of the material deeper into the scaffold, as reported in emulsion theory [168] and previously by *Sherborne et al* [309]. A higher intensity UV lamp was tried, with better curing results, but a more brittle final construct, due to the full evaporation of solvents whilst curing.

Successful emulsions characterised under SEM showed the wide range of pore and window morphologies obtained by varying internal and external parameters. Far from resembling round-like pores, PGS emulsions evidenced highly interconnected yet irregular pores at high mixing speeds (850 rpm). These features are comparable with scaffolds made by salt-leaching [300] and sol-gel/solvent evaporation [124] to introduce pores into PGS solutions. Contrarily, emulsions fabricated at 350 rpm resulted in round-like big pores, and small round-like windows. Specifically, at 0.20 and 0.35 g of photoinitiator and 80:20 polymer:DCM ratio emulsions presented a common HIPE morphology. This is also relevant as it aids the theoretical study of pores and interconnects [280].

It has been reported that the nature of the mould substrate against which a PolyHIPE material is prepared has a profound influence on its surface morphology and degree of adhesion to the mould [310]; polymers were cured against glass surfaces on top and bottom layers, and silicon (PDMS) moulds on the sides. As the area in contact with the cells was the top and bottom mainly, the contact with the glass and therefore the change in morphology was limited.

It was observed that the presence of some solvent could support the successful production of emulsions. From the above experiment onwards, it was decided that PGS solution be used without any extra DCM, to reduce the number of solvents used during the emulsification, because it could increase the risk of cytotoxicity when used in biological applications. Additionally, a further study was developed on the role of solvents in emulsions, as explored for PCL HIPEs in the literature [109].

HIPes for non-medical applications use non-polar liquid solvents. The addition of polar ones, such as water, can slow the reaction. As the solvent evaporates, the viscosity increases. This process is limited by the emulsion, which traps some solvent within the forming water droplets.

On this matter, the solvents used for the single and double solvent emulsion stability experiments were selected due to their presence in different points of the polymer production or the emulsification process, and as a reference from PCL scaffolds. DCM, DCE, chloroform and toluene solvents were trialled. Despite the wide use of organic solvents in the chemical and medical industries, most pose a risk when used for biomedical applications as solvent residues can be cytotoxic [311, 312]. For this reason, the use of biocompatible solvents like limonene [313] and p-cymene [314] is recommended for future work.

The stability point of single solvents was determined for toluene, chloroform, DCM and DCE. The criteria were the presence of defined pores, separation during mixing, and separation after mixing. Defined pores were found in 70.83% of the experiments (34/48), with only a few cases of non-porous and non-defined porous in toluene experiments, reinforcing the suitability of selected solvents to create quasi-stable emulsions.

Solvents are added as porogenic supporters as they decrease the viscosity of the organic phase, which reduces the overall viscosity of the mix, allowing droplets to travel and distribute through the emulsion [294, 109].

As expected, solvent free emulsions were watery with no apparent difference between the oil and the aqueous phases, inverting into a water-in-oil-in-water (W/O/W) emulsion, as shown in literature for PCL [109]. Higher solvent volumes tend to produce division in scaffolds. Contrarily, emulsion separation during mixing was not frequent on solvent-added emulsions, however it was observed that some emulsions seemed to reach a water adsorption limit before the 3 ml of water was completely added. Theoretically, HIPes can be created with a higher volume as high as 99%, as long as the stability (or instability) of the emulsion allows it [306]. As emulsions are formed non-spontaneously and are thermodynamically unstable, the polymer and surfactant in the oily phase play a crucial role in stabilising the emulsion and allowing more and/or bigger droplets to be created. When the layers thin to a limit, effects like coalescence occur [140]. This was the case for the emulsions that separated during mixing, especially for most DCM and DCE emulsions at higher polymer:DCM ratios. Their limit was set at 1.5 and 2.5 ml of water for DCM and DCE respectively. Despite interruption of the water addition when the emulsion appeared to have reached its limit of absorption, chloroform emulsions and higher volumes of polymer:DCM ratios still presented coalescence. Separation after

mixing was present in equal numbers (10/16) for all polymer:DCM ratios, with a higher incidence on higher volumes of solvents and in chloroform. Separation after mixing was higher for 90:10 emulsions, with all solvents except toluene.

The differences in densities for the oil phase for the three different polymer:DCM ratios is $\pm 0.0003 \frac{g}{cm^3}$, which is not significant. However, the densities between the different solvents varies from 0.86, 1.25, 1.33 and $1.49 \frac{g}{cm^3}$ for toluene, DCE, DCM and chloroform respectively, which creates a different emulsification dynamic, increased by the volume of solvent used, which is 1:1 versus the polymer one.

Results were also visually compared using LightSheet microscopy as it is a non-invasive technique that allows imaging in three-dimensions [315]. From both the experimental and imaging data, patterns can be addressed:

a) Chloroform:

Chloroform supported the creation of big pores and an increase in the continuous phase viscosity. The literature supports the role of chloroform in creating porous structures as this solvent increases the viscosity of the oil phase, increasing the difference in viscosity between the water and the oil phase [109]. At higher viscosities, the droplet transportation is limited (as explained by Stoke's Law), limiting the water distribution within the emulsion, hence the big pores [316].

As observed, at lower polymer:DCM ratios and higher solvent concentrations, bigger pores are found, at a size that may threaten the emulsion's stability. This could also be related to Ostwald ripening, where big pores grow at the expense of the small ones [317], and also to the literature reporting that by increasing the mixing speed, stable emulsions could form at high concentrations of chloroform [306].

b) Dichloromethane:

DCM is the solvent used to dissolve and process PGS. It has the higher densities of the solvents herein used ($1.33 \frac{g}{cm^3}$). The differences between phase densities and the viscosity of an emulsion limits the maximum internal phase volume that can be incorporated (water phase absorbed) [318]. As observed in most cases, after adding a certain amount of water (usually between 2 and 2.5 ml), the emulsion broke up and coalesced.

c) Dichloroethane:

DCE has a density between those of chloroform and DCM. From all the four solvents, DCE was the one with more consistent results: water absorption was optimal for most scaffolds and for all of them with 2.5 ml; and an increased emulsion viscosity. In all cases, DCE scaffolds showed round pores and windows, both of them easily distinguishable from each other in size and location. Finally, they seem to be highly interconnected. Little is found in the literature of DCE as a solvent for emulsions, but it can be presumed that its density has a positive impact on the overall density of the viscosity of the oil phase (lower) and the interfacial tension, behaving in a point in-between chloroform and DCM.

d) Toluene:

This solvent was the only one that would allow absorbance of all 3 ml of water without dividing during or after mixing. It has been reported in the literature that toluene increased the stability of PCLMA HIPEs due to the larger difference in polarity between water and toluene, and to the lower interfacial tension (linked to emulsion stability) of toluene in the oil phase, which also reduces the risk of coalescence [319]. A low interfacial tension will promote the dispersion of the internal phase; the work required to break droplets into smaller ones is small, hence the formation of smaller pores [320].

Additionally, it has been recommended that increasing the repulsion between droplets, and enhancing Gibbs elasticity, will help to avoid coalescence [140]. According to Gibbs Equation, the stability of a bubble depends on the elasticity of their thin liquid membrane. The higher the elasticity, the more stable the bubble will be [321].

This can be achieved by using higher or mixed surfactant films or by reducing the droplet packing, thus increasing the oil phase between droplets. It has been exemplified that toluene emulsions that possessed smaller pores tended to be more stable during and after mixing for all solution volumes and polymer:DCM ratios. At lower solvent concentrations, the size of pores and windows is similar; such small cavities can be the result of the amount of surfactant available in the continuous phase, a larger area versus the small-dispersed phase [318]. Despite the benefits of using toluene, pore morphology was not consistent nor exhibited defined round-like pores, mainly at higher solvent concentrations.

Scaffolds from all 48 experiments were left washing in water for 17 days to track their shrinkage. Tracking was done by measuring changes in both volume and density, as the former describes the overall shrinkage and the latter the removal of non-crosslinked polymer [322]. The maximum

shrinkage was observed on higher solvent concentrations, mainly from day 10 to 17, and for DCE, which had the biggest pores. Differences in densities over time were higher for 90:10 polymer:DCM ratio, 0.70 g of solvent, and toluene. These phenomena can be attributed to material shrinkage because of solvent elution from the scaffold. Although many polymers and experiments have reported material shrinkage due to drying [119, 319, 318], all of them refer to the change in structure when scaffolds have dried, but not to the effect of the solution in which scaffolds are washed and stored. However, this topic has been explored in depth for gels and colloids, prone to swelling and deswelling (shrinking) effects [323].

Results from the single solvent experiments allowed for determination of the stability region and the role of solvents in PGSM emulsions. However, as shown with PCL [109] and HEMA [324] emulsions, a combination of solvents can provide ideal support for the emulsification process and enable tailoring pore and window features. Toluene was selected as it allowed to absorb more water, and DCE for its round pore morphologies. Even though all created porous structures, only 0.25:0.75 DCE:Toluene kept its stability during and after mixing. This successful result has not been previously reported, while the literature comments upon the use of toluene and DCE independently [325, 326].

The mechanical properties of PGS have been reported for 50 and 80% DM; the experimental values are reported as 3.17 and 6.84 MPa respectively for bulk structures. On the other hand, the porous scaffolds were found to be 0.79 and 0.26 MPa. The literature agrees on ranges of tensile strength between 0.05 and 1.50 MPa. Additionally, previous reports noted an increase in the mechanical properties of PGS synthesised at higher temperatures (110 to 130°C), from 0.06 to 1.20 MPa of Young's moduli [327, 328]. In terms of compressive strength, bulk materials reported 5.09 MPa for 50% PGSM, which is consistent with other polymers like PCLMA and PLLA. However, at higher methacrylation degrees, the compressive strength could not be measured. The exponential increment of mechanical properties between 50 and 80% PGSM is significant, both in tensile and compressive tests, and in bulk and porous forms, and it was previously reported by Pashneh-Tala in 2018 [119]. This has also been reported in other methacrylated polymers like hyaluronic acid [329], and gelatine methacrylate hydrogels [330].

As previously stated, LightSheet microscopy is based on the contrast between scanned liquids/solids. Aiming to obtain clearer images, the refraction index (RI) of PGS was determined. Current methods to determine the RI of crystals follow Snell's Law [331] but proved inefficient for blocks of PGSM, even though it is translucent when photocrosslinked [299]. PGSM's RI was determined by immersing a block material into a variety of solvents. When the solution and the polymer had a close to similar RI, the polymer would start to "become invisible". This is because of the lack of optical scattering,

being reflection and refraction. The light rays pass through both materials keeping more or less the initial direction, treating all as a single material. Therefore, edges are only noticeable from the single reflection of some light rays over the surface of the material, but rays are minimally bent (refracted) or not at all [332]. Xylene was found to be the ideal solvent, with toluene close behind, with RI of 1.4958 and 1.4969 respectively [333]. These values are similar to the ones reported for methacrylated polymers [334] and are highly impacted by the molar refraction of hydroxyl and ester groups [335].

Finally, micro-CT scans were used to analyse the 3D constructs. Few big-round pores were found in the surface and centre of PGS 50%; the pore morphology is round for such pores, but less round-like for the rest, which also exhibit smaller cavities. Such types of micro-features have been associated with polymer collapse during polymerisation [277] with certain polymers, however, porous PGS structures report similar morphologies [300, 124].

Contrarily, the average pore in PGS 80% is more spherical, with a higher average size than PGS 50%. Such differences can be due to the individual polymer densities and the stability of the emulsions when polymerised. Variations in pore morphology were also found in porous albumin-based hydrogels at different degrees of methacrylation [336].

4.6. Conclusions

PGSM was successfully synthesised at 30, 50 and 80% degree of methacrylation. Its characterisation showed glycerol and sebacic acid peaks, and also those features associated with methacrylate groups. Molecular weights and polydispersity indices correspond to the ones reported in the literature.

Manufacturing elements to produce PGSM HYPEs were individually assessed to understand their role in the emulsification process. Mixing speed, temperature and source of light allowed the identification of ideal parameters: 350 rpm, room temperature, and 5 minutes at 100 W of exposure.

Afterwards, the relation between the volume of photoinitiator and polymer:DCM ratio was explored at different mixing speeds, being able to identify attractive micro morphologies (cavities); 0.2 g of photoinitiator, 350 rpm and 90:10 polymer:DCM ratio were considered the best.

A study on the role of solvents in the emulsions for single and double solvents also helped to determine the best combination of solvents to support the emulsification process. Even though each type of solvent contributed in a different way, toluene and DCE were found to benefit the emulsion, enhancing water absorption, and the creation of bigger pores.

SEM, LightSheet microscopy and micro-CT scanning were used to characterise and analyse pore sizes, morphologies, and interconnectivity. Such techniques were optimised and have deepened the level of understanding that can be obtained on HIPES and PGS HIPES for which literature is still poor.

Appendix: Determination of the refraction index

Digital microscopy techniques recommend using immersion liquids between the front lens of the objective and the cover slip to improve the optical resolving power whilst imaging. The oil that is commonly used has a refractive index close that of the glass, helping to reduce any reflections created from the object to the objective. Otherwise, reflection from the object could cause a loss of light and noise.

PolyHIPEs become white when the emulsion is created, due to the difference between the refraction index of the oil and the aqueous phase [337]. Aiming to mimic the benefits of the immersion oil, the refractive index of PGSM HIPEs was explored by using bulk PGSM blocks.

As PGSM is a semi-transparent polymer, the polymer solution was crosslinked with PI (5% w/w) and a source of UV light. The determination of the theoretical refractive index was attempted by emitting a sharp beam of visible light through the polymer block, illustrated in *Fig. 46*. The refraction index was then measured through Snell's Law [334], but failed due to the insignificant change of angle.

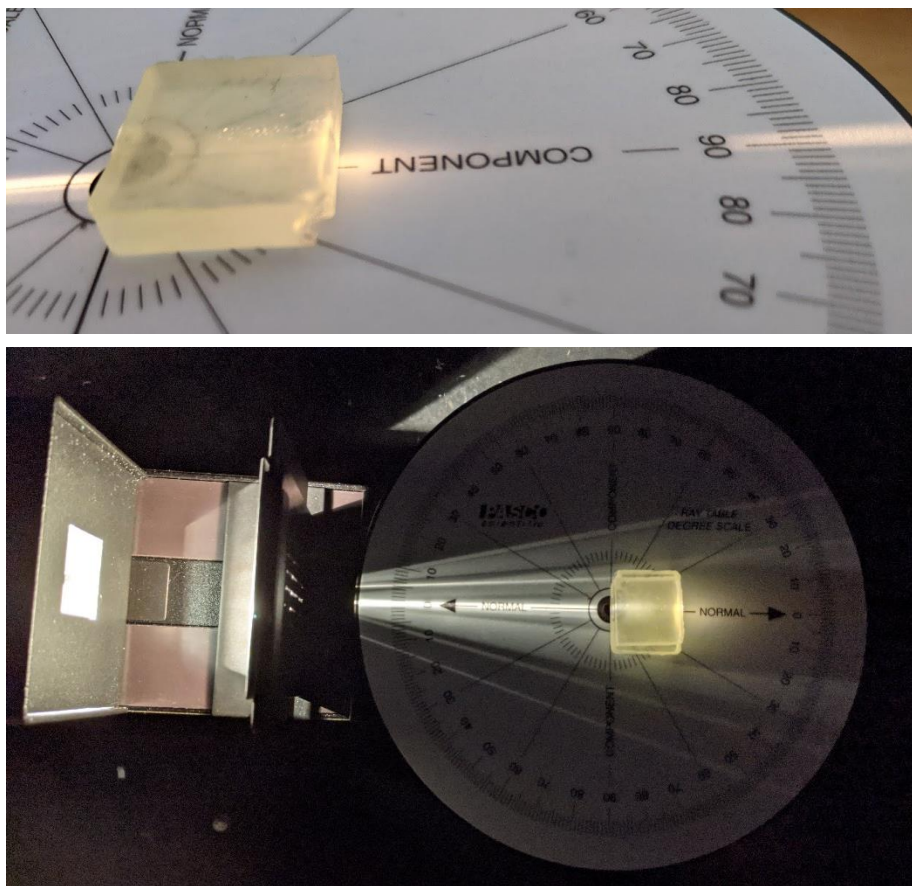
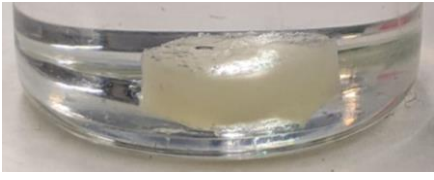
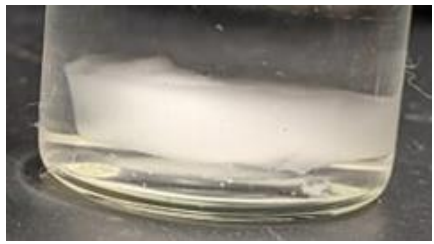


Fig. 46. The theoretical refractive index is calculated using a refractometer as shown above: a thin beam of light is directed to the block of material (bulk PGS polymer) and the angle of refraction is measured against the scale.

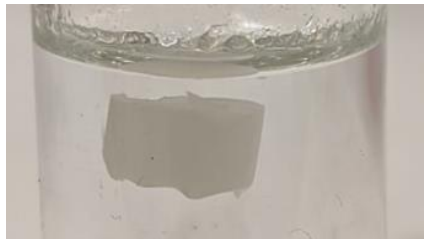
No significant change was observed on the scale therefore a more empirical approach was taken. Porous scaffolds were submerged in the chemical solutions displayed on *Table 19* for 5 days and left in a low-speed rocker, so all the internal pores were filled with the solution. Scaffolds were then imaged, and their transparency was assessed visually *Fig. 47*.

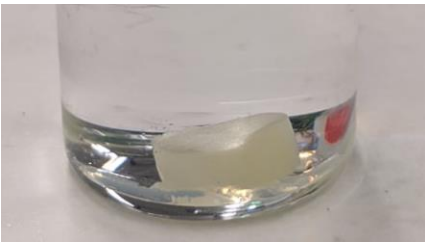
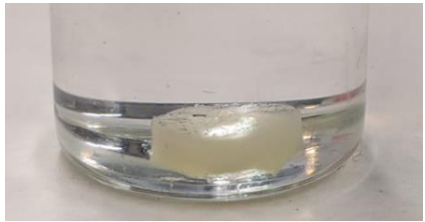
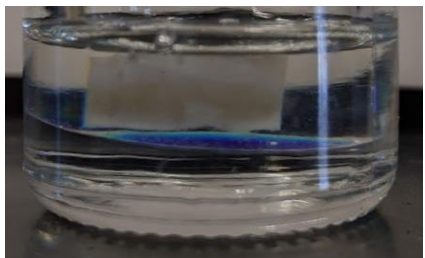
Xylene seems to be the closest, although the ideal refractive index solvent is still not completely known.

Table 19. Porous PGSM scaffolds were submerged on the reagents below (organised in ascendent order). The ID column is related to Fig. 47, with random scaffolds selected for visual assessment on day 3.

ID	Reactive	Refractive Index (n)	Effect on PGSM HIPEs
	Water	1.3100	
12	Acetone	1.3600	
9	Glycerol 25%	1.3600	
3	Glycerol 50%	1.3900	

	Glucose 5%	1.3357	
	Glucose 10%	1.3448	
	Glucose 15%	1.3532	
2	Glucose 20%	1.3584	
	Glucose 25%	1.3668	
7	Glucose 35%	1.3918	

6	Glucose 45%	1.4018	
5	Glucose 50%	1.4117	
	Glucose 70%	1.4380	
1	Glycerol 75%	1.4400	
11	Chloroform	1.4400	
	Glucose 80%	1.4510	

	Glucose 90%	1.4640	
4	Mineral Oil	1.4700	
10	Glycerol 99%	1.4700	
8	Paraffin Oil	1.4800	
	Toluene	1.4969	
	Xylene	1.5054	

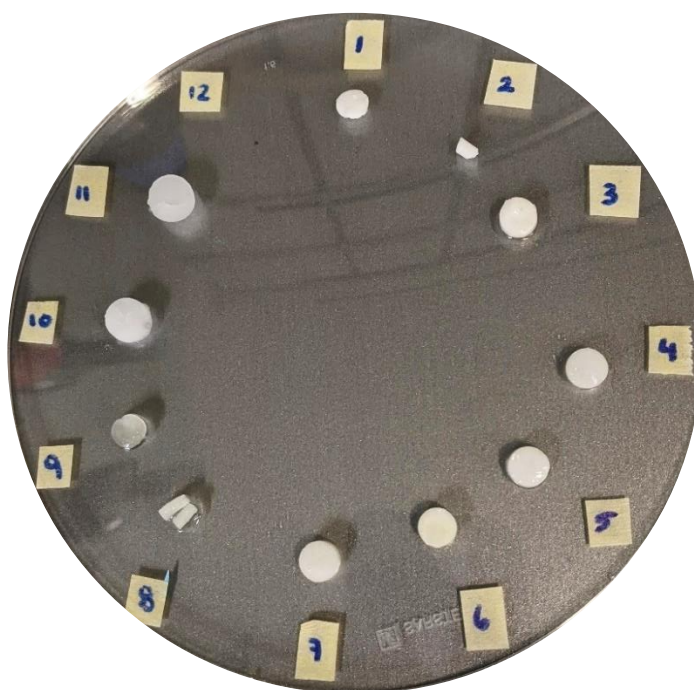


Fig. 47. Roulette of scaffolds exposed for 5 days to the reagents on Table 19. The effect on transparency of the scaffolds is reflected on the order of the labels (1 and top right being the less transparent).

Chapter V: PCLMA - PGSM polyHIPEs

5.1. Introduction

Polycaprolactone (PCL) and poly(glycerol) sebacate (PGS) have been extensively reported on as biomaterials, specifically for soft tissue engineering [108, 109, 299, 265, 119]. Both materials are characterised by their biodegradability and their ability to easily blend with other polymers [338, 339], hydrogels [114] [293] and particles [291] [340] [341].

PCL is a robust polyester with a Young's Modulus of 200-230 MPa [112], will degrade within a couple of years [112], an elongation at break of around 300% [342], and a thermal stability that allows it to be extruded, moulded, emulsified, and printed. PGS, on the other hand, has a Young's Modulus between 0.05 and 6 MPa [342], a degradation period of under one year, an elongation to break of up to 500% [343] and the possibility of being crosslinked through several mechanisms [300].

Both materials have been reported as biocompatible for cell work *in vitro* [344, 134], however only PCL has been trialled *in vivo* [345, 346].

The last couple of years have seen an increase in the publication of work with blends of PCL and PGS for soft tissue engineering applications, including the addition of particles of interest like hydroxyapatite [347] and bioglass [348]. Electrospun scaffolds for heart valves were manufactured for a controlled degradation that could allow the mechanical properties to be preserved, whilst allowing ECM to be deposited and replacing the material simultaneously [349]. This was similarly explored years after it was found that the PGS also increased PCL wettability on PGS/PCL/CQD (carbon quantum dots) electrospun scaffolds [350]. The controlled degradability has also been explored for cartilage tissue engineering by creating salt leached PCL/PGS scaffolds [351] and it was found that during the degradation of PGS on the surface of the scaffolds, the crystallisation ability of PCL increased, enhancing mechanical properties for longer time [349].

This chapter explored PCL and PGS as a blend for the creation of HIPEs of interest to osteochondral tissue engineering. As the structure of the osteochondral units is formed by two main layers previously matched to PCL (bone) and PGS (cartilage), the blend of polymers could serve as the interlayer or an optimised PGS layer.

5.2. Aims and objectives

The aim of this chapter is to manufacture PCL-PGS HIPEs that can be used as the interlayer between bone (PCL) and cartilage (PGS) layer, or as an optimised cartilage layer, in the construction of osteochondral tissue engineering. For such, the following steps are required:

- i) Developing PCL-PGS polyHIPEs formulation for stable emulsions.
- ii) Determining mechanical properties of PCL-PGS bulk and porous structures.
- iii) Analysing the PGS HIPE morphology using digital imaging and scanning.
- iv) Developing PCL-PGS bilayer polyHIPEs.

5.3. Materials and Methods

Main materials and methods have been outlined in Section 2; specific methodologies for both polycaprolactone, poly(glycerol) sebacate and polycaprolactone – co- poly(glycerol) sebacate are contained in Section 3.3 of Chapter 3.

5.3.1. Bulk PCL:PGS for mechanical testing

Bulk monoliths were created by mixing a known solution of polymer A and polymer B (PCL and PGS respectively), for at least 2 hours at 375 rpm and room temperature, with 5% of photoinitiator, in a dark vial. Porous samples were created by firstly mixing both weights of polymers as previously described, and then creating emulsions according to *Chapter 2, Section 5.3.2*. Mixes were then injected into PDMS moulds designed in accordance with ASTM D638-10 and reduced by a factor of 3.83 so it could fit the maximum sample size of the testing machine. Bulk and porous polymers were cured under a UV lamp for 5 minutes on each side.

Bulk samples were clamped into a Mecmesin OmniTest single-column materials tester using a 25 N load cell for porous samples, and a 250 N load cell for bulk samples. Porous samples were fragile: therefore, a cardboard support similar to the one described in *Chapter 2* was used. Samples were tested at a speed of 6 mm/min and the test was left until the point of break. Young's modulus was determined using the linear region of the load-displacement curve.

5.4. Results

5.4.1. PCL – PGS Blends

5.4.1.1. Homogeneity of PCL-PGS mix

Bulk polymers samples were created as a first trial of blending two methacrylated polymeric solutions together, polycaprolactone (PCL-HM) and poly(glycerol) sebacate (PGSM-50%). Measured weights of both materials were mixed at 375 rpm and room temperature for 5 minutes with 5% w/w of photoinitiator. Curing was developed under a UV lamp for 5 minutes on each side. Even though the mixture was visually homogeneous, irregularities during the mechanical testing (values between 0.52 and 8.64 MPa) determined that a more thorough mixing was required. The uneven distribution of polymers and photoinitiator is observed in Fig. 48.

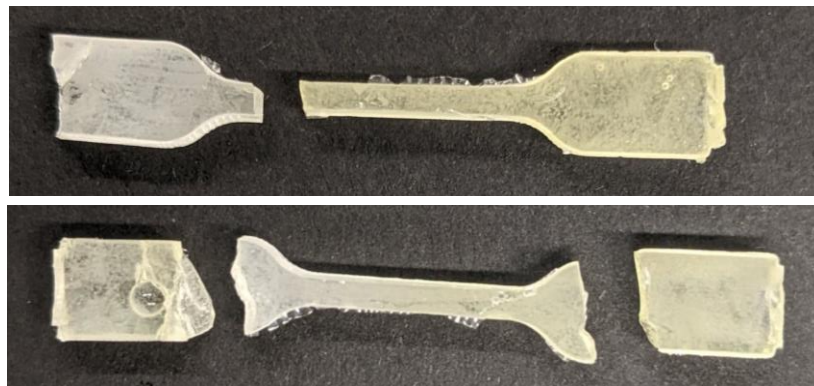


Fig. 48. Non-homogeneous PCLMA – PGSM blends for tensile testing. This is evidenced by the difference in photoinitiator mediated crosslinking (even if they were exposed to the same height and distance from UV light), and the uneven break of the dogbones (usually closer to the middle of the thin layer).

5.4.1.2. Mechanical testing of bulk PCL-PGS mix

Dog-bone samples were manufactured to determine the Young's Modulus of PCL-PGS mixes, as evidenced in Fig. 49. The values of pure PCL and pure PGS were found to be on the extremes of the ones reported for PCL-PGS blends, as expected. Additionally, a linear trend was observed on PCL-PGS blends as the PCL content increases. It is important to note that the Young Modulus for PGS 80% DM was 6.84 MPa, that is higher than 05PCL-95PGS, 10PCL-90PGS, 15PCL-85PGS and 20PCL-80PGS blends.

5.4.2. PCLMA-PGSM polyHIPEs

5.4.2.1. The role of solvents in emulsion stability

As both PCLMA and PGSM scaffolds discussed in Chapter III and IV use different types and volumes of solvent, the combinations shown in Table 20 were developed to determine the solvent that would generate a more stable emulsion, and an attractive pore morphology.

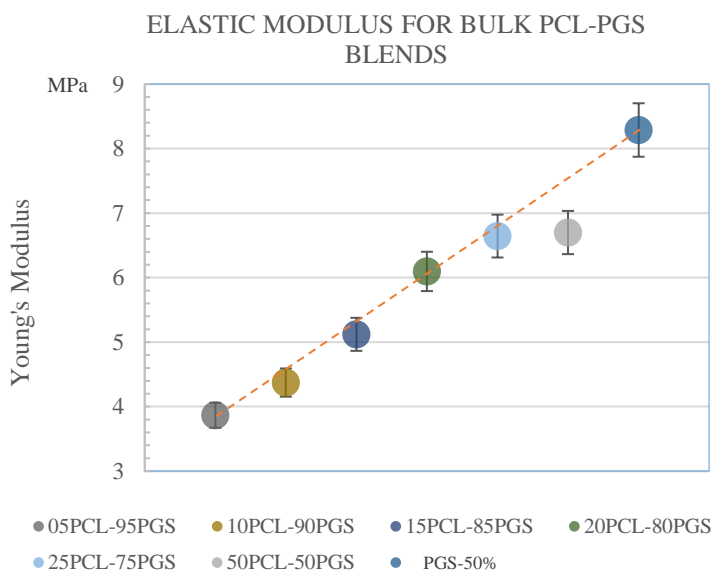
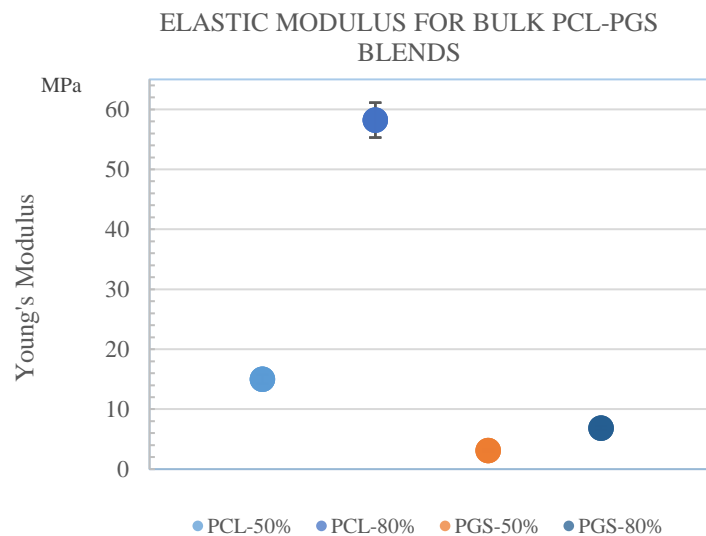


Fig. 49. Mechanical testing (tensile tests) was performed on PCL-PGS methacrylated polymers. Results for pure PCL-HM, PCL-80%, PGS-50% and PGS-80% have been included as reference.

According to Table 20, the combinations that proved to be more stable were as below. The viscosity of such emulsions is also reported and was tested by tilting the vials and observing the flow of the polymer.

Table 20. Successful (stable) emulsions and their viscosity observed with naked eye.

Polymer	Solvent	Viscosity
50 PCL : 50 PGS	4DCE:6T	Medium viscosity
50 PCL : 50 PGS	6DCE:4T	High viscosity
50 PCL : 50 PGS	4CHL:6T	High viscosity
75 PCL : 25 PGS	4DCE:6T	Medium viscosity
75 PCL : 25 PGS	6DCE:4T	Low viscosity
75 PCL : 25 PGS	4CHL:6T	Medium viscosity

To understand how the stability of the scaffolds relates to the structure of the pores and windows, SEM imaging was performed on all 12 combinations on Table 21. Results are shown in Fig. 50.

As observed in images 1-4, emulsions with higher volumes of PGS show a less organised HIPE structure, with random big spherical pores of up to 100 μm (mean range between 57.37 and 98.03 μm) and smaller pores with mean values between 14.39 and 23.44 μm . Windows within the pores are not easily identified and resemble cracks in the pores. Image 4 show random pores significantly bigger than the rest, denoting Ostwald ripening or coalescence resulting in Ostwald ripening.

Emulsions 5-8 are more balanced in terms of pore morphology, with a more homogeneous distribution of big pores through the scaffold, with mean sizes ranging between 15.08 and 66.61 μm . In such emulsions, smaller pores are found between 4.74 and 15.61 μm . Both big and small pores also present small and abundant round windows (>20 per pore).

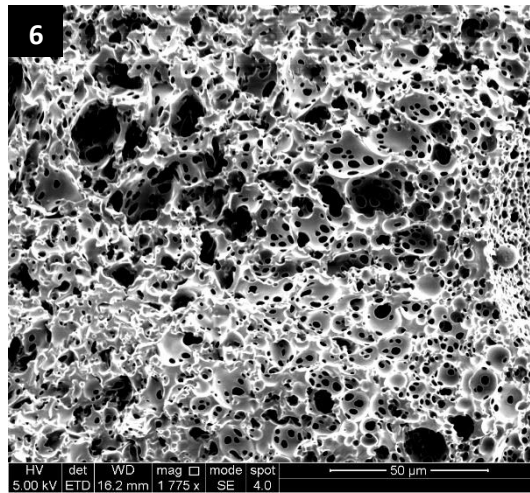
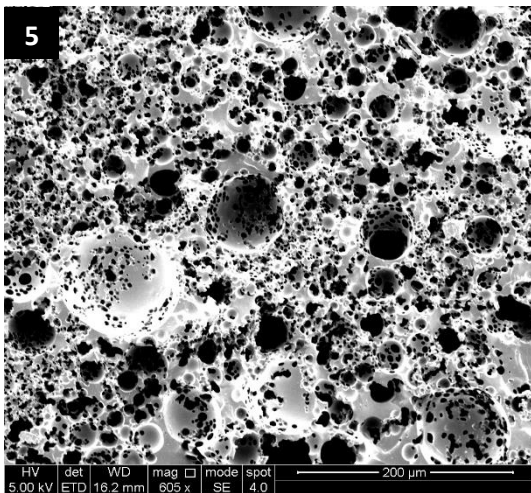
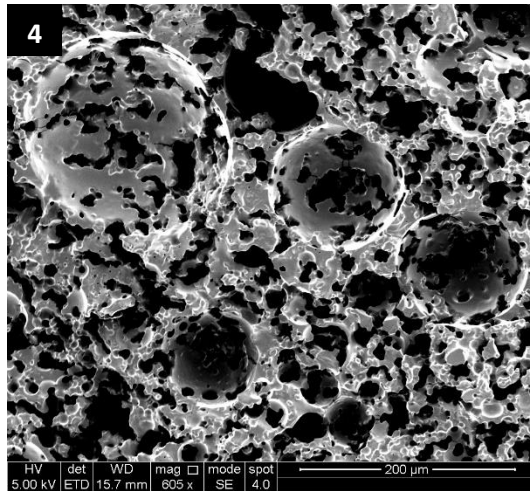
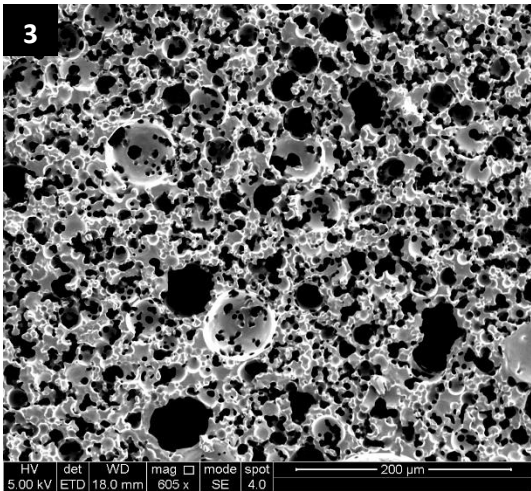
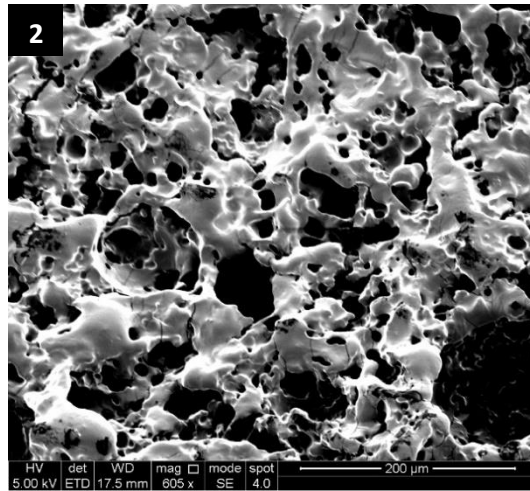
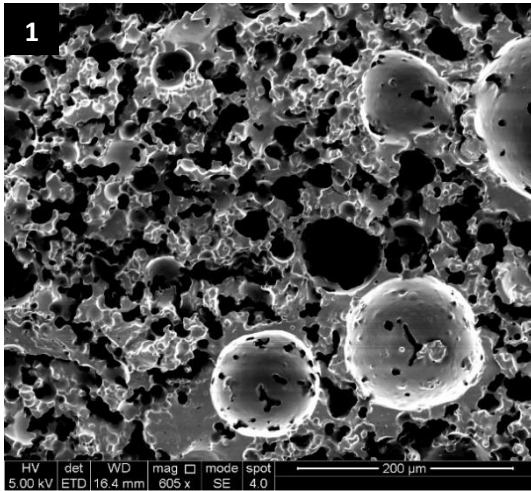
Emulsions 9-12, with higher volumes of PCL, showed spherical well-defined pores. The difference between big and small/medium size pores is smaller (magnitude between 2 and 3); big pores have a mean range from 19.26 and 26.59 μm , and smaller pores from 6.42 and 9.37 μm . The windows are less numerous than on 50PCL:50PGS emulsions (<20 per pore) and with larger diameters (3.53 $\mu\text{m} \pm 2 \mu\text{m}$).

Bigger pores are observed on higher quantities of chloroform (6CHL:4T) whilst more stable emulsions are present at higher volumes of toluene and DCE (4DCE:6T and 6DCE:4T).

Finally, at higher ratios of PGS, the difference between big pores and small/medium pores is higher (3 or 4 times), associated with less homogeneous pore morphologies.

Table 21. Combinations of PCL:PGS at 25:75, 50:50 and 75:25 to identify stable emulsions and the impact of type and solvent ratio (chloroform, toluene and DCE). The quantities in brackets in the last column, represent the volume of water that could not be absorbed by the emulsion or that was released during the emulsion coalescence.

ID	Polymer (0.5 g)	Surfactant	Solvent (100% w/w)	Photo initiator	Stirring	T	Water intake	UV lamp treatment	Divided during (DM) or after mixing (AM)
1	25 PCL : 75 PGS	10% w/w	6CHL:4T	5% w/w	350 rpm	T _{room}	3 ml	5 min p/side	DM, AM (1ml) Coalescence
2	25 PCL : 75 PGS		4CHL:6T						AM (0.5ml) Coalescence
3	25 PCL : 75 PGS		6DCE:4T						DM,AM (1ml) Coalescence
4	25 PCL : 75 PGS		4DCE:6T						AM (0 ml)
5	50 PCL : 50 PGS		6CHL:4T						AM Phase inversion
6	50 PCL : 50 PGS		4CHL:6T						N
7	50 PCL : 50 PGS		6DCE:4T						N
8	50 PCL : 50 PGS		4DCE:6T						N
9	75 PCL : 25 PGS		6CHL:4T						AM Phase inversion
10	75 PCL : 25 PGS		4CHL:6T						N
11	75 PCL : 25 PGS		4DCE:6T						N
12	75 PCL : 25 PGS		6DCE:4T						N



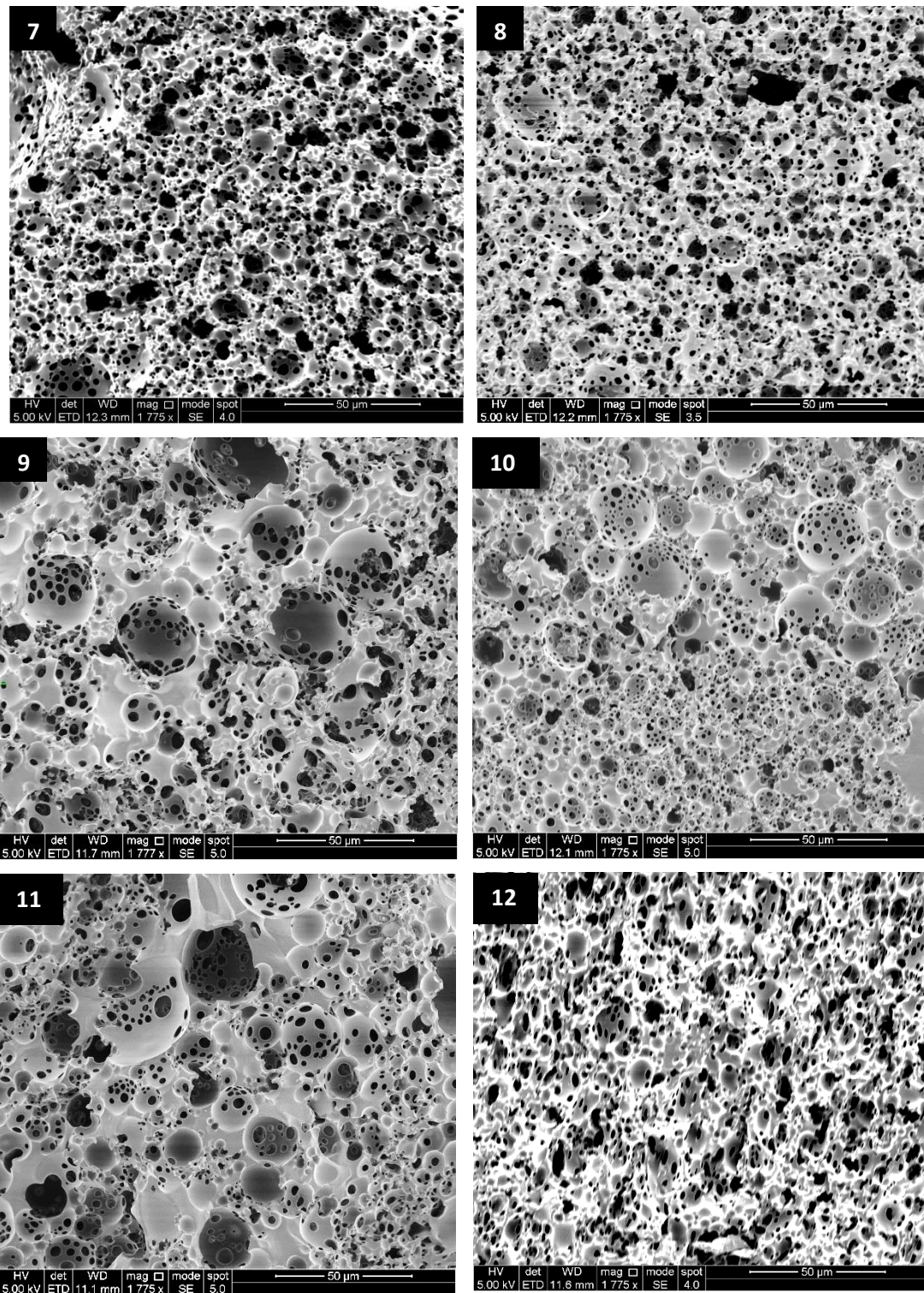


Fig. 50. SEM images of cross sections of PCL-PGS scaffolds. Images are labelled as 1-12 according to their recipe (Table 21). Images 1-5 were taken at 605x and 6-12 at 1775× of magnification. The change in magnification is for pore morphology and average size to easily appreciated.

5.4.2.2. Scan of the 3D structures

A 50PCL:PGS50 scaffold was scanned under micro-CT to understand the pore morphology and distribution. A thresholding technique was used to identify the pores within the scaffold. A reconstructed image of the porosity within the scaffold is shown in Fig. 51.

It was found that pores were indeed interconnected on the horizontal plane. This was observed by analysing the 2D slices (xy plane) of the reconstruction. As shown in Fig. 52, areas with the same colour are connected to each other and labelled as independent when they have at least 6 neighbouring points. It was also observed that pores are interconnected in the other axis. A pore of big diameter was selected and observed through the several xy axis, observing how some of its networked areas changed (increased or disappeared) as the point of observation moved (Fig. 52).

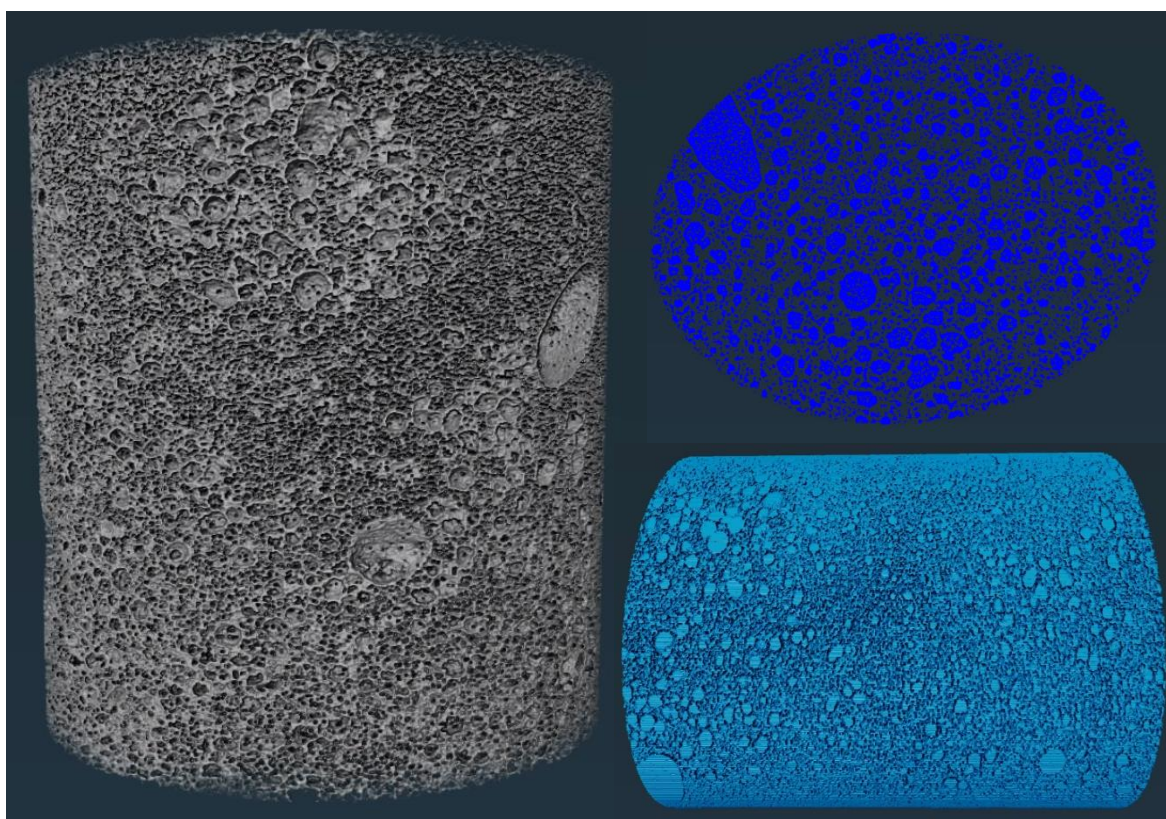


Fig. 51. Micro-CT reconstruction of a 50PCL-PGS50 polyHIPE. A) 3D structure of the scaffold. B) Thresholding technique on 2D to identify pores and windows. C) Volume rendering of the threshold showing pores within the scaffold.

The histograms in Fig. 53 shows the distribution of pores on two dimensional planes (xy) for PCL:PGS blend scaffolds. The individual average pore size is $40.039 \mu\text{m}$, with a minimum of $8.92 \mu\text{m}$ and a maximum of $257.76 \mu\text{m}$. The values above $300 \mu\text{m}$ are related to higher number of neighbouring

pores, which are then counted as individual pores and overreported. This was confirmed by targeting such pores on Avizo. This is also evidenced in the coloured zones of Fig. 52.

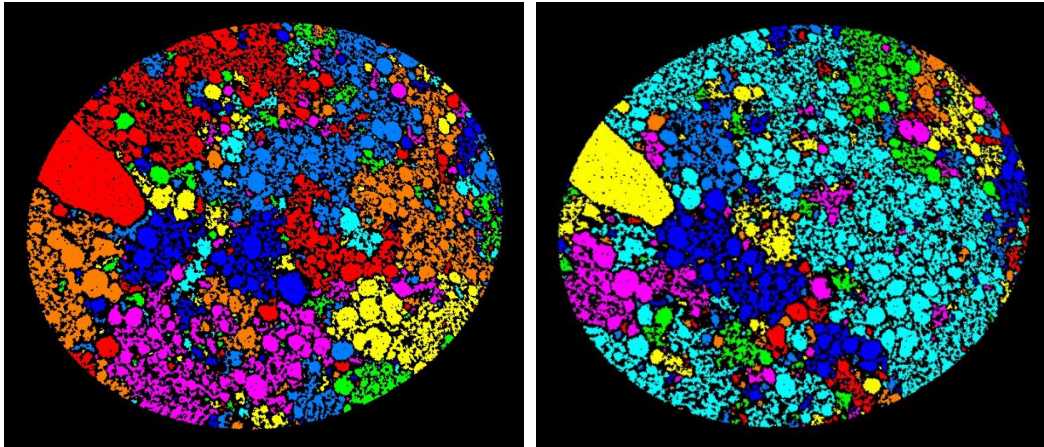


Fig. 52. 2D micro-CT scans of 50PCL-PGS50 polyHIPE. Each image represents a different slice of the reconstructed scaffold. Regions with different colours exemplify the connection between pores on the xy axis. Additionally, pore interconnectivity can be observed between both images by tracking the big pore on the top left side; changing slides show how interconnectivity varies (increases-decreases) over the y axis.

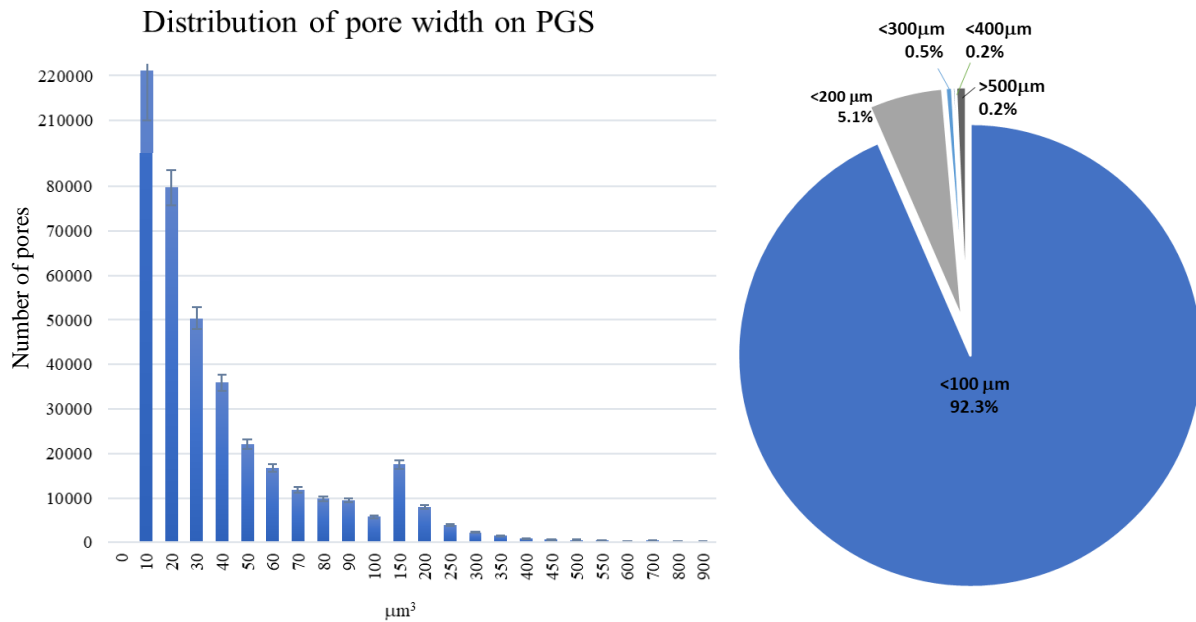


Fig. 53. Histogram and pie chart showing the pore width distribution for PCL:PGS blend (50:50).

5.4.3. PCL – PGS Bilayer Scaffolds

50% PCLMA and 80% PGSM polymer solutions were used to produce two stable emulsions that were then poured one over another before being cured together under the UV light source for 5

minutes on each side. Initially, only the PGSM layer was stained with blue food colourant to differentiate the emulsions. Images under the visible eye and digital microscope can be observed below.

Afterwards, the bilayer scaffolds were produced and independently dyed; blue for PGS and red for PCL solutions. The scaffolds were then sliced using the vibratome and imaged under the digital microscope as illustrated on Fig. 54 and Fig. 55.

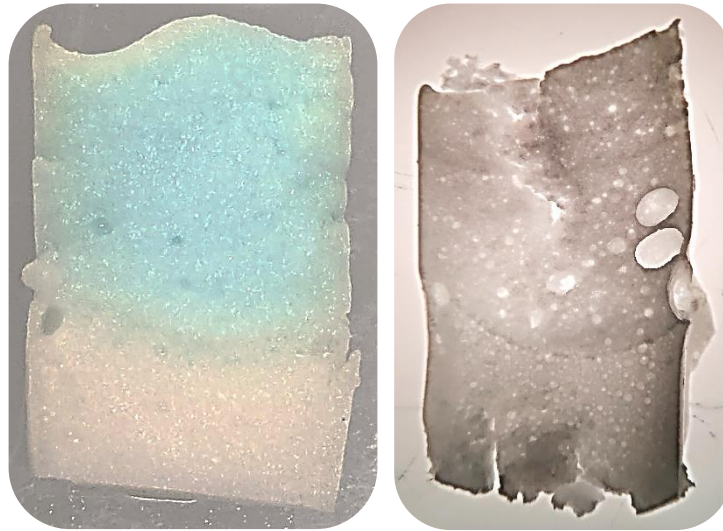


Fig. 54. PGS – PCL bilayer scaffold imaged at naked eye, and digital microscope. 80% PGSM (top layer) has been dyed in blue to differentiate from the 50% PCLMA layer (bottom). Difference in porosities is easily observed.

Compressive tests were developed on the bilayer scaffolds using a 25 N load cell and a rate of 0.1 mm/min. The compressive force was exerted on the top layer (PGS – blue), simulating how the implant would receive and bear loads in the body. The maximum load before break was 6.387 N, and the Young Modulus 0.215 MPa. It was observed that the load was mainly borne by the PGSM layer, whilst the break occurred on the PCLMA layer. Stages of the test are illustrated in Fig. 57.

Some large holes can be found at the interface, which can be attributed to an early collapse of the scaffold, or by the trapping of air bubbles through the layering process (PCL layer over PGS layer inside of a 2ml syringe). The latter could explain why those pores cannot be found on Fig. 54.

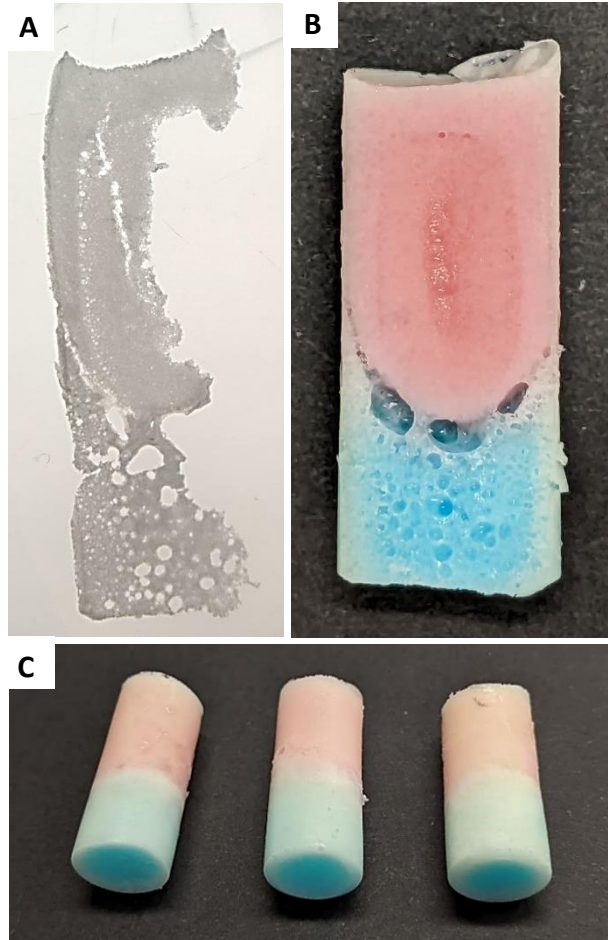


Fig. 55. PCL-PGS bilayer scaffolds (C) sliced using a scalpel (B) and a vibratome (A) observed under the digital microscope. The top layer (red) is made of 80% PGSM and the bottom (blue) of 50% PCLMA.

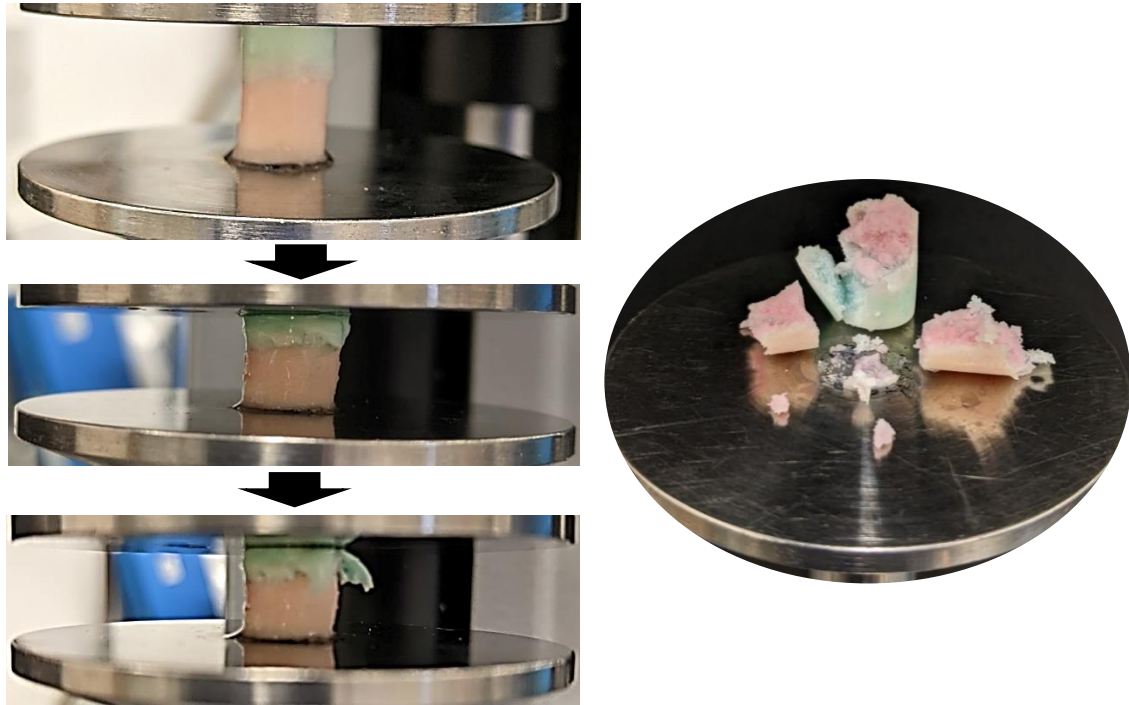


Fig. 57. Compressive tests on PCL-PGS bilayer scaffolds. Compression was made using a 25 N load cell and at a rate of 0.1 mm/min. The red layer is 80% PGSM and the blue layer is 50% PCLMA.

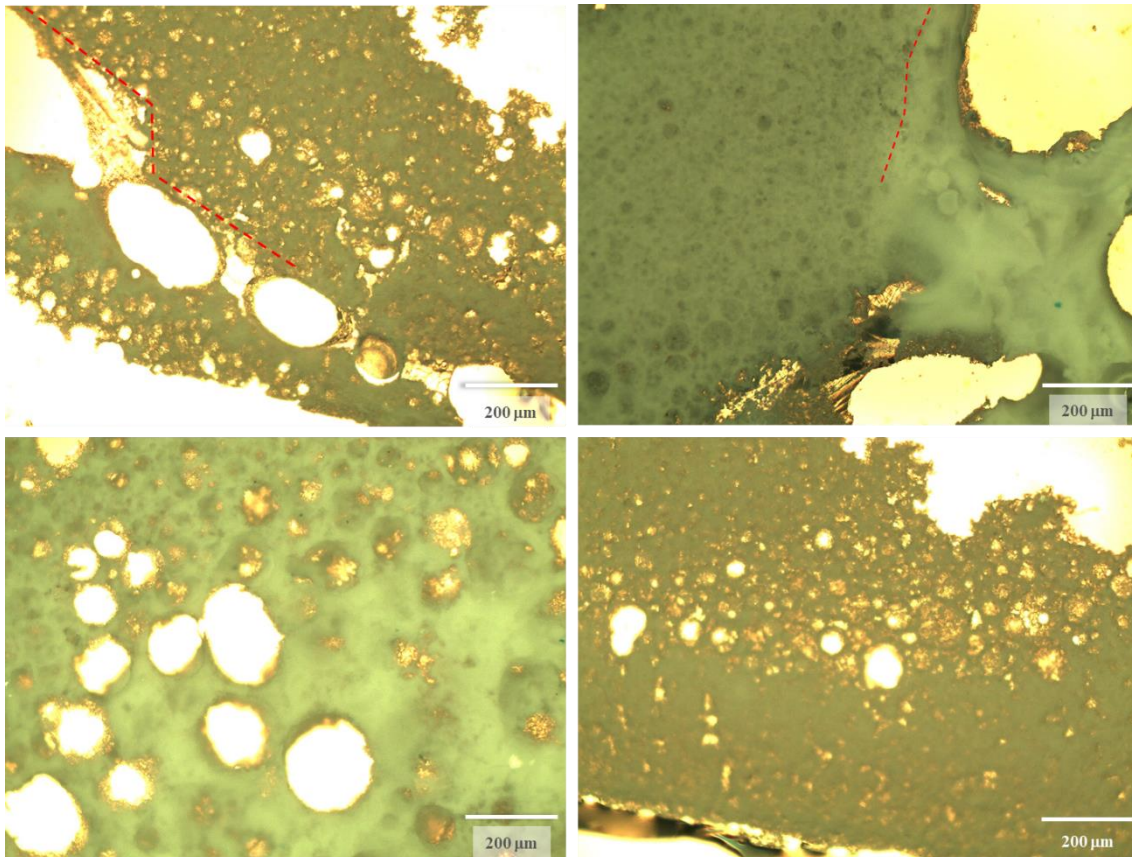


Fig. 56. Digital microscope images on the interlayer between PCL-PGS bilayer scaffolds (A,B), 50% PCLMA layer (C), and 80% PGSM layer (D). Magnification used was 4x and scale bars are 200 μm .

5.5. Discussion

PCL and PGS are biodegradable polyesters that have been individually and conjunctively proposed for soft tissue engineering applications due to their tuneable chemical and mechanical properties, and their biocompatibility with biological systems *in vitro* and *in vivo* [352].

PCL and PGS have been blended chemically and mechanically. In the first case, a co-polymerisation is performed during the synthesis where glycerol, sebacic acid and ϵ -caprolactone polymerise through a polycondensation reaction at high temperatures and under a nitrogen-rich environment, followed by a purification process [353]. Through the second method, PCL and PGS are dissolved individually or together into a small volume of solvent and mixed at high speeds for 4-12 hours [354, 355, 356]. As PGS is usually thermosensitive, high temperatures are not recommended, but a few groups have used sonication [357]. As demonstrated in literature, thorough mixing is required, otherwise results like the irregularities reported in the results are obtained. Successful blends are considered “compatible blends” and are associated with the interfacial interactions between the two polymers [358].

Polar solvents are used to react, wash, and purify the polymer solution, but novel approaches to PCL-PGS co-polymerised and blends are looking to reduce the variety and total volume of solvents due to environmental and biocompatible issues. For example, PCL-PGS electrospun scaffolds for cardiac tissues used acetic acid as a benign solvent [359]. Finally, crosslinking has been done through vacuums and high temperatures but no evidence of photocrosslinkable PCL-PGS scaffolds have been found.

The mechanical properties of PCL-PGS were determined through tensile tests, using bulk samples of PCL HM and 80% DM, and PGS 50% and 80% DM as reference. All blends were developed with PGS 50%. As expected, the values of 25PCL-75PGS, 50PCL-50PGS, and 75PCL-25PGS were located in-between the reference points. The elastic Modulus (Young’s Modulus) of PGS was reported to be around 0.3MPa, which coincides with non-reinforced PGS [357, 354]. Similarly, PGSM, and PCLMA-PGSM values had Young’s Modulus between 3 and 6 MPa, as reported in electrospun matrices [357, 355]. Also, it was observed that a Young’s Modulus of PGS 80% was above those reported for PCL, PGS, and PCL-PGS blends, underscoring the impact of the degree of methacrylation on the mechanical properties [119]. Even if this makes sense from the mechanical point of view, it was noted by *Sant et. al.*, that during the degradation process, PGS on the surface of

the scaffold would break apart, increasing the crystallisation ability of PCL and thus enhancing its mechanical properties for a longer time [355].

The big difference in tensile strength of pure PGSM between low and high degrees of methacrylation could be related to the hyperbranched molecular structure of PGSM. When the molecular weight is high (7,000 Mw) and the degree of methacrylation is low, there might be less opportunity for these molecules to crosslink with each other. An internal crosslink could obstruct hidden methacrylate groups from reacting, affecting the homogeneity of the crosslinking [119].

Porous PCL-PGS constructs have been mainly produced using 3D printing [352] and electrospinning [354, 355, 356] techniques for controlled macro and microporosities. Electrospinning allows for the creation of ultrafine fibres, whilst 3D printing enables robust and homogeneous structures to be produced. However, emulsion templating has a benefit in that it allows high porosity, high interconnectivity and high tunability [276] of cavities with large superficial area to be achieved, distributed in various axes (spherical volume).

As previously discussed, the temporary stability of an emulsion plays a decisive role for manufacturing HIPEs that can be cured into polyHIPEs [168]. PCLMA and PGSM were individually emulsified using different solvents: chloroform/toluene and toluene/DCE (*Chapter III and IV*). Different formulations combining abovementioned solvents were performed to identify the ratio and binary solvent composition that better suited the polymer blend. The combined viscosity of the polymers had to be matched with the ratio and volume of solvents, so that the density of the oil phase allowed the formation of desired droplet sizes and morphologies [155]. This was only obtained in emulsions with at least 50% PCL and could be explained due to the variation of densities between the PCL-PGS mixes (~3.8% per ratio) and their impact on the formation of a stable emulsion, especially when mixed with low density solvents. Even though most experiments reported blends of at least 50% of PCL, some of the elastic patches created by *Huang et al.* showed phase separation, remarking the difference between polymer solutions [352].

Successful emulsions were selected due to their ideal viscosity (medium to high [109]), and attractive morphology (round and interconnected pores). The SEM images showed different distribution of pore and windows sizes, and scaffold homogeneity. Scaffolds with lower PGS showed bigger pores than any other PCL-PGS ratio (>200 μ m), and a high interconnectivity between pores. The pore morphology at first look does not seem to be round, however, if it is observed to a closer magnification, it can be seen that smaller pores and windows within the big pores could have coalesced between each

other, forming elongated cavities with semi-round/oval morphologies. The presence of this internal (and somehow non-disruptive) emulsion phenomena could be associated with shear stress created by the mixing and the thickness (high viscosity) of the oil phase [137]. All these emulsions divided during and/or after mixing due to coalescence and in all cases, only 2 ml of water were absorbed. In such experiments, no new droplets would be created, even though there was still enough oil phase to be “stretched” [360]. This could be further confirmed by the analysis of surface area using micro-CT scanning.

Emulsions 50:50 were quite similar in terms of pore sizes and distribution, even though at higher volumes of chloroform, bigger pores were formed. The size of the windows was kept similar for all 4 experiments, and the pores are tightly packed. Finally, emulsions with lower PGS ratios showed an increase in the overall pore size, with a higher number of windows per pore. The morphology of the pores is characteristic of PCL and is tightly packed, especially at higher volumes of toluene.

As hypothesised for PGS solvent experiments, emulsions developed with DCE and toluene showed higher internal phases and greater interconnectivity between pores, related to a full absorbance of the 3 ml of water. On the contrary, all emulsions with higher ratios of chloroform showed a type of emulsion phenomenon after mixing, being coalescence or phase separation. Phase separation has been hypothesised as a next step for coalescent emulsions [361]. Phase inversion describes the conversion between the oil and water phase by either a kinetic or a thermodynamic basis [362]. This effect can occur in close-packed W/O systems that reach a limit of inner water droplets [360] and water diffusion between the inner and outer water phase, leading to the formation of microspheres [361]. Such microspheres were identified on the surface of emulsions 75:25 PCL-PGS emulsions manufactured with DCE and toluene and shown in Fig. 58.

Finally, micro-CT scans of 50:50 PCL-PGS scaffolds showed a homogeneous distribution of pores on the surface and the inner layers of the construct. The thresholding and labelling of pores also allowed for confirmation of the interconnectivity of pores on both xy and yz axis. This was done by tracking big pores through 2D pore labelling y axis, and the interconnected areas on the same plane (xy axis). Such observations were also shared by several research groups working on porosities in mineral and rock formations [363].

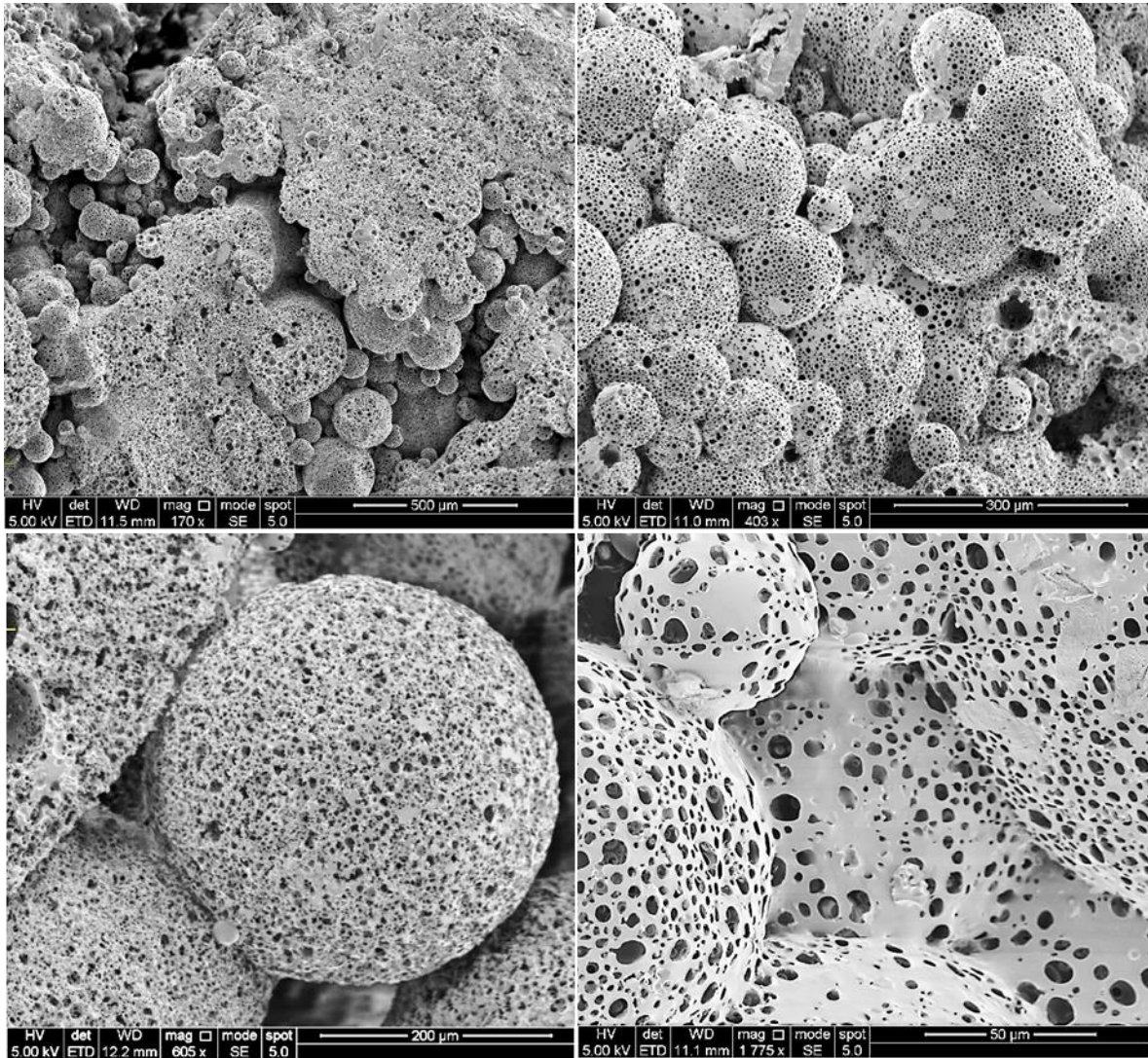


Fig. 58. Microspheres created by phase inversion on PCL-PGS 75:25, creating a W/O/W double emulsion.

5.6. Conclusions

This chapter aimed to explore PCL-PGS blends as a complementary use for single PCL and PGS layers as 3D scaffolds for osteochondral applications. The right blending mechanism was determined to ensure right dissolution of both polymers and ensure their homogeneous distribution in bulk and porous structures.

The mechanical properties of different PCL-PGS ratios were determined and found to be in-between pure LM/HM PCLMA and 50%/80% PGSM, used as reference materials. Their behaviour through the degradability process will have to be assessed to determine the decrease of mechanical properties.

Ideal solvents were determined for all PCL-PGS ratios depending on the stability of the emulsion, and the pore size / morphology, as imaged on SEM microscopy; best results were shown on 50:50 and 75:25 PCL-PGS with DCE and toluene as solvents. Emulsion phenomena (coalescence and phase inversion) were identified on 75:25 PCL-PGS emulsions leading to the formation of microspheres, identified as W/O/W double emulsions.

Micro-CT scans on PCL-PGS scaffolds allowed for the identification and labelling of cavity areas on three-dimensions and confirmed the interconnectivity of pores and windows on all axes.

Chapter VI: PolyHIPE treatment and hydrogels

6.1. Introduction

The objective of proposed PCLMA and PGSM scaffolds is to provide host cells and tissues with the support required for them to produce extracellular matrices and regenerate. In the process of preparing scaffolds to be in contact with biological material, materials need to undergo washing, drying and sterilisation procedures that can modify the mechanical and chemical properties of the biomaterial. Therefore, it is important to identify techniques that do not compromise the stability and characteristics of the materials so they can perform at their best.

As observed in the previous chapter, both PCLMA and PGSM scaffolds suffered from changes after being cured, and during washing and drying protocols. Further experimentation on this matter has been included in this chapter, including the exposure of materials to several surface tension-washing solutions, and to slow, steady, and immediate freezing techniques as drying techniques.

PolyHIPEs from PCLMA and PGSM have a high porosity and are highly interconnected. Under wet conditions, they behave like sponges and can be exposed to small loads of tension, compression, and shear stress, whilst still retaining and returning to their normal state. However, their high internal phase also puts them at risk of collapse. One interesting approach for wet and dry scaffolds is the use of particles or materials that can coat and/or fill the cavities of HIPEs, providing them extra stability. Proposals on this matter include mineral particles and hydrogels. Similarly, such materials would not only ameliorate the biomaterial's mechanical properties but enhance their behaviour with biological bodies and potentially be used for small molecule delivery.

Hydrogels are polymer networks with high water contents (hence hydrophilic), that have the possibility of absorbing from 10-20% up to thousands of times their weight in water [364]. Hydrogels have received special attention for the last 50 years due to their chemical composition, as they can behave as matrices to retain, encapsulate and/or carry molecules of interest (macromolecules, drugs, particles) and cells [365]. Herein, the properties of natural hydrogels (gelatin) are explored to crosslink and carry particles of interest (sugars), for a potential use of such solutions as coatings and/or supplements on the cavities of polyHIPEs.

6.2. Aims and objectives

This chapter aims to prepare PCLMA, PGSM and PCL-PGS scaffolds for a successful contact with biological material, where they can provide an optimal support for the regeneration of tissues and environments. For this, the following objectives were set:

- i. To define the ideal methodology for washing HIPE scaffolds that preserves their internal and external structure.
- ii. To define the ideal methodology for drying HIPE scaffolds that preserves their internal and external structure.
- iii. To determine ideal formulations to achieve hydrogel crosslinking via oxidising sugars.
- iv. To determine ideal formulations for hydrogels as sugar carriers.
- v. To examine hydrogel degradation and release patterns for hydrogels and sugars of interest.
- vi. To explore how HIPEs and hydrogels can work together as supplemented porous constructs.

6.3. Materials and Methods

Main materials and methods have been outlined in Section 2 of Chapter II. Those concerning only this chapter have been included below.

6.3.1. Hydrogels

Hydrogel	Solution
Alginate matrices	1 – 2 % w/w solution
Sucrose matrices	1 – 2 % w/w solution
Gelatin matrices	1, 5 and 10% w/w solution
Gelatin disks	1, 5 and 10% w/w solution
Gelatin - Sucrose disks	As described in Table 22
Gelatin - Glucose disks	As described in Table 22

6.3.1.1. Alginate matrices

As described in *Section 2.2.9.1. of Chapter II.*

6.3.1.2. Sucrose matrices

Sucrose solutions were prepared by dissolving the desired amount (1-2%) in boiling water and left stirring for at least 3 hours in a boiling water bath. Vials of the solution were stored at 4°C.

6.3.1.3. Gelatin matrices

Described in *Section 2.2.9.2. of Chapter II.*

6.3.1.3.1. Gelatin disks

Gelatin solutions from bovine skin were warmed up and stirred in a 40-60°C water bath until completely liquid. They were immediately poured onto metallic rings located in well plates, and whose surface is covered with wax paper to prevent hydrogels from sticking to the surface of the well plate. Hydrogels were then stored at 4°C. Smaller disks were fabricated using PDMS moulds.

6.3.2. Hydrogel-co-sugars

6.3.2.1. As crosslinker

A sucrose or glucose solution was prepared according to the desired concentration (w/v) and kept stirring under a bath with boiling water. A known grammage of gelatin was added to the sugar solution and left stirring for 3 hours until all the gelatin was dissolved. The solutions were stored at 4°C.

6.3.2.2. As sugar carrier

A glucose solution was prepared according to the desired concentration (w/v) and kept stirring under a water bath with boiling water. A known grammage of gelatin was added to the sugar solution and left stirring for 3 hours until all the gelatin was dissolved. The solutions were stored at 4°C.

6.3.3. Release experiments

6.3.3.1. Experiment setup

Gelatin disks were weighted before the experiment. They were then individually located in a well plate and 2 ml of PBS/0.1% sodium azide was added. The well plates were stored at 37°C. 600 µl of each well plate was removed at 30 min, 1 hr, 2hr, 5hr, 12hr, 24hr, 72hr, day 6, day 13, day 20 and day 27. At each measuring time, the liquid was removed, and the disks were weighed. The well samples were stored at 4°C prior to be measured using the BCA assay.

6.3.3.2. BCA Assay

BCA reagents A and B (Sigma Aldrich – BCA1) are commonly stored at 4°C. Reagent A (bicinchoninic acid, sodium carbonate, sodium tartrate and sodium bicarbonate in 0.1N NaOH, pH 11.25) was mixed with Reagent B (4% (w/v) $\text{CuSO}_4 \cdot 5\text{H}_2\text{O}$) in a 50:1 proportion to create the working reagent; 2 ml of working reagent is required for each sample. Reagents were mixed until obtaining a uniform light green solution.

A standard curve was developed by preparing 6 protein standards with concentrations: 0, 0.2, 0.4, 0.6, 0.8 and 1.0 mg/ml, and measured using the FTIR procedure described below. The readings were then graphed, and the resulting linear equation from the regression was used to determine the concentration of samples with unknown gelatin concentrations.

Samples with unknown concentrations of protein were prepared by diluting them to a concentration ranging from 0.2 to 1.0 mg/ml in deionised water. 2 ml of the BCA working reagent was added to each protein sample and vortexed gently. Each sample was then poured into a cuvette. One protein standard was used as control for the experiment. The samples were then incubated at 60°C for 15 minutes prior to being measured.

6.3.3.3. Absorbance microplate reader

A Perkin Elmer UV-VIS spectrometer was used to measure the absorbance of the protein released by the hydrogel disks and calculate the protein concentration. A syringe was used to take 50 μl of each protein sample and pour into the liquid sipper located inside of the sample compartment. The readings were performed in a range from 500 to 600 nm, and the reading at 562 nm was isolated afterwards. Each sample was measured 3 times; a control reading was performed at the beginning of each working shift.

6.4. Results

6.4.1. Emulsion optimisation

6.4.1.1. Scaffold collapse

PGSM scaffolds were found to collapse when dried. As imaging techniques through SEM and characterisation techniques (measuring dry mechanical properties) require drying the constructs, a technique that preserves their internal structure is imperative. PGSM scaffolds were found to collapse, as evidenced in Fig. 59.

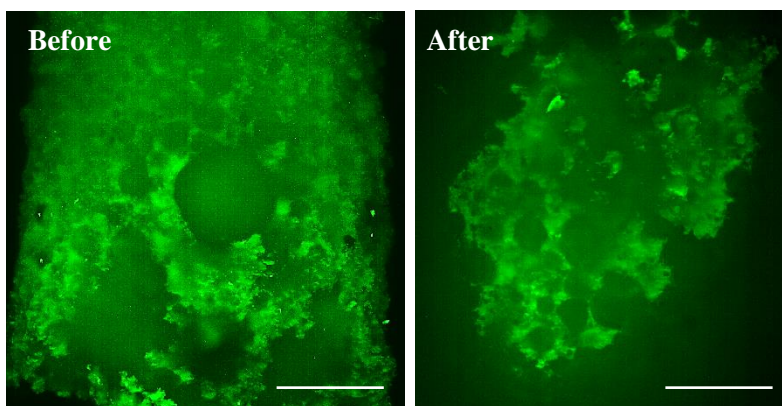


Fig. 59. PCLMA scaffolds before and after being dried in a dark space at room temperature. Almost no shrinkage can be observed as pores retain their size, and their form. Scale is 500 μm .

Among the collapse of the PGSM scaffolds, it was studied what solvent caused the most collapse. This was linked to the Double Solvent experiment developed in Section 4.4.1.3.2. of Chapter IV. The most significant collapses per solvent are found in Fig. 60. It was observed that scaffolds manufactured with only toluene and chloroform tended to completely collapse and form flat disks (A-B). Additionally, at higher concentrations of solvent, the collapse was more severe.

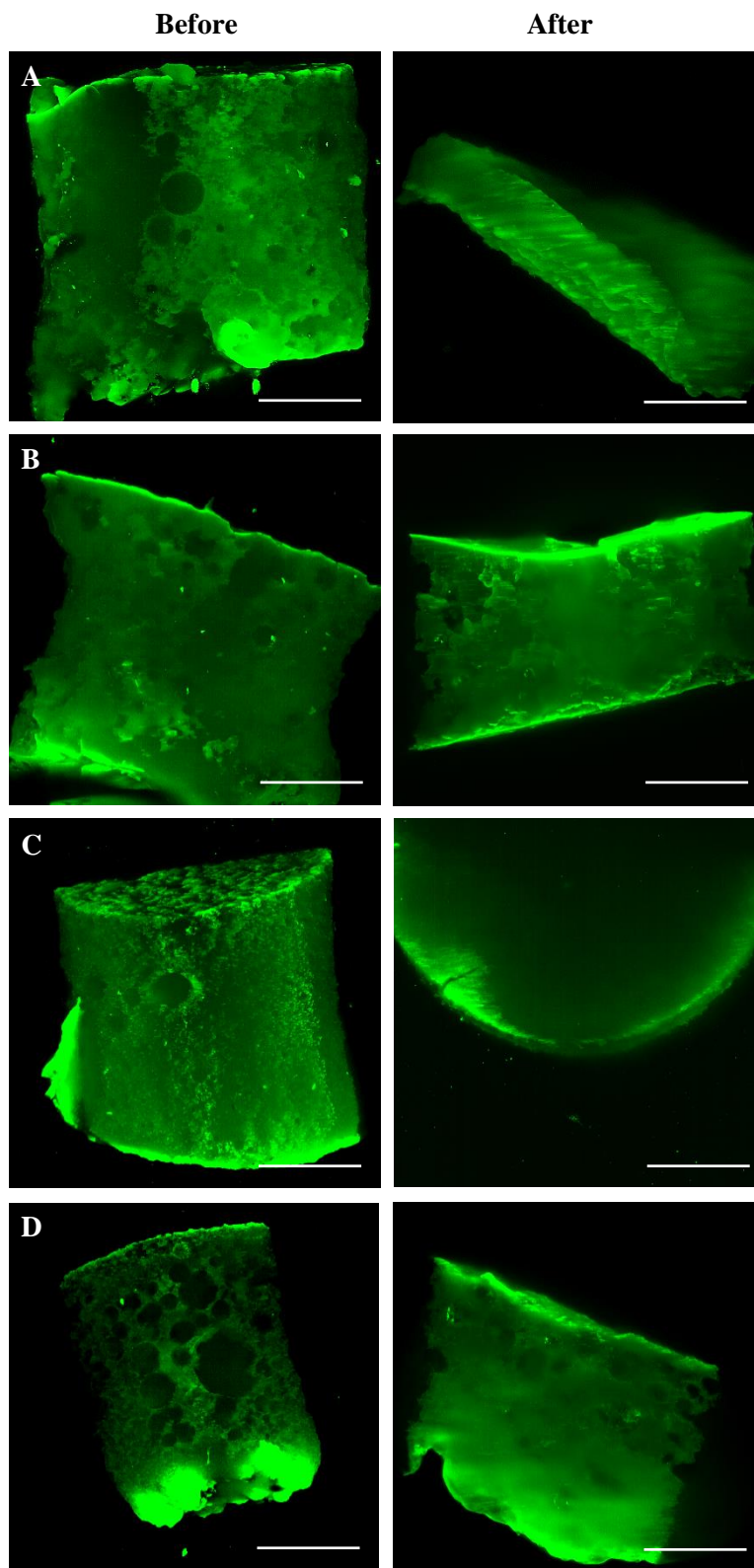


Fig. 60. PGSM scaffolds before and after being dried in a dark space at room temperature. For sample ID refer to experiment in Section 4.4.1.3.2 of Chapter IV. A) 90:10-0.55 Chloroform; B) 90:10-0.55 DCM; C) 90:10-0.25 Toluene; D) 90:10-0.55 DCE. Scale is 500 μm .

To better understand the collapse of the material, the washing and drying procedures were explored.

6.4.1.2. Washing procedure

According to the methodology, scaffolds were submerged in methanol for 3 days (100%, 80%, and 60%) and water for another 3 days. A combination of both washing and drying techniques has the potential to promote the collapse of scaffolds. For instance, the surface tension plays an important role in preserving the pore geometry, size, and therefore, interconnection. By using liquids with low surface tension that fill the pores, the structure could be better preserved. Water and methanol have values of 72.8 and 22.7 mN/m respectively [366]. Polyethylene glycol (PEG) 99% was used as the first has a surface tension of 43.5 mN/m [367] which is lower than water, which is the solution in contact with all scaffolds prior to being dried.

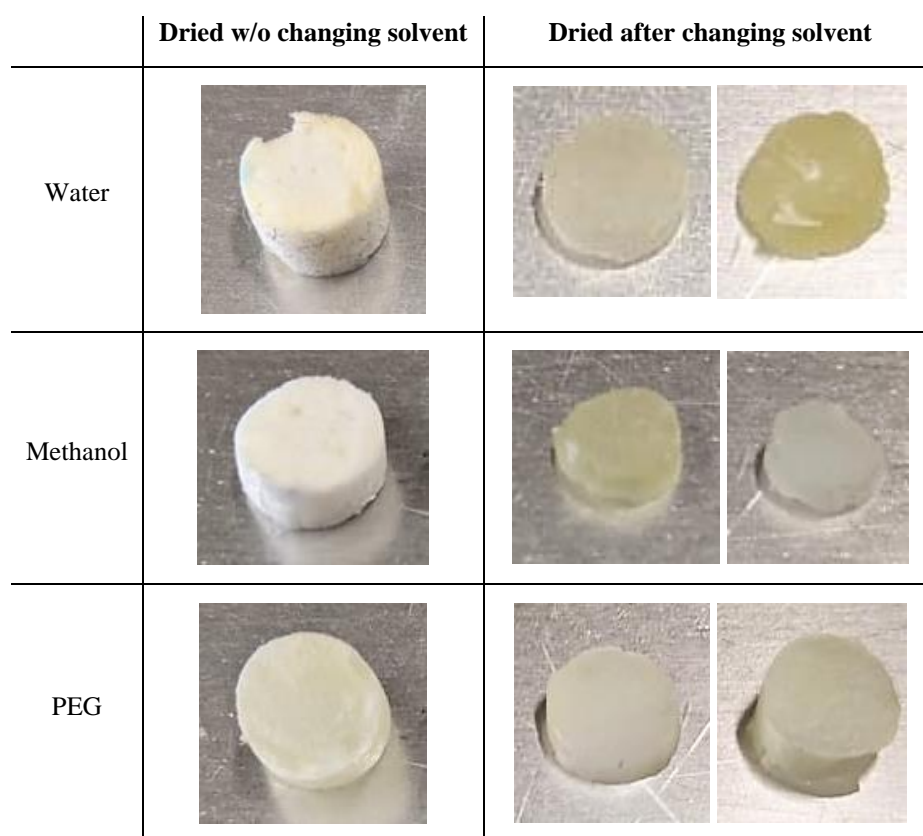


Fig. 61. PGSM scaffolds dried by freeze-drying after being washed with single or combined solvents (Water-methanol, methanol-water, PEG-water). Total collapse is observed in all cases with change of solvent, and partial collapse on PEG samples.

It was hypothesised that the change of solvent could be another reason why scaffolds collapsed. If methanol had a lower surface tension than PEG, drying them directly could prevent collapse. However, this could also impact on the cytotoxicity of the scaffolds. To explore this, scaffolds were

washed in single solvents (water, methanol, and PEG), and then freeze-dried. Results can be observed in Fig. 61.

6.4.1.3. Drying procedure

As previously mentioned, original drying methods were performed at room temperature, in dry-dark conditions overnight. However, as scaffolds are photo and thermosensitive, they tended to collapse, as shown in Fig. 60. Therefore, scaffolds were firstly frozen, either slowly by being left overnight at -80°C, or through a temperature shock using liquid nitrogen. Scaffolds were then dried using a freeze-dryer overnight. Results can be observed in Fig. 62.

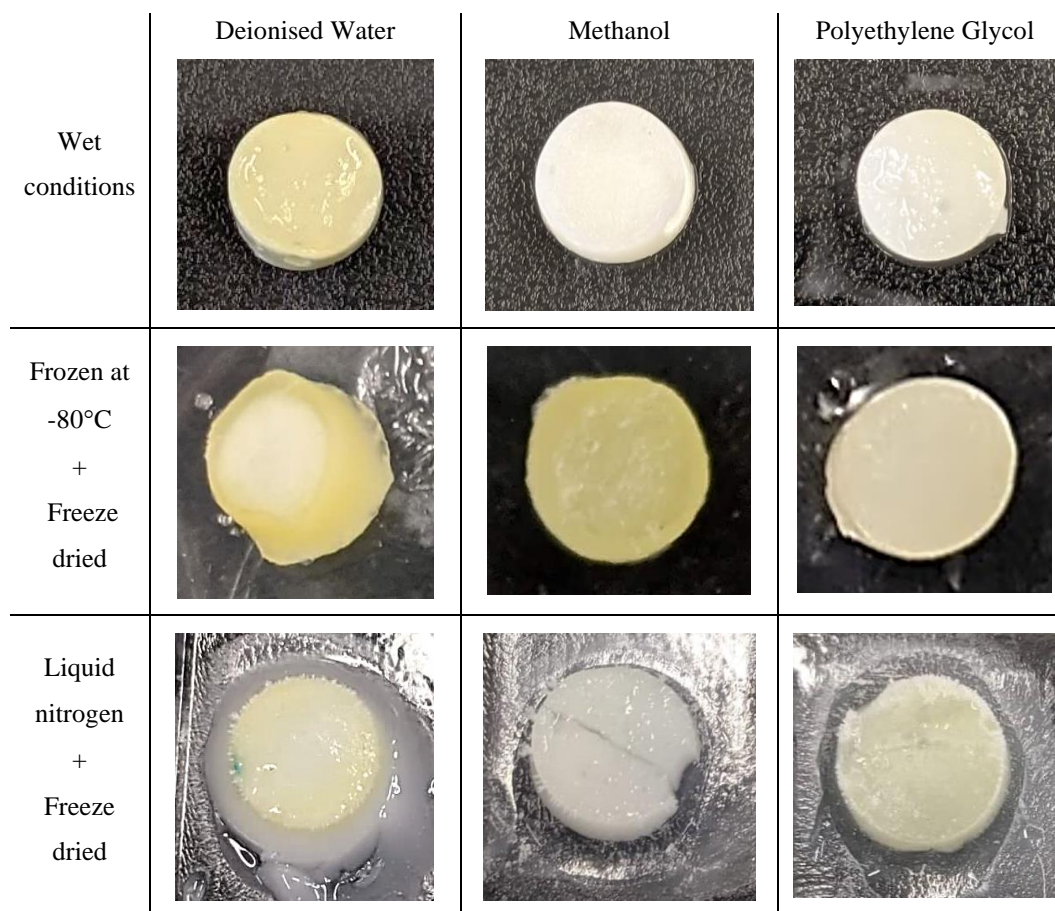


Fig. 62. PGS-50% scaffolds submerged in deionised water, methanol, and polyethylene glycol 99% were frozen by slowly reducing the temperature (freezer) and temperature shock (liquid nitrogen). Afterwards, they were freeze-dried overnight.

As an important note, samples washed with water and in wet conditions present a yellow coloration related to residues from the manufacturing process, likely a small residual photoinitiator. This

reinforces the importance of the washing process, especially if they were to be used with biological material.

Water and methanol scaffolds that were slowly frozen collapsed through the freeze-drying process. The process of collapse can be observed in Fig. 62 where the collapsed parts have a yellow colouring, and no porosity can be observed. This is fully observable in the methanol sample. The samples previously submerged in PEG did not collapse as they were not fully dry by the end of the drying period. These samples were left at room temperature for another 6 days until they were fully dried.

Samples frozen with liquid nitrogen collapsed in a different way. Even though they do not have the yellow colouring present in bulk (or collapsed) polymer, they did decrease their dimensions and in the case of methanol and PEG, cracked during the freezing period and retained their crystalline-fragile texture after being dried.

Finally, the drying speed was also explored. Even though it was considered that the freeze dryer process would be slow enough to allow samples to dry without losing their structure, an extra layer was added between the well plate where the samples were located, and the drying reservoir. The layer was made of foil paper and hollowed across its length. Using this setup production, a non-collapsed dry PGSM scaffold can be achieved as illustrated in Fig. 63.



Fig. 63. PGSM scaffold was dried overnight using a freeze-dryer. The scaffolds were covered with aluminium foil with holes pierced on it to control the drying speed.

6.4.2. Hydrogels

6.4.2.1. Gelatin crosslinked sugars

Hydrogels can crosslink through various physical and chemical methods. Sugar-mediated gelatin cross-linking was explored as it could serve two objectives, to facilitate hydrogel gelation providing it with more robust mechanical properties, and to enrich such polymer structure with molecules of interest to the cells.

For this experiment, gelatin (Gel) from bovine skin was used as the hydrogel matrix, and glucose (Gluc) as crosslinking sugar. Sucrose (Suc) was also included in the first experiments, as a reference structure of a non-reducing sugar working with hydrogels. The aldehyde group of reducing sugars (e.g. Gluc) react with free amino groups of the gelatin resulting in the formation of aminoglycoside, which reacts again with another amino group (Gel) to generate a crosslinked structure.

6.4.2.1.1. The effect of Gel:Suc and Gel:Gluc sugar ratio in the viscosity of hydrogels

Gelatin-co-sugar disks were produced as described in the methodology. As a first step, the ideal hydrogel viscosity was studied both at room and at physiological temperature. The aim was to find a formulation that would be solid (gel) at room temperature (10-20°C), and slowly liquify at 37 °C.

The combinations found in Table 22 were used to assist in identifying the ideal relationship between Gel and water. The amount of glucose and sucrose were kept the same although by varying the amount of gelatin, the relation between sugar and hydrogel changed. The disks can be observed in Fig. 64.

Both hydrogels turn observably brown, which is an indication that the cross-linking reaction (also called the Maillard reaction) has proceeded. Sucrose, as a non-reducing disaccharide can likely take part in the reaction because it can dissociate in its constituent components in aqueous conditions (fructose and glucose, both reducing sugars).

Table 22. Sucrose and glucose combinations used to produce Gelatin-co-sugar disks. All ratios are in grams. The state of matter was assessed 10 minutes after the mix was exposed to the temperature.

SUCROSE	Gel: Gluc : dH2O	Solid conc.	Gel conc.	At 4 °C	RT	At 37 °C
a1	02:01:02	60%	40%	Solid	Solid	Solid
b1	04:01:02	63%	50%	Solid	Solid	Solid

GLUCOSE	Gel: Gluc : dH2O	Solid conc.	Gel conc.	At 4 °C	RT	At 37 °C
a1	02:01:02	60%	40%	Solid	Solid	Solid
a2	02:01:04	43%	29%	Solid	Solid	Solid
b1	02:01:08	27%	18%	Solid	Solid	Solid
b2	04:01:08	38%	31%	Solid	Solid	Semi-liquid
c1	02:01:16	16%	11%	Solid	Solid	Liquid
c2	04:01:16	24%	19%	Solid	Solid	Liquid
d1	02:01:32	9%	6%	Solid	Solid	Liquid
d2	04:01:32	14%	11%	Solid	Solid	Liquid

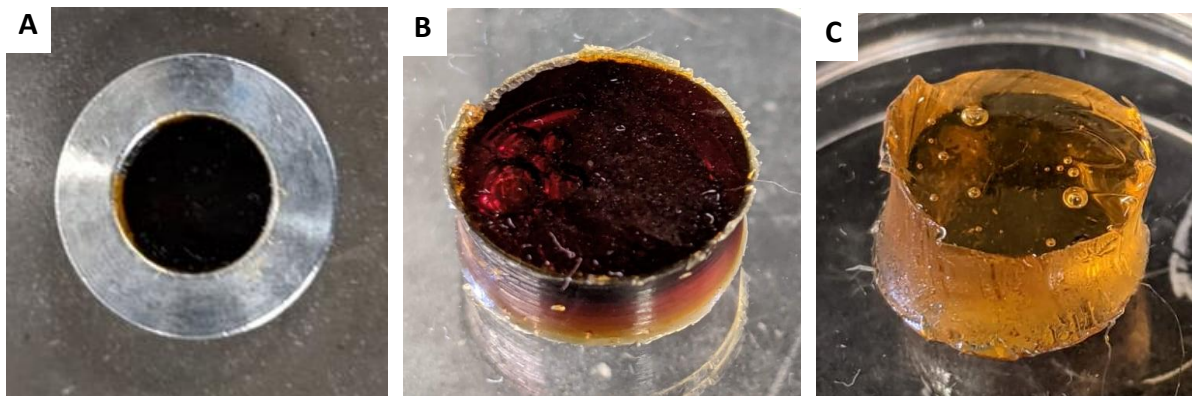


Fig. 64. Gelatin-co-sugar disks produced by moulding (A). The differences in colour between B and C are consequence of the ratio between Gel, Suc and water. B) Sucrose b1; C) Sucrose a1.

6.4.2.1.2. Degradation time of Gel:Suc and Gel:Gluc hydrogels

Gel:Suc and Gel:Gluc disks were then analysed by their degradation time. The experiment was used as a reference to determine what hydrogel composition was better suited for cell encapsulation/release experiments. As mentioned in the methodology, hydrogel disks were submerged in PBS:1% sodium azide solutions and kept at 37 °C. As hydrogels lose their structure as they dissolve, the degradation was tracked by the weight of the samples. Measuring times were at time 30 min and 1 hr, and weights measured at hr 3, 24, 72, 192 (day 13) and 480 (day 20). A stacked graph of the results for Gel:Gluc a1, a2, b1 and b2 can be found below (Fig. 65). All Gel:Suc and Gel:Gluc c1, c2, d1, d2 disks were completely dissolved after 1.5 hours of being located in the incubator and not included in the graph below.

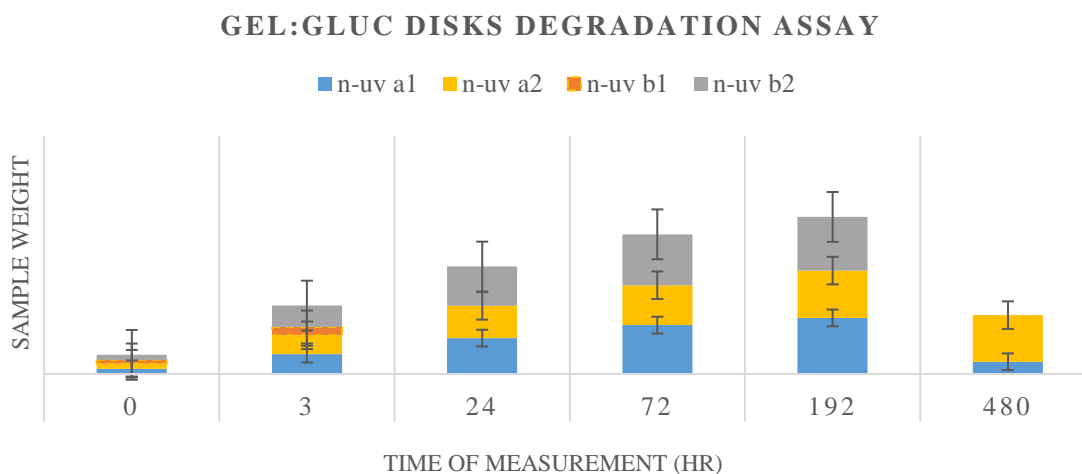


Fig. 65. Gel:Gluc disks on degradation assays with PBS at 37 °C. Stacked lines show the relative change of weight for each group of samples at a given time. uv/n-uv: UV/non-UV light treated. Mean \pm S.D.

An increment in the weights can be observed through time, with a drop in weights at later days. This is caused by the swelling of hydrogel disks at warm temperatures. The water absorbed increased the overall weight of the gel, however, as it slowly disintegrates, the structure starts losing weight in between day 13 and 20, likely releasing gelatin and sugars from the hydrogel.

6.4.2.1.3. The effect of UV light on the degradation of Gel:Suc and Gel:Gluc hydrogels

As the majority of the gelatin disks dissolved in the first few hours, the crosslinking was enhanced by exposing the freshly crosslinked disks to UV light for 5 minutes. This was tried for both Gel:Gluc and Gel:Suc disks and for all combinations presented in Table 22. The behaviour of UV treated disks is reported in Fig. 66. As observed, no differences can be observed to the results above reported on non-UV samples.

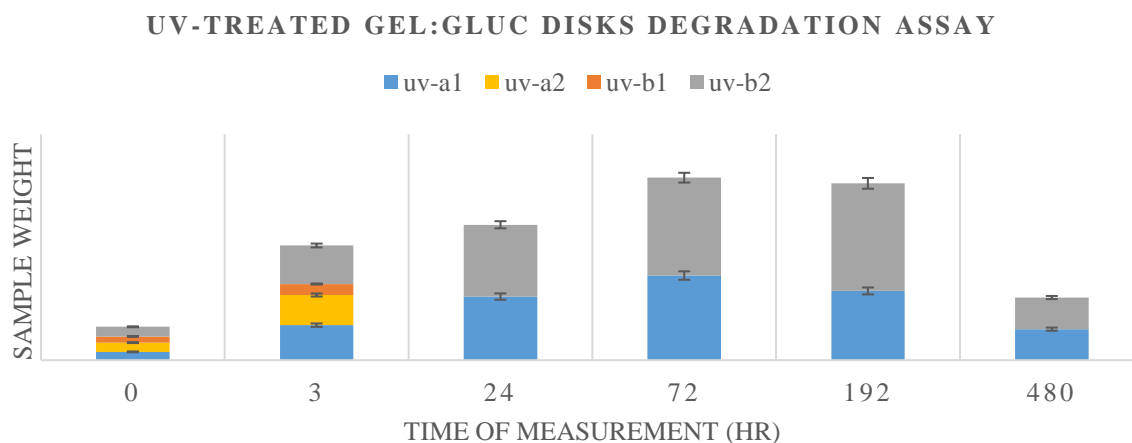


Fig. 66. UV treated Gel:Gluc disks on degradation assays with PBS at 37 °C. Stacked lines show the relative change of weight for each group of samples at a given time. Mean \pm S.D.

The effect of swelling and degradation of Gel:Gluc disks is illustrated in Fig. 67. The coloured bars represent the relative weight of the Gel:Gluc disks at a given point in time; bigger bars represent swelling scaffolds, whilst thin and disappearing bars evidence the degradation of the hydrogels, being dissolved in the alkaline media.

6.4.2.1.4. Gelatin release for Gel:Gluc hydrogels

Gel:Gluc disks were explored as potential carriers for cells and molecules of interest. As they degrade, the gelatin and sugars contained within the hydrogel structure would be released to the well plate. The release pattern (in $\mu\text{l/ml}$) has been tracked through the degradation process (See 6.4.2.1.2.) and measured through the BCA assay (Fig. 67). The concentration of protein was calculated from the measured absorbance at 562 nm, using an FTIR spectrometer (Fig. 68). The release on Gel:Suc disks was also included as a reference.

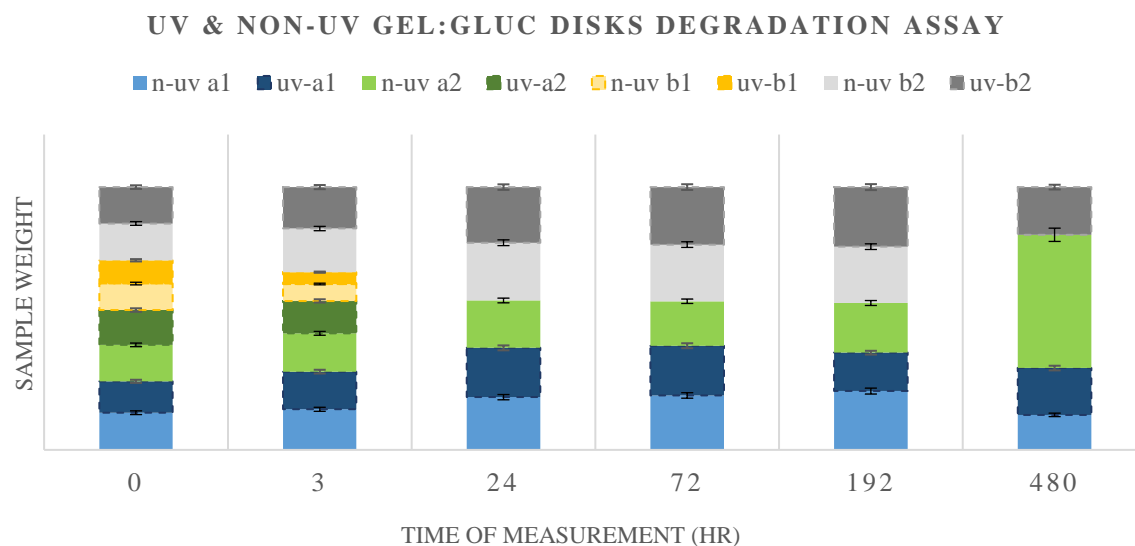


Fig. 67. Histogram representing the relative differences in weight from UV treated (UV) and non-treated (n-UV) Gel:Gluc disks. Mean \pm S.D.

GELATIN RELEASE IN GEL:GLUC DISKS

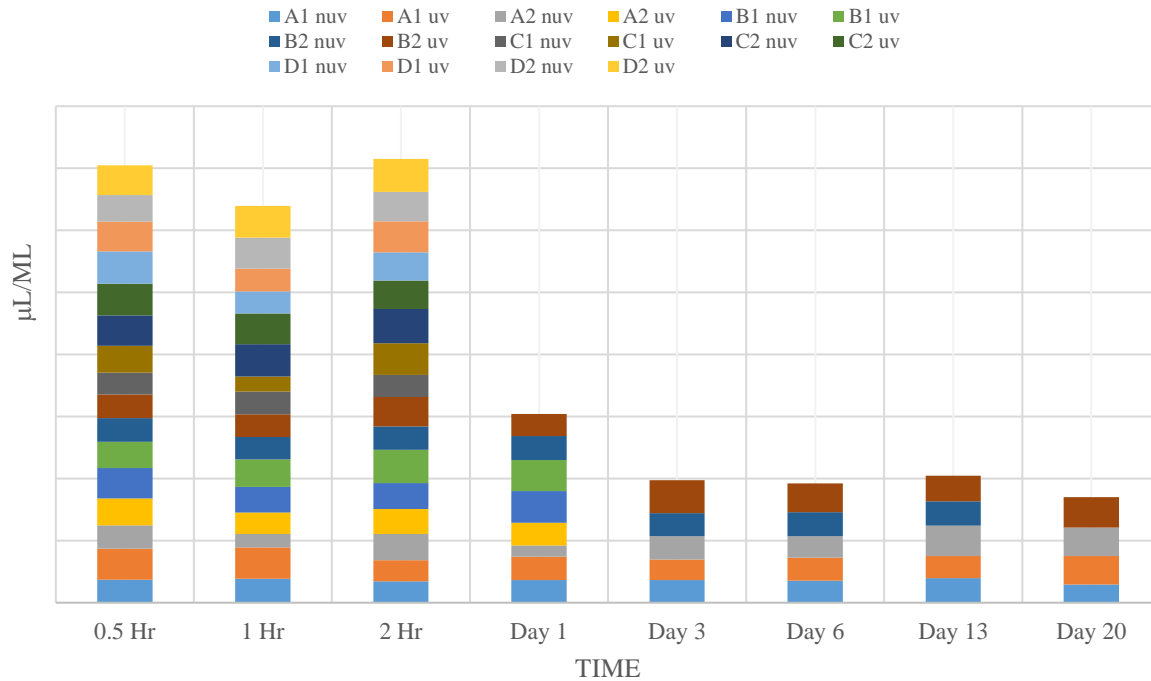


Fig. 69. Patterns of gelatine release on Gel:Gluc disks treated and non-treated with UV light, over 20 days. Gelatin combinations that are not represented after certain days have completely dissolved. Mean \pm S.D.

As observed in Fig. 68, the points of lower release coincide with the peaks in weight (water is mainly absorbed). Disks that degrade at similar times have a parallel pattern; it is also noticeable that disks with longer degradation times have a more stable degradation profile, except for B2 UV and nUV, which show a big decrement in release after day 3, whilst maintaining its gelatinous structure for the rest of the experiment.

GELATIN RELEASE IN GEL:SUC DISKS

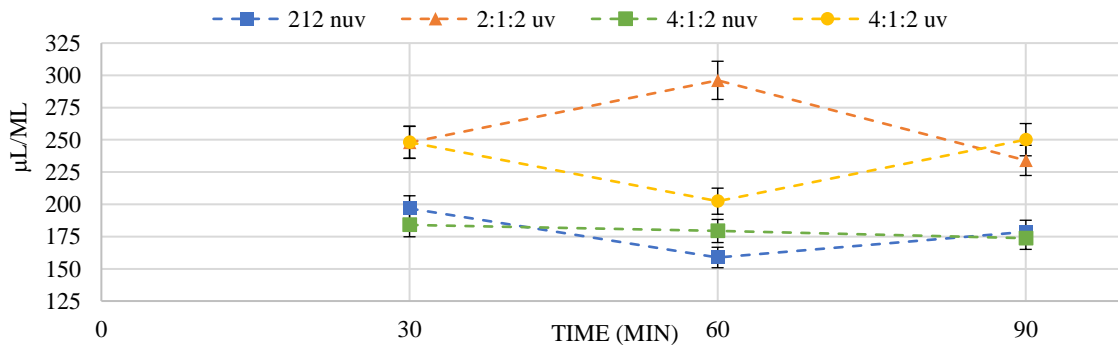


Fig. 68. Release behaviour of gelatin in UV-treated (UV) and non-treated (nUV) Gel:Suc disks over time. The hydrogels were completely dissolved after 90 minutes. The patterns or release were similar between 2:1:2 and 4:1:2 combinations. Mean \pm S.D.

Gel:Gluc compositions treated with UV did not impact significantly in the degradation of the gelatin disks. From all UV and non-UV treated disks, the ones with the most desirable behaviours were A2, B2 and B2 (Fig. 69).

6.4.2.1.4. PolyHIPE scaffolds embedded with Gel:Gluc hydrogels

To better understand if the hydrogels could be used in conjunction with the porous structures, PCLMA polyHIPEs were firstly exposed to a liquid hydrogel B2 solution at 37°C where it was mechanically stimulated (squeezed) so the Gel:Gluc solution could penetrate. It was then frozen and sliced using a vibratome to confirm the hydrogel presence (Fig. 70).

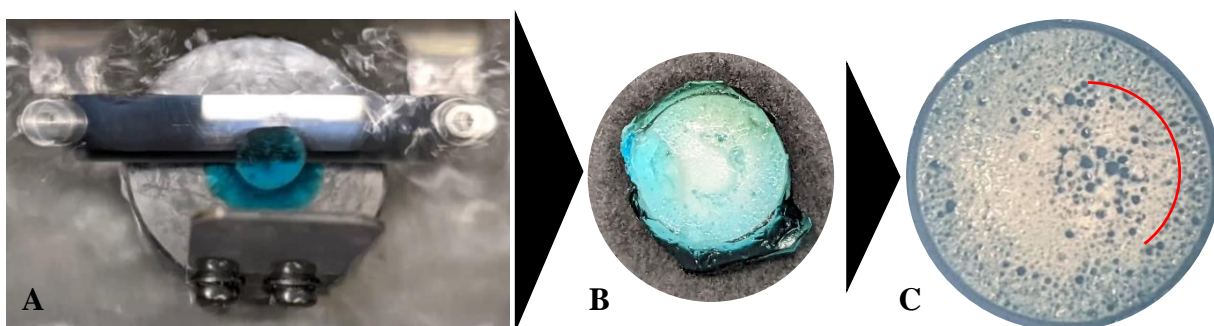


Fig. 70. PCLMA scaffolds submerged in Gel:Gluc B2 solution are sliced using a vibratome. B) The initial penetration of the hydrogel is observed where gelatin has been coloured in blue. C) A 100µm slice of the scaffold is observed under the digital microscope. The red line marks the border where the gelatin penetrated.

As observed, the gelatin only penetrated one third of the scaffold. This was not desirable as cells would face a similar migration problem to the one previously reported. As a possible solution, the scaffold was then immersed in the gelatin solution and vacuumed at room temperature for 3 cycles. Full immersion of the Gel:Gluc solution is observed in Fig. 71.

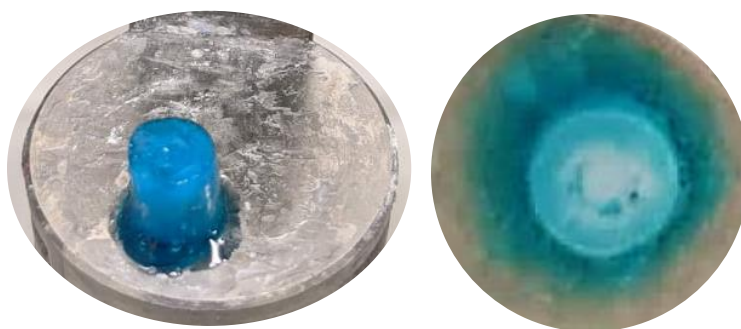


Fig. 71. PCLMA scaffold fully immersed in a Gel:Gluc B2 solution stained with blue dye.

6.4.2.1.5. PolyHIPEs with gelatin as an internal phase

As there is no certainty on the penetration of gelatine in the scaffolds, and the post-treatment could lead to a potential change in pore morphology, a single emulsion was trialled, using gelatine as the internal phase. The emulsion was produced using the following formula and combinations:

Reagent	Weight / Volume	Density (g/ml)
PCLMA	0.4 g	1.2 – 1.3
Surfactant Hypermer	0.04 g	0.94
Solvents: 6CHL:4TOL	0.6 g	1.02
Photoinitiator	0.12 g	1.12
Gelatin solution	2 ml	1.01

Oil Phase		Internal Phase	Water Absorbance	Emulsion Viscosity	Separation After Mixing
Polymer	Other	Gelatin Solution			
LM PCLMA	Surfactant, Solvent and PI	1%	2 ml	High	N
		3%	2 ml	High	N
		5%	2 ml	Middle	N
HM PCLMA		5%	2.5 ml	Middle	N

All emulsions were stable, however they showed a very different macro and micro pore morphology, as shown in Fig. 72 and Fig. 73.

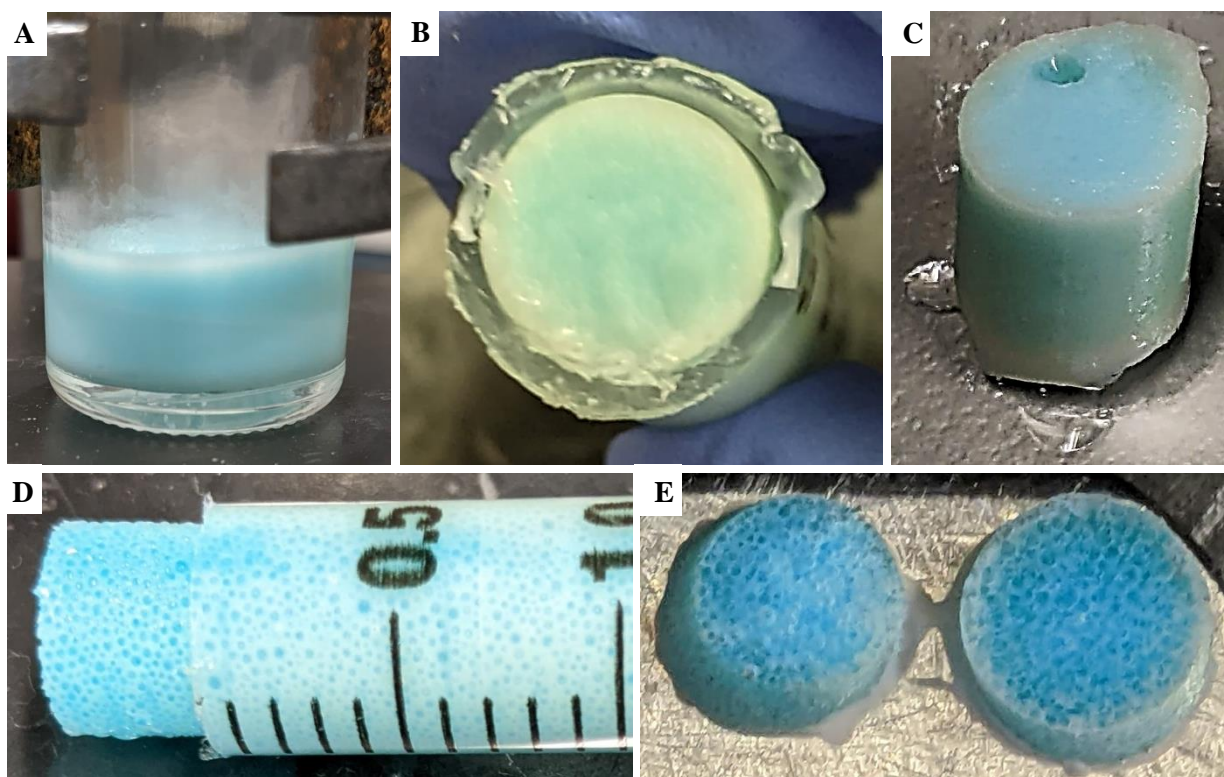


Fig. 72. PCLMA emulsion with gelatin as internal phase. Photocured polyHIPEs with 5% gelatin as internal phase using LM (D-E) and 50% PCLMA (B-C). The diameter of the scaffolds is 8.9 mm.

The average pore size of LM PCLMA HIPEs is $164.33 \pm 29 \mu\text{m}$, and $55.73 \pm 18 \mu\text{m}$ for the 50% PCLMA HIPEs.

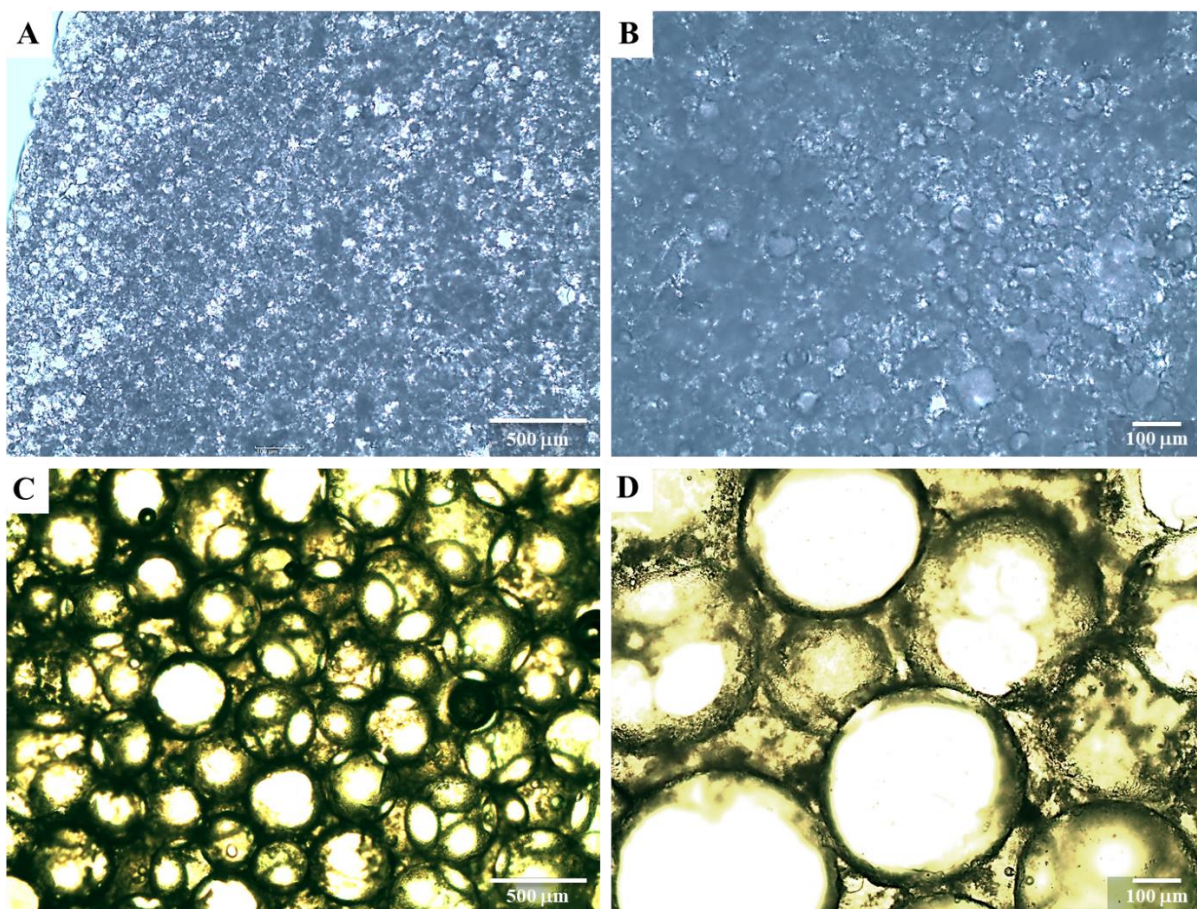


Fig. 73. LM (B,D) and 50% PCLMA (A,C) polyHIPEs with gelatin as internal phase imaged under a digital microscope at 4 and 10x magnification.

6.5. Discussion

6.5.2. Washing and drying scaffolds

PCLMA and PGSM HIPEs have been proposed as 3D supporting structures for soft tissue engineering applications. As previously discussed, the attractiveness of emulsion templating as a manufacturing technique for biomaterials resides in the balance between the mechanical stability of the 3D constructs, and the tunability of porous and interconnected cavities [276, 310]. As such, it is important to ensure those properties are stable before being exposed to biological environments.

In polyHIPE emulsions, post-curing material shrinkage happens when the aqueous phase (and residues of the oily phase) that is contained within the scaffold cavities, is replaced by other substance, or air. If the external pressure on the circumference of the pore is higher than the strength of the polymerised material, it can lead to the partial or total deformation of pores, windows, and the overall volume of the scaffold [368], increasing its density.

It has been reported that emulsions shrink upon drying, and most materials do so within the range of 15-30% [109, 129], although some have been reported at up to 60% when the volumes of cross-linker are kept minimal [324]. Higher shrinkage ratios are also related to higher porosities, and as such, are common in high internal phase emulsions (HIPEs) [369]. As found in experiments with both HIPEs of interest, PCLMA emulsions would undergo a minimal shrinkage during washing and drying, similar to what is reported in the literature [109]. On the contrary, PGSM HIPEs would lose partial or complete integrity and become flat bulk surfaces after being dried through normal techniques (dark space, and ambient parameters). It was found that emulsions prepared with toluene and chloroform caused the biggest shrinkage. A few hypothesis can be drawn to explain this:

- i) *Early shrinkage.* In the case of the internal pore morphology of emulsions emulsified with toluene as solvent, an initial collapse of the structure could have occurred during the initial polymerisation that impacted the stability of the constructs during the crosslinking, eventually collapsing when dried.
- ii) *Internal pressure.* The density of the internal phase is composed by the density of water and the partial density of solvents and surfactant residues. The density of air, water, and toluene is 1.225, 0.997, 0.866 g/ml. This means that the internal density of pores post-curing is somewhere between the density of water and toluene, which is approximately 20-25% lower than air.

It has also been mentioned that the crosslinking degree influences the swelling behaviour [324]; higher crosslinking degrees lead to a decrease in the swelling effect. This is related to the functionalisation of materials; *H. Xu et al.* identified that as the overall content of methyl acrylates increased, the level of shrinkage did as well [370]. This has been associated with the theory on how interconnects are created: during the polymerisation process, the thin walls collapse (or shrink), creating windows that interconnect pores within each other [360].

As drying only occurred after washing procedures, the effect of the washing solvents on the polymerised and photocrosslinked PGSM scaffolds was further explored. Scaffolds need to undergo washing to remove any polymer residues, but mainly to sterilise the constructs before placed in cellular environments (under methanol solutions).

For this, scaffolds were dried using freeze-drying as it has been reported to reduce the shrinkage ratio and is a well-known technique for the development of porous materials [371, 372]. The methodology indicates that scaffolds should be submerged for 3 days in methanol and 3 days in water; scaffolds were prepared according to the double-solvent formulations for PGSM HIEs with toluene and DCM as solvents. Scaffolds dried with the original washing plan showed a total collapse in all cases. Similarly, scaffolds washed the opposite way, that is, first water and then methanol, collapsed as well, but not to the extent of the first ones. On the contrary, scaffolds dried without changing solvents preserved their porous morphology and reduced their volume to approximately 35%.

The surface tension of selected solvents plays an important role in keeping the structure during the freeze-drying process. Because of the high interconnectivity of the scaffolds, their “matrix” is highly permeable, and water molecules diffuse from the inner droplets to the outside the material, decreasing the internal (cavity) pressure. If the material is stiff enough, the liquid inside the cavity becomes unstable and sublimates into vapour. If the matrix is soft, stress relaxation takes place, leading to irreversible pore collapse [373].

Polyethylene glycol 200 was also used in this experiment as a reference solution due to having a surface tension (43.5 mN/m), between that of the water (72.8 mN/m) and the methanol (22.7 mN/m) [366]. Results with scaffolds dried in PEG 200 only took triple the time to get dry but preserved the porous structure, even though it left an “oily” texture on the scaffolds.

Finally, the freezing rate was explored as a means to determine the combination of conditions that would better preserve the porous morphology of PGSM scaffolds. Scaffolds frozen with liquid nitrogen maintained a porous structure but transformed the foamy scaffolds into fragile structures that

broke whilst being dried. On the contrary, scaffolds that were slowly frozen at -80°C totally collapsed when freeze-dried. The drying (and therefore collapse) pattern observed in semidried scaffolds confirmed that the collapse starts on the surface /edges of the scaffold and moves toward the centre.

This can be centred on the theoretical background of diffusion of water from the scaffolds. In theory, in the absence of impurities, the diffusion coefficient depends only on the temperature of the environment and the relative humidity of the chamber. This theory [374] also explains that smaller pores reach full shrinkage faster than large ones, compromising scaffolds with small pore sizes [375]. However, there needs to be an account for the interconnected dynamic of pores, which might modify this drying behaviour. This hinted that the drying speed impacted more than the freezing one (mass transfer may lead over temperature transfer [376]). Slowing down the drying process by the use of a holed foil layer on the top of the container with the drying scaffolds allowed to reduce the drying speed, and to better preserve the structure of the scaffolds.

6.5.3. Hydrogels

One of the big challenges whilst using 3D constructs for biomedical applications relates to the migration of cells throughout the construct; cells tend to attach to the surface of the scaffold and will only migrate a few mm towards the centre of the 3D structure [377]. Hydrogels have been proposed as a means to encapsulate and deliver cells to all areas of the scaffold [378], facilitating their local migration and the production of desired ECM. For a successful cell encapsulation, hydrogels are required to: i) be cyto-compatible, ii) have mild crosslinking conditions, iii) possess proper gelation kinetics, and iv) facilitate mass transport [379].

Hydrogels are naturally unstable materials that can easily dissolve and degrade due to their high-water content and low mechanical properties. However, some of those features can be tailored by crosslinking hydrogels' polymeric networks through chemical or mechanical means [380].

Existing chemical mechanisms include the use of solvents that can be cytotoxic. With the aim of finding biocompatible ways of crosslinking hydrogels, native and oxidised sugars (mono and disaccharides) were proposed by *Cortesi R. et al*, in 1998 [88]. Such sugar-mediated hydrogels would serve two objectives, to facilitate hydrogel gelation providing it with more robust mechanical properties, and to enrich the polymer structure with molecules of interest to the cells, as sugars. Gelatin was crosslinked through the oxidising sugar mechanism with glucose and sucrose used as a reference point. Crosslinked hydrogels would be reversible given that the solutions were heated and stirred to full solution. However, when kept at high temperatures, they would achieve gelation and

become non-reversible matrices. This is probably associated with the crystallisation of the sugars at high temperatures (and with a water shortage [381]), as gelatin will increase its particle mobility above gelation point ($>36\text{ }^{\circ}\text{C}$) which leads to dominant flexible random coils at high temperatures ($\sim 90\text{ }^{\circ}\text{C}$) [382], contrary to what was observed.

The disks were created using a combination of water to gelatin ratios that allowed for the identification of attractive formulas for cell encapsulation including stable at room temperature, semi stable at anatomic temperatures, and with a fast degradation (within 5-7 days). From the given combinations, only one proportion satisfied the state of matter's requirement (sample ID: b2 with 04:01:08 Gel:Glu:dH2O). The effect of sugars on the viscoelastic and sol:gel properties of hydrogels has been explored in agarose:xanthan gum:sucrose/fructose where it was found that changes in the temperature of solution and the sugar type/concentration, impacted the viscoelastic properties of the hydrogel, the sol-gel transition temperature, and the swelling ability of the gel [381]. Similar results were observed in gelatin and sugars where stronger and more thermally stable structures were created [383].

The degradation of Gel:Suc and Gel:Glu was assessed over 480 hours and tracked through weight. All Gel:Suc and half of the Gel:Glu solutions were completely diluted within the 2 hours under physiological conditions, as observed in un-crosslinked porous gelatin sponges [384]. The remaining disks were tracked, and all displayed the same mechanism of weight increase and a rapid decrease after 192 hours. This is attributed to the swelling properties of the hydrogels, which absorbed the PBS solution they were immersed in, whilst degrading. When the degradation was bigger than the ability to absorb more water, the scaffolds lost their integrity and dissolved in the media. This behaviour has been previously reported for pure gelatin and as a composite [385], and it is being explored for the controlled release of drugs [386, 387].

To increase the stability of the crosslinked gelatin hydrogels, *Masutani et al* irradiated their gelatin:glucose films with UV light as it has been demonstrated that the films increased their gel strength and their viscosity, providing them with improved their thermal stability [91]. However, the experiments developed on this matter did not show a significant difference for any of the Gel:Suc and Gel:Glu disks in terms of water swelling, degradation, nor gelatin release.

The degradation of the disks was tracked over time and a small sample was taken at a given time, to register the content of gelatin and build a release profile. This profile showed a similar profile for all Gel:Suc ratios with a stable release at 30 and 90 minutes, but a decrease at 60 minutes. This was also

identified on fast-degradable combinations on Gel:Glu and is linked to previous results on the increase of water absorption. Finally, remaining UV-treated and non-treated disks behaved similarly over time with a stable release of gelatin until day 20. A similar behaviour has been reported for Gel:Suc and Gel:Glu disks on the literature [88].

An early exploration on how the selected Gel:Glu hydrogels and previously developed polyHIPEs would work together was developed. Exposing the hydrogel solution to a liquid gelatin:sugar solution and mechanically stimulating the absorption of the solution within the cavities of the scaffold proved that both materials can exist simultaneously and support the transportation and release of cells through the porous construct. A similar approach has been developed for porous scaffolds by coating them with pure or enriched hydrogels as surface modification [388], or to tune their degradation [93]. Hybrid scaffolds have also been created using solid form techniques where a variety of synthetic polymers (PCL, PLGA and PCL/PLGA blend) were layered with different hydrogels (hyaluronic acid, gelatin and atelocollagen) [389].

The use of gelatin solutions as an internal phase has shown how both techniques can be joined in an integral way, and with a two-fold purpose. On one hand, the gelatin solution is solid at room temperature; this means that it can provide structural support to polymer scaffolds in dry and/or post-treatment conditions. The successful creation of photocurable PLCMA-Gelatin scaffolds shows potential in the use of UV light for sterilisation procedures, as this source of light was non-destructive, mainly for the hydrogel layer.

Additionally, it can support the delivery and release of cells and molecules through the scaffold, proposing a solution to the migration challenge previously reported on 3D porous constructs [390]. However, no similar approach has been found where the cavities of the HIPEs have been repurposed for the transport of cells.

6.6. Conclusions

This chapter had two main objectives. The first one was associated with the optimisation of post-curing techniques that allowed scaffolds to be characterised and sterilised without losing their mechanical and structural properties. The second one aimed at exploring the use of hydrogels as matrices to encapsulate and release molecules of interest into the scaffold, in a homogeneous way.

The natural shrinkage of porous materials and polyHIPEs has been commonly reported in the literature. It was identified that scaffolds could maintain their porous structure given they remained

in a wet environment that did not change constantly. This is, scaffolds washed only in methanol or only in water reported lower shrinkage ratios than the ones washed with methanol:water or water:methanol cycles.

In the cases where scaffolds had to be dried due to characterisation, imaging and/or sterilisation prior to their use *in vitro*, drying techniques would usually lead onto the total collapse of the 3D structure, leading to the loss of porosity and interconnectivity that characterises polyHIPEs. For this, it was identified that the stability of the emulsion post-curing, the freezing media, the speed of freezing and the speed of drying played important roles. The most convenient parameters were reported on PGSM polyHIPEs cured for 10 minutes under the UV light, washed only with methanol, slowly frozen at -80°C, and dried in a freeze dryer overnight, inside of a plastic container covered with a layer of foil paper with holes.

On the second matter, gelatin hydrogels were selected due to their natural properties and their interaction with other materials, and the host body. Gelatin solutions were crosslinked with oxidising sugars (sucrose and glucose) to form disks that would present a solid state at room temperature, and semi-solid at physiological temperature, degrading over time. The degradation of such disks and the release of gelatin over time was tracked through the BCA assay.

Hydrogels were also successfully embedded into PCL LM scaffolds with a homogeneous distribution through the pores and windows of the 3D structure, validating their potential as supplemented polyHIPEs for osteochondral applications.

Chapter VII: Cell response to polyHIPEs for cartilage and bone regeneration

7.1. Introduction

In this chapter the scaffolds discussed previously will be examined for their ability to support cell culture. Optimal conditions for synthesis and material preparation, suitable emulsions, and the most attractive surfaces have been proposed and will be tested herein in simulated cellular environments. The osteochondral tissue is complex [194] due to the variety of tissues and cellular sources cohabitating together, as well as the numerous movements and pressures the tissues are exposed to. The interaction of chemical and biological cues is specialised and specific between articular cartilage and the subchondral bone [18]. Therefore, an analysis on the scaffold's behaviour should include an examination from the simplest to the most accurate environment, as a way of understanding, as well, the role of the implant during the formation of the new tissue.

Native tissues work in synchronicity. Their consistent cells not only occupy the space provided by the layers of tissue, but interact with it, contributing to its construction and maintenance. Hence, an implanted material should have features that attract cells to start inhabiting and modelling their new environment, just like they would do within the native tissue. Some materials' properties are only partially beneficial in assisting this process; a wide variety of these materials can be tailored and enhance chemical and biological interactions [13]. The process of "functionalisation" can be achieved through several methods; the property that describe the affinity of a material to its biological environment is called bioactivity [391].

As a first screening, polymeric non-porous surfaces were exposed to primary and mesenchymal cell lines: BACs and hES-MPs, respectively. Experiments on 2D allow cells to interact with the biomaterial in a simplified way and for the measurement of early cytotoxicity and bioactivity (attachment response). Additionally, imaging is easier. However, cells seeded on 2D have non-representative cell-cell and cell-ECM interactions. Additionally, they have shown a change in morphology as they proliferate and mature [207, 392], which can affect the production of ECM (and related proteins), stimuli responses, differentiation, and other cellular mechanisms. For instance, chondrocytes on monolayer cultures inhibit cell maturation as cells spread and de-differentiate. Similarly, 2D experiments do not simulate the real availability of oxygen, nutrients, and metabolites

as they are either exposed to it all the time, or not at all. Despite these limitations, it gives a notion of the effect of the biomaterial on controlled cell culturing scenarios. Moving on, 3D experiments simulate a closer in situ environment, as cells can move in the three axes on the surface of the scaffold and migrate through the porous structure. Cells that have been seeded on porous 3D scaffolds often pack and cluster on the external rim of the construct, limiting their infiltration to the inner layers of the structures due to the tight matrices. Localised cell proliferation on scaffolds can also create a propensity to collapse during degradation [393]. Cells will migrate to empty spaces and distribute accordingly, depending on the pore size (pore area fraction) and pore interconnectivity [228]. The homogeneity of the distribution and the time necessary for migration will also depend on the stimuli provided by the environment (media and supplements) [394]. Cell migration involves the coordinated orchestration of cellular adhesion, changes in cell morphology & nuclei (to create force and motion), and matrix remodelling [377]. Additionally, different cell types differ in modes of cell migration; for instance, mesenchymal movement (spindle-shaped cells) are associated with slow migration speed dependant on focal adhesions (ECM propelled/anchored cells), whilst amoeboid movement (ellipsoid-shaped cells) have a rapid migration speed and low contractility that leads to low traction [395]. It is also important to note the direction in which cells migrate. Cells can migrate from the surface to the core (when seeded externally) or from the centre to the external surface (when seeded in the scaffold's bulk), proliferating and behaving differently depending upon their location. This process has been tracked through long-term viability and proliferation tests.

One of the biggest challenges for osteochondral regeneration is the source of cells [396]. Even though acellular scaffolds have been used for osteochondral repair, they rely completely on native cell migration. As this could be conceived as a problem due to the availability of cells, it is also quite related to timing; impaired regeneration can be due to inappropriately timed migration [397]. Mature autologous and allogenic cells have been seeded onto porous scaffolds aiming to solve these concerns. Additionally, stem cells have been proposed as they have the capability to differentiate into desired cell types, whilst populating the 3D construct and building their environment (ECM). However, the aberrant differentiation of cell lines and the production of low and/or undesired ECM can have repercussions on the mechanical properties of the neo tissue (and the matrix integrity) [396]. Within the scope of this work, the differentiation pathway was superficially tracked over time through viability, proliferation, and ECM production, by the addition of supplemented media. The individual effect of each supplement was not studied but a justification and discussion behind the use of each reactive will be provided.

7.2. Aims and objectives

This last chapter aims to examine some previous materials to analyse their performance in physiological environments, as well as investigating the cell response to such materials. For this, the following objectives were set:

- i. To investigate the degradation patterns of PCLMA, PGSM and PCL-PGS 3D scaffolds.
- ii. To analyse the cytotoxic response of primary and mesenchymal cells to materials using monolayer culture.
- iii. To determine optimal functionalisation parameters for air plasma treatment on the surface of 3D polyHIPEs.
- iv. To determine optimal size, seeding concentrations and seeding parameters for the ideal cell attachment of primary and mesenchymal cells on 3D polyHIPEs.
- v. To optimise cell attachment and early proliferation of primary and mesenchymal cells on the surface of 3D polyHIPEs.
- vi. To track the production of ECM on 3D polyHIPEs of primary and mesenchymal cells.
- vii. To explore cell differentiation on 3D polyHIPEs for both cartilage and osteochondral tissue regeneration.
- viii. To establish parameters for the creation of a bilayer 3D polyHIPE made of PGSM, PCLMA and/or PCL:PGS for osteochondral applications.

7.3. Materials and Methods

Materials and methods have been outlined in Section 2 of Chapter II.

7.4. Results

7.4.1. Scaffolds in physiological environments: degradation assays

As biodegradable polyesters, PCLMA and PGSM will eventually degrade, reducing the mechanical support that they give to the cells, and producing byproducts which can modify cellular behaviours (growth, production of ECM, differentiation, etc.). The degradation patterns for materials optimised in Chapter III and IV were measured to understand the type and speed of degradation that materials will suffer in terms of volume, weight, and structure.

PCLMA has been reported to have a slow degradation (more than two years) *in situ* [111]. To investigate the degradation profile of both bulk and porous scaffolds, bulk PCLMA were placed in a PBS and an alkaline solution (0.8M). The degradation was tracked for 20 days. The loss of weight and volume was measured (Fig.74).

Digital microscopy confirmed a really slow degradation for bulk 50% PCLMA with only a small reduction in size (mean of 13%). LM PCLMA degraded faster and most of the samples cracked after 30 days. Porous 50% and LM PCLMA showed wall (external) degradation (Fig. 75).

PGSM, on the other hand, is recognised because of its faster degradation (when compared to other polymer biomaterials) [327, 328]. Bulk and porous scaffolds were immersed independently in PBS and an alkaline solution (NaOH 0.8 M) and tracked for 28 days. The degradation profiles are shown in Fig. 76 to Fig. 78.

Porous scaffolds were firstly submerged in 0.8 M NaOH but the degradation was too fast to be tracked (less than 2 hours). Therefore, the concentration was then reduced to 0.1 M. Both losses in volume and weight were reported and have a similar behaviour (Fig. 78). We have observed in previous experiments that the release of sebacic acid during degradation can lead to cytotoxic effects since it lowers the pH. This has also been observed here, the pH was measured on the different solutions (PBS, NaOH 0.8 M and NaOH 0.1 M), noticing changes on NaOH 0.8 M from 13.9 to 9.17 ± 3 and NaOH 0.1 M from 13 to 8.9 ± 4 .

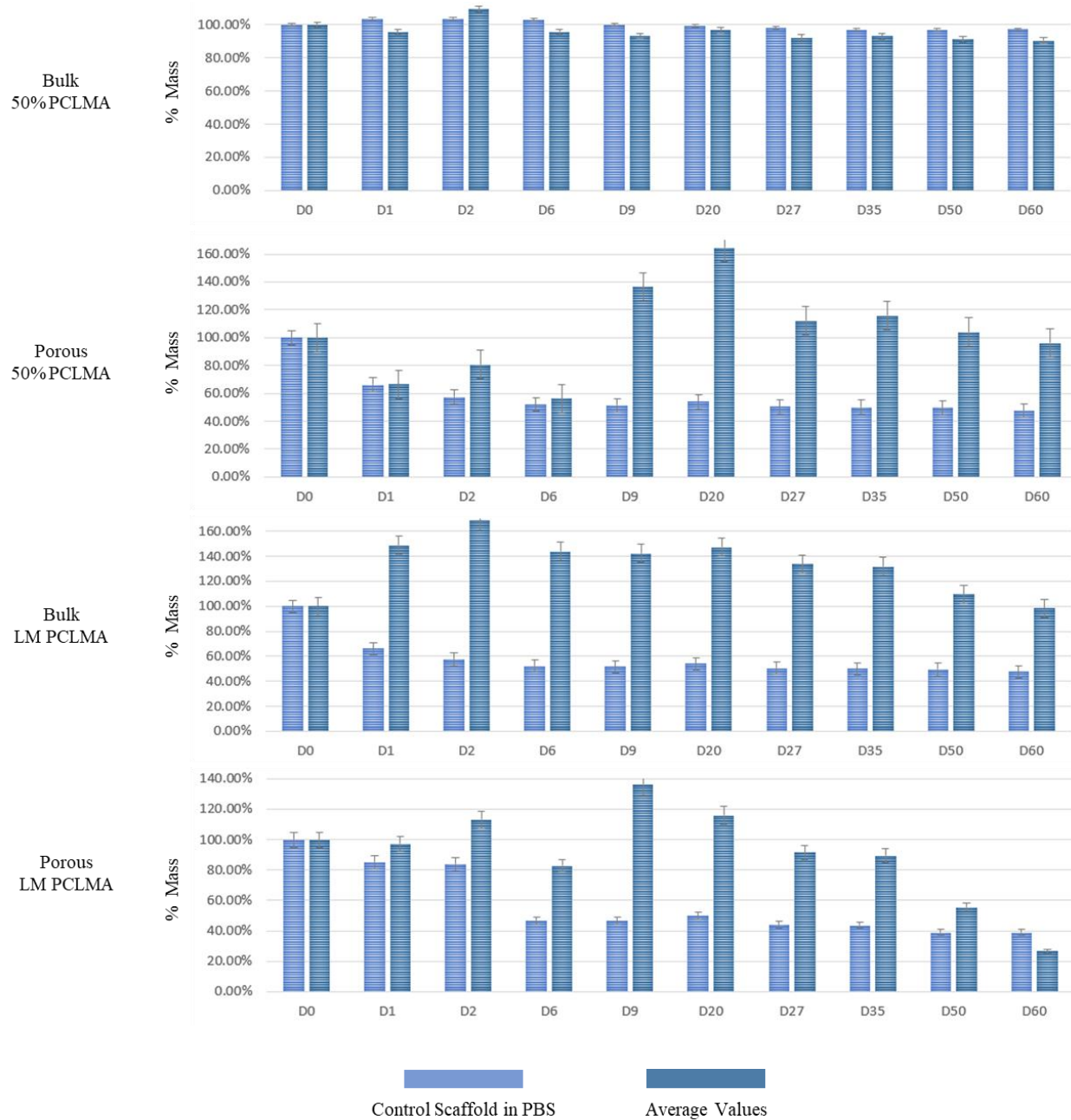


Fig. 74. Degradation assays for LM and 50% PCLMA, in bulk and porous forms, under an alkaline environment, over 60 days. The degradation is expressed as a loss in mass. Grey lines represent the measured samples, averaged in the green line. The line in red is the control sample (scaffolds submerged in PBS). Mean \pm S.D, n = 4.

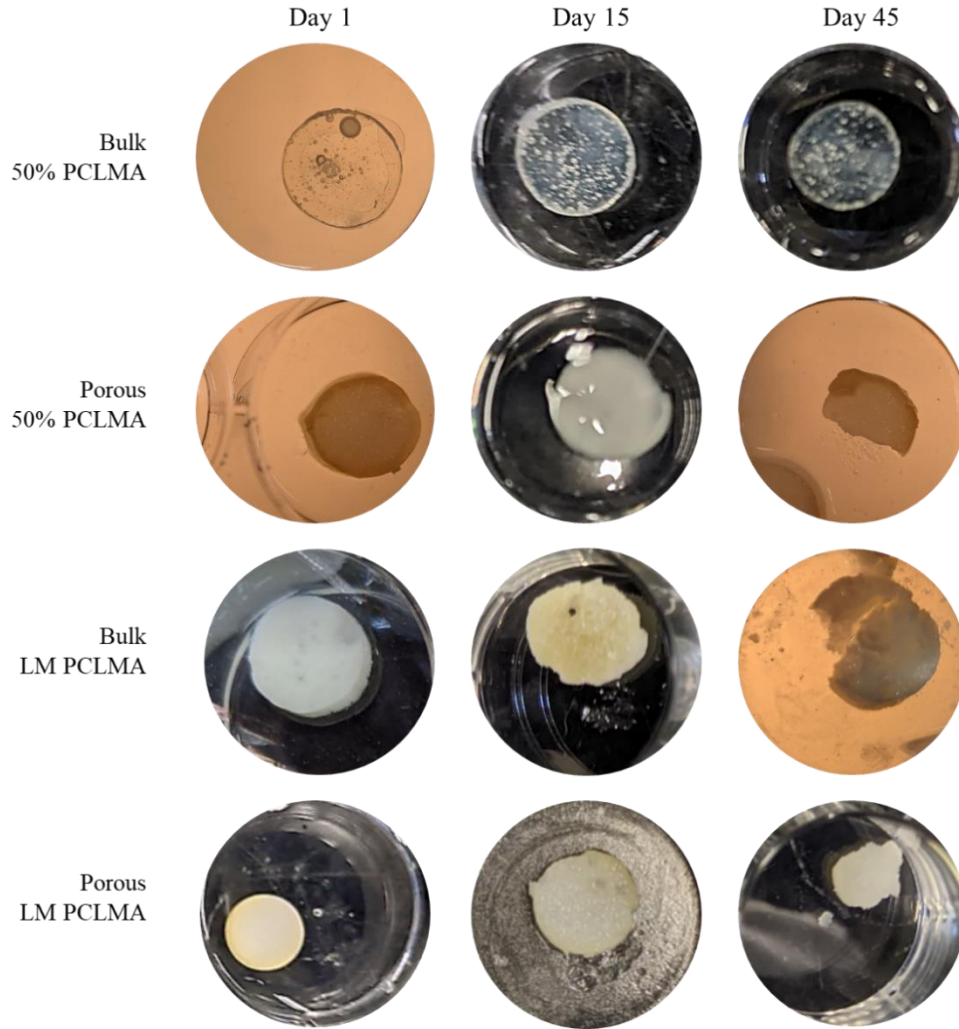


Fig. 75. Digital microscopy images on bulk and porous PCLMA scaffolds.

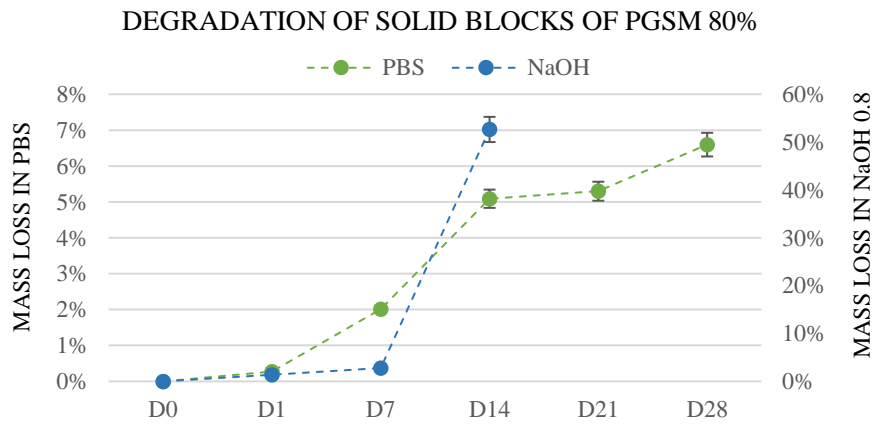


Fig. 76. Degradation profile of PGSM 80% solid blocks under PBS and NaOH 0.8M. Mean \pm S.D, n = 5.

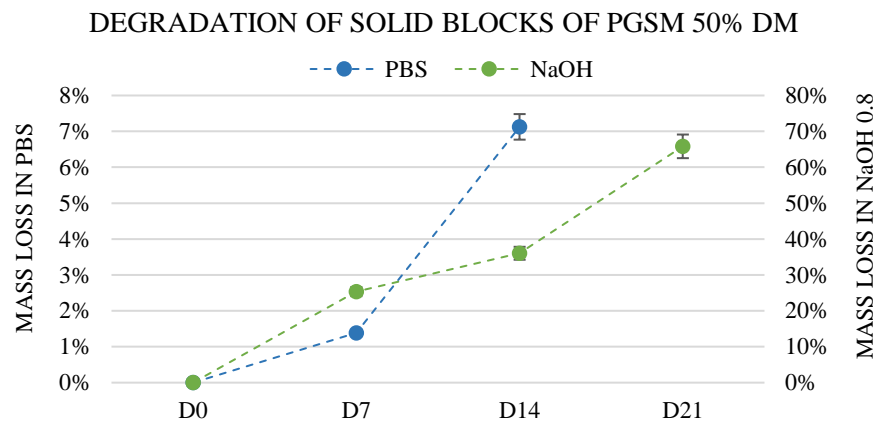


Fig. 77. Degradation profile of PGSM 50% solid blocks under PBS and NaOH 0.8M. Mean \pm S.D, n = 5.

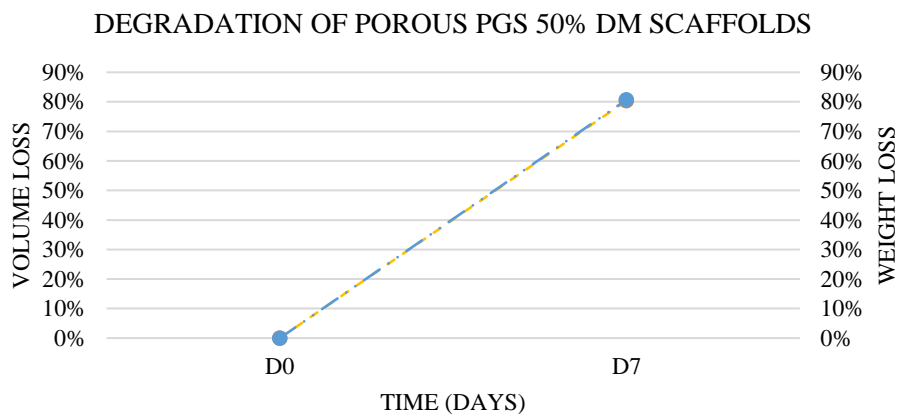


Fig. 78. Degradation profile for porous PGSM-50% scaffolds in NaOH 0.1 M. Assessed through volume and weight loss, both percentages show similar behaviour. Mean \pm S.D, n = 5.

The degradation profile of PCLMA:PGSM was also assessed on porous scaffolds, as the emulsions are of greatest interest for the polymer blend. Results can be found in Fig. 79.

DEGRADATION OF POROUS PCL:PGS SCAFFOLDS

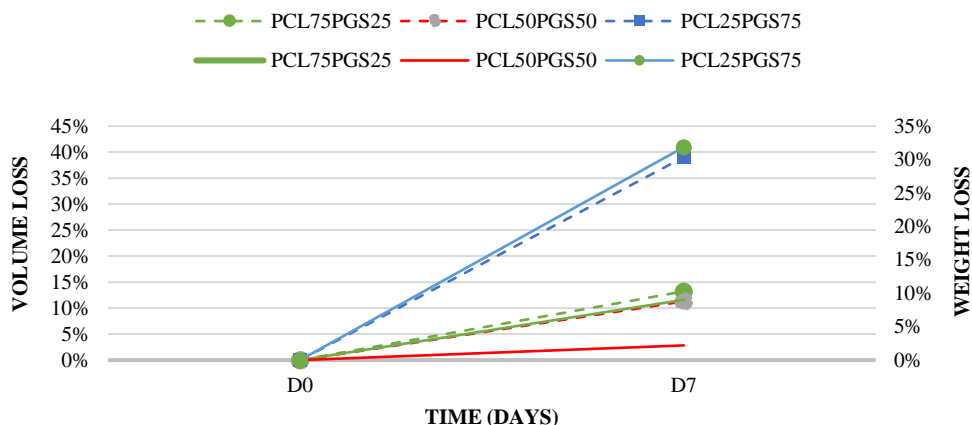


Fig. 79. Degradation profile of porous PCL:PGS scaffolds in NaOH 0.1M. Loss is measured in volume and weight. Mean \pm S.D, n = 5.

7.4.2. Cells response to 2D polymer environments

7.4.2.1. PCLMA and PGSM films

Once the materials have been characterised both mechanically (*Chapters III to V*) and chemically (*Section 7.4.1*), the interaction between the material and the scaffold was explored. To simplify the environment in which the cells would be exposed, bulk thin films of PCLMA and PGSM were manufactured by mixing the polymer solution with 10% w/w of photoinitiator and spin-coated into thin films. After being washed in methanol and water, they were seeded with Y201 cells and fed with serum-free media. Their metabolic activity was tracked for 7 days (Fig. 80).

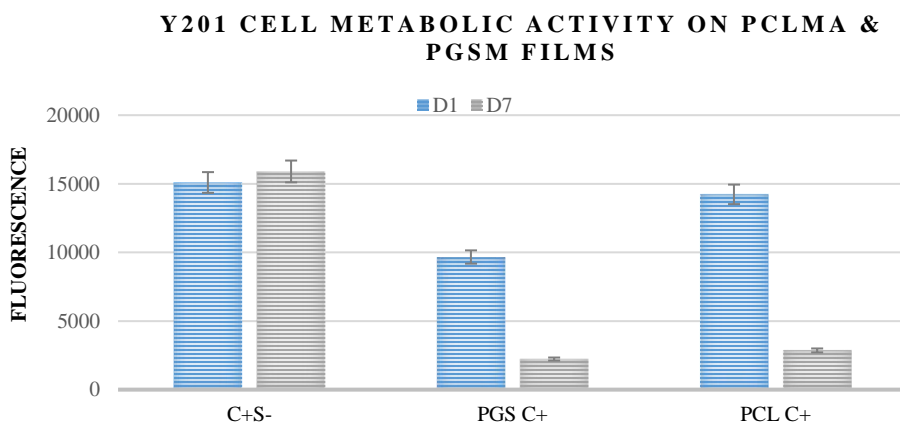


Fig. 80. Resazurin assays performed on PCL and PGS methacrylated films seeded with Y201 cells. (Blue) attachment at D1 and (grey) cell metabolic activity at D7. C-S-: media control, C+S-: cell control, PGS C+: seeded PGSM scaffolds, PCL C+: seeded PCLMA scaffolds. Mean \pm S.D, n = 5.

As observed, cells seem to successfully attach to the surface of the films and proliferate early, however the sustained proliferation can be compromised by the lack of space and a change in morphology (they showed to contract into round-like bodies).

In Fig. 81, Y201 cells have a spindle-like morphology whilst proliferating and become round when going through apoptosis or changes in the stiffness of the substrate [398]. The images also show cells successfully attaching to the surface of the films on day 1, and cells still attached to the films on day 7, but with the change in morphology and probably death.

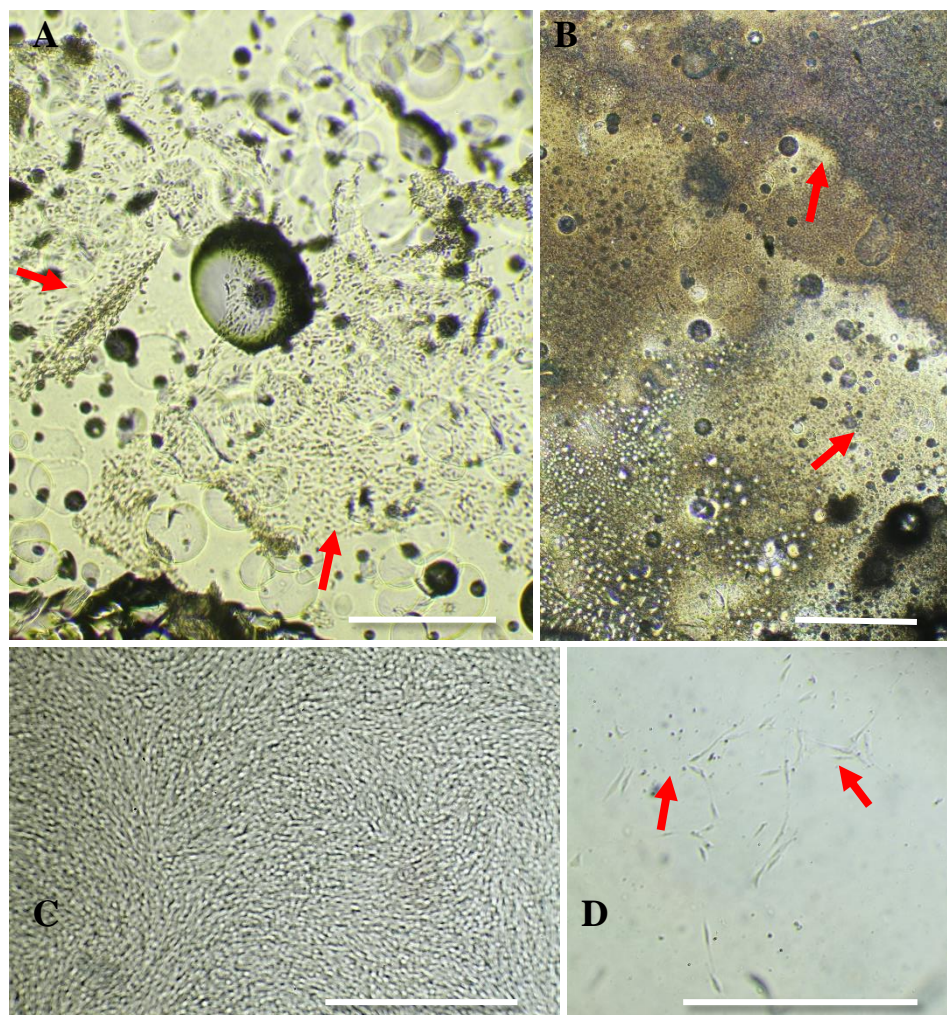


Fig. 81. Y201 cells seeded on polymeric films. A) Cells at day 1, successfully attaching to the films. B) Cells at day 7, attached and proliferated on the films, but with a round morphology, associated with apoptosis. C) Confluent Y201 cells on well plates. D) Cell non-attached to the films, growing between the well plate and the film. Scale bars are 400 μm .

To investigate how features on the surface of the film impacted on the cell attachment, the experiment was repeated, but half of the PCL and PGS films were previously coated with air plasma for 60 s at 50 W. The effect of the coating is shown in Fig. 82. This indicates that plasma coating does improve the cell attachment to both of the scaffolds.

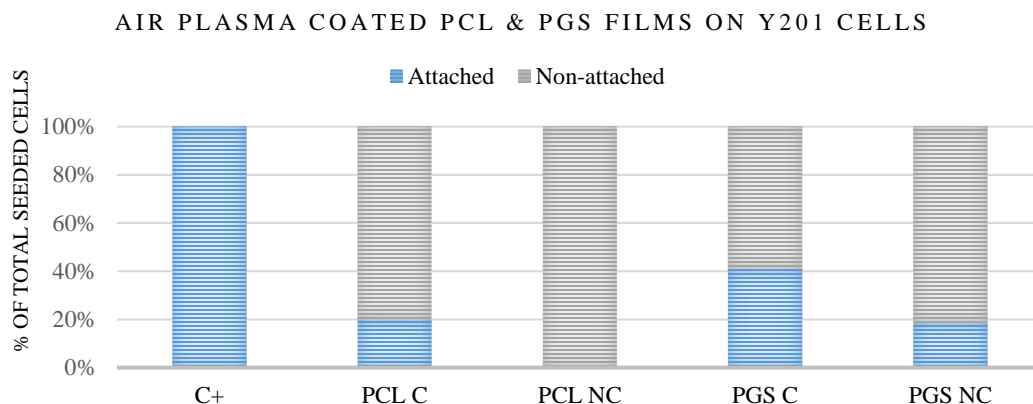


Fig. 82. The effect of air plasma on PCL and PGS methacrylated films was explored by seeding them with Y201 cells and tracking their attachment on day 1. C+: cells control, PCL C/NC: PCLMA coated/non coated films, PGS C/NC: PGSM coated/non coated films. Mean \pm S.D, n = 10.

7.4.2.2. Hydrogel films

Another way of functionalising the surface of scaffolds is through coatings. Such process can be done with hydrogels which offer a tailored viscosity and attractive chemistry. Due to their high-water volume, hydrogels can flow and cover bulk and porous surfaces. Additionally, they can endow the coated surface with certain chemical, improving their attractiveness to cells and molecules. To understand if this could be of value, the interaction between cells and hydrogels was first explored.

As a first step, blends of gelatin and a source of sugar were prepared and put in contact with Y201 cells. As shown in Chapter VI, gelatin-sugar blends were produced into thin films by spin-coating. To examine the response of cells to the gelatin-sugar blends, the films were seeded with 50,000 cells and their metabolic activity tracked for 7 days; the comparison between cells seeded on the well plate (C+), and three different Gel:Gluc solutions (B2, C1, C2) is reported in Fig. 83.

Y201 CELLS PROLIFERATION ON GEL:GLU FILMS

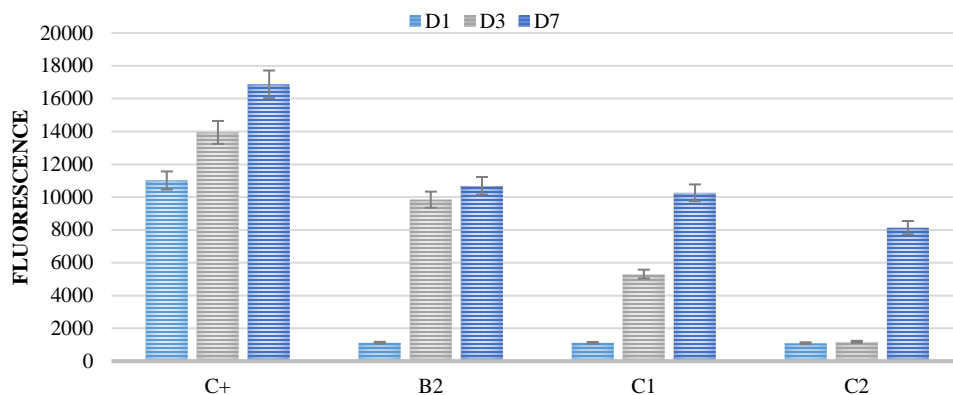


Fig. 83. Y201 cells were seeded on Gel:Glu B2, C1 and C2 films to assess their metabolic activity over 7 days. C+: control, cell seeded on tissue culture plastic. As a reference Gel:Glu:dH₂O composition of B2: 04:01:08, of C1: 02:01:16, and of C2: 04:01:16. Mean \pm S.D, n = 5.

All three combinations of Gel:Glu encouraged cell proliferation over the time, with a more linear behaviour on B2 films. The rapid increase by C1 and C2 from day 3 to 7 can be due to the film's degradation and release of sugars into the media (Fig. 84).

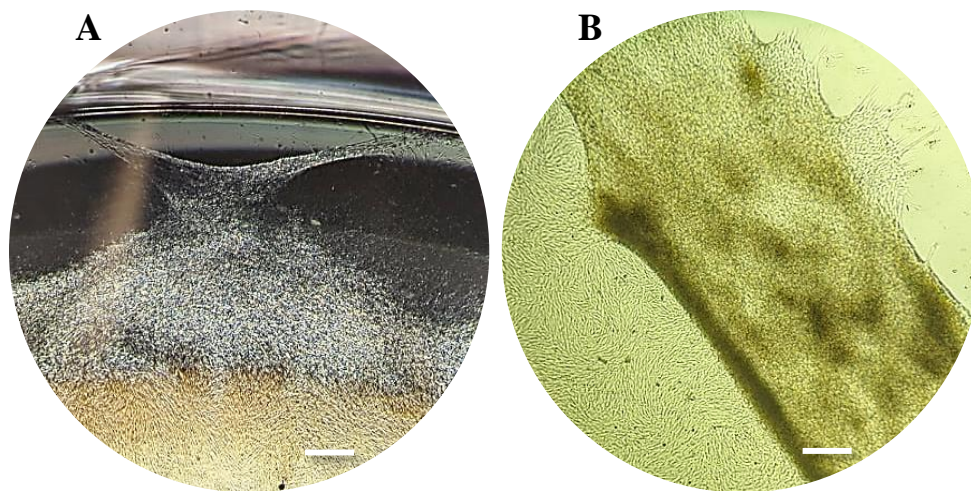


Fig. 84. A) Cell films' unity help them migrate through the degrading Gel:Glu surface. B) Gel:Glu has folded over itself, trapping some cells within; however, some colonies are looking for some empty space and move into the surface of the well plate. Scale bar is 100 μ m.

7.4.3. Cells response to 3D polymer environments

At this point, there was an initial understanding of the behaviour of the material in an aggressive environment (alkaline, mimicking cellular), and of the interaction between cells and the polymeric material, and cells with hydrogel solutions.

The next step was to take the somehow controlled environment of two-dimension experiments, and scale into the three dimension, getting one step closer to the reality of cells and tissues.

7.4.3.1. PCLMA LM and HM polyHIPE scaffolds

7.4.3.1.1. The effect of surface functionalisation on cell attachment: air plasma

As evidenced above, cells reported higher metabolic activity on air plasma coated surfaces. The experiment was then scaled up to the scaffolds to investigate if such positive effect would be observed as well. For that, the surface of PCL scaffolds was treated with a range of powers (5 – 95 W) and times (0.5 – 7 min) with the aim of improving the scaffold's attractiveness to cells.

The wettability of PCLMA scaffolds was measured through the water contact angle, as described in *Chapter 2, Section 22.5*. The polymer surfaces were functionalised using an air plasma machine. One

Wettability of PCLMA scaffolds at different exposure scenarios (power and time).

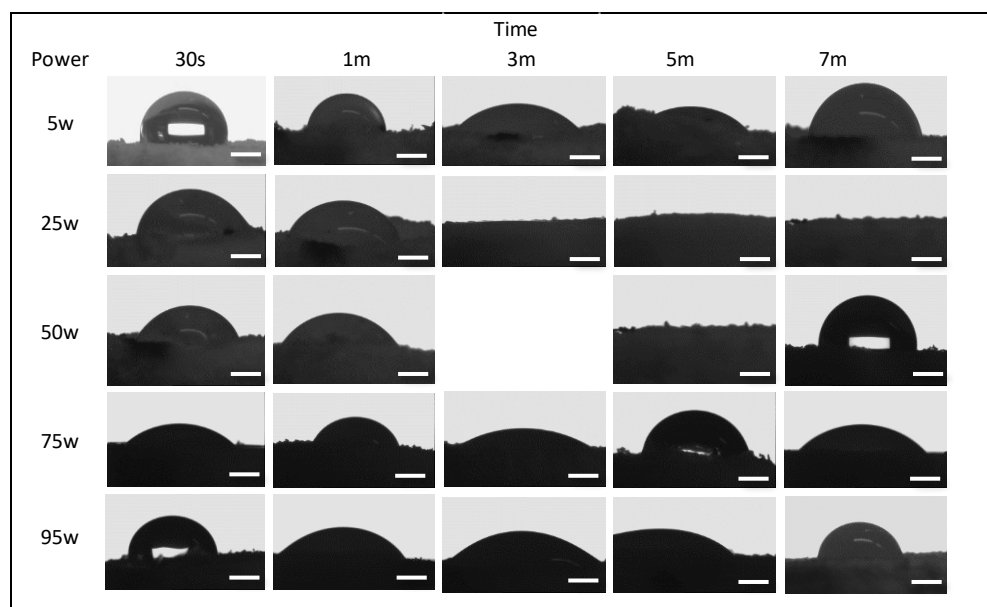


Fig. 85. Front images of a water droplet injected on the surface of PCLMA scaffolds. Images are taken after 5 seconds. The water contact angle was registered from the above images and reported in Table 23. These are representative images of 5 samples per variable. Scale bars are 0.5 mm.

different sample was exposed at each combination of power/time and the image gas taken after 5 seconds. Results are shown in Fig. 85 and Table 23.

Table 23. The changes in wettability are registered below. Values between 0 ° and 90 ° indicate hydrophilic surfaces; whilst 90 ° to 180 ° angles indicate hydrophobic surfaces. All values are in degrees. *: sample compromised. ** < 5 degrees.

watts\time	30s	1m	3m	5m	7m
5w	102.4	91.6	62.1	73.1	58.4
25w	77.7	68.9	40.7	12.5	25.3
50w	73.3	80.8	*	**	112.5
75w	68.3	84.7	48.1	92.6	83.1
95w	107.1	74.6	100.6	81.5	82.5

Values below and close to 50° are associated with active surfaces [399, 400, 401]. As observed, surfaces treated with 3 min and 25 W, 75 W and 7 min for 5 W, are close to such values.

Optimised experiments have been tried on Y201 cells. Before being seeded, the constructs were soaked overnight into FBS to allow the serum proteins to attach to the scaffolds and support cell attachment and early proliferation. The cells' behaviour on PCL LM and HM are shown in Fig. 86. On day 1, cell attachment was around 50.5% ± 1.5 for all coated and non-coated scaffolds, as well as for LM and HM scaffolds. These results were not as expected and can be a consequence of the early experimentation on 3D structures and Y201 cells, as the fluorescence readings were quite low (between 1800 and 2200 au) for what has been previously reported on that cell line. However, the difference between coated and non-coated scaffolds is still obvious.

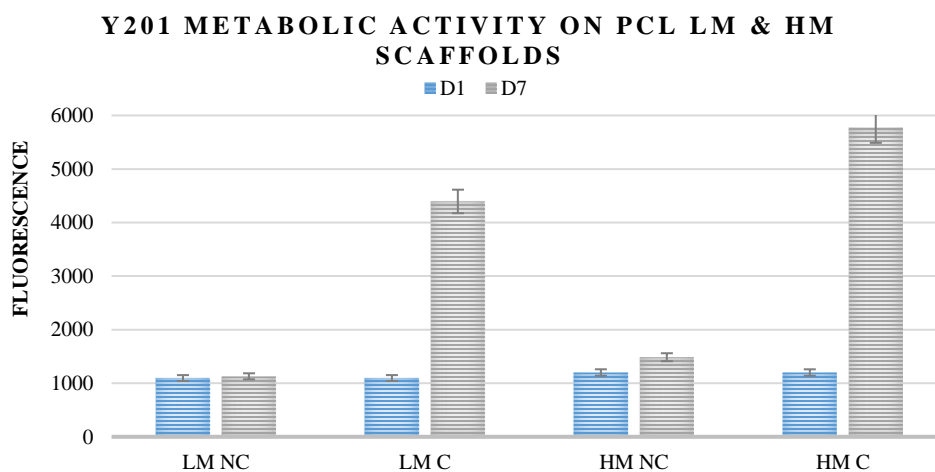


Fig. 86. Y201 cells seeded onto PCL LM & HM scaffolds, coated and non-coated with air plasma. Their proliferation has been tracked for 7 days using Resazurin metabolic assay. LM C/NC: low methacrylation coated/non-coated, HM C/NC: high methacrylation coated/non-coated. Mean ± S.D, n = 5.

7.4.3.1.2. Ideal combination between scaffold size and surface functionalisation for cell attachment

As it was reported above, the air plasma coating could support the cell attachment for the first hours after seeding, therefore that surface functionalisation technique was implemented in future experiments.

As a next step, we studied the availability of space where cells can attach and proliferate without facing limitation in nutrients and area to perform their metabolic activities. For that reason, three sizes of scaffolds were trialled.

Initially, hES-MP cells were seeded onto PCLMA LM and 50% DM cylindrical scaffolds. The optimisation experiments on 3D and hES-MPs allowed for definition of the most adequate size of scaffold, cell seeding concentration and time in-between seeding. Table 24 illustrates the experiment and the best results obtained from Resazurin metabolic assays. Attached and non-attached cells were calculated by measuring the metabolic activity from the scaffolds alone and of the empty used well plates.

Table 24. Parameters considered to choose the ideal PCL scaffold.

Scaffold size	Air plasma	Cell behaviour
Small	Coated	Attached
		Non-attached
	Non coated	Attached
		Non-attached
Medium	Coated	Attached
		Non-attached
	Non coated	Attached
		Non-attached
Big	Coated	Attached
		Non-attached
	Non coated	Attached
		Non-attached

These experiments allowed to select big (4-6 mm wide), coated scaffolds as the optimal constructs for cell seeding as the cell attachment at day 1 was observed to be 43%, whereas only 4% of total cells attached on non-coated scaffolds and only 11% on the coated, smaller scaffolds. Additionally, the highest metabolic activity was identified on scaffolds with one-hour in-between seedings (on each side) as the waiting time (before turning around and/or adding media).

7.4.3.1.3. The effect of the degree of methacrylation of PCL HIPEs on cell proliferation

The previous experiment narrowed down the optimal seeding conditions. And, as reported in Chapter III, the mechanical properties of both PCLMA LM and 50% DM materials were attractive for the bone tissue engineering applications. Therefore, an analysis on the effect of the degree of methacrylation on cell culture was developed. The metabolic activity over 14 days of hES-MPs seeded on both materials is shown in Fig. 87.

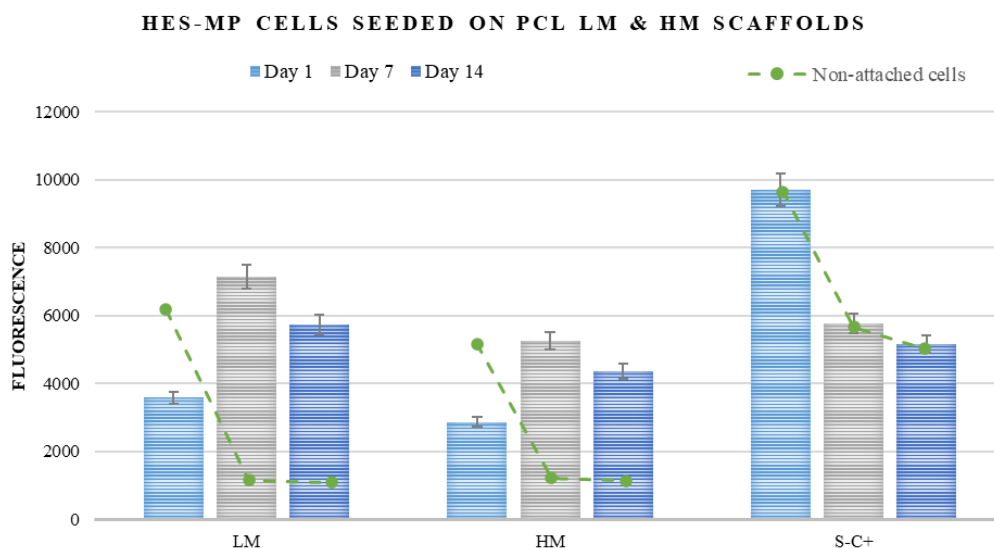


Fig. 87. hES-MP cells were seeded on PCL LM & HM and their metabolic behaviour tracked for 14 days. The green dotted line shows the cells that were not attached to the scaffolds and their viability over the time. S-C+: cells control. Mean \pm S.D, $n = 10$.

7.4.3.2. PGSM 50 and 80% polyHIPE scaffolds

The ideal combination between scaffold size and surface functionalisation for cell attachment and proliferation.

The next step was to perform the same optimisation experiments on PGSM 50% and 80% scaffolds.

During the pandemic, all reservoirs of BAC cells were lost therefore only part of the work was developed on these cells. The optimisation experiments allowed for determination of the most adequate size of scaffold, cell seeding concentration and time in-between seeding. Results are shown in Fig. 88.

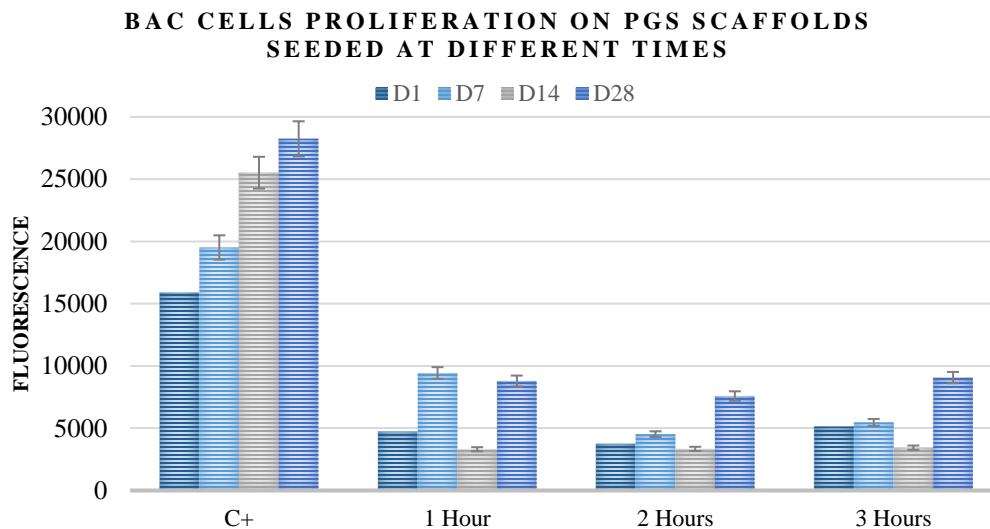


Fig. 88. This experiment tested three different times in-between seeding and adding media for BAC cells on PGS 50% scaffolds. The ideal time was explored to optimise the number of cells attached and how that affected cell numbers over 28 days of culture. Mean \pm S.D, n = 10.

As evidenced with PCL scaffolds, the best early attachment and proliferation results on PGS scaffolds was shown when media was added one hour after seeding/turning around. A decrease in metabolic activity at day 14 was observed in several experiments, with not obvious explanation.

7.4.3.2.1. The effect of the degree of methacrylation of PCL HIPEs on cell proliferation

After determining the ideal seeding parameters, a comparison between materials was made. PGSM scaffolds of two degrees of methacrylation (50 and 80%) were seeded with BAC cells to assess their metabolic activity. The attachment on day 1 was 75% on PGSM 80% DM, compared to 35% on 50% DM. The metabolic activity of BACs dependant on the degree of methacrylation was assessed over 28 days and illustrated in Fig. 89.

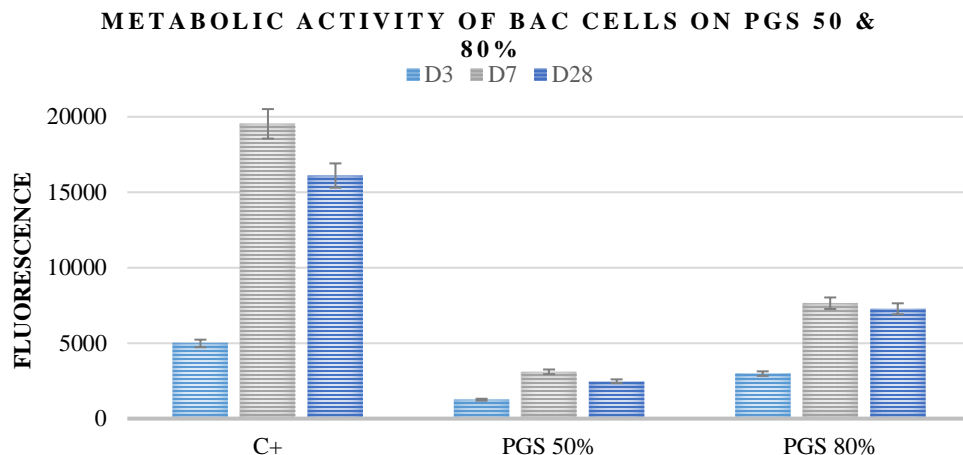


Fig. 89. BAC cells were seeded onto PGSM 50 and 80% scaffolds. Their metabolic activity was tracked over 28 days. C+: cells control. Mean \pm S.D, n = 10.

Even though PGS 80% showed a higher metabolic activity over time, it was decided that PGS 50% possessed a porosity and mechanical properties more attractive to the project, therefore all experiments were continued with this degree of methacrylation. This was defined in *Chapter IV, Section 4.4.3.2*.

7.4.3.2.2. The effect of surface functionalisation on cell attachment: fibronectin

As a subsequent step, the scaffolds should be surface functionalised. Initially it was intended to use air plasma as it has impacted positively on PCL scaffold cell cultures.

However, as explained in Chapter VI, PGSM scaffolds still presented problems whilst being dried. Therefore, a liquid coating was explored.

When hydrogels coat surfaces, they allow their proteinic composition to be exposed in the surface, attracting cells and other molecules. Fibronectin has been reported to support proliferation and differentiation during chondrogenesis. We want to propose PGSM scaffolds as the chondral layer for osteochondral scaffolds, so fibronectin was chosen as a first choice of coating.

Scaffolds were immersed in a 50 μ g/ml solution of fibronectin and left there overnight before being seeded with Y201 cells. Results of viability between day 1 and day 7 are shown in Fig. 90. However, cells did not seem to be affected by the fibronectin coating.

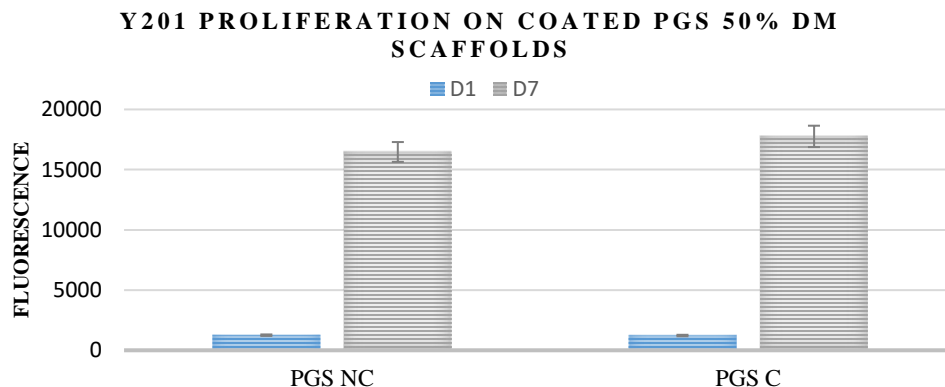


Fig. 90. PGSM scaffolds were coated with a 50 µg/ml solution of fibronectin and seeded with Y201 cell. Their metabolic activity was assessed by Resazurin assays over 7 days. Mean ± S.D, n = 5.

7.4.3.2.3. The effect of surface functionalisation on cell attachment: gelatin

As an alternative to fibronectin coating, scaffolds were submerged in a 0.1% (w/v) gelatin solution instead. As the original methodology included an additional step where scaffolds were submerged in FBS before seeding, some of the scaffolds retained this step, and some scaffold were simply coated with gelatin. Sterilisation of gelatin and gelatin-FBS scaffolds was performed with UV light for 1.5 hours. Scaffolds enriched with FBS were then located in a well plate with the surface covered with an FBS solution and kept there for at least 2 hours before being seeded. The attachment at D1 was observed to be 34.5% for Gel-coated scaffolds, 54.67% for Gel-FBS-coated scaffolds, and 61.7% for non-coated scaffolds. Early proliferation is shown in Fig. 91. As observed, the coating with hydrogels (gelatin and alginate) did not significantly impact on cell attachment nor early proliferation, however when added to the FBS step, it showed an important difference over time.

ATTACHMENT AND PROLIFERATION OF BACS ON GEL-PGS 50% SCAFFOLDS

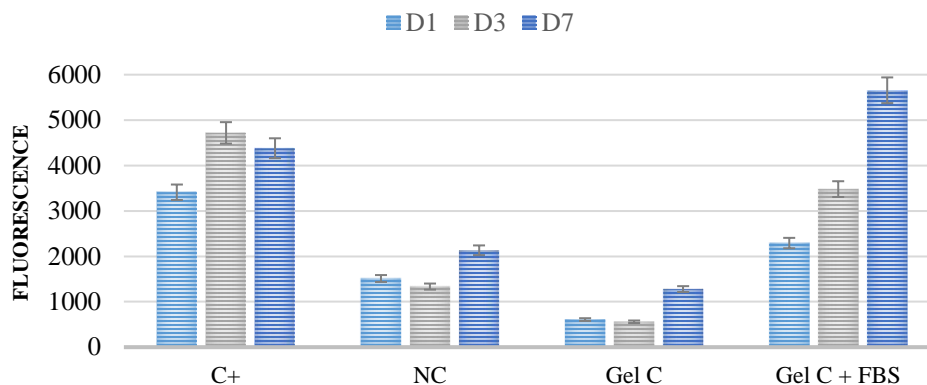


Fig. 91. Attachment and proliferation of BAC cells on Gel-coated and Gel-FBS-coated PGS 50% scaffolds were assessed through Resazurin assays. C+: cell control, NC: non-coated, Gel C: Gel-coated scaffolds, Gel C + FBS: Gel-FBS-coated scaffolds. Mean \pm S.D, n = 10.

7.4.3.2.4. The effect of space limitation on cell attachment: PDMS rings

It was also hypothesised that the cell attachment could be improved by limiting the culturing and the “feeding area” (are on the well plate). To explore this, PDMS rings were manufactured and used as a barrier tightly surrounding the scaffolds, limiting the space where cells could interact and forming their attachment on the surface rather than on the well plate. The PDMS rings were only kept for 24 hours after seeding. However, they impacted negatively on cell attachment and affected cell metabolic activity for the following 6 days (Fig. 92).

PDMS RINGS ON BAC CELL ATTACHMENT

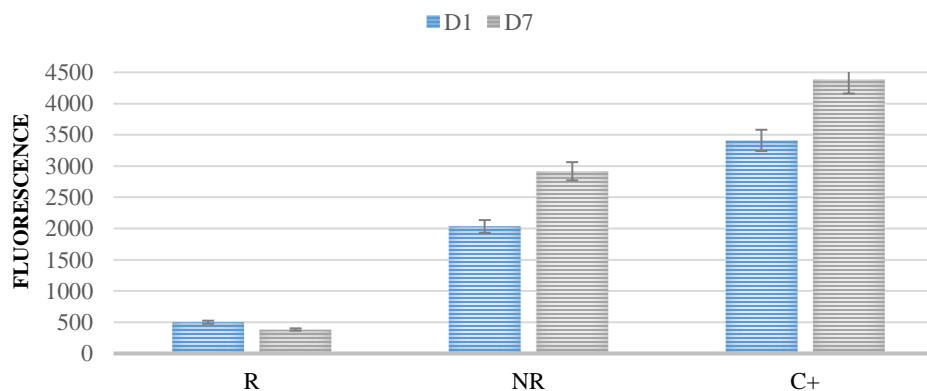


Fig. 92. Silicon (PDMS) rings were placed on the edges of PGS 50% scaffolds to improve cell attachment. C+: cells control, R: scaffolds with rings, NR: scaffolds without rings. Mean \pm S.D, n = 5.

7.4.3.3. Production of ECM and early differentiation

The conditions that were selected above were considered optimal enough to move on to the next stage: production of ECM as a result of proliferation and early differentiation. These experiments were done using hES-MP and BAC cell lines, looking to initiate differentiation to the osteogenic and chondrogenic lineage respectively.

For this, components on the produced extracellular matrix (ECM) like collagen, glycosaminoglycans (GAGs), calcium and alkaline phosphatase were measured over time.

7.4.3.3.1. On PCL scaffolds for osteo regeneration

These results were developed in collaboration with MSc students Sierra Kucko, Saida Musaeva and Ghazaleh Mazaheri Tehrani.

7.4.3.3.1.1. Alkaline Phosphatase (ALP) Activity

ALP is considered one of the most reliable biomarkers for osteogenic differentiation as ALP is a byproduct of osteoblastic activity. ALP assays were run on low (LM) and high (HM) methacrylated PCL scaffolds on day 14 of a culture with hES-MP cells. As observed in Fig. 93, there is not a significant difference between the materials, and the values are similar for what is reported for hES-MP cells on 3D scaffolds [402]. ALP activity is reported in UI/ml.

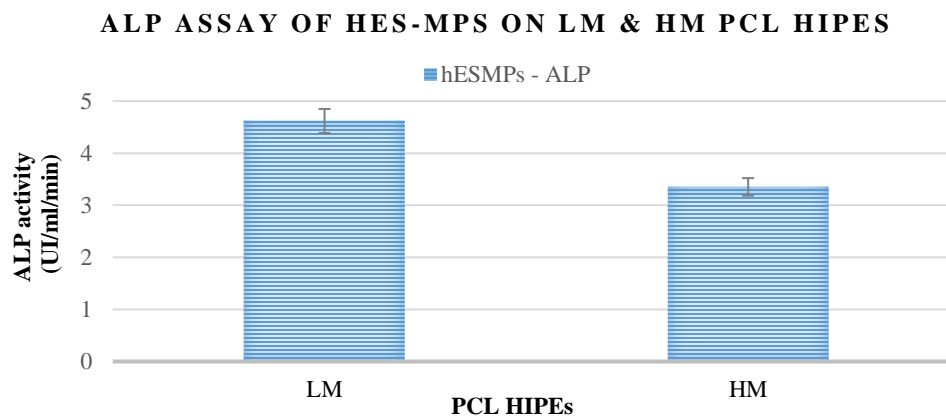


Fig. 93. ALP assay on LM and HM PCL scaffolds seeded with hES-MPs for 21 days. Mean \pm S.D, n = 5.

7.4.3.3.1.2. Collagen detection

Mesenchymal cells can undergo endochondral osteogenesis. For that reason, the production of collagen was measured. Experiments were developed in monolayer and 3D cultures for three different hES-MP cell seeding concentrations (25k, 50k and 75k). In 2D, the collagen production increased over time (Fig. 95). However, it was more observable in Fig. 94-A, where Sirius Red staining exhibited some degree of alignment that was visually apparent (Fig. 94B).

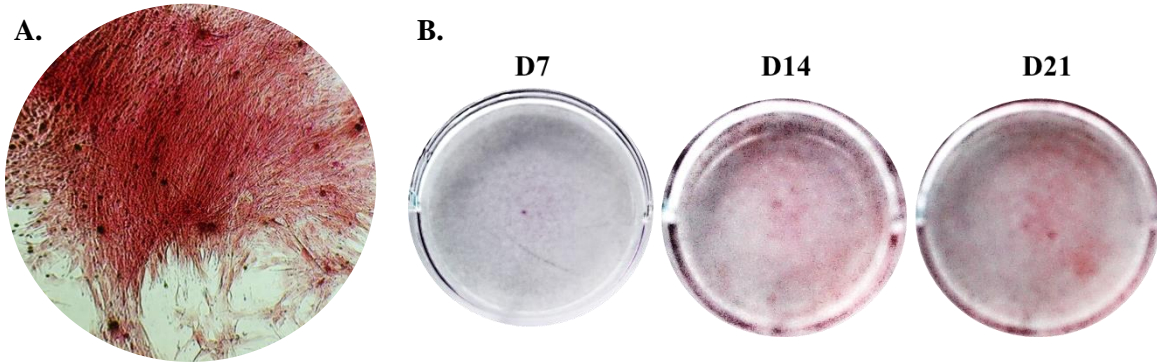


Fig. 94. A. The alignment of red fibrils can be observed. This evidences the spindle like morphology of hES-MPs and their behaviour as a culture, as well as the fibrous structure of the released collagen (25k cell, 2D culture). B. SRS does not show a significant change over the 21 days of the experiment. $n = 3$.

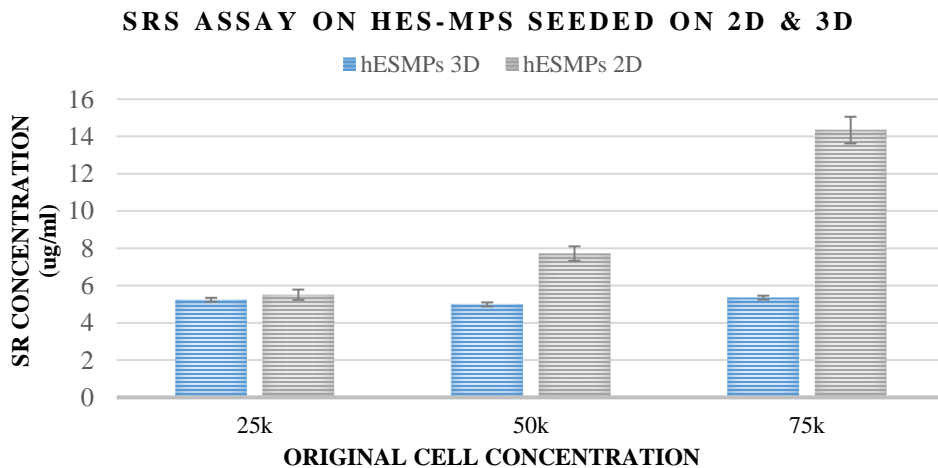


Fig. 95. Sirius Red assay performed on 2D and 3D cultures of hES-MP cells on day 21. Three different cell concentrations have been trialled to see the impact of cell concentration on production of ECM. Mean \pm S.D, $n = 5$.

7.4.3.3.1.3. Alizarin Red (AR) Assay

AR concentration was measured as an indicator of collagen deposition. Three different cell seeding densities were explored in both monolayer and 3D cell cultures. The mineralisation of hES-MPs has also been assessed in terms of initial cell concentration. This was tried only on PCL-LM as the results on PCL-HM were not significantly different from the TCP surface, used as a control (Fig. 96 and Fig. 97).

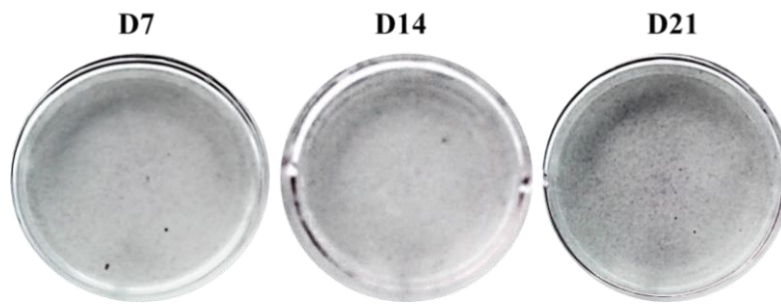


Fig. 96. Alizarin Red assays showed a visible difference on mineral deposition over the 21 days of the experiment; $n = 3$.

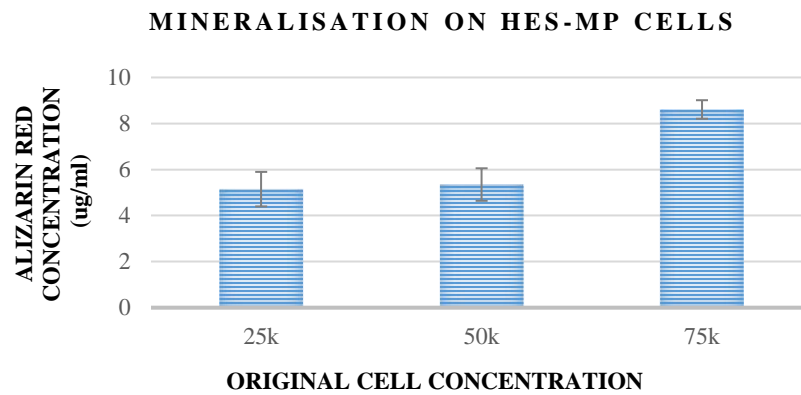


Fig. 97. An Alizarin Red assay was performed at day 21 on PCL-LM scaffolds seeded with different hES-MP cell concentrations. Mean \pm S.D. $n = 10$.

7.4.3.3.1.4. Glycosaminoglycan (GAG) and proteoglycan (Saf O) assays

Alcian Blue and Safranin O assays were additionally run as colorimetric assays to track the presence of glycosaminoglycans and proteoglycans respectively, in monolayer experiments over 21 days. The production of GAGs and proteoglycans was steady for the 21 days. As hES-MP cells were fed with osteochondral media, such results were expected (Fig. 98).

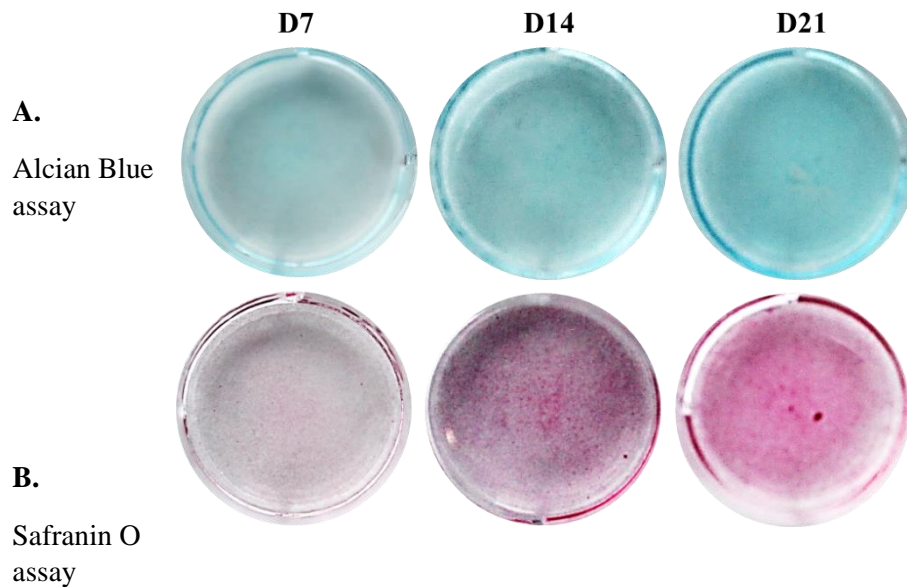


Fig. 98. A. Alizarin Red and B. Safranin O assays on 2D experiments of hES-MP cells over 21 days; n = 3.

7.4.3.3.2. On PGS scaffolds for chondral regeneration

The osteochondral layer is formed by a bone and a cartilage layer. We attempted to mimic the bone material with PCLMA scaffolds above assayed, and the chondral layer with PGSM material. Abovementioned efforts on PCLMA scaffolds were repeated on PGSM constructs. BAC and Y201 cells were used as they are and can differentiate into a chondral lineage respectively. Their metabolic activity and ECM production was reported as follows.

The metabolic activity of cells seeded on 50% PGSM over a period of 28 days is found in Fig. 99. As observed, cellular activity shows a sustained increment in metabolic activity when fed with CEM (chondrogenic media) versus the original BM (basal media). Another factor that was identified as important was the seeding concentration (data not included), where 50,000 cells seemed the optimal volume, similar to what was reported on PCLMA.

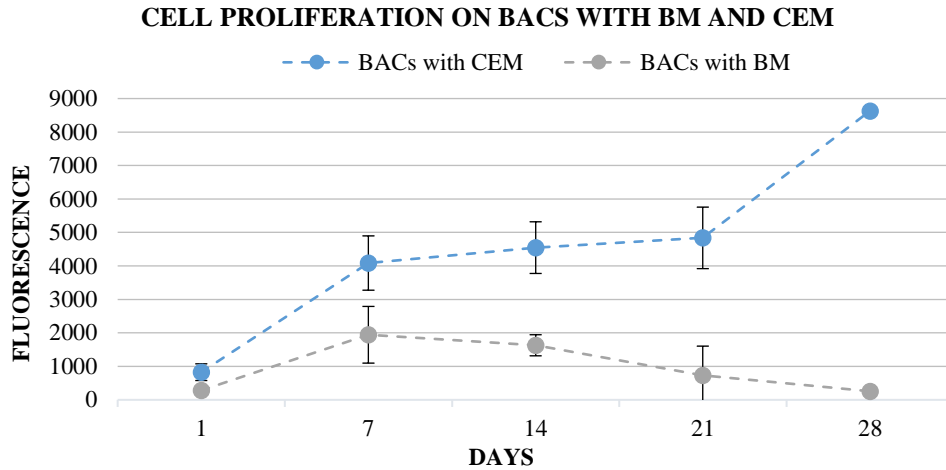


Fig. 99. Cell viability for BACs on PGS 50% scaffolds, fed with BM and CEM media for over 28 days. Mean \pm S.D, n = 10.

7.4.3.3.2.1. Collagen detection

To detect the presence of collagen, the scaffolds were fed for 21 days, and a Sirius Red assay was performed on day 21 and 28. The results herein show the effect of initial cell concentration that was seeded onto the scaffolds on the collagen concentration ($\mu\text{g/ml}$) (Fig. 100 - Fig. 102).

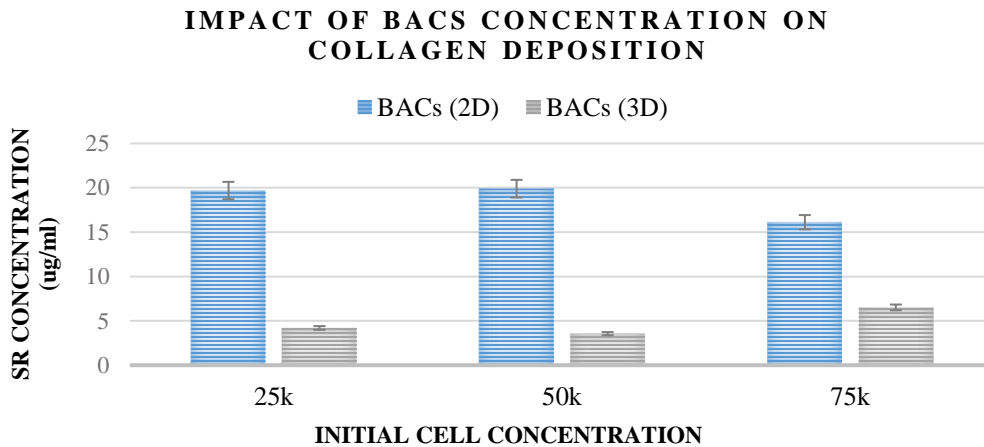


Fig. 100. The effect of the initial cell concentration on collagen deposition was studied on BAC cells seeded on PGS 50% scaffolds on day 21. Mean \pm S.D, n = 10.

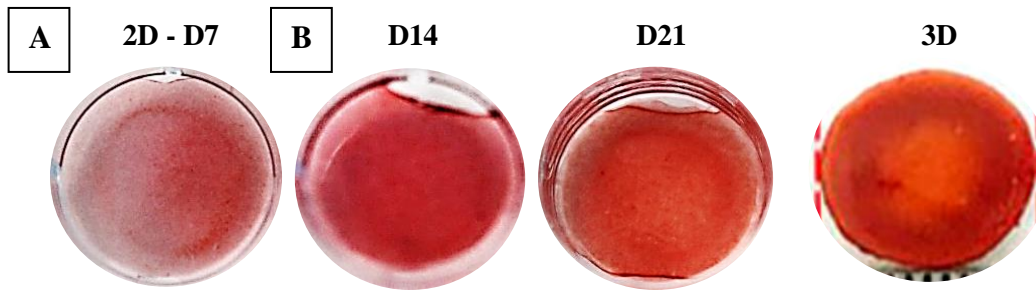


Fig. 101. A) SRS Experiments for BAC cells on 2D. B) SRS on a PGS 50% scaffold on day 21; $n = 3$.

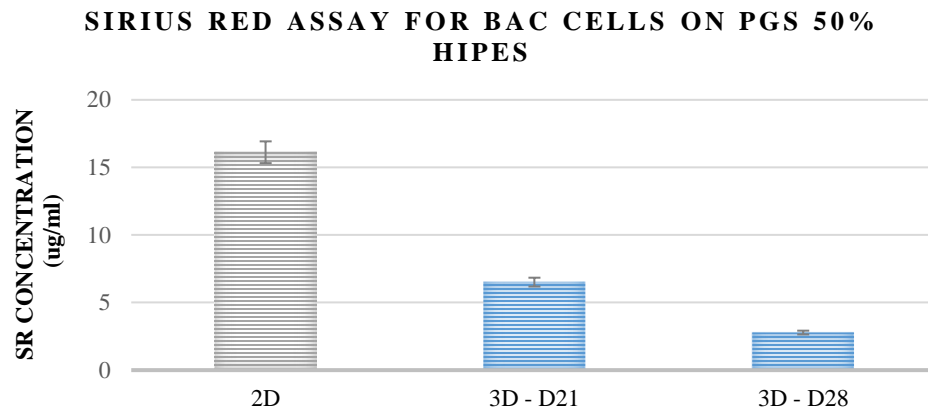


Fig. 102. Sirius Red Assay for BAC cells seeded on PGS 50% scaffolds. The assay was run on day 21 and 28 for 3D and only on day 21 for 2D, as it was used as a reference. Mean \pm S.D, $n = 10$.

7.4.3.3.2.2. Glycosaminoglycan (GAG) detection

GAGs are large linear polysaccharides that place a crucial role in cell signaling processes, and they are present in the ECM of cartilage. They play a role in the functional regeneration of cartilage. Alcian Blue assay was used to visually track GAGs at two cell concentrations (25,000 and 75,000 cells) and measured at day 21 and 28. These concentrations are reported on Fig. 103 and Fig. 104.

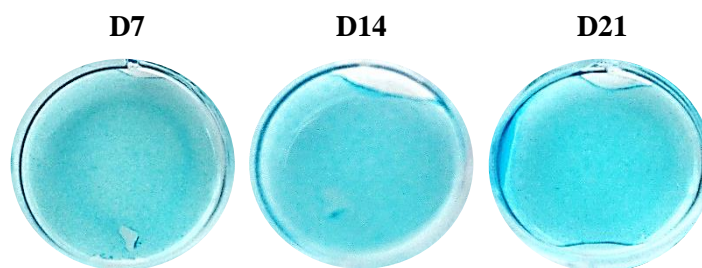


Fig. 103. Alcian Blue assays on 2D experiments of BAC cells seeded with 75,000 cells; $n = 3$.

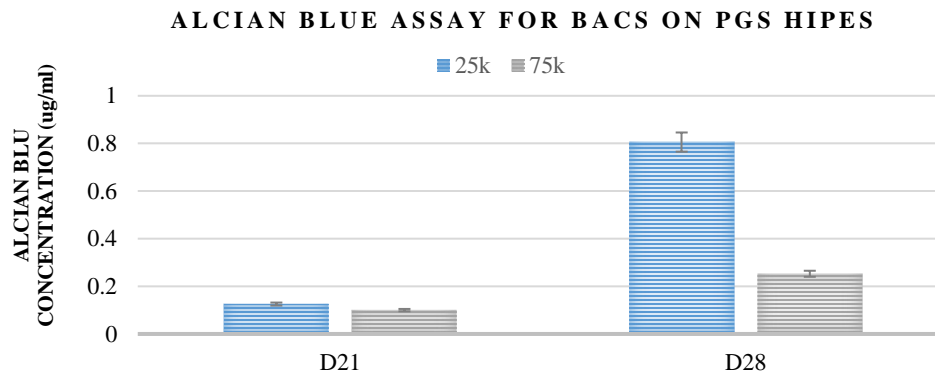


Fig. 104. Alcian Blue assays for the detection of GAGs on PGS HIPES seeded with BAC cells. The measurements were performed on day 21 and 28. Mean \pm S.D, n = 10.

7.4.3.3.2.3. Alizarin Red (ARS) and Safranin O

Finally, ARS and Safranin O assays were additionally run as colorimetric assays to track the presence of calcification and proteoglycans respectively, in 2D cell experiments over 21 days.

As illustrated on Fig. 105, there is a visible change over time in the presence of both calcium and proteoglycans, the latter being the most significant one, as expected on chondral cell lines.

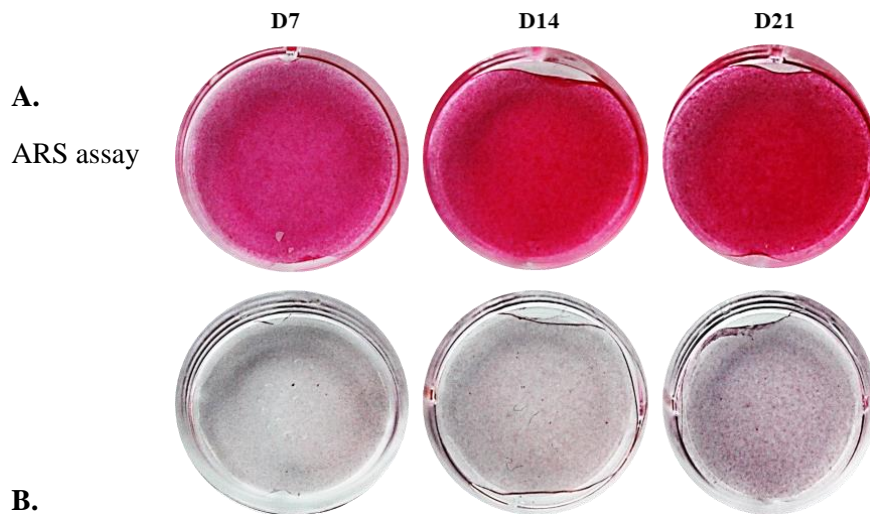


Fig. 105. A. Alizarin Red and B. Safranin O assays on 2D experiments of BAC cells over 21 days; n = 3.

7.4.4. Cell encapsulation

Cells seeded on both PCLMA and PGSM scaffolds have shown that they could attach and proliferate on the surface of the scaffolds. Additionally, they could somehow migrate into the scaffold structure. However, this migration can be too slow, compromising the integrity of the scaffold and the cell behaviour.

As cells have shown promising results when put in contact with hydrogels, a new experiment explored if they could be encapsulated and released as a packed unit on the surface and within the structure of the scaffolds. Gelatin and sodium alginate hydrogels were proposed due to their organic origin and their accessible degradation.

7.4.4.1. In calcium alginate

7.4.4.1.1. Beads

Calcium alginate beads were manufactured as described in *Chapter II, Section 2.2.9.1*. MLO5 and hES-MP cells were independently added to a sodium alginate solution at 37°C prior being submerged on a bed of calcium chloride. Cytotoxicity to both components was tested independently on 2D and reported in Fig. 106. MLO5 cells were used as a control due to their accelerated metabolism.

In an effort to understand how the volume of cells encapsulated and the concentration of sodium alginate would affect the integrity of the beads and cell viability, beads of 1 and 2% sodium alginate were created containing 60,000 and 120,000 cells per bead. A solution of trisodium citrate chelator was used to dissolve the beads at day 7 and the metabolic activity of the cells was measured through Resazurin assay. It was observed a high variability among the results (hypothesised to be due to the lack of reproducibility on bead morphology and size and the use of harsh chemicals to dissolve the alginate). However, the experiment supported cell viability and attachment to the plastic surface post-encapsulation.

CYTOTOXICITY OF HES-MPS & MLO5 CELLS ON CALCIUM ALGINATE

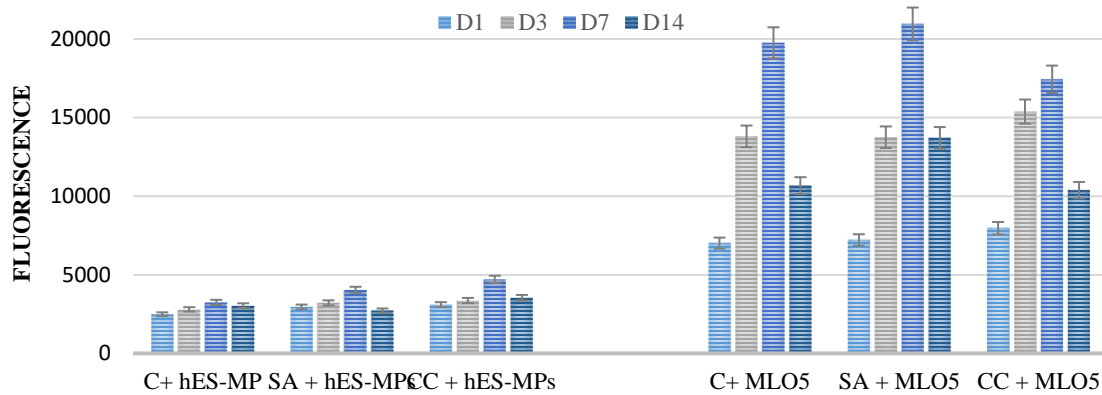


Fig. 106. Cytotoxicity assay of hES-MP and MLO5 cells on sodium alginate (SA) and calcium chloride (CC) surfaces, to assess the response of cells to the individual components of calcium alginate. C+: cells control. Mean \pm S.D, n = 5.

The degradation of the hydrogel matrix was tracked over 7 days, and it showed to be dependent on the cell metabolism, as shown in Fig. 107. Finally, the viability of the cell lines was assessed through MTT assays as the Resazurin salts cannot penetrate the hydrogel matrix.

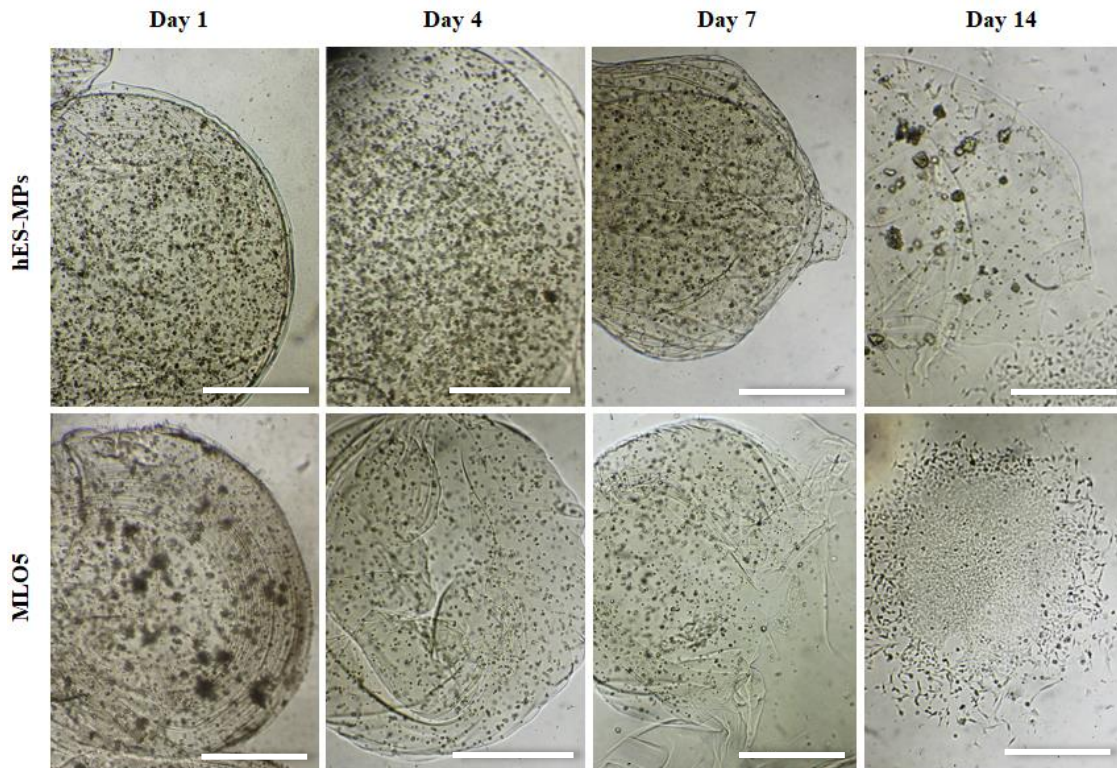


Fig. 107. Optical images of hES-MP and MLO5 cells encapsulated in calcium alginate beads and their natural degradation over 14 days. N = 5. Scale bars are 200 μ m.

The assays did not report significant values on the viability of the cells but created crystals that were observed under the microscope, evidencing the presence of active cells.

As observed by day 7 post-encapsulation, both alginate structures showed signs of disintegration, and by day 14, the bead had completely degraded in the case of MLO5 cells. In both cases cells remained in a circular formation, attaching to the surface of the well plate, and commencing a slow but steady proliferation for another week, when the experiment was interrupted.

7.4.4.1.2. Beads and polyHIPEs

The encapsulated cells were then mechanically stimulated into a PCL polyHIPE with the aim of supporting its homogeneous distribution within the scaffold, thus ameliorating cell proliferation and migration. Early results on cell proliferation are illustrated by results on Resazurin assays in Fig. 108.

Low values of fluorescence showed no significant difference between encapsulated and non-encapsulated scaffolds. However, the difference in behaviour between cell lines is easily observed, as well as an increase in cell viability on day 7 for hES-MP cells and day 14 for MLO5 cells, probably associated with the degradation of the hydrogel matrix and release of proteins into the scaffold, and the media.

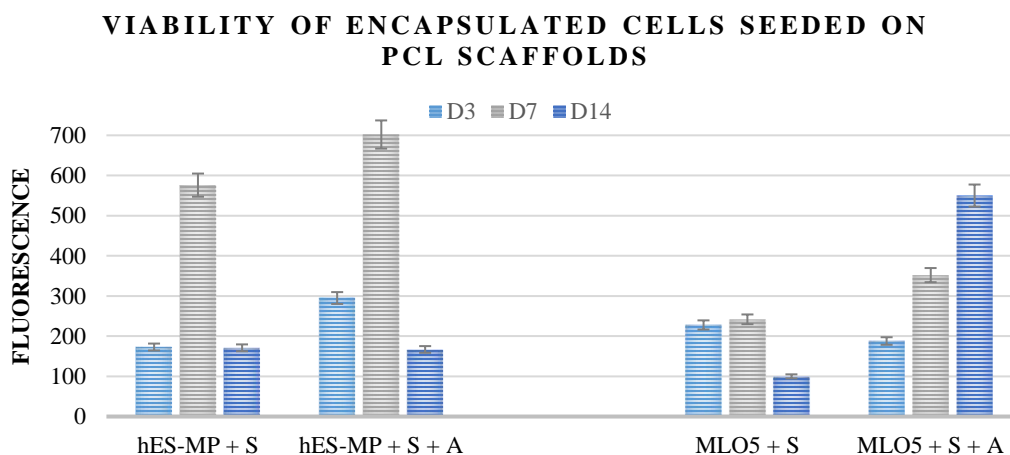


Fig. 108. hES-MP and MLO5 cells were encapsulated on calcium alginate beads and mechanically pushed into PCL-HM scaffolds. Their viability was tracked for 21 days. Mean \pm S.D, $n = 5$.

7.5. Discussion

This last chapter aimed at integrating all efforts in the material and the cellular fields. Both single materials and 3D environments were exposed to cellular lines of interest to investigate their immediate response and examine their behaviour through time. Such results support the use of PCLMA, PGSM and hydrogel-co-sugars as biomaterials for the early regeneration of cartilage and bone, and for their use as 3D porous scaffolds for osteochondral regeneration.

In the first instance, we investigated the behaviour of bulk and polyHIPEs in body-like environments. Their degradation patterns were observed under PBS and alkaline solutions (accelerated environment), comparing their mass and weight loss. PCL is a slow-degrading aliphatic polyester which suffers from structural degradation; its byproducts are released at the end of its degradation, and do not cause pH shifts as they are not acidic [111]. The hydrolytic degradation of PCL is autocatalytic and highly dependent on the chemical composition of PCL, for instance, its molecular weight. The literature has reported numerous contrasting results in which bulk PCL decreased significantly over the course of months, but with a noticeable reduction of its molecular number [111, 403, 404]. The differences between papers might be attributed to the diversity of manufacturing and post-manufacturing processes. It can also be related to the experiments' setups (e.g., size and form of sample, volume of media) [405, 406] which may promote a fully bulk degradation or a mix between surface-eroding and bulk, observed by the thinning of PCL fibres before their full degradation. However, bulk PCLMA exposed to the PBS buffer for 2 months only reported a mass loss of 2% and 13.37% for 50% and LM PCLMA.

Porous PCLMA scaffolds reported a different degradation pattern. In the first 5 days, their mass and density increased over time, related to the swelling of scaffolds by the alkaline solution. However, a loss in mass denotes an initiation of the degradation. This marks a structural change in which the slow degradation of the PCLMA layers led to a collapse of the voids, causing the scaffold to lose their structural integrity. This has also been observed in PCL networks [403], and electrospun PCL fibres [405]. Additionally, another research group working with electrospun scaffolds reported a change in the pore morphology as the degradation increased, with bigger pore sizes as the fibre thinned, before collapsing after 5 weeks [407].

Contrarily, PGS is better known for its “faster” degradation, where the polyester chains are broken down and degraded by hydrolysis [349, 408]. Bulk PGS immersed in PBS and NaOH solutions

showed a similar pattern in degradation (even if different timings), as they showed cracks in the surface before the scaffold broke into small pieces that degraded individually. The cracking behaviour was also observed on *Q-Z Chen's* PGS films [409] (and others [410, 408]) however they observed a volume increase due to water intake through time. Additionally, *in vivo* PGS scaffolds implanted in rat backs for 28 days confirmed PGS degraded through surface erosion maintaining the implant's geometry and mechanical strength, with an absence of surface cracks. In the present work, no water absorbance or a presence of cracking was observed; such differences with the literature may be due to the functionalisation process (methacrylation) performed on our scaffolds [411]. Ester crosslinks can degrade via hydrolysis, while methacrylate cross-links (shown in our scaffolds) cannot.

The degradation of porous PCL-PGS scaffolds showed a lower weight and volume loss than the individual materials, reinforcing the original assumption that by blending both materials together, the mechanical properties would be also enhanced, preserving the benefits of both PCL and PGS. Electrospun PCL-PGS fibrous scaffolds reported a weight loss of approximately 16% by day 7 [349], which is in line to our results ranging between 5 and 30%, depending on the PCL:PGS ratio. As it was previously identified on bulk PGS scaffolds, *S. Sant et al.* reported that surface erosion dominated the degradation of PCL-PGS scaffolds. Finally, *in vivo* trials of PGS disks on rats showed that in a physiological environment, PGS will predominantly be eroded by hydrolytic surface erosion [328]. This means that for large scaffolds the scaffold will gradually and linearly decrease in size during degradation, while their overall mechanical properties are not overly affected.

Scaffolds are implanted in a highly regulated environment, in particular for pH (7.4) and temperature (37 °C). Implanted materials are exhibited to enzymatic and cell mediated degradation, in particular during the inflammatory stage of wound healing around an implant [119]. Enzymatic degradation mediated by esterases will strongly affect the *in vivo* degradation of both PGSM and PCLMA. On the other hand, because of their highly hydrophobic character, both polymers are slowly degrading (~ months/years). Therefore, accelerated environments like alkaline, acidic, and enzymatic are commonly used. Alkaline experiments on bulk PCLMA and PGSM showed an increase of 10x in their degradation and a final mass loss higher than 70%. The differences in the degrees of methacrylation between 50 and 80% PGSM only varied in $\pm 10\%$ of mass loss. Despite higher methacrylation degrees being associated with higher mechanical properties it was found that lower methacrylation degrees reported less mass loss than higher DMs. This can be explained by the methacrylic cross-links of PGSM scaffolds (increased by the DM), which will not degrade through hydrolysis.

PCL and PGS methacrylated films were tested on 2D cell cultures to explore their cytotoxicity. It has been extensively reported the use of both prepolymer solutions *in vivo and in vitro* in a safe manner, but the addition of methyl groups and the use of photoinitiators could negatively impact on the soft reaction of cells to the polymers. *B.A. Dikici, et al.* worked with 3 and 4 arm methacrylated PCL and confirmed their compatibility with 2D and 3D *in vitro*, and *in vivo* applications [109]. Similarly, PGS non-methacrylated and methacrylated scaffolds have proven safe for a variety of cell lines, including cartilage [412], cardiac [409], and neural [413].

Polycaprolactone (PCL) is recognised due its robust mechanical, malleability, and co-blending properties. However, it falls short in terms of hydrophobicity, cell activity and hypersensitivity to certain protein groups [414]. Polyglycerol sebacate (PGS), being a softer material, does share the bioinert properties with PCL. PCL and PGS blends showed a higher viability than PCL itself, as reported by *Sant et al.* on PGS-PCL scaffolds with valvular interstitial cells for cardiac TE [349]. Similar efforts developed with electrospun scaffolds aimed to use benign solvents. However, it was noted an acidification of the cell media through the natural degradation of the scaffolds [118]. Even though this change in the media pH was also identified in our experiments, it did not significantly affect Y201 cell's behaviour. Nonetheless, PCL-PGS multi-layer scaffolds were 3D printed and electrospun with bioactive glasses that allowed the stabilisation of the acidity of the media during *in vitro* experiments [356].

The functionalisation of these materials, individually and as a blend, has been achieved through various approaches: i) the addition of external molecules [415] and particles [341, 344, 340] to the internal structure of materials, ii) the use of coatings and decorations on the outer layers (or surface of materials) of the material, and iii) through the treatment of material surfaces. As a main objective, all these initiatives aim to attract and start chemical cues that support the attachment, proliferation, migration, and differentiation of cell lines [416].

Surface activation procedures like plasma treatments can clean and activate material surfaces; by deposition or etching of functional groups and atoms [417]. When a gas is exposed to an energy source (waves and/or electricity), it becomes a mixture of free radicals, ions, and electrons that can clear surfaces from certain components, or reveal hidden ones [193]. Using plasma activation on biopolymers has proven not only to improve the material wettability (hydrophobicity), but to enhance molecule and cell attachment. Air plasma treated PCLMA and PGSM films significantly increased the cell attachment on Y201 cells. Even though it has been mentioned that surface plasma treatment

has no direct impact on cell growth [418, 419], an enhanced cell attachment does support a higher number of metabolically active cells proliferating and showed an overall improvement over time [279, 420, 420].

Cell adhesion was initially explored in the early 90's and showed enhanced results on contact angles between 65-70° for fibroblast cells on several polymer surfaces including polyethylene, polytetrafluoroethylene, poly(ethyleneterephthalate), polystyrene, and polypropylene [421]. More recently, human fibroblasts and endothelial probed better cell adhesion with contact angles between 48-62° and 35-50° respectively [401, 400].

Tailoring the functionalisation of surfaces has also been performed specifically on porous scaffolds and specifically on HIPEs, through acrylic-acid functionalisation [422], and air plasma [279, 423, 424]. Our PCLMA scaffolds treated with air (oxygen) plasma at different powers and times registered a range in wettability with θ values between 112.5° and 12.5°, with the majority of results on the hydrophilic spectrum (0° to 90°). In our case plasma coating improved both the cell attachment and proliferation as also reported on plasma-treated poly(styrene-EHA-DVB) polyHIPEs [425].

Wettability is usually connected to surface roughness, as evidenced on plasma treated electrospun PCL fibres. As the contact angle decreased, so did the fibre roughness, improving the cell attachment and early migration [416]. Additionally, it has been related to the film thickness from two perspectives. First, as mentioned by *Owen et. al.* in his work with EHA/IBOA polyHIPEs [279], the plasma activation/etching has a reach of only a few mm. Similarly, *Barry et. al.* showed that large objects (up to 1 cm) could be coated with plasma coating. Looking for an uniform coating, and taking into account our scaffolds were 6-8 mm long and 4-6 mm high, the scaffolds were coated on both sides.

Even though the prime objective of coating is to trigger early cell attachment, balanced hydrophilic surfaces can also promote cell migration to lower layers of the scaffold [401]. Second, it was found that the θ varied between 5-10% on polystyrene films as they increased in thickness [426]. This is a reference on the importance of determining ideal treatment conditions depending on the features of the scaffold. On the other extreme, most of reported plasma treated porous surfaces have reported collapse and destruction of the specimens when they were exposed to the plasma functionalisation for too long, or at too high powers [423, 427], as reported in the results section of this chapter.

Sometimes, surface functionalisation can also be achieved by the addition of full layers, or coatings, of bioactive materials. Hydrogels have been proposed as material coatings whose natural sources are well received by the cellular bodies and provide these entities with a proactive environment in all areas of the scaffold and can be tailored to remain for longer than energy treatments, without compromising the structural integrity of scaffolds [428]. Hydrogels can have a positive or a neutral charge from which both the underlying material and the targeted cells can benefit [429]. Additionally, as hydrogels are polymer chains with high contents of water, they can be tailored to adsorb and encapsulate molecules that could start chemical cues or attract cell lines, when exposed. PCLMA scaffolds coated with fibronectin and gelatin solutions were exposed to Y201 cells to assess an improvement in cell attachment and early proliferation. It was found that fibronectin did not significantly affect any of the metabolic activity. Fibronectin was selected as its arginine-glycine-aspartic acid (RGD) sequence directly interacts with cells via integrin binding and there is wide evidence on improved performance on biomaterial surfaces [430]. Fibronectin coated surfaces showed a positive variation in attachment and proliferation on endothelial cells [430]; but emphasised on the effect of the structure's topography on the adhesion of fibronectin ligands to the material. Similarly, fibronectin showed better results when fibronectin was conjugated rather than adsorbed to porous poly(carbonate)urethane scaffolds [431], which can explain the results reported in this chapter.

Contrarily, gelatin coatings crosslinked by covalent and chemical means have shown good adhesion, proliferation, elongation, and migration of cells on both 2D and 3D environments [432]. Our results agreed with these studies statements and reported a more significant improvement in cell attachment and proliferation when soaked on FBS prior to being seeded with cells. This can be associated with the incorporation of chemical cues within the gelatin, from which cells benefited, as confirmed by gelatin-HA scaffolds for bone TE applications [433]. Alternative glucose-gelatin-based crosslinking methods have been explored to prevent the use of more toxic crosslinking procedures such as acetaldehyde-based cross-linking [88]. The addition of sugars has proved to increase the viscoelastic properties of the material, as well as the water uptake [381]. These mixed carbohydrate systems have also been photo-crosslinked to increase the gel strength and delay the hydrogel biodegradability, whilst releasing the sugars and proteins [91]. For example, gelatin-heparin hydrogels were manufactured using Gel-MA and the glycosaminoglycan to promote chondrogenic differentiation and a tailored degradation [93].

Abovementioned initiatives aim to make the surface and inner structure of biomaterials more attractive to cells. However, novel approaches are looking to support cells moving through the construct's build, by re-introducing one of the oldest delivery technologies, cell encapsulation [434]. The initial objectives of cell encapsulation were to immobilise and isolate cell bodies from their surroundings, to support their mobility and transplantation. However, cell encapsulation can also be used as a means to concentrate and mobilise cell communities, distributing them in an either homogeneous or spatially defined way on new surfaces or constructs [435].

We chose gelatin and alginate as hydrogels for cell encapsulation because they comply with the properties required for an ideal cell encapsulation, such as biocompatibility, which is one of the biggest challenges that cell encapsulation faces for *in vitro* and *in vivo* applications. Moreover, the tunability of the hydrogels' crosslinking method, swelling, diffusion, and degradability [436], makes alginate and gelatin adaptable to a variety of cell lines and TE applications.

As observed in the results, a delicate balance should exist between the size of the bead, the cell density, and the degradation rate; a bead with too low mechanical properties can lead to early cell release, a high initial density can cause excessive proliferation which will restrict nutrient availability, and a delayed start on the hydrogel's degradation can limit nutrient permeability and lead to cell apoptosis. MLO5 cell metabolism promoted a faster degradation on alginate beads, compared with hES-MP cells. However, both cell lines retained a good viability after encapsulation. This has been reported in diverse settings, for example, human MSCs encapsulated in RGD modified alginate microspheres showed an improved cell attachment, growth, and release of angiogenic markers through the supplemented-encapsulation process [437].

Early experiments between alginate and PCLMA scaffolds showed good viability results for the duration of the experiment (14 days). A decrease in proliferation was observed from day 7 to 14 on hES-MP cells, which can be associated with the cycle of the cell line, but also to a possible saturation on the scaffold surface; cells have been reported to struggle to migrate into inner layers of the scaffolds. For such, cell beads were introduced to the polyHIPE constructs by mechanical means. Encapsulated hMSCs were encapsulated and printed using a redox-initiated PEG hydrogel carrier and released in a period of 5-7 days. The distribution of cells was homogeneous through the 3D printed construct, especially in isolated areas like the middle of the scaffold, even though the study also identified a decrease in the cell density on day 14 [435].

On the same line, gelatin-sugar beads were created for cell encapsulation and as a carrier for their immersion to polyHIPE structures. Gelatin is naturally biocompatible and biodegradable, which has also shown fit for the production of controlled release systems in film and particle form [93, 94]. Initially, sugar mediated gelatin crosslinked was achieved when the aldehyde groups of glucose (or aldose sugars) react with the free amino groups of gelatin, forming an aminoglycoside; the latter will continue reacting with other groups, hence creating a crosslinked network [88]. Gelatin-glucose disks were successfully created and tested as 2D platforms for culturing Y201. However, cell encapsulation proved a challenge as the amount of sugar required to crosslink the gelatin-sugar disks caused the cell stress and death prior to their release. No further experiments were conducted on these hydrogels. Future work would recommend using gelatin-glucose solutions for cell encapsulation thermally crosslinked, where the gelatin behaves like a carrier hydrogel supplemented with glucose. Such experiments could also be repeated using 2-deoxy-D-ribose (2dDR) sugar as a stimulator for angiogenesis [438].

Photocrosslinkable gelatin was also proposed as a means to crosslink cells encapsulated in gelatin-sugar hydrogel solutions. *Hoshikawa et al.* developed a styrenated gelatin that was crosslinked by presence of UV light and contained chondrocytes that proliferated and produced type II collagen after being released [439]. Gelatin methacryloyl (GelMA) has also shown a big potential for its moulding and 3D printing, as the bioink can be tailored to the need of various cell lines and constructs [89].

7.6. Summary

The objective of this chapter was to integrate the work presented in *Chapters III to VI*, where PCLMA and PGSM polymeric scaffolds were optimised so their mechanical and biochemical characteristics would be attractive for cell attachment, cell growth and early cell differentiation.

To assess this, different stages of the process were tested independently, and then integrated into one final experiment. Initially, the degradation patterns of solid and porous polymer disks under alkaline environments were reported in an effort to understand how the material would behave in a cell-like environment. Then, a variety of cell lines were exposed to monolayers of PCL and PGS to assess the material cytotoxicity, obtaining good attachment and metabolic activity.

As a next step, the cells were exposed to 3D scaffolds with numerous modifications that allowed to select the best material features (size and coating), and culture conditions (seeding concentrations,

seeding time, and supplemented media). Air plasma coated scaffolds with the highest surface areas showed the best results in cell attachment, and gelatin coated scaffolds showed a higher metabolic activity over time. Additionally, supplemented medias enhanced the production of ECM matrix for both osteo and chondral lineages, which set the foundations for future work on cell differentiation.

These experiments have allowed to determine the minimum parameters for each mimicked bone and cartilage layer, which will hopefully allow for the development of a cocultured bilayer PCLMA-PGSM scaffold.

7.7. Annex

7.7.1. The effect of space limitation on cell proliferation: Channelled scaffolds

As a preliminary trial to guide cells into specific areas of the scaffold and support their migration to the rest of the scaffold, channels were introduced using a needle Ga 14 (nominal O.D. of 2.1mm) as the design in Fig. 109 shows. Results showed that all cells fell into the well plate; therefore, further adjustments are required.

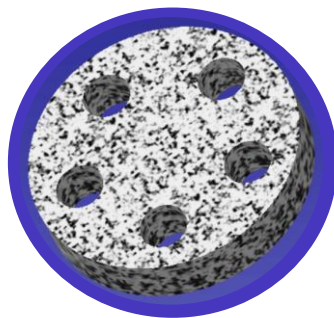


Fig. 109. *Model of a channelled scaffold using a flat ended Ga 14 needle.*

Chapter VIII: Future Work

8.1. Research & Development

8.1.1. Scaffold optimisation

Two polymer materials have been explored for the creation of water-in-oil emulsions. Successful emulsions have been manufactured and photocured, producing polycaprolactone methacrylate and poly(glycerol) sebacate methacrylate polyHIPEs. A bilayer scaffold has been produced to mimic the structure of the osteochondral unit in human joints. Future work needs to be developed to:

- *Tailor degradability to functionality.*
Making sure the properties of the polyHIPEs fulfil the mechanical and degradation patterns required by the biological environments.
- *Integration of scaffold and hydrogels.*
It has been shown that polyHIPEs can be created using hydrogel solutions as internal phase. Further development can include the use of photocrosslinkable hydrogels like GelMA.
- *Sustainability.*
Emulsions can be optimised to use reagents which are less toxic to the environment and potentially cytotoxic. For example, solvents like p-cymene and limonene can be used instead of toluene, chloroform and DCE.

8.1.2. Cell culture

The final step regards the successful implementation of material technology and biological response. Bilayer scaffolds (with and or without the hydrogel supplemented materials) should aim to attach, proliferate, and migrate into inner layers, however, to also:

- *Cell encapsulation in polyHIPEs.*
Cells have been encapsulated into alginate, but this can be done in gelatin and GelMA for a double photo-crosslinking and the creation of polyHIPEs emulsions with embedded cells.
- *Cell differentiation.*
Early differentiation has been explored in this project with positive results. However further exploration on the chondral and osteo differentiation of MSCs is required through the morphology of the 3D scaffolds and the supplemented media.

- *Co-culturing techniques.*

Chondral and bone cells should be seeded on bilayer scaffolds independently and with the use of a coculturing technique to understand the interaction between the material and the cell lines, as well as further metabolic pathways as the production of ECM and differentiation.

8.2. Commercialisation of PCLMA and PGSM polyHIPES

This doctoral project was submitted as part of the *Innovation to Market* programme at the London Business School. A market exploration and early commercialisation pathway was developed between September 2021 and March 2022.

8.2.1. Key Findings

The technology presented in this project aims to mimic this structural organisation and to adapt to the existing body environments. The designed and optimised 3D structures are made of biodegradable synthetic materials (some of them already FDA approved) [443]. Such structures are highly porous and interconnected and have been tested *in vitro* and *in vivo* for a variety of cell lines and organisms, proving that they are indeed biocompatible and bioactive [110, 347].

As my doctoral programme is in regenerative medicine, the first application was the biomedical industry, where this structure was proposed as an osteochondral plug for bone and cartilage tissue engineering.

The initial commercial hypothesis was that the scaffolds could be focused on musculoskeletal diseases to prevent the need for surgical procedures associated with partial and total joint replacements. To test our hypothesis, we developed a SWOT analysis focusing on the biomedical industry, and we identified that the market has an increasing demand globally.

In the UK alone, 1 in 10 people will develop a musculoskeletal disease, increasing the burden on the NHS. Additionally joint replacement surgeries are not new to the customer nor to manufacturers, and the replacement market is moving to a more mature stage [199].

Inherent in this is the threat that big players are already well positioned, with the budget and resources to spend enough time getting through the approval process and the challenges of product scalability.

Therefore, even though there are big opportunities in the market we believe the weaknesses and threats are more significant.

By exploring the potential uses of 3D scaffolds, the team identified that it could be used in almost any environment that requires the use of 3D structures to support the attachment and proliferation of cells and/or the development of lab-grown tissues.

Specifically, the development of lab grown tissues in the food industry has gained recent interest due to its benefits from the environmental, nutritional, and economical perspective.

The livestock industry is estimated to represent about 16.5% of all human-induced carbon dioxide emissions. Additionally, more than 1/3 of Americans and 2/3 of the world population are choosing to consume less meat for health reasons [444].

The alternative meat industry is expected to reach \$75 billion by 2027, the main constituent of which will be the plant-based food market, which is projected to grow by 1,000% over the next 10 years, reaching \$140 billion. The US, Singapore and Western Europe are key players in research and development of ventures in this area. For example, UK biotechs raised \$2.8 billion in 2020 [445].

This young market represents a big opportunity for our technology, specifically in the lab-grown meat industry. Already more than 70 cultivated meat startups exist worldwide, and most companies are transitioning from R&D to scalable manufacturing processes. As a reference, the growth trajectory of lab grown meat is expected to be about 2100 tonnes and £19 billion in 2030, with UK manufacturers taking between 10 and 15% of the market [445].

There are 3 main stages in the meat value chain: raw materials, the manufacturing process, and the distribution channels. Our role would be within the development of raw materials.

As a general overview of the process of meat cultivation, the first step includes the harvest of cells from healthy bovine samples. Those cells are then grown in two dimensions to make sure they are safe and high quality. The third step is where we come in. The cells growing in a two-dimensional plane need to be scaled to a three-dimensional environment so they can start creating the texture, colour and juiciness associated with meat. The procedure can be developed through various scaffolds, being them microporous, hydrogels or electrospun matrices which are then introduced into bioreactors to scale the creation of muscle tissue, and finally collected after a few weeks prior to being packed and distributed [446].

Our scaffolds fall into the microporous structure and have advantages over the others as they will provide a steady yet adaptive environment for cells to grow, and create tissue, but will biodegrade before reaching the customer's mouth. Even though this process may seem incongruous, the production of fermented beverages like beer and yoghurt, use 4 out of 5 steps (except the scaffolding).

Our 3D porous and biodegradable scaffolds can support both the research and manufacturing processes by offering porous scaffolds that:

- i) encourage the proliferation of skeletal (muscle) cells;
 - ii) provide structural support for the differentiation of skeletal cells that leads to tissue formation;
- and,
- iii) degrade before the muscle tissue is harvested.

Our competitive advantage is centred in:

- i) the ability to control the porosity and interconnectivity of our material;
 - ii) the biocompatibility of material-cell interactions;
 - iii) the controlled biodegradation of the scaffolds;
 - iv) the tuneability of the scaffolds' size and form to support both R&D (in vitro) and harvesting stages (bioreactors);
- and,
- v) the scalability and cost-effectiveness of the manufacturing process.

Through a thorough market exploration process we have identified companies around the world which are interested in acquiring our technology and enabling future collaboration to develop their cultured meat processes. They confirm that they require a biodegradable structure, that is porous enough for cells to attach, proliferate and create the own tissue, and that mimics as much as possible the natural structure of meat (being poultry, beef or seafood). We also identified that B2B companies developing meat supplements like fat do not operate within the same market as us and they do not a scaffolding step. We additionally had conversations with two venture capital firms that have

programmes (accelerators) focused on food and biotech ventures, who are willing to consider us should we fulfil their application requirements.

Finally, there are risks associated with a developing market; most companies are still in their early stages and develop their own technologies in-house due to limited resources and budget. Additionally, our technology was originally developed for biomedical applications. Therefore, further research is needed to obtain a Proof of Concept and/or Minimum Viable Product. However, we strongly believe that our current results are promising and can be furthered through collaborations with the Clean Meat consortium at the University of Sheffield, and other interested parties (e.g., Gaia Foods in Singapore).

We have developed our material costing and know that 1 cm³ of material will cost us £1.60. We considered the normal dimensions of a chicken breast, a burger patty and tenderloin and calculated the production price (assuming the companies would require one cm³ of our product to produce one cm³ of meat). Even though the prices seem to increase exponentially with our products there are a few things to consider. The first is internal. Our manufacturing process has not been translated to a production line therefore learning curves and lean manufacturing techniques would reduce the time and cost per cm³.

The second refers to the maturity of the market. Genome sequencing can be used as a suitable example. When genome sequencing was successfully achieved, the price of achieving a single run was around 1 million dollars. 20 years later the cost for running a human genome sequence is only 1,000 US dollars [448].

The same can be assumed with lab-grown meat. A Dutch researcher manufactured the first cultivated meat in 2013 for a price of 300,000 dollars per patty, and in only 8 years that price has greatly decreased. Future Meat announced early last year that they could produce 100 g of chicken breast for only 4 dollars, composed of mixed plant protein. Therefore, it is clear that the progress both in the technology and the process development has rapidly developed [449].

Whilst the market is still young, we feel we are well placed and prepared to scale up our initiative, therefore allowing us to be at the forefront of this development and shape how the sector will create impact.

An ICE was submitted in March 2022 to start negotiations with the University of Sheffield on the licensing and commercialisation of polyHIPEs scaffolds for lab-grown meat applications.

A final pitch was held at the end of the programme, where industry guests and potential investors provided feedback on the presentations. The slides can be found below.

London Business School

HIPeRGrowth

Seed. Grow. Eat.

London Business School

The Team

London Business School + University of Sheffield Team

M. Fernanda Velazquez

Who am I?
PhD in Biomaterials & Regenerative Medicine
Commercialisation Officer (starting soon)

What do I bring to the team?
Technical & manufacturing expertise and commercialisation experience

Oliver Sisson

Who am I?
Former Google and Coursera software engineer from Australia; MBA 2022

What do I bring to the team?
Entrepreneurship experience and technical acumen

Lillian Gao

Who am I?
Former Accenture consultant, marketer + data analyst at startups from the USA; MBA 2022

What do I bring to the team?
Digital marketing and analytics expertise, operating model transformation

Cristiane Cruz

Who am I?
Mother of two, leader in transformational initiatives across the AMEI region for Air Liquide, EMBA 2022, and an entrepreneur in the making.

What do I bring to the team?
Financial experience, and project management passion.

2

Agenda

- 1** Discovery
The Technology
Initial Commercial Hypothesis
- 2** Translation
Potential Market + Customers
Biomedical & Pharma Industry
Alternative Meats Industry
- 3** Growth
Lab-Grown Meats
Value Chain
Risks / Cost Positioning
- 4** Next Steps



3

The Technology

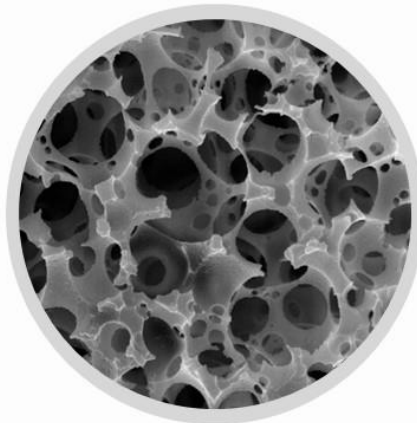
Porous & biodegradable scaffolds that can be adapted or tailored to specific needs

Biodegradable

- Made from synthetic polymers (FDA approved) with tuneable biodegradability

In vitro results

- Tested in chondrocytes, fibroblasts, hTERT, & embryonic cell lines – from mouse, bovine & porcine origin



Porous

- Tailored pore size and interconnectivity for ideal cell growth and tissue growth

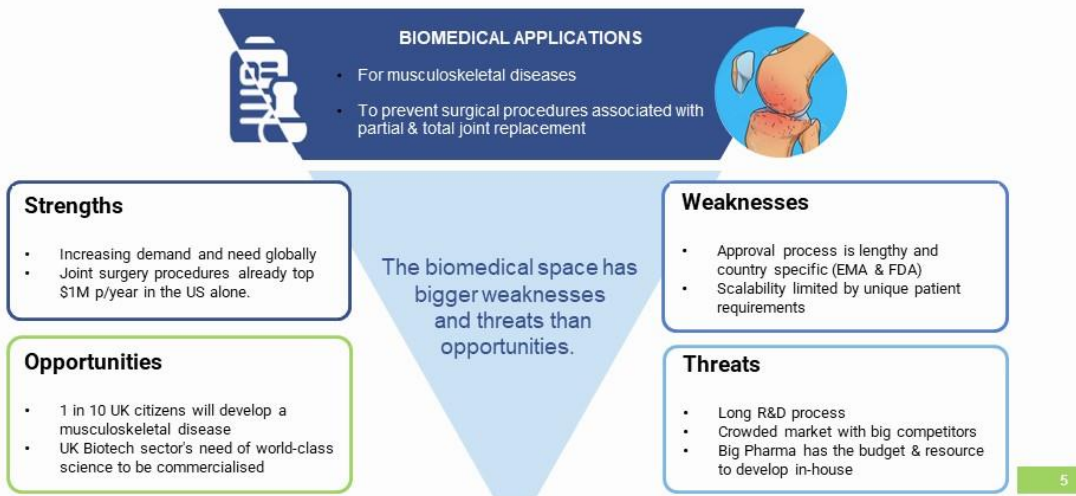
Original

- First explored as a double-layered scaffold for tissue engineering in arthritis

4

Initial Commercial Hypothesis

The initial commercial hypothesis was for biomedical use cases and potential surgical use



Potential Market + Customers

Market fit and future potential research led us to the alternative meats industry



Synthetic Meat Industry

SWOT reveals strong opportunities for commercialization, especially as a first-mover.

Strengths

- Technology can adapt and tailor to the companies' needs
- Scaffolds encourage continuous growth of a variety of cells
- Faster timeframe than other industries

Weaknesses

- Approval process is required (GRAS &/or FDA)
- R&D still required to determine how to integrate fully into the food industry
- Sensitive nature of food means extra precaution must be taken at every step

Opportunities

- Growing demand worldwide (cultivated meat is now included in long-term agrotech strategy plans)
- Few companies currently serving the market
- Manufacturing companies looking to scale

Threats

- Young and niche market
- Ventures are currently developing technologies in-house (limited budget)



Image from Forbes

8

Lab-Grown Meats

Our scaffolds focus specifically on the lab grown meats sector within alternative meats.



\$140B

The estimate of the livestock industry for human consumed meat (ASC).



66%

More than 1/3 of Americans and 2/3 of the world's population are choosing to consume less meat or switch to meat alternatives.

(ASC, 2020)



\$7B

The value of alternative meats. From this, \$4B represents plant-based meats.



£3B

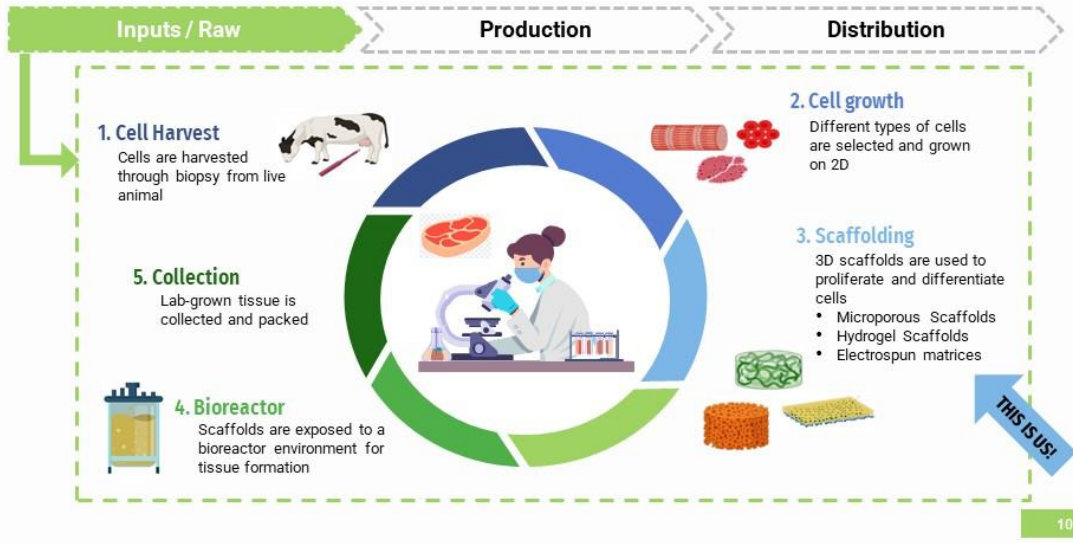
UK biotech startups raised £3 billion in 2020, a significant injection of capital into the market. The US invested \$14 billion.

(FierceBiotech, 2020)



9

Lab Grown Meats Value Chain



Market Exploration

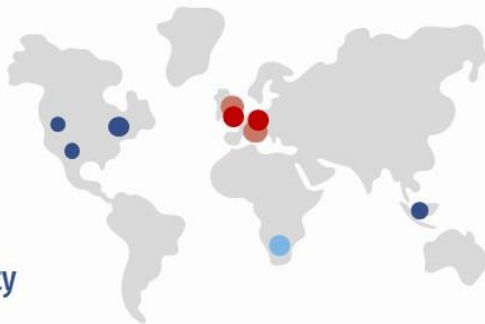
Potential customers



No opportunity



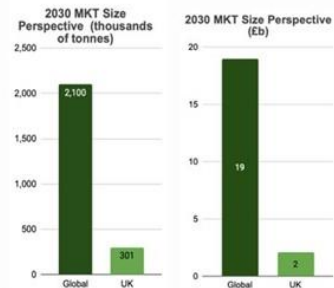
Fat producers
(Suppliers for lab-grown companies)



Potential investors



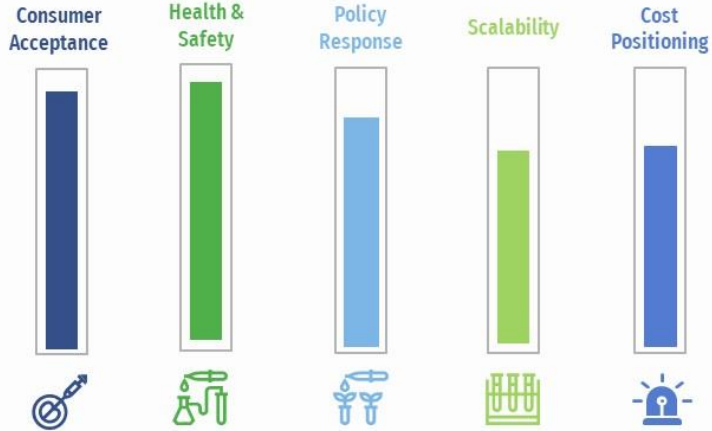
Potential market



Risks

The biggest unknown remains customer acceptance for lab grown meats.

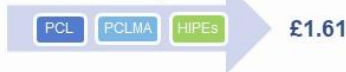
Based on qualitative reports and surveys (McKinsey, GFI).



Cost Positioning

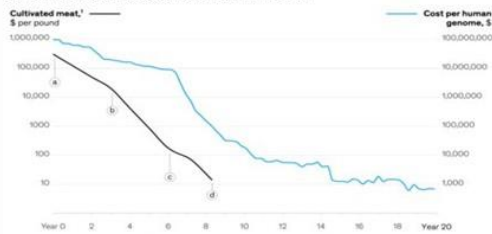
Based on our forecasts, we believe that our scaffold can help solve the cost positioning risk.

Cost of Production per cm³



The cost of cultivated meat has come down at an even faster rate than another well-known biotechnology—genome sequencing.

Comparative cost of changing technologies (logarithmic scale)



- 2013: Dutch scientist developed and produced first cultivated meat at ~\$300,000 a burger⁴
- 2016: Memphis Meats produced a "cultivated meatball" for ~\$20,000/lb⁵
- 2019: Future Meat Technologies reduced production costs of chicken to \$150/lb, and beef to \$200/lb⁶
- 2021: Future Meat Technologies announced it produced a 4 oz chicken breast at \$4 (with mixed plant protein)⁷



Meat	Chicken Breast	Burger Patty	Tenderloin
Our Cost	£225	£190	£124
Plant-based	£-	£3	£-
MKT Value	~ £2.5	~ £2	~ £15



Next Steps

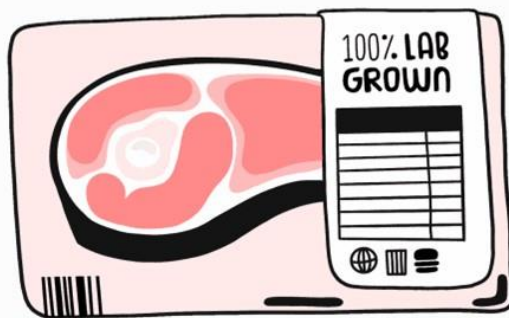
HIPeRGrowth needs £200,000 investment to take our scaffolds to the next step

Technology Validation

	Phase I	Phase II	Phase III
Time	3 months	6 months	9 months
Tasks	<ul style="list-style-type: none"> • Further market research • IP negotiation • Exposure of scaffolds to bioreactor & muscle cells • UoS Food Consortium • Pre-Accelerator programme 	<ul style="list-style-type: none"> • Collaboration agreements • IP protection • Scalability assays • Accelerator • Pre-Accelerator programme 	<ul style="list-style-type: none"> • GRAS approval • Purchasing agreements • Accelerator programme & funding strategy
Resources	<ul style="list-style-type: none"> • 2 human resources (each focused on science and business side) • Laboratory facilities (UoS) • Support from Commercialisation Officer (UoS) • Mentorship (optional) 		



13



Thanks for listening

Any questions?

Image from The Sheaf

15

SDG Impact

The United Nations Sustainable Development Goals (SDGs) directly point towards finding alternative and sustainable ways to feed the world's growing population.

Reduce the risk of pathogens and improve product traceability



Help feed Earth's growing population - projected to reach 10 billion people by 2050



Decreasing reliance on agriculture, which in turn decreases CO2 emissions released into the atmosphere

Associated Risks



Consumer Acceptance:

- Though trends towards alternative meats are rising, there is still strong resistance from consumers from a taste POV

Cost Positioning:

- High development costs will likely transfer over at least in part to the final price of lab grown meat products

Policy Response:

- Regulatory restrictions could limit entry options, i.e. limiting global partnerships

Health & Safety:

- Consumers are still largely unfamiliar with lab grown meats and may be skeptical towards its safety for ingestion

Competition:

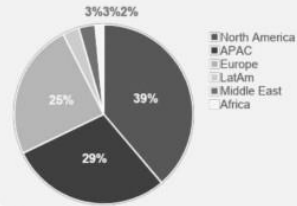
- The strong environmental need to decrease animal consumption will push existing players to develop R&D in house



Investment

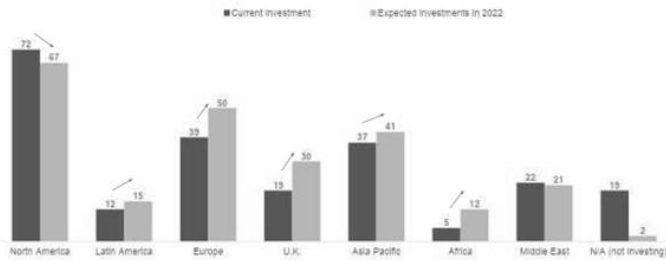
Investors plan to expand outside of North America.

Region of headquarters



Current and expected 2022 investments in alternative protein companies by region

Number of investor participants, multi-select question

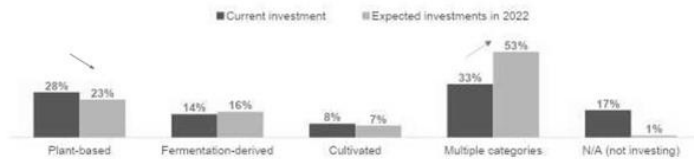


Source: GFI investor survey, As of December 2021.

Investors are diversifying their alternative protein holdings.

Current and expected 2022 investments in alternative protein companies by protein category

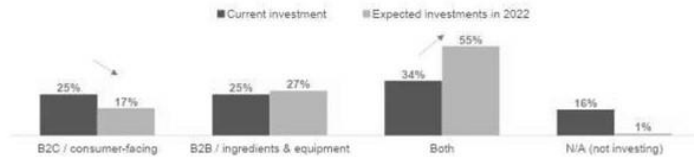
Percent of investor participants



Investors have reduced interest in investing solely in plant-based companies, in favor of investing across protein categories.

Current and expected 2022 investments in alternative protein companies by business model

Percent of investor participants



Investors have reduced interest in investing solely in B2C companies, in favor of investing across business models.

Source: GFI investor survey, As of December 2021.

References

- [1] T. Dwyer, R. Martin, R. Kendra and et al, "Reliability and Validity of the Arthroscopic International Cartilage Repair Society Classification System: Correlation With Histological Assessment of Depth," *Arthroscopy: The Journal of Arthroscopic & Related Surgery*, vol. 33, no. 6, pp. 1219-1224, 2017.
- [2] D. Brambilla, P. Luciani and J. Leroux, "Breakthrough discoveries in drug delivery technologies: The next 30 years," *Journal of Controlled Release*, vol. 190, pp. 9-14, 2014.
- [3] J. Tobin, "Global marketing authorisation of biomaterials and medical devices," *Regulatory Affairs for Biomaterials and Medical Devices*, Kidlington, Elsevier, pp. 93-108, 2015.
- [4] V. A. Org, "The State of Musculoskeletal Health," Versus Arthritis, Chesterfield, UK, 2019.
- [5] N. J. Registry, "Joint replacement statistics," National Joint Registry, United Kingdom, 2020.
- [6] N. N. J. Registry, "National Joint Registry - 16th Annual Report," Pad Creative Ltd, Hertfordshire, UK, 2019.
- [7] E. Kaplan, "Some Aspects of Functional Anatomy of the Human Knee Joint," *Clinical Orthopaedics*, vol. 23, pp. 18-29, 1962.
- [8] M. T. Hirschmann and W. Müller, "Complex function of the knee joint: the current understanding of the knee," *Knee Surgery, Sports Traumatology, Arthroscopy*, vol. 23, pp. 2780-2788, 2015.
- [9] R. F. La Prade, A. H. Engebretsen, T. V. Ly, S. Johansen, F. A. Wentorf and L. Engebretsen, "Then Anatomy of the Medial Part of the Knee," *The Journal of Bone and Joint Surgery*, Vols. 89-A, no. 9, pp. 2000-2010, 2007.
- [10] R. Passmore and J. Robson, A companion to medical studies, volume 1: Anatomy, Biochemistry, Physiology and Related Subjects, Oxford: Blackwell Scientific, 4th Edition, 1968.
- [11] T. D. White, M. T. Black and P. A. Folkens, "Chapter 12 - Leg: Femur, Patella, Tibia, and Fibula," in *Human Osteology (Third Edition)*, California, Elsevier Inc. / Academic press, 2012, pp. 241-270.
- [12] R. A. Pedowitz, J. J. O'Connor and W. H. Akeson, in *Daniel's Knee Injuries: Ligament and Cartilage Structure, Function, Injury and Repair*, Philadelphia, USA, Wolters Kluwer Health, 2003, pp. 3-22.
- [13] M. Ondresik, J. M. Oliveira and R. L. Reis, "Chapter 1: Advances for Treatment of Knee OC Defects," in *Osteochondral Tissue Engineering*, USA, Springer, 2018, pp. 3-9.
- [14] S. R. Goldring and M. B. Goldring, "Changes in the osteochondral unit during osteoarthritis: structure, function and cartilage-bone crosstalk," *Nature Reviews Rheumatology*, vol. 12, pp. 632-644, 2016.
- [15] M. A. Bruno, G. E. Gold and T. J. Mosher, *Arthritis in Color: Advanced Imaging of Arthritis.*, USA: Saunders Elsevier, 2009.

- [16] D. Shepherd and B. Seedhom, "Thickness of human articular cartilage in joints of the lower limb," *Annals of Rheumatic Diseases*, vol. 58, no. 27, pp. 27-34, 1999.
- [17] M. Müller-Gerbl, E. Schulte and R. Putz, "The thickness of the calcified layer of articular cartilage: a function of the load supported?," *Journal of Anatomy*, vol. 154, pp. 103-111, 1987.
- [18] S. Camarero-Espinosa and J. Cooper-White, "Tailoring biomaterial scaffolds for osteochondral repair," *International Journal of Pharmaceutics*, vol. 523, pp. 476-489, 2016.
- [19] A. Zelinka and R. Kandel, "In vitro formed deep zone cartilage tissues: A model to study formation of the zone of calcified cartilage.," *Osteoarthritis and Cartilage*, vol. 27, pp. S164-S165, 2019.
- [20] M. B. Goldring and S. R. Goldring, "Articular cartilage and subchondral bone in the pathogenesis of osteoarthritis," *Annals of the New York Academy of Science*, vol. 1192, pp. 230-237, 2010.
- [21] N. Broom and C. Poole, "A functional-morphological study of the tidemark region maintained in a non-viable physiological condition.," *Journal of Anatomy*, vol. 135, no. 1, pp. 65-82, 1982.
- [22] H. Madry, C. N. van Dijk and M. Mueller-Gerbl, "The basic science of the subchondral bone," *Knee Surgery, Sports Traumatology, Arthroscopy*, vol. 18, pp. 419-433, 2010.
- [23] G. Li, J. Yin, J. Gao, T. S. Cheng, N. J. Pavlos, C. Zhang and M. H. Zheng, "Subchondral bone in osteoarthritis: insight into risk factors and microstructural changes," *Arthritis Research & Therapy*, vol. 15, no. 6, pp. 1-12, 2013.
- [24] Y. Kameo, K.-i. Tsubota and T. Adachi, "Chapter 13: 3D Trabecular Remodeling in Human Proximal Femur: Approach to Understanding Wolff's Law," in *Bone Adaption*, Tokyo, Springer, 2018, pp. 177-185.
- [25] L. B. Lane, A. Villacin and P. G. Bullough, "The Vascularity and Remodelling of Subchondral Bone and Calcified Cartilage in Adult Human Femoral and Humeral Heads," *The Journal of Bone and Joint Surgery*, Vols. 59-B, no. 3, pp. 272-278, 1977.
- [26] H. Fischer, *Darstellung und Anordnung der kollagenen Fibrillen in der Matrix des Gelenkknorpels. Dissertation.*, Freiburg i.Br., Germany: Albert-Ludwigs-Universitaet Freiburg, 1988.
- [27] S. Khurana, K. Govindaraj, M. Karperien and J. Post, "RunX2 and SOX9 protein mobility correlates to osteogenic and chondrogenic differentiation of mesenchymal stem cells," *Osteoarthritis and Cartilage*, vol. 26, no. 1, pp. s109-s110, 2018.
- [28] P. Katsimbri, "The biology of normal bone remodelling," *European Journal of Cancer Care*, vol. 26, no. e12740, pp. 1-5, 2017.
- [29] K. Kuettner and A. Cole, "Cartilage degeneration in different human joints," *Osteoarthritis Cartilage*, vol. 13, no. 2, pp. 93-103, 2005.
- [30] J. Buckwalter, "Articular Cartilage Injuries," *Clinical Orthopaedics and Related Research*, vol. 402, no. 2, pp. 21-37, 2002.
- [31] H. Pereira, I. F. Cegiz, C. Vilela, P. Ripoll and et al, "Emerging concepts in treating cartilage, osteochondral defects and osteoarthritis of the knee and ankle," in *Osteochondral Tissue Engineering, Advances in Experimental Medicine and Biology*, USA, Springer Nature, 2018, pp. 25-29.

- [32] S. Crichley, G. Cunniffe, A. O'Reilly and P. Diaz-Payno, "Regeneration of Osteochondral Defects Using Developmentally Inspired Cartilaginous Templates," *Tissue Engineering Part A*, vol. 25, no. 3-4, pp. 1-13, 2019.
- [33] H. Lydon, A. Getgood and F. Henson, "Healing of osteochondral defects via endochondral ossification in an ovine model," *Cartilage*, vol. 10, no. 1, pp. 94-101, 2019.
- [34] C. Sanchez, A. Bay Jensen, T. Pap and M. Dvir-Ginzberg, "Chondrocyte secretome: a source of novel insights and exploratory biomarkers in osteoarthritis," *Osteoarthritis and Cartilage*, vol. 25, no. 8, pp. 1199-1209, 2017.
- [35] S. Suri and D. A. Walsh, "Osteochondral alterations in osteoarthritis," *Bone*, vol. 51, no. 2, pp. 204-212, 2012.
- [36] G. Jimenez, J. Cobo-Molinos, C. Antich and E. Lopez-Ruiz, "Chapter 3. Osteoarthritis: Trauma vs Disease," in *Osteochondral Tissue Engineering*, USA, Springer Research, 2018, pp. 61-68.
- [37] M. Grynblas, B. Alpert, I. Katz, I. Lieberman and K. Pritzker, "Subchondral bone in osteoarthritis," *Calcified Tissue International*, vol. 49, pp. 20-26, 1991.
- [38] D. Burr, "The importance of subchondral bone in osteoarthritis," *Current Opinion in Rheumatology*, vol. 10, no. 3, pp. 256-262, 1998.
- [39] P. S. Russell, "Selective Transplantation," *Annals of Surgery*, vol. 201, no. 3, pp. 255-262, 1985.
- [40] B. McGrory, J. Gallagher, M. Kraay, J. Jacobs and W. Robb, "Editorial: Minimally Invasive and Small-incision Joint Replacement Surgery," *Clinical Orthopaedics and Related Research*, vol. 440, pp. 251-254, 2005.
- [41] C. Wainwright, "Age at hip or knee joint replacement surgery predicts likelihood of revision surgery," *Bone Joint Journal*, vol. 93B, no. 10, pp. 1411-1415, 2011.
- [42] C. D. Hoemann, C.-H. Lafantaisie-Favreau and V. Lascau-Coman, "The Cartilage-bone interface," *The Journal of Knee Surgery*, vol. 25, no. 02, pp. 085-098, 2012.
- [43] E. Kon, G. Filardo, M. Brittberg, M. Busacca, V. Condello, L. Engebretsen, S. Marlovits, P. Niemeyer, P. Platzer, M. Posthumus, P. Verdonk, R. Verdonk, J. Victor, W. van der Merwe, W. Widuchowski, C. Zorzi and M. Marcacci, "A multilayer biomaterial for osteochondral regeneration shows superiority vs microfractures for the treatment of osteochondral lesions in a multicentre randomized trial at 2 years," *Knee Surgery, Sports Traumatology Arthroscopy*, vol. 26, pp. 2704-2715, 2018.
- [44] P. Feczko, L. Hangody, J. Varga, L. Bartha, Z. Diószegi, G. Bodó, Z. Kendik and L. Módis, "Experimental results of donor site filling for autologous osteochondral mosaicplasty," *Arthroscopy: The Journal of Arthroscopic & Related Surgery*, vol. 19, no. 7, pp. 755-761, 2003.
- [45] K. Huch, K. Kuettner and P. Dieppe, "Osteoarthritis in Ankle and Knee Joints," *Seminars in Arthritis and Rheumatism*, vol. 26, pp. 667-674, 1997.
- [46] O. E. Yausep, I. Madhi and D. Trigkilidas, "Platelet rich plasma for treatment of osteochondral lesions of the talus: A systematic review of clinical trials.," *Journal of Orthopaedics*, vol. 18, pp. 218-225, 2020.

- [47] A. Guney, E. Yurdakul, I. Karaman, O. Bilal, I. H. Kafadar and M. Oner, "Medium-term outcomes of mosaicplasty versus arthroscopic microfracture with or without platelet-rich plasma in the treatment of osteochondral lesions of the talus," *Knee Surgery, Sports Traumatology, Arthroscopy*, vol. 24, pp. 1293-1298, 2016.
- [48] K. A. Ross, J. Robbins, M. E. Easley and J. G. Kennedy, "Autologous Osteochondral Transplantation for Osteochondral Lesions of the Talus," *Operative Techniques in Orthopaedics*, vol. 24, no. 3, pp. 171-180, 2014.
- [49] Y. Yonetani, Y. Tanaka, T. Kanamoto, N. Nakamura, K. Nakata and S. Horibe, "Autologous Osteochondral Transplantation in Full-thickness Patella Chondral Lesion: A Case Series," *Journal of Orthopaedic Case Reports*, vol. 9, no. 1, pp. 53-57, 2019.
- [50] A. V. Stone, D. R. Christian, M. L. Redondo and A. B. Yanke, "Osteochondral Allograft Transplantation and Osteochondral Autograft Transfer," *Operative Techniques in Sports Medicine*, vol. 26, no. 3, pp. 183-188, 2018.
- [51] E. Basad, F. R. Wissing and P. Fehrenbach, "Matrix-induced autologous chondrocyte implantation in the knee: clinical outcomes and challenges," *Knee Surgery Sports Traumatology Arthroscopy*, vol. 23, no. 12, pp. 3729-3735, 2015.
- [52] G. H. Welsch, T. C. Mamisch, S. E. Domayer, R. Dorotka, F. Kutscha-Lissberg, S. Marlovits, L. M. White and S. Trattnig, "Cartilage T2 Assessment at 3-T MR Imaging: In Vivo Differentiation of Normal Hyaline Cartilage from Reparative Tissue after Two Cartilage Repair Procedure- Initial Experience," *Musculoskeletal Imaging*, vol. 247, no. 1, pp. 154-161, 2008.
- [53] A. Beck, D. Wood, C. J. Vertullo, J. Ebert, G. Janes, M. Sullivan and M.-H. Zheng, "Morphological Assessment of MACI Grafts in Patients with Revision Surgery and Total Joint Arthroplasty," *Cartilage*, vol. 00, no. 0, pp. 1-14, 2019.
- [54] S. Dalal, N. Shah, D. Pardiwala, D. Rajan, S. Sanghavi and C. Bhanji, "Gel-Based Autologous Chondrocyte Implantation (GACI) in the Knee: Multicentric Short Term Study," *International Journal of Medical, Health, Biomedical, Bioengineering and Pharmaceutical Engineering*, vol. 9, no. 12, pp. 883-886, 2015.
- [55] T.-H. Yoon, M. Jung, C.-H. Choi, H.-S. Kim, Y.-H. Lee, Y.-S. Choi, S.-J. Kim and S.-H. Kim, "Arthroscopic gel-type autologous chondrocyte implantation presents histologic evidence of regenerating hyaline-like cartilage in the knee with articular cartilage defect," *Knee Surgery, Sports Traumatology, Arthroscopy*, vol. 28, pp. 941-951, 2020.
- [56] D. van Duijvenbode, F. Jonkers, Y. Könst, B. van Royen, R. Benink and M. Hoozemans, "Gel-type autologous chondrocyte implantation for cartilage repair in patients with prior ACL reconstruction: A retrospective two year follow-up," *The Knee*, vol. 23, no. 12, pp. 241-245, 2016.
- [57] K. M., D. S.M., H. M.B., V. S.D., R. J.F., B. D.D. and S. A.J., "Image-Guided Techniques Improve the Short-Term Outcome of Autologous Osteochondral Cartilage Repair Surgeries," *Cartilage*, vol. 4, no. 2, pp. 153-164, 2013.
- [58] M. Monzon, C. Liu, S. Ajami and M. Oliveira, "Functionally graded additive manufacturing to achieve functionality specifications of osteochondral scaffolds," *Bio-design and Manufacturing*, vol. 1, pp. 69-75, 2018.

- [59] L. Andriolo, D. Reale and A. Di Martino, "Cell free scaffolds in cartilage knee surgery: a systematic review and meta-analysis of clinical evidence," *Sage Publishing: Cartilage*, pp. 1-16, 2019.
- [60] B. Christensen, C. Foldager, J. Jensen, N. Jensen and M. Lind, "Poor osteochondral repair by a biomimetic collagen scaffold: 1-to 3-year clinical and radiological follow-up," *Knee Surgery Sports Traumatology Arthroscopy*, vol. 24, no. 7, pp. 2380-2387, 2016.
- [61] R. D'Ambrosi, F. Valli, P. De Luca, N. Ursino and F. G. Usuelli, "MaioRegen Osteochondral Substitute for the Treatment of Knee Defects: A Systematic Review of the Literature," *Journal of Clinical Medicine*, vol. 8, no. 783, pp. 1-14, 2019.
- [62] M. Kaipel, S. Trattning and S. Domayer, "Clinical and bioimaging results following osteochondral lesion repair using MaioRegen allograft," *Orthopaedic Journal of Sports Medicine*, vol. 4, no. 3, p. Supp 2, 2016.
- [63] W. J. Long, J. W. Greene and F. D. Cushner, "Early clinical outcomes associated with a novel osteochondral allograft transplantation system in the knee," *Hindawi Publishing Corporation. Advances in Orthopedic Surgery.*, vol. 2016, pp. 1-6, 2016.
- [64] H. Sofu, N. Kockara, A. Oner, Y. Camurcu, A. Issin and V. Sahin, "Results of hyaluronic acid-based cell-free scaffold application in combination with microfracture for the treatment of osteochondral lesions of the knee: 2-year comparative study," *Arthroscopy*, vol. 33, no. 1, pp. 209-216, 2017.
- [65] M. Brix, M. Kaipel, R. Kellner, M. Schreiner, S. Apprich, H. Boszotta, R. Windhager, S. Domayer and S. Trattning, "Successful osteoconduction but limited cartilage tissue quality following osteochondral repair by a cell free multilayered nano-composite scaffold at the knee," *International Orthopaedics*, vol. 40, pp. 625-632, 2016.
- [66] D. T. Mathis, R. Kaelin, H. Rasch, M. P. Arnold and M. T. Hirschmann, "Good clinical results but moderate osseointegration and defect filling of a cell-free multi-layered nano-composite scaffold for treatment of osteochondral lesions of the knee," *Knee Surgery, Sports Traumatology, Arthroscopy*, vol. 26, pp. 1273-1280, 2018.
- [67] J. Verhaegen, S. Clockaerts, G. Van Osch, J. Somville, P. Verdonk and P. Mertens, "TruFit Plug for Repair of Osteochondral Defects - Where is the Evidence? Systematic Review of Literature," *Cartilage*, vol. 6, no. 1, pp. 12-19, 2015.
- [68] E. Kon, G. Filardo, F. Perdisa, G. Venieri and M. Marcacci, "Clinical results of multilayered biomaterials for osteochondral regeneration," *Journal of Experimental Orthopaedics*, vol. 1, no. 10, pp. 1-8, 2014.
- [69] F. Perdisas, E. Kon, A. Sessa, L. Andriolo, M. Busacca, M. Marcacci and G. Filardo, "Treatment of Knee Osteochondritis Dissecans With a Cell-Free Biomimetic Osteochondral Scaffold: Clinical and Imaging Findings at Midterm Follow-up," *The American Journal of Sports Medicine*, vol. 46, no. 2, pp. 314-321, 2017.
- [70] A. Khademhosseini and R. Langer, "A decade of progress in tissue engineering," *Nature Protocols*, vol. 11, no. 10, pp. 1775-1781, 2016.
- [71] N. Zoratto and P. Matricardi, "Chapter 7: Semi-IPN- and IPN-Based Hydrogels," in *Osteochondral Tissue Engineering*, Springer International Publishing AG, 2018, pp. 155-188.

- [72] T. Andersen, P. Auk-Emblem and M. Dornish, "3D Cell Culture in Alginate Hydrogels," *High-Throughput*, vol. 4, no. 2, pp. 133-161, 2015.
- [73] I. D. Hay, Z. U. Rehman, A. Ghafoor and B. H. Rehm, "Bacterial biosynthesis of alginates," *Journal of Chemical Technology & Biotechnology*, vol. 85, pp. 752-759, 2010.
- [74] I. Oliveira, A. L. Carvalho, H. Radhouani, C. Goncalves, J. M. Oliveira and R. L. Reis, "Promising Biomolecules," in *Osteochondral Tissue Engineering*, USA, Springer Research, 2018, pp. 195-200.
- [75] S. Saravanan, R. Leena and N. Selvamurugan, "Chitosan based biocomposite scaffolds for bone tissue engineering," *International Journal of Biological Macromolecules*, vol. 93, no. Part B, pp. 1354-1365, 2016.
- [76] K. Yong Lee and D. J. Mooney, "Alginate: Properties and biomedical applications," *Progress in Polymer Science*, vol. 37, pp. 106-126, 2012.
- [77] D. Gothard, E. Smith, J. M. Kanczler, C. R. Black and J. A. Wells, "In Vivo Assessment of Bone Regeneration in Alginate/Bone ECM Hydrogels with Incorporated Skeletal Stem Cells and Single Growth Factors," *Plos One*, vol. 10, no. 12, 2015.
- [78] Y. Kolambkar, K. Dupont, J. Boerckel, N. Huebsch, D. Mooney, D. Hutmacher and R. Guldberg, "An alginate-based hybrid system for growth factor delivery in the functional repair of large bone defects," *Biomaterials*, vol. 32, pp. 65-74, 2011.
- [79] Y. Lopez-Morales, A. Abarrategi, V. Ramos, C. Moreno-Vicente, L. Lopez-Duran, J. Lopez-Lacomba and F. Marco, "In vivo comparison of the effects of rhBMP-2 and rhBMP-4 in osteochondral tissue regeneration," *European Cells and Materials*, vol. 20, pp. 367-378, 2010.
- [80] C. Sharma, A. Kumar Dinda, P. D. Potdar, C.-F. Chou and N. Chandra Mishra, "Fabrication and characterization of novel nano-biocomposite scaffold of chitosan-gelatin-alginate-hydroxyapatite for bone tissue engineering," *Materials Science and Engineering: C*, vol. 64, pp. 416-427, 2016.
- [81] J. Venkatesan, I. Bhatnagar, P. Manivasagan, K.-H. Kang and S.-K. Kim, "Alginate composites for bone tissue engineering: A review," *International Journal of Biological Macromolecules*, vol. 72, pp. 269-281, 2015.
- [82] H. Dashtdar, M. Raman Murali, L. Selvaratnam, H. B. Raghavendran, A. Mahmud Suhaeb, T. S. Ahmad and T. Kamarul, "Ultra-structural changes and expression of chondrogenic and hypertrophic genes during chondrogenic differentiation of mesenchymal stromal cells in alginate beads," *Biochemistry, biophysics and molecular biology*, vol. 4, no. e1650, pp. 1-23, 2016.
- [83] K. Schutz, F. Despang, A. Lode and M. Gelinsky, "Cell-laden biphasic scaffolds with anisotropic structure for the regeneration of osteochondral tissue," *Journal of tissue engineering and regenerative medicine*, vol. 10, pp. 404-417, 2016.
- [84] M. Gómez Guillén, B. Giménez, M. López Caballero and P. Montero García, "Functional and bioactive properties of collagen and gelatin from alternative sources: A review," *Food Hydrocolloids*, vol. 25, pp. 1813-1827, 2011.
- [85] S. Dumitriu and V. I. Popa, "Polym," in *Polymeric Biomaterials: Structure and function*, Florida, CRC Press: Taylor & Francis Group, 2013, pp. 290-293.

- [86] M. Nikkhah, M. Akbari, A. Paul, A. Memic, A. Dolatshahi-Pirouz and A. Khademhosseini, "Chapter 3. Gelatin-Based Biomaterials for Tissue Engineering And Stem Cell Bioengineering," in *Biomaterials from Nature for Advanced Devices and Therapies, First Edition*, USA, Wiley, 2016, pp. 37-63.
- [87] J. Ratanavaraporn, R. Rangkupan, H. Jeeratawatchai, S. Kanokpanont and S. Damrongsakkul, "Influences of physical and chemical crosslinking techniques on electrospun type A and B gelatin fiber mats," *International Journal of Biological Macromolecules*, vol. 47, no. 4, pp. 431-438, 2010.
- [88] R. Cortesi, C. Nastruzzi and S. Davis, "Sugar cross-linked gelatin for controlled release: microspheres and disks," *Biomaterials*, vol. 19, pp. 1641-1649, 19998.
- [89] G. Ying, N. Jiang, C. Yu and Y. S. Zhang, "Three-dimensional bioprinting of gelatin methacryloyl (GelMA)," *Bo-Design and Manufacturing*, vol. 1, no. 4, pp. 215-224, 2018.
- [90] Y. Schuurman, P. A. Levett, M. W. Pot, P. R. van Weeren, W. J. Dhert, D. W. Hutmacher, F. P. Melchels, T. J. Klein and J. Malda, "Gelatin-Methacrylamide Hydrogels as Potential Biomaterials for Fabrication of Tissue-Engineered Cartilage Constructs," *Macromolecular Bioscience*, vol. 13, pp. 551-561, 2013.
- [91] E. M. Masutani, C. K. Kinoshita, T. T. Tanaka, A. K. Ellison and B. A. Yoza, "Increasing Thermal Stability of Gelation by UV-Induced Cross-Linking with Glucose," *International Journal of Biomaterials*, vol. 2014, no. ID 979636, pp. 1-9, 2014.
- [92] M. Gohel, R. Parikh, A. Amin and A. Surati, "Preparation and Formulation Optimization of Sugar Crosslinked Gelatin Microspheres of Diclofenac Sodium," *Indian Journal of Pharmaceutical Sciences*, vol. 67, no. 5, pp. 575-581, 2005.
- [93] G. C. Brown, K. S. Lim, B. L. Farrugia, G. J. Hooper and T. B. Woodfield, "Covalen incorporation of Heparin Improves Chondrogenesis in Photocurable Gelatin-Methacryloyl Hydrogels," *Macromolecular Bioscience*, vol. 17, no. 12, pp. 1-13, 2017.
- [94] T. Hughes, L. Li, C. Lu, M. Chen, H. Ma, L. Wang, X. Hao, K. Mclean and C. Hao, "Photocurable gelatin hydrogels for cell encapsulation," in *Conference Abstract: 10th World Biomaterials Congress*, Canada, 2016.
- [95] J. Kim, S. Im, J. Hun Kim, S. Moon Kim, S.-M. Lee, J. Lee, J. Pil Im, J. Woo and S. E. Moon, "Artificial Perspiration Membrane by Programmed Deformation of Thermoresponsive Hydrogels," *Advanced Materials*, vol. 32, no. 6, pp. 1-7, 2019.
- [96] M. G. Raucci, U. D'Amora, A. Ronca, C. Demitri and L. Ambrosio, "Bioactivation Routes of Gelatin-Based Scaffolds to Enhance at Nanoscale Level Bone Tissue Regeneration," in *Bontiers of Bioengineering and Biotechnology*, 7, 27, 2019.
- [97] M. E. Hoque, T. Nuge, T. Kim Yeow, N. Nordin and R. Prasad, "Gelatin based scaffolds for tissue engineering - A review," *Polymers Research Journal*, vol. 9, no. 1, pp. 15-32, 2015.
- [98] Y. Wen, B. Jiang, J. Cui, G. Li, M. Yu and et al, "Superior osteogenic capacity of different mesenchymal stem cells for bone tissue engineering," *Oral and Maxillofacial surgery*, vol. 116, no. 5, pp. e324-e332, 2013.

- [99] M. C. Echave, C. Pimenta-Lopes, J. L. Pedraz, M. Mehrali, A. Dolatshahi-Pirouz, F. Ventura and G. Orive, "Enzymatic crosslinked gelatin 3D scaffolds for bone tissue engineering," *International Journal of Pharmaceutics*, vol. 562, pp. 151-161, 2019.
- [100] X. Li, J. Ding, J. Wang, X. Zhuang and X. Chen, "Biomimetic biphasic scaffolds for osteochondral defect repair," in *5th China-Europe Symposium on Biomaterials in Regenerative Medicine (CESB 2015)*, China, 2015.
- [101] F. Gao, Z. Xu, Q. Liang, H. Li, L. Peng, M. Wu, X. Zhao, X. Cui, C. Ruan and W. Liu, "Osteochondral regeneration with 3D-printed biodegradable high-strength supramolecular polymer reinforced-gelatin hydrogel scaffolds," *Advanced Science*, vol. 6, no. 15, pp. 1-12, 2019.
- [102] D. van Krevelen and K. t. Nijenhuis, *Properties of Polymers: their correlation with chemical structure; their numerical estimation and prediction from additivive group contributions*, UK: Elsevier, 2009.
- [103] P. Kumar, K. R. Gajbhiye, K. M. Paknikar and V. Gajbhiye, "Chapter 1 - Current Status and Future Challenges of Various Polymers as Cancer Therapeutics," in *Polymeric Nanoparticles as a Promising Tool for Anti-cancer Therapeutics*, India, Academic Press Elsevier Inc., 2019, pp. 1-20.
- [104] G.-R. B., S. C.M., C. S., I.-J. S. and G. S., "Mammalian Cell Viability: Methods and Protocol: Chapter 14 - Confocal Imaging Protocols for Live/Dead Staining in Three-Dimensional Carriers," *Methods in Molecular Biology*, vol. 740, pp. 127-140, 2011.
- [105] T. Tariverdian, T. Navaei, P. Milan, A. Samadikuchaksaraei and M. Mozafari, "Chapter 16: Functionalized polymers for tissue engineering and regenerative medicine," in *Advanced Functional Polymers for Biomedical Applications*, Iran, Elsevier, Inc., 2019, pp. 323-357.
- [106] F. O'Brien, B. Harley, I. Yannas and L. Gibson, "The effect of pore size on cell adhesion in collagen-GAG scaffolds," *Biomaterials*, vol. 26, no. 4, pp. 433-441, 2005.
- [107] Q. Zhang, H. Lu, N. Kawazoe and G. Chen, "Pore size effect of collagen scaffolds on cartilage regeneration," *Acta Biomaterialia*, vol. 10, no. 5, pp. 2005-2013, 2014.
- [108] M. Abrisham, M. Noroozi, M. Panahi-Sarmad, M. Arjmand, V. Goodarzi, Y. Shakeri, H. Golbaten-Mofrad, P. Dehghan, A. Seyfi Sahzabi, M. Sadri and L. Uzun, "The role of polycaprolactone-triol (PCL-T) in biomedical applications: A state-of-the-art review," *European Polymer Journal*, vol. 131, p. 109701, 2020.
- [109] B. Aldemir Dikici, C. Sherborne, G. C. Reilly and F. Claeysens, "Emulsion templated scaffolds manufactured from photocurable polycaprolactone," *Polymer*, vol. 175, pp. 243-254, 2019.
- [110] M. Messori, M. Degli Esposti, K. Paderni, S. Pandini, S. Passera, T. Ricco and M. Toselli, "Chemical and thermomechanical tailoring of the shape memory effect in poly(ϵ -caprolactone)-based systems," *Journal of Material Sciences*, vol. 48, pp. 424-440, 2013.
- [111] M. Bartnikowski, T. R. Dargaville, S. Ivanovski and D. W. Hutmacher, "Degradation mechanisms of polycaprolactone in the context of chemistry, geometry and environment," *Progress in Polymer Science*, vol. 96, pp. 1-20, 2019.
- [112] M. Xu, C. Guo, H. Dou, Y. Zuo, Y. Sun, J. Zhang and W. Li, "Tailoring the degradation and mechanical properties of poly(ϵ -caprolactone) incorporating functional ϵ -caprolactone-based copolymers," *Polymer Chemistry*, vol. 10, pp. 3786-3796, 2019.

- [113] C. G. Pitt, R. W. Hendren, A. Schindler and S. C. Woodward, "The enzymatic surface erosion of aliphatic polyesters," *Journal of Controlled Release*, vol. 1, no. 1, pp. 3-14, 1984.
- [114] R. Yao, J. He, G. Meng, B. Jiang and F. Wu, "Electrospun PCL/Gelatin composite fibrous scaffolds: mechanical properties and cellular responses," *Journal of Biomaterials Science, Polymer Edition*, vol. 27, no. 9, pp. 824-838, 2016.
- [115] G. Schrimpf and P. Friedl, "Growth of Human Vascular Endothelial-Cells on various Types of Microcarriers.," *Cytotechnology*, vol. 13, no. 3, pp. 203-211, 1993.
- [116] T. Zhang, R. A. Sanguramath, S. Israel and M. S. Silverstein, "Emulsion Templating: porous polymers and beyond," *Macromolecules*, vol. 52, pp. 5445-5479, 2019.
- [117] M. Jafari, Z. Paknejad, M. Rezai Rad, S. Reza Motamedian, M. Jafar Eghbal, N. Nadjmi and A. Khojasteh, "Polymeric scaffolds in tissue engineering: a literature review," *Journal of Biomedical Materials Research Part B*, vol. 105 B, pp. 431-459, 2017.
- [118] L. Vogt, L. Ramos Rivera, L. Liverani, A. Piegat, M. El Fray and A. R. Boccaccini, "Poly(ϵ -caprolactone)/poly(glycerol sebacate) electrospun scaffolds for cardiac tissue engineering using benign solvents," *Material Science and Engineering: C*, vol. 103, p. 109712, 2019.
- [119] S. Pashneh-Tala, R. Owen, H. Bahmaee, S. Rekstyte, M. Malinauskas and F. Claeysens, "Synthesis, characterization and 3D micro-structuring via 2-photon polymerization of poly(glycerolsebacate)-methacrylate-An elastomeric degradable polymer," *Frontiers in Physics*, vol. 6, pp. 1-41, 2018.
- [120] X. J. Loh, A. Abdul Karim and C. Owh, "Poly(glycerol sebacate) biomaterial: synthesis and biomedical applications," *Journal of Materials Chemistry B*, vol. 3, no. 39, pp. 7633-7804, 2015.
- [121] C. A. Sundback, J. Y. Shyu, Y. Wang, W. C. Faquin, R. S. Langer, J. P. Vacanti and T. A. Hadlock, "Biocompatibility analysis of poly(glycerol sebacate) as a nerve guide material," *Biomaterials*, vol. 26, no. 27, pp. 5454-5464, 2005.
- [122] S. Zaky, K. Lee, J. Gao, A. Jensen, K. Verdelis, Y. Wang, A. Almarza and C. Sfeir, "Poly(glycerol sebacate) elastomer supports bone regeneration by its mechanical properties being closer to osteoid tissue rather than to mature bone," *Acta Biomaterialia*, vol. 54, pp. 95-106, 2017.
- [123] J. C. Silva, R. N. Udangawa, J. Chen, C. D. Mancinelli, F. F. Garrudo, P. E. Mikael, J. M. Cabral, F. C. Ferreira and R. J. Linhardt, "Kartogenin-loaded coaxial PGS/PCL aligned nanofibers for cartilage tissue engineering," *Materials Science and Engineering: C*, vol. 107, p. 110291, 2020.
- [124] X. Zhao, Y. Wu, Y. Du, X. Chen, B. Lei, Y. Xue and P. X. Ma, "A highly bioactive and biodegradable poly(glycerol sebacate)-silica glass hybrid elastomer with tailored mechanical properties for bone tissue regeneration," *Journal of Materials Chemistry B*, vol. 3, pp. 3222-3233, 2015.
- [125] M. Kharaziha, M. Nikkhah, S. Shin, N. Annabi, N. Masoumi, A. Gaharwar, G. Camci-Unal and A. Khademhosseini, "PGS:Gelatin nanofibrous scaffolds with tuneable mechanical structural properties for engineering cardiac tissues," *Biomaterials*, vol. 34, no. 27, pp. 6355-6356, 2013.
- [126] M. Trevelin Souza, S. Tansaz, E. Dutra Zanotto and A. R. Boccaccini, "Bioactive glass fiber-reinforced PGS matrix composites for cartilage regeneration," *Materials MDPI*, vol. 10, no. 83, pp. 1-14, 2017.

- [127] S. Salehi, T. Bahners, J. Gutmann, S.-L. Gao, E. Mader and T. Fuchsluger, "Characterization of structural, mechanical and nano-mechanical properties of electrospun PGS/PCL fibers," *RSC Advances*, vol. 33, pp. 1-15, 2014.
- [128] E. M. Jeffries, R. A. Allen, J. Gao, M. Pesce and Y. Wang, "Highly elastic and suturable electrospun poly(glycerol sebacate) fibrous scaffolds," *Acta Biomaterialia*, vol. 18, pp. 30-39, 2015.
- [129] H.-J. Wu, M.-H. Hu, H.-Y. Tuan-Mu and J.-J. Hu, "Preparation of aligned poly(glycerol sebacate) fibrous membranes for anisotropic tissue engineering," *2019*, vol. 100, pp. 30-37, 2019.
- [130] Y.-C. Yeh, C. B. Highley, L. Ouyang and J. A. Burdick, "3D printing of photocurable poly(glycerol sebacate) elastomers," *Biofabrication*, vol. 8, no. 045004, pp. 1-10, 2016.
- [131] B. Lei, B. Guo, K. J. Rambhia and P. X. Ma, "Hybrid polymer biomaterials for bone tissue regeneration," *Frontiers in Medicine*, vol. 13, no. 2, pp. 189-201, 2019.
- [132] B. Jian, W. Wu, Y. Song, N. Tan and C. Ma, "Microporous elastomeric membranes fabricated with polyglycerol sebacate improved guided bone regeneration in a rabbit model," *International Journal of Nanomedicine*, vol. 14, pp. 2683-2692, 2019.
- [133] J. M. Kemppainen and S. J. Hollister, "Tailoring the mechanical properties of 3D-designed poly(glycerol sebacate) scaffolds for cartilage applications," *Journal of Biomedical Materials Research Part A*, vol. 94A, no. 1, pp. 9-18, 2010.
- [134] C. G. Jeong and S. J. Hollister, "A comparison of the influence of material on in vitro cartilage tissue engineering with PCL, PGS, and POC 3D scaffold architecture seeded with chondrocytes," *Biomaterials*, vol. 31, no. 15, pp. 4304-4312, 2010.
- [135] R. Rai, M. Tallawi, A. Grigore and A. R. Boccaccini, "Synthesis, properties and biomedical applications of poly(glycerol sebacate) (PGS): A review," *Progress in Polymer Science*, vol. 37, no. 8, pp. 1051-1078, 2012.
- [136] P. A. Netti, "Part II: Tissue engineering applications of biomedical foams," in *Biomedical foams for tissue engineering applications*, UK, Woodhead Publishing, 2014, pp. 3-39.
- [137] A. W. Pacek, P. Cullen, R. J. Romañach, Rielly Chris and N. Abatzoglou, "Chapter 9. Emulsions," in *Pharmaceutical Blending and Mixing*, Chichester, John Wiley & Sons, Incorporated, 2015, pp. 183-190.
- [138] G. E. Totten and V. J. De Negri, "Chapter 14. Emulsions," in *Handbook of Hydraulic Fluid Technology*, CRC Press LLC, 2011, p. 6.
- [139] A. Fernandez-Nieves, A. Manuel Puertas and N. Garti, "Chapter 15. Emulsions," in *Fluids, Colloids and Soft Materials: An Introduction to Soft Matter Physics*, New Jersey, John Wiley & Sons, Incorporated, 2016, pp. 576-587.
- [140] T. F. Tadros, "5 Mechanism of emulsification and the role of the emulsifier," in *Emulsions: Formation, Stability, Industrial Applications*, Germany, De Gruyter, Inc., 2016, pp. 47-59.
- [141] M. Chakraborty, C. Bhattacharya and S. Datta, "Chapter 4. Emulsion Liquid Membranes: Definitions and Classification, Theories, Module Design, Applications, New Directions and Perspectives," in *Liquid Membranes: Principles and Applications in chemical Separations and Wastewater Treatment*, Elsevier B.V., 2010, pp. 141-180.

- [142] N. R. Cameron, "High internal phase emulsion templating as a route to well-defined porous polymers," *Polymer*, vol. 46, no. 5, pp. 1439-1449, 2005.
- [143] N. A. Sears, P. S. Dhavalikar and E. M. Cosgriff-Hernandez, "Emulsion Inks for 3D Printing of High Porosity Materials," *Macromolecular Rapid Communications*, vol. 37, pp. 1369-1374, 2016.
- [144] D. Barby and H. Ziq, "Substrate carrying a porous polymeric material," Unilever PLC Patent ZA8204501, USA, 1984.
- [145] P. Hazot, J. Chapel, C. Pichot, A. Elaissari and T. Delair, "Preparation of Poly(N-ethyl methacrylamide) Particles via an Emulsion/Precipitation Process: The Role of the Crosslinker," *Journal of Polymer Science Part A: Polymer Chemistry*, vol. 40, no. 11, pp. 1808-1817, 2002.
- [146] W. Busby, N. R. Cameron and C. A. Jahoda, "Emulsion-derived foams (polyHIPEs) containing poly(ϵ -caprolactone) as matrixes for tissue engineering," *Biomacromolecules*, vol. 2, pp. 154-164, 2001.
- [147] C. Griffith and H. Daigle, "A comparison of the static and dynamic stability of Pickering emulsions," *Colloids and Surfaces A: Physicochemical and Engineering Aspects*, vol. 586, p. 124256, 2020.
- [148] Y. Zhu, Y. Zheng, L. Zong, F. Wang and A. Wang, "Fabrication of magnetic hydroxypropyl cellulose-g-poly(acrylic acid) porous spheres via Pickering high internal phase emulsion for removal of Cu^{2+} and Cd^{2+} ," *Carbohydrate Polymers*, vol. 149, pp. 242-250, 2016.
- [149] S. Sharma, A. Verma, B. V. Teja, G. Pandey, N. Mittapelly, R. Trivedi and P. Mishra, "An insight into functionalized calcium based inorganic nanomaterials in biomedicine: Trends and transitions," *Colloids and Surfaces B: Biointerfaces*, vol. 133, pp. 120-139, 2015.
- [150] Y. Zhu, R. Zhang, S. Zhang, Y. Chu and J. Chen, "Macroporous Polymers with Aligned Microporous Walls from Pickering High Internal Phase Emulsions," *Langmuir*, vol. 32, no. 24, pp. 6083-6088, 2016.
- [151] Y. Sun, Y. Li, J. Xu, L. Huang, T. Qiu and S. Zhong, "Interconnectivity of macroporous molecularly imprinted polymers fabricated by hydroxyapatite-stabilized Pickering high internal phase emulsions-hydrogels for the selective recognition of protein," *Colloids and Surfaces B: Biointerfaces*, vol. 155, pp. 142-149, 2017.
- [152] I. Gurevitch and S. Silverstein, "Polymerized Pickering HIPEs: Effects of Synthesis Parameters on Porous Structure," *Journal of Polymer Science: Part A: Polymer Chemistry*, vol. 48, pp. 1516-1525, 2010.
- [153] S. Melle, M. Lask and G. G. Fuller, "Pickering Emulsions with Controllable Stability," *Langmuir*, vol. 21, pp. 2158-2162, 2005.
- [154] Y. Hu, H. Gao, Z. Du, Y. Liu, Y. Yang and C. Wang, "Pickering high internal phase emulsion-based hydroxyapatite-poly(ϵ -caprolactone) nanocomposite scaffolds," *Journal of Materials Chemistry B*, vol. 3, pp. 3848-3857, 2015.
- [155] W. D. Harkins, "A General theory of the Reaction Loci in Emulsion Polymerization," *The Journal of Chemical Physics*, vol. 13, no. 9, pp. 381-382, 1945.
- [156] M. S. Silverstein, "PolyHIPEs: Recent advances in emulsion-templated porous polymers," *Progress in Polymer Science*, vol. 39, no. 1, pp. 199-234, 2014.

- [157] J. W. Vanderhoff, "Mechanism of Emulsion Polymerization," *Journal of Polymer Science: Polymer Symposium*, vol. 72, pp. 161-198, 1985.
- [158] W. V. Smith and R. H. Ewart, "Kinetics of Emulsion Polymerization," *The Journal of Chemical Physics*, vol. 16, no. 6, pp. 592-599, 1948.
- [159] G. Odian, "Chapter 4. Other characteristics of emulsion polymerization," in *Principles of Polymerization*, Jersey, United States of America, Wiley-Interscience, 2004, p. 367.
- [160] H. Tobita and A. Hamielec, "Modeling Emulsion Copolymerization: Crosslinking Kinetics," *Makromolekulare Chemie*, Vols. 35-36, no. 1, pp. 193-212, 1990.
- [161] P. Krajnc, J. F. Brown and N. R. Cameron, "Monolithic Scavenger Resins by amine Functionalizations of Poly(4-vinylbenzyl chloride-co-divinylbenzene) PolyHIPE materials," *Organic Letters*, vol. 4, no. 15, pp. 2497-2500, 2002.
- [162] N. R. Cameron, D. C. Sherrington, I. Ando and H. Kurosu, "Chemical modification of monolithic poly(styrene-divinylbenzene) PolyHIPE materials," *Journal of Materials Chemistry*, vol. 6, no. 5, pp. 719-726, 1996.
- [163] J. D. Lichtenhan, Y. A. Otonari and M. J. Carr, "Linear Hybrid Polymer Building Blocks: Methacrylate-Functionalized Polyhedral Oligomeric Silsesquioxane Monomers and Polymers," *Macromolecules*, vol. 28, pp. 8435-8437, 1995.
- [164] G. Smets, P. Hous and N. Deval, "Cyclopolymerization. IV. Structure of Polymethacrylic Anhydride and Kinetics of Polymerization of Methacrylic Anhydride," *Journal of Polymer Science: Part A*, vol. 2, pp. 4825-4834, 1964.
- [165] H. Tobita, K. Kimura, K. Fujita and M. Nomura, "Crosslinking kinetics in emulsion copolymerization of methyl methacrylate/ethylene glycol dimethacrylate," *Polymer*, vol. 34, no. 12, pp. 2569-2574, 1993.
- [166] U. Müller, S. Jockusch and H.-J. Timpe, "Photocrosslinking of Silicones. VI. Photocrosslinking Kinetics of Silicone Acrylates and Methacrylates," *Journal of Polymer Science Part A: Polymer Chemistry*, vol. 30, pp. 2755-2764, 1992.
- [167] D. Johnson, C. Langford, M. Didsbury, B. Lipp, S. Przyborski and N. Cameron, "Fully biodegradable and biocompatible emulsion templated polymer scaffolds by thiol-acrylate polymerization of polycaprolactone macromonomers," *Polymer Chemistry*, vol. 6, no. 41, pp. 7256-7263, 2015.
- [168] C. Decker, "Photoinitiated crosslinking polymerisation," *Progressive Polymer Science*, vol. 21, pp. 593-650, 1996.
- [169] N. Sears, "Emulsion Inks for 3D Printing of High Porosity Materials," *Macromolecular Journals*, vol. 37, pp. 1369-1374, 2016.
- [170] K. Yue, X. Li, K. Schrobback, A. Sheikhi, N. Annabi and J. Leijten, "Structural analysis of photocrosslinkable methacryloyl-modified protein derivatives," *Biomaterials*, vol. 139, pp. 163-171, 2017.
- [171] B. G. Amsden, A. Sukarto, D. K. Knight and S. N. Shapka, "Methacrylated Glycol Chitosan as a Photopolymerizable Biomaterial," *Biomacromolecules*, vol. 8, no. 12, pp. 3758-3766, 2007.

- [172] J. Barry, H. Gidda, C. Scotchford and S. Howdle, "Porous methacrylate scaffolds: supercritical fluid fabrication and in vitro chondrocyte responses," *Biomaterials*, vol. 25, no. 17, pp. 3559-3568, 2004.
- [173] O. A. Chanes-Cuevas, A. Perez-Soria, I. Cruz-Maya, V. Guarino and M. A. Alvarez-Perez, "Macro-, micro- and mesoporous materials for tissue engineering applications," *Materials Science*, vol. 5, no. 6, pp. 1124-1140, 2018.
- [174] M. Ahumada, E. Jacques, C. Calderon and F. Martinez-Gomez, "Chapter 14. Porosity in Biomaterials: A Key Factor in the Development of Applied Materials in Biomedicine," in *Handbook of Ecomaterials*, Springer, Cham, 2019, pp. 3503-3522.
- [175] B. Tian, J. Liu, T. Dvir, L. Jin, J. H. Tsui, Q. Qing, Z. Suo, R. Langer, D. S. Kohane and C. M. Lieber, "Macroporous nanowire nanoelectric scaffolds for synthetic tissues," *Nature Materials*, vol. 11, pp. 986-994, 2012.
- [176] A. Herrera, J. Hellwig, H. Leemhuis, R. von Klitzing, I. Heschel, G. Duda and A. Petersen, "From macroscopic mechanics to cell-effective stiffness within highly aligned macroporous collagen scaffolds," in *Materials Science and Engineering: C*, 103, 2019, p. 109760.
- [177] X. Wang, R. Feiner, H. Luan, Q. Zhang, S. Zhao, Zhang Yi, M. Han, Y. Li, R. Sun, H. Wang, T.-L. Liu, X. Guo, H. Oved, N. Noor, A. Shapira, Y. Zhang, Y. Huang, T. Dvir and J. A. Rogers, "Three-dimensional electronic scaffolds for monitoring and regulation of multifunctional hybrid tissues," *Extreme Mechanics Letters*, vol. 35, p. 100634, 2020.
- [178] R. Milo and R. Phillips, "1. Size and Geometry," in *Cell Biology by the Numbers*, Garland Science, 2015, pp. 44-50.
- [179] K. Malec, J. Górska, M. Hubalewska-Mazgaj, P. Glowacz, M. Jarosz, P. Brzewski, G. D Sulka, M. Jaskula and I. Wybranska, "Effects of nanoporous anodic titanium oxide on human adipose derived stem cells," *International Journal of Nanomedicine*, vol. 11, pp. 5349-5360, 2016.
- [180] W.-K. Cheah, K. Ishikawa, R. Othman and F.-Y. Yeoh, "Nanoporous biomaterials for uremic toxic adsorption in artificial kidney systems: A review," *Journal of Biomedical Materials Research Part B: Applied Biomaterials*, vol. 105, no. 5, pp. 1232-1240, 2016.
- [181] M. Gholipourmalekabadi, M. Mozafari, M. Bandehpour, M. Salehi, M. Sameni, H. H. Caicedo, A. Mehdipour, H. G. Hamidabadi, A. Samadikuchaksaraei and H. Ghanbarian, "Optimization of nanofibrous silk fibroin scaffold as a delivery system for bone marrow adherent cells: in vitro and in vivo studies," *Biotechnology and Applied Biochemistry*, vol. 62, no. 6, pp. 785-794, 2014.
- [182] U. Thamma, T. Kowal, M. Falk and H. Jain, "Influence of nanoporosity on the nature of hydroxyapatite formed on bioactive calcium silicate model glass," *Journal of Biomedical Materials Research Part B: Applied Biomaterials*, vol. 107, no. 4, pp. 886-899, 2018.
- [183] K. Kyobum, A. Yeatts, D. Dean and J. P. Fisher, "Stereolithographic bone scaffold design parameters: osteogenic differentiation and signal expression," *Tissue Engineering Part B, Reviews*, vol. 16, no. 5, pp. 523-539, 2010.
- [184] J. Naranda, M. Susec, U. Maver, L. Gradisnik and M. Gorenjak, "Polyester type polyHIPE scaffolds with an interconnected porous structure for cartilage regeneration," *Scientific Reports*, vol. 6, no. 28695, pp. 1-12, 2016.

- [185] S. Wu, X. Liu, K. W. Yeung, C. Liu and X. Yang, "Biomimetic porous scaffolds for bone tissue engineering," *Materials Science and Engineering Research*, vol. 80, pp. 1-36, 2014.
- [186] S. Mantila, J. Williams, P. Krebsbach and S. Hollister, "Pore size effects of polycaprolactone scaffolds on in vivo bone tissue engineering," *Journal of Biomedical Material Research*, vol. 92, no. 1, pp. 359-368, 2010.
- [187] H. Lee, G. H. Yang, M. Kim, J. Lee, J. Huh and G. Kim, "Fabrication of micro/nanoporous collagen/dECM/silk-dibromin biocomposite scaffolds using a low temperature 3D printing process for bone tissue regeneration," *Materials Science and Engineering: C*, vol. 84, pp. 140-147, 2018.
- [188] V. Karageorgiou and D. Kaplan, "Porosity of 3D biomaterial scaffolds and osteogenesis," *Biomaterials*, vol. 26, pp. 5474-5491, 2005.
- [189] S. Bauer, P. Schmuki, K. von der Mark and J. Park, "Engineering biocompatible implant surfaces: Part I: Materials and surfaces," *Progress in Materials Science*, vol. 58, no. 3, pp. 261-326, 2013.
- [190] Y. Tamada and Y. Ikada, "Effect of Preadsorbed Proteins on Cell Adhesion to Polymer Surfaces," *Journal of Colloid and Interface Science*, vol. 155, no. 2, pp. 334-339, 1993.
- [191] L. Minati, C. Migliaresi, L. Lunelli, G. Viero, M. Dalla Serra and G. Speranza, "Plasma assisted surface treatments of biomaterials," *Biophysical Chemistry*, vol. 229, pp. 151-164, 2017.
- [192] P. Chu, J. Chen, L. Wang and N. Huang, "Plasma-surface modification of biomaterials," *Materials Science and Engineering: R: Reports*, vol. 36, no. 5-6, pp. 143-206, 2002.
- [193] A. E. Wiacek, K. Terpilowski, M. Jurak and M. Worzakowska, "Low-temperature air plasma modification of chitosan-coated PEEK biomaterials," *Polymer Testing*, vol. 50, pp. 325-334, 2016.
- [194] M. T. Rodrigues, M. E. Gomes and R. L. Reis, "Current strategies for osteochondral regeneration: from stem cells to pre-clinical approaches," *Current Opinion in Biotechnology*, vol. 22, no. 5, pp. 726-733, 2011.
- [195] R. Hinton, Y. Jing, J. Jing and et al, "Roles of chondrocytes in Endochondral Bone Formation and Fracture Repair," *Journal of Dental Research*, vol. 96, pp. 23-30, 2016.
- [196] J. Lui, S. Yue, A. Lee, B. Kikani and et al, "Persistent SOX9 expression in hyperthropic chondrocytes suppresses transdifferentiation into osteoblasts," *Bone*, vol. 125, pp. 169-177, 2019.
- [197] P. G. Alexander, R. Gottardi, H. Lin, T. P. Lozito and R. S. Tuan, "Three-dimensional osteogenic and chondrogenic systems to model osteochondral physiology and degenerative joint diseases," *Experimental Biology and Medicine*, vol. 239, no. 9, pp. 1080-1095, 2017.
- [198] M. Vries-van Melle, M. Tihaya, N. Kops, W. Koevoet and et al, "Chondrogenic differentiation of human bone marrow-derived mesenchymal stem cells in a simulated osteochondral environment is hydrogel dependent," *European Cells & Materials*, vol. 3, no. 27, pp. 112-123, 2014.
- [199] B. Kristjansson and S. Honsawek, "Mesenchymal stem cells for cartilage regeneration in osteoarthritis," *World Journal of Orthopedics*, vol. 8, no. 9, pp. 674-680, 2017.
- [200] A.-M. Yousefi, P. F. James, R. Akbarzadeh, A. Subramanian, C. Flavin and H. Oudadesse, "Prospect of Stem Cells in Bone Tissue Engineering: A Review," *Stem Cells International*, vol. 2016, no. 6170487, pp. 1-13, 2016.

- [201] J. Zou, B. Bai and Y. Yao, "Progress of co-culture systems in cartilage regeneration," *Expert Opinion on Biological Therapy*, vol. 18, no. 11, pp. 1151-1158, 2018.
- [202] M. G. Scioli, A. Bielli, P. Gentile, V. Cervelli and A. Orlandi, "Combined treatment with platelet-rich plasma and insulin favours chondrogenic and osteogenic differentiation of human adipose-derived stem cells in three-dimensional collagen scaffolds," *Journal of Tissue Engineering and Regenerative Medicine*, vol. 11, pp. 2398-2410, 2017.
- [203] T. N. Snyder, K. Madhavan, M. Intrator, R. C. Dregalla and D. Park, "A fibrin/hyaluronic acid hydrogel for the delivery of mesenchymal stem cells and potential for articular cartilage repair," *Journal of Biological Engineering*, vol. 8, no. 10, pp. 1-11, 2014.
- [204] A. E. Erickson, J. Sun, S. K. L. Lan Levensgood, S. Swanson, F.-C. Chang, C. T. Tsao and M. Zhang, "Chitosan-based composite bilayer scaffolds as an in vitro osteochondral defect regeneration model," *Biomedical Microdevices*, vol. 21, no. 34, pp. 1-16, 2019.
- [205] E. Makris, A. H. Gomoll, K. N. Malizos, J. C. Hu and K. A. Athanasiou, "Repair and tissue engineering techniques for articular cartilage," *Rheumatology Nature Reviews*, vol. 11, pp. 21-34, 2015.
- [206] H. Mizuno, "Adipose-derived Stem Cells for Tissue Repair and Regeneration: Ten Years of Research and a Literature Review," *Journal of Nippon Medical School*, vol. 76, no. 2, pp. 56-66, 2009.
- [207] V. Keller, A. Deiwick, M. Pflaum and S. Schlie-Wolter, "Correlation between ECM guidance and actin polymerization on osteogenic differentiation of human adipose-derived stem cells," *Experimental Cell Research*, vol. 347, no. 2, pp. 339-349, 2016.
- [208] K. L. Burrow, J. A. Hoyland and S. M. Richardson, "Human Adipose-Derived Stem Cells Exhibit Enhanced Proliferative Capacity and Retain Multipotency Longer than Donor-Matched Bone Marrow Mesenchymal Stem Cells during Expansion In Vitro," *Stem Cells International*, vol. 2017, p. 2541275, 2017.
- [209] N. K. Dubey, V. K. Mishra, R. Dubey, S. Syed-Abdul, J. R. Wang, P. D. Wang and W.-P. Deng, "Combating Osteoarthritis through Stem Cell Therapies by Rejuvenating Cartilage: A Review," *Stem Cells in Cartilage Diseases and Repair*, vol. 2018, p. 5421019, 2018.
- [210] J. J. Patel, L. E. Bourne, B. K. Davies, T. R. Arnett, V. E. MacRae, C. P. Wheeler-Jones and I. R. Orriss, "Differing calcification processes in cultured vascular smooth muscle cells and osteoblasts," *Experimental Cell Research*, vol. 380, no. 1, pp. 100-113, 2019.
- [211] Y. Dai, T. Shen, L. Ma, D. Wang and C. Gao, "Regeneration of osteochondral defects in vivo by a cell-free cylindrical poly(lactide-co-glycolide) scaffold with a radially oriented microstructure," *Journal of Tissue Engineering and Regenerative Medicine*, vol. 12, no. 3, 2017.
- [212] D. S. Clearfield, X. Xin, S. Yadav, D. W. Rowe and M. Wei, "Osteochondral Differentiation of Fluorescent Multireporter Cells on Zonally-Organized Biomaterials," *Tissue Engineering: Part A*, vol. 25, no. 5-6, pp. 468-486, 2019.
- [213] Y.-J. Seong, I.-G. Kang, E.-H. Song, H.-E. Kim and S.-H. Jeong, "Calcium Phosphate-Collagen Scaffold with Aligned Pore Channels for Enhanced Osteochondral Regeneration," *Advanced Healthcare Materials*, vol. 6, no. 24, p. 1700966, 2017.

- [214] D. Clearfield, A. Nguyen and M. Wei, "Biomimetic multidirectional scaffolds for zonal osteochondral tissue engineering via a lyophilization bonding approach," *Journal of Biomedical Materials Research Part A*, vol. 106A, pp. 948-958, 2018.
- [215] Y. Qin, G. Li, C. Wang, D. Zhang, L. Zhang, H. Fang and J. Yin, "Biomimetic bilayer scaffold as an incubator to induce sequential chondrogenesis and osteogenesis of ASCs for construction of osteochondral tissue," *ACS Biomaterials Science & Engineering*, vol. 6, no. 5, pp. 3070-3080, 2020.
- [216] Dai, Y. Dai, Z. Gao, L. Ma, D. Wang and C. Gao, "Cell-Free HA-MA/PLGA Scaffolds with Radially Oriented Pores for In Situ Inductive Regeneration of Full Thickness Cartilage Defects," *Macromolecular Bioscience*, vol. 16, no. 11, pp. 1632-1642, 2016.
- [217] X. Feng, P. Xu, T. Shen, Y. Zhang, J. Ye and C. Gao, "Influence of pore architectures of silk fibroin/collagen composite scaffolds on the regeneration of osteochondral defects in vivo," *Journal of Materials Chemistry B*, vol. 8, no. 3, pp. 391-405, 2020.
- [218] A. Di Luca, A. Longoni, G. Criscenti, I. Lorenzo-Moldero, M. Klein-Gunnewiek, J. Vancso, C. van Blitterswijk, C. Mota and L. Moroni, "Surface energy and stiffness discrete gradients in additive manufactured scaffolds for osteochondral regeneration," *Biofabrication*, vol. 8, no. 1, pp. 1-13, 2016.
- [219] A. Prasopthum, M. Cooper, K. M. Shakesheff and J. Yang, "Three-Dimensional Printed Scaffolds with Controlled Micro-/Nanoporous Surface Topography Direct Chondrogenic and Osteogenic Differentiation of Mesenchymal Stem Cells," *ACS Applied Materials & Interfaces*, vol. 11, pp. 18896-18906, 2019.
- [220] K. Markstedt, A. Mantas, I. Tournier, H. Martínez Ávila, D. Hägg and P. Gatenholm, "3D Bioprinting Human Chondrocytes with Nanocellulose-Alginate Bioink for Cartilage Tissue Engineering Applications," *BioMacromolecules*, vol. 16, no. 5, pp. 1489-1496, 2015.
- [221] L. García-Martínez, F. Campos, C. Godoy-Guzmán, M. d. C. Sánchez-Quevedo, I. Garzón, M. Alaminos, A. Campos and V. Carriel, "Encapsulation of human elastic cartilage-derived chondrocytes in nanostructured fibrin-agarose hydrogels," *Histochemistry and Cell Biology*, vol. 147, pp. 83-95, 2017.
- [222] Z. Miao, Z. Lu, H. Wu, H. Liu, M. Li, D. Lei, L. Zheng and J. Zhao, "Collagen, agarose, alginate, and Matrigel hydrogels as cell substrates for culture of chondrocytes in vitro: A comparative study," *Journal of Cellular Biochemistry*, vol. 119, no. 10, pp. 7924-7933, 2017.
- [223] P. A. Parmar, L. W. Chow, J.-P. St-Pierre, C.-M. Horejs, Y. Y. Peng, J. A. Werkmeister, J. A. Ramshaw and M. M. Stevens, "Collagen-mimetic peptide-modifiable hydrogels for articular cartilage regeneration," *Biomaterials*, vol. 54, pp. 213-225, 2015.
- [224] K. B. Fonseca, D. B. Gomes, K. Lee, S. G. Santos, A. Sousa, E. A. Silva, D. J. Mooney, P. L. Granja and C. C. Barrias, "Injectable MMP-Sensitive Alginate Hydrogels as hMSC Delivery Systems," *BioMacromolecules*, vol. 15, no. 1, pp. 380-390, 2014.
- [225] J. Puértolas, J. Vellido, S. Sánchez-Salcedo, A. Nieto, E. Gómez-Barrena and M. Vallet-Regí, "Compression behaviour of biphasic calcium phosphate and biphasic calcium phosphate-agarose scaffolds for bone regeneration," *Acta Biomaterialia*, vol. 7, no. 2, pp. 841-847, 2011.
- [226] L.-P. Yan, J. Silva-Correia, M. B. Oliveira, C. Vilela, H. Pereira, R. A. Sousa, J. F. Mano, A. L. Oliveira, J. M. Oliveira and R. L. Reis, "Bilayered silk/silk-nanoCaP scaffolds for osteochondral

tissue engineering: In vitro and in vivo assessment of biological performance,” *Acta Biomaterialia*, vol. 12, pp. 227-241, 2015.

- [227] P. Kazimierczak, A. Benko, M. Nocun and A. Przekora, “Novel chitosan/agarose/hydroxyapatite nanocomposite scaffold for bone tissue engineering applications: comprehensive evaluation of biocompatibility and osteoinductivity with the use of osteoblasts and mesenchymal stem cells,” *International Journal of Nanomedicine*, vol. 14, pp. 6615-6630, 2019.
- [228] C. Stüdle, Q. Vallmajó-Martín, A. Haumer, J. Guerrero, M. Centola, A. Mehrkens, D. J. Schaefer, M. Ehrbar, A. Barbero and I. Martin, “Spatially confined induction of endochondral ossification by functionalized hydrogels for ectopic engineering of osteochondral tissues,” *Biomaterials*, vol. 171, pp. 219-229, 2018.
- [229] T. Shen, Y. Dai, X. Li, S. Xu, Z. Gou and C. Gao, “Regeneration of the Osteochondral Defect by a Wollastonite and Macroporous Fibrin Biphasic Scaffold,” *ACS Biomaterials Science & Engineering*, vol. 4, no. 6, pp. 1942-1953, 2018.
- [230] D. Su, L. Jiang, X. Chen, J. Dong and Z. Shao, “Enhancing the Gelation and Bioactivity of Injectable Silk Fibroin Hydrogel with Laponite Nanoplatelets,” *ACS Applied Materials & Interfaces*, vol. 8, no. 14, pp. 9619-9628, 2016.
- [231] X. Zhai, C. Ruan, Y. Ma, D. Cheng, M. Wu, W. Liu, X. Zhao, H. Pan and W. W. Lu, “3D-Bioprinted Osteoblast-Laden Nanocomposite Hydrogel Constructs with Induced Microenvironments Promote Cell Viability, Differentiation, and Osteogenesis both In Vitro and In Vivo,” *Advanced Science*, vol. 5, no. 3, p. 1700550, 2017.
- [232] T. J. Levingstone, A. Matsiko, G. R. Dickson, F. O'Brien and J. P. Gleeson, “A biomimetic multi-layered collagen-based scaffold for osteochondral repair,” *Acta Biomaterialia*, vol. 10, no. 5, pp. 1996-2004, 2014.
- [233] S. Kazemnejad, M. Khanmohammadi, S. Mobini, M. Taghizadeh-Jahed, S. Khanjani, S. Arasteh, H. Golshahi, G. Torkaman, R. Ravanbod, H. Heidari-Vala, A. Moshiri, M.-N. Tahmasebi and M.-M. Akhondi, “Comparative repair capacity of knee osteochondral defects using regenerated silk fiber scaffolds and fibrin glue with/without autologous chondrocytes during 36 weeks in rabbit model,” *Cell and Tissue Research*, vol. 364, pp. 559-572, 2016.
- [234] F. Chicatun, E. Rezabeigi, N. Muja, M. T. Kaartinen, M. D. McKee and S. N. Nazhat, “A bilayered dense collagen/chitosan hydrogel to model the osteochondral interface,” *Emergent Materials*, vol. 2, pp. 245-262, 2019.
- [235] E. J. Sheehy, T. Vinardell, C. T. Buckley and D. J. Kelly, “Engineering osteochondral constructs through spatial regulation of endochondral ossification,” *Acta Biomaterialia*, vol. 9, no. 3, pp. 5484-5492, 2013.
- [236] N. T. Khanarian, N. M. Haney, R. A. Burga and H. H. Lu, “A functional agarose-hydroxyapatite scaffold for osteochondral interface regeneration,” *Biomaterials*, vol. 33, no. 21, pp. 5247-5258, 2012.
- [237] H.-w. Cheng, K. D. Luk, K. M. Cheung and B. P. Chan, “In vitro generation of an osteochondral interface from mesenchymal stem cell-collagen microspheres,” *Biomaterials*, vol. 32, no. 6, pp. 1526-1535, 2011.

- [238] Y. Du, H. Liu, Q. Yang, S. Wang, J. Wang, J. Ma, I. Noh, A. G. Mikos and S. Zhang, "Selective laser sintering scaffold with hierarchical architecture and gradient composition for osteochondral repair in rabbits," *Biomaterials*, vol. 137, pp. 37-48, 2017.
- [239] J.-H. Shim, K.-M. Jang, S. K. Hahn, J. Y. Park, H. Jung, K. Oh, K. M. Park, J. Yeom, S. H. Park, S. W. Kim, J. H. Wang, K. Kim and D.-W. Cho, "Three-dimensional bioprinting of multilayered constructs containing human mesenchymal stromal cells for osteochondral tissue regeneration in the rabbit knee joint," *Biofabrication*, vol. 8, no. 014102, 2016.
- [240] A. C. Daly, P. Pitacco, J. Nulty, G. M. Cunniffe and D. J. Kelly, "3D printed microchannel networks to direct vascularisation during endochondral bone repair," *Biomaterials*, vol. 162, pp. 34-46, 2018.
- [241] J. Liao, T. Tian, S. Shi, X. Xie, Q. Ma, G. Li and Y. Lin, "The fabrication of biomimetic biphasic CAN-PAN hydrogel with a seamless interfacial layer applied in osteochondral defect repair," *Bone Research*, vol. 5, no. 17018, pp. 1-15, 2017.
- [242] M. Vainieri, D. Wahl, M. Alini, G. van Osch and S. Grad, "Mechanically stimulated osteochondral organ culture for evaluation of biomaterials in cartilage repair studies," *Acta Biomaterialia*, vol. 81, pp. 256-266, 2018.
- [243] J. Yang, Y. S. Zhang, K. Yue and A. Khademhosseini, "Cell-laden hydrogels for osteochondral and cartilage tissue engineering," *Acta Biomaterialia*, vol. 57, pp. 1-25, 2017.
- [244] K. Ghosal, U. Bhattacharjee and K. Sarkar, "Facile green synthesis of bioresorbable polyester from soybean oil and recycled plastic waste for osteochondral tissue engineering," *European Polymer Journal*, vol. 122, p. 109338, 2020.
- [245] C. Ding, Z. Qiao, W. Jiang, H. Li, J. Wei, G. Zhou and K. Dai, "Regeneration of a goat femoral head using a tissue-specific, biphasic scaffold fabricated with CAD/CAM technology," *Biomaterials*, vol. 34, no. 28, pp. 6706-6716, 2013.
- [246] S. M. Bittner, B. T. Smith, L. Diaz-Gomez, C. D. Hudgins, A. J. Melchiorri, D. W. Scott, J. P. Fisher and A. G. Mikos, "Fabrication and mechanical characterization of 3D printed vertical uniform and gradient scaffolds for bone and osteochondral tissue engineering," *Acta Biomaterialia*, vol. 90, pp. 37-48, 2019.
- [247] B. Zhang, L. Guo, H. Chen, Y. Ventikos, R. J. Narayan and J. Huang, "Finite element evaluations of the mechanical properties of polycaprolactone/hydroxyapatite scaffolds by direct ink writing: Effects of pore geometry.," *Journal of the Mechanical Behavior of Biomedical Materials*, vol. 104, p. 103665, 2020.
- [248] X. Meng, R. Ziadlou, S. Grad, M. Alini, C. Wen, Y. Lai, L. Qin, Y. Zhao and X. Wang, "Animal Models of Osteochondral Defect for Testing Biomaterials," *Biochemistry Research International*, vol. 2020, pp. 1-12, 2020.
- [249] B. Ju Kim, Y. Arai, B. Choi, S. Park, J. Ahn, I.-B. Han and S.-H. Lee, "Restoration of articular osteochondral defects in rats by a bi-layered hyaluronic acid hydrogel plug with TUDCA-PLGA microsphere," *Journal of Industrial and Engineering Chemistry*, vol. 61, pp. 295-303, 2018.
- [250] G. Filardo, F. Perdisa, M. Gelinsky, F. Despong, M. Fini, M. Marcacci, A. P. Parrilli, A. Roffi, F. Salamanna, M. Sartori, K. Schütz and E. Kon, "Novel alginate biphasic scaffold for osteochondral

regeneration: an in vivo evaluation in rabbit and sheep models,” *Tissue Engineering Constructs and Cell Substrates*, vol. 29, no. 74, pp. 1-13, 2018.

- [251] E. C. McCarty, R. R. Fader, J. J. Mitchel, R. E. Glenn, H. G. Potter and K. P. Spindler, “Fresh Osteochondral Allograft Versus Autograft: Twelve-Month Results in Isolated Canine Knee Defects,” *The American Journal of Sports Medicine*, vol. 44, no. 9, pp. 2354-2365, 2016.
- [252] E. Ruvinov, T. T. Re'em, F. Witte and S. Cohen, “Articular cartilage regeneration using acellular bioactive affinity-binding alginate hydrogel: A 6-month study in a mini-pig model of osteochondral defects,” *Journal of Orthopaedic Translation*, vol. 16, pp. 40-52, 2019.
- [253] I. Dias, C. Viegas and P. Carvalho, “Chapter 20. Large Animal Models for Osteochondral Regeneration.,” in *Advances in Experimental Medicine and Biology*, 29736586, 2018, pp. 441-501.
- [254] T. J. Levingstone, A. Ramesh, R. T. Brady, P. A. Brama, C. Kearney, J. P. Gleeson and F. J. O'Brien, “Cell-free multi-layered collagen-based scaffolds demonstrate layer specific regeneration of functional osteochondral tissue in caprine joints,” *Biomaterials*, vol. 87, pp. 69-81, 2016.
- [255] M. C. Fugazzola and P. R. van Weeren, “Surgical osteochondral defect repair in the horse - a matter of form or function?,” *Equine Veterinary Journal*, vol. 00, pp. 1-11, 2020.
- [256] C. Chen, A. M. Eissa, T. L. Schiller and N. R. Cameron, “Emulsion-templated porous polymers prepared by thiol-ene and thiol-yne photopolymerisation using multifunctional acrylate and non-acrylate monomers,” *Polymer*, vol. 126, pp. 395-401, 2017.
- [257] R. Delaine-Smith, S. MacNeil and G. Reilly, “Matrix production and collagen structure are enhanced in types of osteogenic progenitor cells by a simple fluid shear stress stimulus,” *European Cells and Materials*, vol. 24, pp. 162-174, 2012.
- [258] S. Puwanun, *Developing a tissue engineering strategy for cleft palate repair*, The University of Sheffield: Doctoral Thesis, 2014.
- [259] M. Aydelotte and K. Kuettner, “Differences between sub-populations of cultured bovine articular chondrocytes. I. Morphology and cartilage matrix production.,” *Connective Tissue Research*, vol. 18, no. 3, pp. 205-222, 1988.
- [260] S. James, J. Fox, F. Afsari, J. Lee, S. Clough, C. Knight, J. Ashmore, P. Ashton, O. Preham, M. Hoogduijn, R. De Almeida Rocha Ponzoni, Y. Hancock, M. Coles and P. Genever, “Multiparameter Analysis of Human Bone Marrow Stromal Cells Identifies Distinct Immunomodulatory and Differentiation-Competent Subtypes,” *Stem Cell Reports*, vol. 4, pp. 1004-1015, 2015.
- [261] R. J. Carnachan, M. Bokhari, S. A. Przyborski and N. R. Cameron, “Tailoring the morphology of emulsion-templated porous polymers,” *Soft Matter*, vol. 2, pp. 608-616, 2006.
- [262] M. Ovadia and M. S. Silverstein, “High porosity, responsive hydrogel copolymers from emulsion templating,” *Polymer International*, vol. 65, pp. 280-289, 2016.
- [263] D. V. Soldatov, I. L. Moudrakovski, E. V. Grachev and J. A. Ripmeester, “Micropores in Crystalline Dipeptides as Seen from the Crystal Structure, He Pycnometry, and ^{129}Xe NMR Spectroscopy,” *JACS Articles*, vol. 128, pp. 6737-6744, 2006.

- [264] M. Nowicki, W. Zhu, K. Sarkar, R. Rao and L. G. Zhang, “3D printing multiphasic osteochondral tissue constructs with nano to micro features via PCL based bioink,” *Bioprinting*, vol. 17, p. e00066, 2020.
- [265] J. Field, J. W. Haycock, F. M. Boissonade and F. Claeysens, “A Tuneable, Photocurable, Poly(Caprolactone)-Based Resin for Tissue Engineering - Synthesis, Characterisation and Use in Stereolithography,” *Molecules*, vol. 26, no. 1199, pp. 1-22, 2021.
- [266] M. Messori, M. Degli Esposti, K. Paderni, S. Pandini, S. Passera, T. Ricco and M. Toselli, “Chemical and thermomechanical tailoring of the shape memory effect in poly(ϵ -caprolactone)-based systems,” *Journal of Material Sciences*, vol. 48, pp. 424-440, 2013.
- [267] M. Lang and C.-C. Chu, “Functionalised multiarm poly(ϵ -caprolactone)s: synthesis, structure analysis, and network formation,” *Journal of Applied Polymer Science*, vol. 86, pp. 2296-2306, 2002.
- [268] F. Boschetti and G. M. Peretti, “Tensile and compressive properties of healthy and osteoarthritic human articular cartilage,” *Biorheology*, vol. 45, pp. 337-344, 2008.
- [269] C. L. Camp, M. J. Stuart and A. J. Krych, “Current Concepts of Articular Cartilage Restoration Techniques in the Knee,” *Sports Health*, vol. 6, no. 3, pp. 265-273, 2014.
- [270] R. Rowland, M. Colello and D. J. Wyland, “Osteochondral Autograft Transfer Procedure: Arthroscopic Technique and Technical Pearls,” *Arthroscopy Techniques*, vol. 8, no. 7, pp. e713-e719, 2019.
- [271] A. H. Technologies, “Trufit CB Plug & Trufit BGS Plug,” Advanced Healing Technologies, U.S., 2012.
- [272] W. Busby, N. R. Cameron and C. A. Jahoda, “Emulsion-Derived Foams (PolyHIPEs) Containing Poly(ϵ -caprolactone) as Matrixes for Tissue Engineering,” *Biomacromolecules*, vol. 2, pp. 154-164, 2001.
- [273] A. Yadav, J. Pal, B. Nandan and R. K. Srivastava, “Macroporous scaffolds of crosslinked Poly(ϵ -caprolactone) via high internal phase emulsion templating,” *Polymer*, vol. 176, pp. 66-73, 2019.
- [274] D. Martinez-Moreno, G. Jiménez, C. Chocarro-Wrona, E. Carrillo, E. Montañez, C. Galocha-León, B. Clares-Naveros, P. Gálvez-Martín, G. Rus, J. de Vicente and J. Marchal, “Pore geometry influences growth and cell adhesion of infrapatellar mesenchymal stem cells in biofabricated 3D thermoplastic scaffolds useful for cartilage tissue engineering,” *Materials Science and Engineering: C*, vol. 122, no. 111933, 2021.
- [275] V. O. Ikem, A. Menner and A. Bismarck, “High Internal Phase Emulsions Stabilized Solely by Functionalized Silica Particles,” *Angewandte Chemie*, vol. 120, pp. 8401-8403, 2008.
- [276] B. Aldemir Dikici and F. Claeysens, “Basic Principles of Emulsion Templating and Its Use as an Emerging Manufacturing Method of Tissue Engineering Scaffold,” *Frontiers in Bioengineering and Biotechnology*, vol. 8, no. 875, 2020.
- [277] M. Perez-Garcia, A. Carranza, J. Puig, J. Pojman, F. del Monte, G. Luna-Barcenas and J. Mota-Morales, “Porous monoliths synthesized via polymerization of styrene and divinyl benzene in nonaqueous deep-eutectic solvent-base HIPEs,” *RSC Advances*, vol. 5, pp. 23255-23260, 2015.

- [278] A. Carranza, J. Pojman and J. Mota-Morales, “Deep-eutectic solvents as a support in the nonaqueous synthesis of macroporous poly(HIPEs),” *RSC Advances*, vol. 4, pp. 41584-41587, 2014.
- [279] R. Owen, C. Sherborne, T. Paterson, N. H. Green, G. C. Reilly and F. Claeysens, “Emulsion templated scaffolds with tunable mechanical properties for bone tissue engineering,” *Journal of the Mechanical Behaviour of Biomedical Materials*, vol. 54, pp. 159-172, 2016.
- [280] I. Pulko and P. Krajnc, “High Internal Phase Emulsion Templating – A Path To Hierarchically Porous Functional Polymers,” *Macromolecular Rapid Communications*, vol. 33, no. 20, pp. 1731-1746, 2012.
- [281] T. Gitli and M. S. Silverstein, “Bicontinuous hydrogel-hydrophobic polymer systems through emulsion templated simultaneous polymerizations,” *Soft Matter*, vol. 4, no. 12, pp. 2475-2485, 2008.
- [282] A. Menner and A. Bismarck, “New evidence for the mechanism of the pore formation in polymerising high internal phase emulsions or why polyHIPEs have an interconnected pore network structure,” *Macromolecular Symposia*, vol. 242, no. 1, pp. 19-24, 2006.
- [283] A. C. Jones, B. Milthorpe, H. Averdunk, A. Limaye, T. J. Senden, A. Sakellariou, A. P. Sheppard, R. M. Sok, M. A. Knackstedt, A. Brandwood, D. Rohner and D. W. Huttmacher, “Analysis of 3D bone ingrowth into polymer scaffolds via micro-computed tomography imaging,” *Biomaterials*, vol. 25, no. 20, pp. 4947-4954, 2004.
- [284] G. H. van Lenthe, H. Hagenmüller, M. Bohner, S. J. Hollister, L. Meinel and R. Müller, “Nondestructive micro-computed tomography for biological imaging and quantification of scaffold-bone interaction in vivo,” *Biomaterials*, vol. 28, pp. 2479-2490, 2007.
- [285] D. Sadeq, S. Iglauer, M. Lebedev, T. Rahman, Y. Zhang and A. Barifcani, “Experimental pore-scale analysis of carbon dioxide hydrate in sandstone via X-Ray micro-computed tomography,” *International Journal of Greenhouse Gas Control*, vol. 79, pp. 73-82, 2018.
- [286] M. J. Moore, E. Jabbari, E. L. Ritman, L. Lu, B. L. Currier, A. J. Windebanck and M. J. Yaszemski, “Quantitative analysis of interconnectivity of porous biodegradable scaffolds with micro-computed tomography,” *Journal of Biomedical Materials Research Part A*, vol. 71A, no. 2, pp. 258-267, 2004.
- [287] J. Kaczmarczyk, M. Dohnalik and J. Zalewska, “The interpretation of X-ray Computed Microtomography images of rocks as an application of volume images processing and analysis,” *18th International Conference in Central Europe on Computer Graphics, Visualization and Computer Vision*, pp. 23-30, 2010.
- [288] A. L. Goertzen, F. J. Beekman and S. R. Cherry, “Effect of Voxel Size in CT Simulations,” *IEEE Nuclear Science Symposium*, vol. 3, pp. 20/93-20/97, 2000.
- [289] L. Elomaa, S. Teixeira, R. Hakala, H. Korhonen, D. W. Grijpma and J. V. Seppälä, “Preparation of poly(ϵ -caprolactone)-based tissue engineering scaffolds by stereolithography,” *Acta Biomaterialia*, vol. 7, pp. 3850-3856, 2011.
- [290] N. Thadavirul, P. Pavasant and P. Supaphol, “Development of polycaprolactone porous scaffolds by combining solvent casting, particulate leaching, and polymer leaching techniques for bone tissue engineering,” *Journal of Biomedical Materials Research: Part A*, vol. 102, no. 10, pp. 3379-3392, 2013.
- [291] K. Gómez-LIzárraga, C. Flores-Morales, M. Del Prado-Audelo, M. Álvarez-Pérez, M. Piña-Barba and C. Escobedo, “Polycaprolactone- and polycaprolactone/ceramic-based 3D-biopltted porous scaffolds

- for bone regeneration: A comparative study,” *Materials Science and Engineering: C*, vol. 79, pp. 326-335, 2017.
- [292] M. Fanovich and P. Jaeger, “Sorption and diffusion of compressed carbon dioxide in polycaprolactone for the development of porous scaffolds,” *Materials Science and Engineering: C*, vol. 32, no. 4, pp. 961-968, 2012.
- [293] A. R. Sarasam, A. I. Samli, L. Hess, M. A. Ihnat and S. V. Madihally, “Blending Chitosan with Polycaprolactone: Porous Scaffolds and Toxicity,” *Macromoleculer Bioscience*, vol. 7, no. 9-10, pp. 1160-1167, 2007.
- [294] N. Cameron and D. Sherrington, “High Internal Phase Emulsions (HIPES) - Structure, Properties and Use in Polymer Preparation,” *Advances in Polymer Science*, vol. 126, pp. 163-215, 1996.
- [295] Y. Lumelsky, J. Zoldan, S. Levenberg and M. S. Silverstein, “Porous Polycaprolactone - Polystyrene Semi-interpenetrating Polymer Networks Synthesized within High Internal Phase Emulsions,” *Macromolecules*, vol. 41, pp. 1469-1474, 2008.
- [296] Y. Wang, G. A. Ameer, B. J. Sheppard and R. Langer, “A tough biodegradable elastomer,” *Nature Biotechnology*, vol. 20, pp. 602-606, 2002.
- [297] A. Nadim, S. N. Khorasani, M. Kharaziha and S. M. Davoodi, “Design and characterization of dexamethasone-loaded poly(glycerol sebacate)-polycaprolactone / gelatin scaffolds by coaxial electro spinning for soft tissue engineering,” *Materials Science and Engineering C*, vol. 78, pp. 47-58, 2017.
- [298] Y.-L. Wu, A. R. D'Amato, A. M. Yan, R. Q. Wang, X. Ding and Y. Wang, “Three-Dimensional Printing of Poly(glycerol sebacate) Acrylate Scaffolds via Digital Light Processing,” *ACS Applied Biomaterials*, vol. 3, no. 11, pp. 7575-7588, 2020.
- [299] D. Singh, A. J. Harding, E. Albadawi, F. M. Boissonade and F. Claeysens, “Additive manufactured biodegradable poly(glycerol sebacate methacrylate) nerve guidance conduits,” *Acta Biomaterialia*, vol. 78, pp. 48-63, 2018.
- [300] M. Wang, D. Lei, Z. Liu, S. Chen, L. Sun, Z. Lv, P. Huang, Z. Jiang and Z. You, “A poly(glycerol sebacate) based photo/thermo dual curable biodegradable and biocompatible polymer for biomedical applications,” *Journal of Biomaterilas, Science, Polymer Edition*, vol. 28, no. 15, pp. 1728-1739, 2017.
- [301] R. Owen, C. Sherborne, R. Evans, G. Reilly and F. Claeysens, “Combined Porogen Leaching and Emulsion Templating to produce Bone Tissue Engineering Scaffolds,” *International Journal of Bioprinting*, vol. 6, no. 2, pp. 99-113, 2020.
- [302] A.-j. Wang, “Photocurable high internal phase emulsions (HIPEs) containing hydroxyapatite for additive manufacture of tissue engineering scaffolds with multi-scale porosity,” *Materials Science and Engineering*, vol. 67, pp. 51-58, 2016.
- [303] A. Martynenko, “True, Particle, and Bulk Density of Shrinkable Biomaterials: Evaluation from Drying Experiments,” *Drying Technology*, vol. 32, no. 11, pp. 1319-1325, 2014.
- [304] Y.-L. Wu, A. R. D'Amato, A. M. Yan, R. Q. Wan, X. Ding and Y. Wang, “Three-Dimensional Printing of Poly(glycerol sebacate) Acrylate Scaffolds via Digital Light Processing,” *ACS Applied Biomaterials*, vol. 3, no. 11, pp. 7575-7588, 2020.

- [305] G. B. McKenna, K. M. Flynn and Y. Chen, "Swelling in crosslinked natural rubber: experimental evidence of the crosslink density dependence of χ ," *Polymer*, vol. 31, pp. 1937-1945, 1990.
- [306] C. Sherborne, The development and characterisation of biocompatible emulsion templated foams for additive manufacturing, Department of Materials Science and Engineering: The University of Sheffield, 2015.
- [307] A. Eibel, D. E. Fast and G. Gescheidt, "Choosing the ideal photoinitiator for free radical photopolymerizations: predictions based on simulations using established data," *Polymer Chemistry*, vol. 9, pp. 5107-5115, 2018.
- [308] S. C. Ligon-Auer, M. Schwentenwein, C. Gorsche, J. Stampfl and R. Liska, "Toughening of photo-curable polymer networks: a review," *Polymer Chemistry*, vol. 7, pp. 257-286, 2016.
- [309] C. Sherborne, R. Owen, G. C. Reilly and F. Claeysens, "Light-based additive manufacturing of PolyHIPEs: Controlling the surface porosity for 3D cell culture applications," *Materials & Design*, vol. 156, pp. 494-503, 2018.
- [310] N. R. Cameron, "High internal phase emulsion templating as a route to well-defined porous polymers," *Polymer*, vol. 46, no. 5, pp. 1439-1449, 2005.
- [311] M. A. Rathbun, R. G. Craig, C. T. Hanks and F. E. Flisko, "Cytotoxicity of a BIS-GMA dental composite before and after leaching inorganic solvents," *Virtual Collection: Bioworld Structures*, vol. 25, no. 4, pp. 443-457, 1991.
- [312] N. Soriani Yaacob, N. Hamzah, N. N. Mohamed Kamal, S. A. Zainal Abidin, C. S. Lai, V. Navaratnam and M. N. Norazmi, "Anticancer activity of a sub-fraction of dichloromethane extract of *Strobilanthes crispus* on human breast and prostate cancer cells in vitro," *BMC Complementary and Alternative Medicine*, vol. 10, no. 42, pp. 1-14, 2010.
- [313] L. Pérez-Mosqueda, L. A. Trujillo-Cayado, F. Carrillo, P. Ramírez and J. Muñoz, "Formulation and optimization by experimental design of eco-friendly emulsions based on d-limonene," *Colloids and Surfaces B: Biointerfaces*, vol. 128, pp. 127-131, 2015.
- [314] N. Dib, C. M. O. Lépori, N. M. Correa, J. J. Silber, R. D. Falcone and L. García-Río, "Biocompatible Solvents and Ionic Liquid-Based Surfactants as Sustainable Components to Formulate Environmentally Friendly Organized Systems," *Polymers*, vol. 13, no. 1378, pp. 1-34, 2021.
- [315] C.-H. Lu, W.-C. Tang, Y.-T. Liu, S.-W. Chang, F. C. M. Wu, C.-Y. Chen, Y.-C. Tsai, S.-M. Yang, C.-W. Kuo, Y. Okada, Y.-K. Hwu, P. Chen and B.-C. Chen, "Lightsheet localization microscopy enables fast, large-scale, and three-dimensional super-resolution imaging," *Communications Biology*, vol. 2, no. 177, 2019.
- [316] W. Busby, "Emulsion-Derived Foams (PolyHIPEs) Containing Poly(ϵ -caprolactone) as Matrices for Tissue Engineering," *Biomacromolecules*, vol. 2, pp. 154-164, 2001.
- [317] A. Kabalnov, A. Pertzov and E. Shchukin, "Ostwald Ripening in Emulsions," *Journal of Colloid and Interface Science*, vol. 118, no. 2, pp. 590-597, 1987.
- [318] J.-H. Chen, T. T. Mai Le and K.-C. Hsu, "Application of PolyHIPE Membrane with Tricaprylmethylammonium chloride for Cr(VI) Ion Separation: Parameters and Mechanism of Transport Relating to the Pore Structure," *Membranes*, vol. 1, no. 11, pp. 1-17, 2018.

- [319] B. Aldemir Dikici, C. Sherborne, G. Reilly and F. Claeysens, "Emulsion templated scaffolds manufactured from photocurable polycaprolactone," *Polymer*, vol. 175, pp. 243-254, 2019.
- [320] A. Barbetta and N. Cameron, "Morphology and Surface Area of Emulsion-Derived (PolyHIPE) Solid Foams Prepared with Oil-Phase Soluble Porogenic Solvents: Span 80 as Surfactant," *Macromolecules*, vol. 37, pp. 3188-3201, 2004.
- [321] E. Lucassen-Reynders, "Interfacial Viscoelasticity in Emulsions and Foams," *Food Structure*, vol. 12, no. 1, pp. 1-12, 1993.
- [322] A. Y. Sergienko, H. Tai, M. Narkis and M. S. Silverstein, "Polymerized high internal-phase emulsions: Properties and interaction with water," *Journal of Applied Polymer Science*, vol. 84, pp. 2018-2027, 2002.
- [323] A. Nussinovitch and M. Peleg, "An empirical model for describing weight changes in swelling and shrinking gels," *Food Hydrocolloids*, vol. 4, no. 1, pp. 69-70, 1990.
- [324] S. Kovacic, D. Stefanec and P. Krajnc, "Highly Porous Open-Cellular Monoliths from 2-Hydroxyethyl Methacrylate Based High Internal Phase Emulsions (HIPEs): Preparation and Void Size Tuning," *Macromolecules*, vol. 40, no. 22, pp. 8056-8060, 2007.
- [325] A. Barbetta, M. Dentini, E. M. Zannoni and M. E. De Stefano, "Tailoring the Porosity and Morphology of Gelatin-Methacrylate PolyHIPE Scaffolds for Tissue Engineering Applications," *Langmuir*, vol. 21, no. 26, pp. 12333-12341, 2005.
- [326] C. J. Atkins, D. K. Seow, G. Burns, J. S. Town, R. A. Hand, D. W. Lester, N. R. Cameron, D. M. Haddleton and A. M. Eissa, "Branched macromonomers from catalytic chain transfer polymerisation (CCTP) as precursors for emulsion-templated porous polymers," *Polymer Chemistry*, vol. 11, pp. 3841-3848, 2020.
- [327] Q.-Z. Chen, A. Bismarck, U. Hansen, S. Junaid, M. Q. Tran, S. E. Harding, N. N. Ali and A. R. Boccaccini, "Characterisation of a soft elastomer poly(glycerol sebacate) designed to match the mechanical properties of myocardial tissue," *Biomaterials*, vol. 29, no. 1, pp. 47-57, 2008.
- [328] I. Pomerantseva, N. Krebs, A. Hart, C. M. Neville, A. Y. Huang and C. A. Sundback, "Degradation behavior of poly(glycerol sebacate)," *Journal of Biomedical Materials Research: Part A*, vol. 91A, no. 4, pp. 1038-1047, 2008.
- [329] S. A. Bencherif, A. Srinivasan, F. Horkay, J. O. Hollinger, K. Matyjaszewski and N. R. Washburn, "Influence of the degree of methacrylation on hyaluronic acid hydrogels properties," *Biomaterials*, vol. 29, no. 12, pp. 1739-1749, 2008.
- [330] S. Krishnamoorthy, B. Noorani and C. Xu, "Effects of Encapsulated Cells on the Physical-Mechanical Properties and Microstructure of Gelatin Methacrylate Hydrogels," *International Journal of Molecular Sciences*, vol. 20, no. 20, p. 5061, 2019.
- [331] J. A. Pojman, V. Viner, B. Binici, S. Lavergne and M. Winsper, "Snell's law of refraction observed in thermal frontal polymerization," *Chaos*, vol. 17, no. 033125, 2007.
- [332] J. C. Stover, *Optical Scattering: Measurement and Analysis*, SPIE, 1995.
- [333] C. Wohlfarth and M. Lechner, *Refractive Indices of Pure Liquids and Binary Liquid Mixtures (Supplement to III/38)*, Springer-Verlag Berlin Heidelberg, 2008.

- [334] A. R. Katritzky, S. Sild and M. Karelson, "Correlation and Prediction of the Refractive Indices of Polymers by QSPR," *Journal of Chemical Information and Computer Sciences*, vol. 38, pp. 1171-1176, 1998.
- [335] J.-g. Liu and M. Ueda, "High refractive index polymers: fundamental research and practical applications," *Journal of Materials Chemistry*, vol. 19, pp. 8907-8919, 2009.
- [336] D. Lantigua, M. A. Nguyen, X. Wu, S. Suvarnapathaki, S. Kwon, W. Gavin and G. Camci-Unal, "Synthesis and characterization of photocrosslinkable albumin-based hydrogels for biomedical applications," *Soft Matter*, vol. 16, pp. 9242-9252, 2020.
- [337] C. Sherborne and F. Claeysens, "Considerations Using Additive Manufacture of Emulsion Inks to Produce Respiratory Protective Filters Against Viral Respiratory Tract Infections Such as the COVID-19 Virus," *International Journal of Bioprinting*, vol. 7, no. 1, pp. 47-65, 2021.
- [338] L. Jiang, Y. Jiang, J. Stiadle, X. Wang, L. Wang, Q. Li, C. Shen, S. L. Thibeault and L.-S. Turng, "Electrospun nanofibrous thermoplastic polyurethane/poly(glycerol sebacate) hybrid scaffolds for vocal fold tissue engineering applications," *Materials Science and Engineering: C*, vol. 94, pp. 740-749, 2019.
- [339] H. Bi, Z. Ren, G. Ye, H. Sun, R. Guo, X. Jia and M. Xu, "Fabrication of cellulose nanocrystal reinforced thermoplastic polyurethane/polycaprolactone blends for three-dimension printing self-healing nanocomposites," *Cellulose*, vol. 27, pp. 8011-8026, 2020.
- [340] F. Hajiali, S. Tajbakhsh and A. Shojaei, "Fabrication and Properties of Polycaprolactone Composites Containing Calcium Phosphate-Based Ceramics and Bioactive Glasses in Bone Tissue Engineering: A Review," *Polymer Reviews*, vol. 58, no. 1, pp. 164-207, 2018.
- [341] M. T. Souza, S. Tansaz, E. D. Zanotto and A. R. Boccaccini, "Bioactive Glass Fiber-Reinforced PGS Matrix Composites for Cartilage Regeneration," *Materials*, vol. 10, no. 1, p. 83, 2017.
- [342] R. Foudazi, B. Zhao, P. Gokun, I. Manas-Zloczower, S. J. Rowan and D. L. Feke, "The Effect of shear on the Evolution of Morphology in High Internal Phase Emulsions Used as Templates for Structural and Functional Polymer Foams," *ACS Applied Polymer Materials*, vol. 2, pp. 1579-1586, 2020.
- [343] M. Gultekinoglu, S. Öytürk, B. Chen, M. Edirisinghe and K. Ulubayram, "Preparation of poly(glycerol sebacate) fibers for tissue engineering applications," *European Polymer Journal*, vol. 121, p. 109297, 2019.
- [344] L. Hou, X. Zhang, P. E. Mikael, L. Lin, W. Dong, Y. Zheng, T. J. Simmons, F. Zhang and R. J. Linhardt, "Biodegradable and Bioactive PCL-PGS Core-Shell Fibers for Tissue Engineering," *ACS Omega*, vol. 2, no. 10, pp. 6321-6328, 2017.
- [345] S. Heang Oh, I. K. Park, J. M. Kim and J. H. Lee, "In vitro and in vivo characteristics of PCL scaffolds with pore size gradient fabricated by a centrifugation method," *Biomaterials*, vol. 28, pp. 1664-1671, 2006.
- [346] S. Gomes, G. Rodrigues, G. Martins, M. Roberto, M. Mafra, C. Henriques and J. Silva, "In vitro and in vivo evaluation of electrospun nanofibers of PCL, chitosan and gelatin: A comparative study," *Materials Science and Engineering: C*, vol. 46, pp. 348-358, 2015.

- [347] M. Rostamian, M. Reza Kalaei, S. Raeisi Dehkordi, M. Panahi-Sarmad, M. Tirgar and V. Goodarzi, "Design and characterisation of poly(glycerol-sebacate)-co-poly(caprolactone) (PGS-co-PCL) and its nanocomposites as novel biomaterials: The promising candidate for soft tissue engineering," *European Polymer Journal*, vol. 138, no. 109985, 2020.
- [348] A. B. Touré, E. Mele and J. K. Christie, "Multi-layer Scaffolds of Poly(caprolactone), Poly(glycerol sebacate) and Bioactive Glasses Manufactured by Combined 3D Printing and Electrospinning," *Progress in Electrospun Nanofibers and Nanocomposites*, vol. 10, no. 626, pp. 1-16, 2020.
- [349] S. Sant, D. Iyer, A. K. Gaharwar, A. Patel and A. Khademhosseini, "Effect of biodegradation and de novo matrix synthesis on the mechanical properties of valvular interstitial cell-seeded polyglycerol sebacate-polycaprolactone scaffolds," *Acta Biomaterialia*, vol. 9, no. 4, pp. 5963-5973, 2013.
- [350] S. Rastegar, M. Mehdikhani, A. Bigham, E. Poorazizi and M. Rafienia, "Poly glycerol sebacate/ polycaprolactone/ carbon quantum dots fibrous scaffold as a multifunctional platform for cardiac tissue engineering," *Materials Chemistry and Physics*, vol. 266, no. 124543, 2021.
- [351] Y. Liu, K. Tian, J. Hao, T. Yang, X. Geng and W. Zhang, "Biomimetic poly(glycerol sebacate)/polycaprolactone blend scaffolds for cartilage tissue engineering," *Journal of Materials Science: Materials in Medicine*, vol. 30, no. 53, pp. 1-11, 2019.
- [352] S. Huang, D. Lei, Q. Yang, Y. Yang, C. Jiang, H. Shi, B. Qian, Q. Long, W. Chen, Y. Chen, L. Zhu, W. Yang, L. Wang, W. Hai, Q. Zhao, Z. You and X. Ye, "A perfusable, multifunctional epicardial device improves cardiac function and tissue repair," *Nature Medicine*, vol. 27, pp. 480-490, 2021.
- [353] M. Rostamian, M. Reza Kalaei, S. Raeisi Dehkordi, M. Panahi-Sarmad, M. Tirgar and V. Goodarzi, "Design and characterization of poly(glycerol-sebacate)-co-poly(caprolactone) (PGS-co-PCL) and its nanocomposites as novel biomaterials: The promising candidate for soft tissue engineering," *European Polymer Journal*, vol. 138, no. 109985, 2020.
- [354] S. Rastegar, M. Mehdikhani, A. Bigham, E. Poorazizi and M. Rafienia, "Poly glycerol sebacate/ polycaprolactone/ carbon quantum dots fibrous scaffold as a multifunctional platform for cardiac tissue engineering," *Materials Chemistry and Physics*, vol. 266, no. 124543, 2021.
- [355] S. Sant, D. Iyer, A. K. Gaharwar, A. Patel and A. Khademhosseini, "Effect of biodegradation and de novo matrix synthesis on the mechanical properties of valvular interstitial cell-seeded polyglycerol sebacate-polycaprolactone scaffolds," *Acta Biomaterialia*, vol. 9, pp. 5963-5973, 2013.
- [356] A. B. Touré, E. Mele and J. K. Christie, "Multi-layer Scaffolds of Poly(caprolactone), Poly(glycerol sebacate) and Bioactive Glasses Manufactured by Combined 3D Printing and Electrospinning," *Nanomaterials*, vol. 10, no. 626, 2020.
- [357] Y. Liu, K. Tian, J. Hao, T. Yang, X. Geng and W. Zhang, "Biomimetic poly(glycerol sebacate)/polycaprolactone blend scaffolds for cartilage tissue engineering," *Journal of Materials Science: Materials in Medicine*, vol. 30, no. 53, pp. 1-11, 2019.
- [358] T. Semba, K. Kitagawa, U. S. Ishiaku and H. Hamada, "The Effect of Crosslinking on the Mechanical Properties of Polylactic Acid/Polycaprolactone Blends," *Journal of Applied Polymer Science*, vol. 101, pp. 1816-1825, 2005.

- [359] L. Vogt, L. Ramos Rivera, L. Liverani, A. Piegat, M. El Fray and A. R. Boccaccini, "Poly(ϵ -caprolactone)/poly(glycerol sebacate) electrospun scaffolds for cardiac tissue engineering using benign solvents," *Materials Science and Engineering: C*, vol. 103, no. 109712, 2019.
- [360] R. Foudazi, "HIPEs to PolyHIPEs," *Reactive and Functional Polymers*, vol. 164, no. 104917, 2021.
- [361] Z. Li, H. Liu, L. Zeng, H. Liu, S. Yang and Y. Wang, "Preparation of High Internal Water-Phase Double Emulsions Stabilised by a Single Anionic Surfactant for Fabricating Interconnecting Porous Polymer Microspheres," *Langmuir*, vol. 30, no. 41, pp. 12154-12163, 2014.
- [362] F. Bouchama, G. van Aken, A. Autin and G. Koper, "On the mechanism of catastrophic phase inversion in emulsions," *Colloids and Surfaces A: Physicochemical and Engineering Aspects*, vol. 231, no. 1-3, pp. 11-17, 2003.
- [363] Z. Li, D. Liu, Y. Cai, P. Ranjith and Y. Yao, "Multi-scale quantitative characterization of 3-D pore-fracture networks in bituminous and anthracite coals using FIB-SEM tomography and X-ray μ -CT.," *Fuel*, vol. 209, pp. 43-53, 2017.
- [364] A. S. Hoffman, "Hydrogels for biomedical applications," *Advanced Drug Delivery Reviews*, vol. 64, no. Supplement, pp. 18-23, 2012.
- [365] Q. Chai, Y. Jiao and X. Yu, "Hydrogels for Biomedical Applications: Their Characteristics and the Mechanisms behind Them," *Hydrogels in Tissue Engineering*, vol. 3, no. 1, p. 6, 2017.
- [366] Dataphysics, "Surface tension values of some common test liquids for surface energy analysis," DataPhysics Instruments GmbH.
- [367] N. G. Tsierkezos and I. E. Molinou, "Surface Tension of the 4-Methyl-2-Pentanone/Ethyl Benzoate Binary System in the Temperature Range from 278.15 to 308.15K," *Journal of Solution Chemistry*, vol. 35, no. 2, pp. 279-296, 2006.
- [368] I. D. Rosca, F. Watari and M. Uo, "Microparticle formation and its mechanism in single and double emulsion solvent evaporation," *Journal of Controlled Release*, vol. 99, no. 20, pp. 271-280, 2004.
- [369] B. Sergent, M. Birot and H. Deleuze, "Preparation of thiol-ene porous polymers by emulsion templating," *Reactive and Functional Polymers*, vol. 72, no. 12, pp. 962-966, 2012.
- [370] H. Xu, X. Zheng, Y. Huang, H. Wang and Q. Du, "Interconnected Porous Polymers with Tunable Pore Throat Size Prepared via Pickering High Internal Phase Emulsions," *Langmuir*, vol. 32, pp. 38-45, 2015.
- [371] H. Schoof, J. Apel, I. Heschel and G. Rau, "Control of pore structure and size in freeze-dried collagen sponges," *Journal of Biomedical Materials Research*, vol. 58, no. 4, pp. 352-357, 2002.
- [372] J. T. Yan Lee and K. Lau Chow, "SEM Sample Preparation for Cells on 3D Scaffolds by Freeze-Drying and HMDS," *Scanning*, vol. 34, pp. 12-25, 2012.
- [373] A. Kovalenko, K. Zimny, B. Mascaro, T. Brunet and O. Mondain-Monval, "Tailoring of the porous structure of soft emulsion-templated polymer materials," *Soft Matter*, vol. 12, pp. 5154-5163, 2016.
- [374] M. P. Milner, L. Jin and S. B. Hutchens, "Creasing in evaporation-driven cavity collapse," *Soft Matter*, vol. 13, no. 38, pp. 6894-6904, 2017.

- [375] P. T. A. Nguyen, M. Vandamme and A. Kovalenko, "Collapse and cavitation during the drying of water-saturated PDMS sponges with closed porosity," *Soft Matter*, vol. 16, pp. 9693-9704, 2020.
- [376] Z. Shaozhi, P. Yu, L. Dongpo, Z. Youming, C. Guangming and L. Heng, "A thermophysical study on the freeze drying of wooden archaeological artifacts," *Journal of Cultural Heritages*, vol. 17, pp. 95-101, 2016.
- [377] K. M. Yamada and M. Sixt, "Mechanisms of 3D cell migration," *Nature Reviews Molecular Cell Biology*, vol. 20, pp. 738-752, 2019.
- [378] S. R. Caliari and J. A. Burdick, "A practical guide to hydrogels for cell culture," *Nature Methods*, vol. 13, pp. 405-414, 2016.
- [379] H. Wang and S. C. Heilshorn, "Adaptable Hydrogel Networks with Reversible Linkages for Tissue Engineering," *Materials Views*, vol. 27, pp. 3717-3736, 2015.
- [380] W. Hennink and C. van Nostrum, "Novel crosslinking methods to design hydrogels," *Advanced Drug Delivery Reviews*, vol. 64, no. Supplement, pp. 223-236, 2012.
- [381] S. Maurer, A. Junghans and T. A. Vilgis, "Impact of xanthan gum, sucrose and fructose on the viscoelastic properties of agarose hydrogels," *Food Hydrocolloids*, vol. 29, no. 2, pp. 298-307, 2012.
- [382] M. Zandi, H. Mirzadeh and C. Mayer, "Early stages of gelation in gelatin solution detected by dynamic oscillating rheology and nuclear magnetic spectroscopy," *European Polymer Journal*, vol. 43, no. 4, pp. 1480-1486, 2007.
- [383] S. Kasapis and I. M. Al-Marhoobi, "Gelatin vs Polysaccharide in Mixture with Sugar," *Biomacromolecules*, vol. 4, pp. 1142-1149, 2003.
- [384] G. Yang, Z. Xiao, H. Long, K. Ma, J. Zhang, X. Ren and J. Zhang, "Assessment of the characteristics and biocompatibility of gelatin sponge scaffolds prepared by various crosslinking methods," *Scientific Reports*, vol. 8, no. 1616, 2018.
- [385] M. Peter, N. Binulal, S. Nair, N. Selvamurugan, H. Tamura and R. Jayakumar, "Novel biodegradable chitosan-gelatin/nano-bioactive glass ceramic composite scaffolds for alveolar bone tissue engineering," *Chemical Engineering Journal*, vol. 158, no. 2, pp. 353-361, 2010.
- [386] T. Anirudhan and A. M. Mohan, "Novel pH switchable gelatin based hydrogel for the controlled delivery of the anti cancer drug 5-fluorouracil," *RSC Advances*, vol. 4, pp. 12109-12118, 2014.
- [387] A. Kuijpers, P. van Wachem, M. van Luyn, J. Plantinga, G. Engbers, J. Krijgsveld, S. Zaat, J. Dankert and J. Feijen, "In vivo compatibility and degradation of crosslinked gelatin gels incorporated in knitted Dacron," *John Wiley & Sons*, 1999.
- [388] X. Liu, Y. Won and P. X. Ma, "Surface modification of interconnected porous scaffolds," *Journal of Biomedical Materials Research Part A*, vol. 74A, no. 1, pp. 84-91, 2005.
- [389] J.-H. Shim, J. Y. Kim, M. Park, J. Park and D.-W. Cho, "Development of a hybrid scaffold with synthetic biomaterials and hydrogel using solid freeform fabrication technology," *IOP Publishing*, vol. 3, no. 034102, pp. 1-9, 2011.
- [390] L. F. Zhang, D. J. Yang, H. Chun Chen, R. Sun, L. Xu, Z. Chun Xiong, T. Govender and C. Dong Xiong, "An ionically crosslinked hydrogel containing vancomycin coating on a porous scaffold for

- drug delivery and cell culture,” *International Journal of Pharmaceutics*, vol. 353, no. 1-2, pp. 74-87, 2008.
- [391] A. Guaadaoui, S. Benaicha, N. Elmajdoub, M. Bellaoui and A. Hamal, “What is a bioactive compound? A combined definition for a preliminary consensus,” *International Journal of Nutrition and Food Sciences*, vol. 3, no. 3, pp. 174-179, 2014.
- [392] M. Kapalczynska, T. Kolenda, W. Przybyła, M. Zajaczkowska, A. Teresiak, V. Filas, M. Ibbs, R. Blizniak, L. Luczewski and K. Lamperska, “2D and 3D cell cultures - a comparison of different types of cancer cell cultures,” *Archives of Medical Science*, vol. 14, no. 4, pp. 910-919, 2018.
- [393] B. A. Blakeney, A. Tambralli, J. M. Anderson, A. Andukuri, D.-J. Lim, D. R. Dean and H.-W. Jun, “Cell infiltration and growth in a low density, uncompressed three-dimensional electrospun nanofibrous scaffold,” *Biomaterials*, vol. 32, no. 6, pp. 1583-1590, 2011.
- [394] M. L. Vainieri, M. Alini, A. Yayon, G. J. van Osch and S. Grad, “Mechanical Stress Inhibits Early Stages of Endogenous Cell Migration: A Pilot Study in an Ex Vivo Osteochondral Model,” *Polymers*, vol. 12, no. 8, p. 1754, 2020.
- [395] F. Qu, F. Guilak and R. L. Mauck, “Cell migration: implications for repair and regeneration in joint disease,” *Nature Reviews Rheumatology*, vol. 15, pp. 167-179, 2019.
- [396] L.-P. Yan, J. M. Oliveira, A. L. Oliveira and R. L. Reis, “Current Concepts and Challenges in Osteochondral Tissue Engineering and Regenerative Medicine,” *ACS Biomaterials Science & Engineering*, vol. 1, no. 4, pp. 183-200, 2015.
- [397] B. T. Corona and S. M. Greising, “Challenges to acellular biological scaffold mediated skeletal muscle tissue regeneration,” *Biomaterials*, vol. 104, pp. 238-246, 2016.
- [398] A. Galarza Torre, J. E. Shaw, A. Wood, H. T. Gilbert, O. Dobre, P. Genever, K. Brennan, S. M. Richardson and J. Swift, “An immortalised mesenchymal stem cell line maintains mechano-responsive behaviour and can be used as a reporter of substrate stiffness,” *Scientific reports*, vol. 8, p. 8981, 2018.
- [399] S. Hee Kim, H. Jung Ha, Y. Kyung Ko, S. Jung Yoon, J. M Rhee, M. Suk Kim, H. Bang Lee and G. Khan, “Correlation of proliferation, morphology and biological responses of fibroblasts on LDPE with different surface wettability,” *Journal of Biomaterials Science: Polymer Edition*, vol. 18, no. 5, pp. 609-622, 2007.
- [400] Y. Yuan, M. P. Hays, P. R. Hardwidge and J. Kim, “Surface characteristics influencing bacterial adhesion to polymeric substrates,” *RSC Advances*, vol. 7, p. 14254, 2017.
- [401] K. L. Menzies and L. Jones, “The Impact of Contact Angle on the Biocompatibility of Biomaterials,” *Optometry and Vision Science*, vol. 87, no. 6, pp. 387-399, 2010.
- [402] M. A. Bokhari, “The enhancement of osteoblast growth and differentiation in vitro on a peptide hydrogel-polyHIPE polymer hybrid material,” *Biomaterials*, vol. 26, pp. 5198-5208, 2005.
- [403] I. Castilla-Cortázar, J. Más-Estellés, J. Meseguer-Dueñas, J. Escobar Ivirico, B. Marí and A. Vidaurre, “Hydrolytic and enzymatic degradation of a poly(ϵ -caprolactone) network,” *Polymer Degradation and Stability*, vol. 97, no. 8, pp. 1241-1248, 2012.

- [404] L. Christopher X.F., D. W. Hutmacher, J.-T. Schantz, M. A. Woodruff and S. Hin Teoh, "Evaluation of polycaprolactone scaffold degradation for 6 months in vitro and in vivo," *Journal of Biomedical Materials Research Part A*, vol. 90A, no. 3, pp. 906-919, 2008.
- [405] M. V. Natu, H. C. de Sousa and M. Gil, "Influence of polymer processing technique on long term degradation of poly(ϵ -caprolactone) constructs," *Polymer Degradation and Stability*, vol. 98, no. 1, pp. 44-51, 2013.
- [406] M. Domingos, F. Chiellini, S. Cometa, E. De Giglio, E. Grillo-Fernandes, P. Bártolo and E. Chiellini, "Evaluation of in vitro degradation of PCL scaffolds fabricated via BioExtrusion. Part 1: Influence of the degradation environment," *Virtual and Physical Prototyping*, vol. 5, no. 2, pp. 65-73, 2010.
- [407] C. X. Lam, S. Hin Teoh and D. W. Hutmacher, "Comparison of the degradation of polycaprolactone and polycaprolactone-(B-tricalcium phosphate) scaffolds in alkaline medium," *Polymer International*, vol. 56, pp. 718-728, 2007.
- [408] S.-L. Liang, X.-Y. Yang, X.-Y. Fang, W. D. Cook, G. A. Thouas and Q.-Z. Chen, "In Vitro enzymatic degradation of poly(glycerol sebacate)-based materials," *Biomaterials*, vol. 32, no. 33, pp. 8486-8496, 2011.
- [409] Q.-Z. Chen, A. Bismarck, U. Hansen, S. Junaid, M. Q. Tran, S. E. Harding, N. N. Ali and A. R. Boccaccini, "Characterisation of a soft elastomer poly(glycerol sebacate) designed to match the mechanical properties of myocardial tissue," *Biomaterials*, vol. 29, no. 1, pp. 47-57, 2008.
- [410] Q.-Z. Chen, X. Yang and Y. Li, "A comparative study on in vitro enzymatic degradation of poly(glycerol sebacate) and poly(xylitol sebacate)," *RSC Advances*, vol. 2, pp. 4125-4134, 2012.
- [411] Y. Wang, Y. M. Kim and R. Langer, "In vivo degradation characteristics of poly(glycerol sebacate)," *Journal of Biomedical Materials Research: Part A*, vol. 66A, pp. 192-197, 2003.
- [412] C. K. Hagandora, J. Gao, Y. Wang and A. J. Almarza, "Poly(Glycerol Sebacate): A Novel Scaffold Material for Temporomandibular Joint Disc Engineering," *Tissue Engineering: Part A*, vol. 19, no. 5 & 6, pp. 729-737, 2013.
- [413] C. A. Sundback, J. Y. Shyu, Y. Wang, W. C. Faquin, R. S. Langer, J. P. Vacanti and T. A. Hadlock, "Biocompatibility analysis of poly(glycerol sebacate) as a nerve guide material," *Biomaterials*, vol. 26, pp. 5454-5464, 2005.
- [414] S. Park, J. Kim, M.-K. Lee, C. Park, H.-D. Jung, H.-E. Kim and T.-S. Jang, "Fabrication of strong, bioactive vascular grafts with PCL/collagen and PCL/silica bilayers for small-diameter vascular applications," *Materials & Design*, vol. 181, p. 108079, 2019.
- [415] Y. Wang, H. Wu, Z. Wang, J. Zhang, J. Zhu, Y. Ma, Z. Yang and Y. Yuan, "Optimized Synthesis of Biodegradable Elastomer PEGylated Poly(glycerol sebacate) and Their Biomedical Application," *Polymers*, vol. 11, no. 6, p. 965, 2019.
- [416] S. Metwally, S. Ferraris, S. Spriano, Z. J. Krysiak, L. Kaniuk, M. M. Marzec, S. Kyun Kim, P. K. Szewczyk, A. Gruszczynski, M. Wytrwal-Sarna, J. E. Karbowniczek, A. Bernasik, S. Kar-Narayan and U. Stachewicz, "Surface potential and roughness controlled cell adhesion and collagen formation in electrospun PCL fibers for bone regeneration," *Materials & Design*, vol. 194, no. 108915, 2020.

- [417] B. D. Ratner, A. Chilkoti and G. P. Lopez, "Plasma Deposition and Treatment for Biomaterial Applications," in *Plasma Deposition, Treatment, and Etching of Polymers*, United States of America, Elsevier Science, 1990, pp. 464-511.
- [418] K. Rabel, R.-J. Kohal, T. Steinberg, B. Rolauffs, E. Adolfoon and B. Altmann, "Human osteoblast and fibroblast response to oral implant biomaterials functionalized with non-thermal oxygen plasma," *Scientific Reports*, vol. 11, no. 17302, 2021.
- [419] J. Wei, M. Yoshinari, S. Takemoto, M. Hattori, E. Kawada, B. Liu and Y. Oda, "Adhesion of mouse fibroblasts on hexamethyldisiloxane surfaces with wide range of wettability," *Journal of Biomedical Materials Research Part B: Applied Biomaterials*, vol. 81B, no. 1, pp. 66-75, 2006.
- [420] J. Barry, M. M. Silva, K. M. Shakesheff, S. M. Howdle and M. R. Alexander, "Using Plasma Deposits to Promote Cell Population of the Porous Interior of Three-Dimensional Poly(D,L-Lactic Acid) Tissue Engineering Scaffolds," *Advanced Functional Materials*, vol. 15, pp. 1134-1140, 2005.
- [421] Y. Tamada and Y. Ikada, "Cell adhesion to plasma-treated polymer surfaces," *Polymer*, vol. 34, no. 10, pp. 2208-2212, 1993.
- [422] A. S. Hayward, N. Sano, S. A. Przyborski and N. R. Cameron, "Acrylic-Acid-Functionalized PolyHIPE Scaffolds for Use in 3D Cell Culture," *Macromolecular Rapid Communications*, vol. 34, no. 23-24, pp. 1844-1849, 2013.
- [423] P. Pakeyangkoon, R. Magaraphan, P. Malakul and M. Nithitanakul, "Surface Modification of High Internal Phase Emulsion Foam as a scaffold for Tissue Engineering Application via Atmospheric Pressure Plasma Treatment," *Advances in Science and Technology*, vol. 77, pp. 172-177, 2012.
- [424] L. Safinia, K. Wilson, A. Mantalaris and A. Bismarck, "Atmospheric Plasma Treatment of Porous Polymer Constructs for Tissue Engineering Applications," *Macromolecular Bioscience*, vol. 7, no. 3, pp. 315-327, 2007.
- [425] C. M. Zeyfert, *Surface Functionalised Emulsion-Templated Porous Polymers for In-Vitro Cell Culture*, Doctoral Thesis: Durham University, 2010.
- [426] Y. Li, J. Q. Pham, K. P. Johnston and P. F. Green, "Contact Angle of Water on Polystyrene Thin Films: Effects of CO₂ Environment and Film Thickness," *Langmuir*, vol. 23, no. 19, pp. 9875-9793, 2007.
- [427] I. Sousa, A. Mendes and P. J. Bártolo, "PCL scaffolds with collagen bioactivator for applications in Tissue Engineering," *Procedia Engineering*, vol. 59, pp. 279-284, 2013.
- [428] N. A. Peppas, J. Z. Hilt, A. Khademhosseini and R. Langer, "Hydrogels in Biology and Medicine: From Molecular Principles to Bionanotechnology," *Advanced Materials*, vol. 18, pp. 1345-1360, 2006.
- [429] G. B. Schneider, A. English, M. Abraham, R. Zaharias, C. Stanford and J. Keller, "The effect of hydrogel charge density on cell attachment," *Biomaterials*, vol. 25, no. 15, pp. 3023-3028, 2004.
- [430] A. Dolatshahi-Pirouz, T. Jensen, D. C. Kraft, M. Foss, P. Kingshott, J. L. Hansen, A. N. Larsen, J. Chevallier and F. Besenbacher, "Fibronectin Adsorption, Cell Adhesion, and Proliferation on Nanostructured Tantalum Surfaces," *ACS nano*, vol. 4, no. 5, pp. 2874-2882, 2010.

- [431] G. Dubey and K. Mequanint, "Conjugation of fibronectin onto three-dimensional porous scaffolds for vascular tissue engineering applications," *Acta Biomaterialia*, vol. 7, no. 3, pp. 1114-1125, 2011.
- [432] J. Thiele, Y. Ma, S. M. Bruckers, S. Ma and W. T. Huck, "25th Anniversary Article: Designer Hydrogels for Cell Cultures: A Materials Selection Guide," *Advanced Materials*, vol. 26, no. 1, pp. 125-148, 2013.
- [433] H.-W. Kim, H.-E. Kim and V. Salih, "Stimulation of osteoblast responses to biomimetic nanocomposites of gelatin-hydroxyapatite for tissue engineering scaffolds," *Biomaterials*, vol. 26, no. 25, pp. 5221-5230, 2005.
- [434] A. Acarregui, G. Orive, J. L. Pedraz and R. M. Hernández, "Therapeutic Applications of Encapsulated Cells," in *Immobilization of Enzymes and Cells*, Totowa, NJ, Humana Press, 2013, pp. 349-364.
- [435] M. Whitely, S. Cereceres, P. Dhavalikar, K. Salhadar, T. Wilems, B. Smith, A. Mikos and E. Cosgriff-Hernandez, "Improved in situ seeding of 3D printed scaffolds using cell-releasing hydrogels," *Biomaterials*, vol. 185, pp. 194-204, 2018.
- [436] G. D. Nicodemus and S. J. Bryant, "Cell Encapsulation in Biodegradable Hydrogels for Tissue Engineering Applications," *Tissue Engineering: Part B*, vol. 14, no. 2, pp. 149-165, 2008.
- [437] J. Yu, K. T. Du, Q. Fang, Y. Gu, S. S. Mihardja, R. E. Sievers, J. C. Wu and R. J. Lee, "The use of human mesenchymal stem cells encapsulated in RGD modified alginate microspheres in the repair of myocardial infarction in the rat," *Biomaterials*, vol. 31, no. 27, pp. 7012-7020, 2010.
- [438] S. Dikici, A. J. Bullock, M. Yar, F. Claeysens and S. MacNeil, "2-deoxy-D-ribose (2dDR) upregulates vascular endothelial growth factor (VEGF) and stimulates angiogenesis," *Microvascular Research*, vol. 131, no. 104035, pp. 1-11, 2020.
- [439] A. Hoshikawa, Y. Nakayama, T. Matsuda, H. Oda, K. Nakamura and K. Mabuchi, "Encapsulation of Chondrocytes in Photopolymerizable Styrenated Gelatin for Cartilage Tissue Engineering," *Tissue Engineering*, vol. 12, no. 8, pp. 2333-2341, 2006.
- [440] E. C. Governance, «MEDICAL DEVICE MATERIAL PERFORMANCE STUDY: Polycaprolactone (PCL) Safety Profile,» 2021.
- [441] M. Abrisham, M. Noroozi, M. Panahi-Sarmad, M. Arjmand, V. Goodarzi, Y. Shakeri, H. Golbaten-Mofrad, P. Dehghan, A. Seyfi Sahzabi, M. Sadri et L. Uzun, «The role of polycaprolactone-triol (PCL-T) in biomedical applications: A state-of-the-art review,» *European Polymer Journal*, vol. 131, p. 109701, 2020.
- [442] L. Hou, X. Zhang, P. E. Mikael, L. Lin, W. Dong, Y. Zheng, T. J. Simmons, F. Zhang et R. J. Linhardt, «Biodegradable and Bioactive PCL-PGS Core-Shell Fibers for Tissue Engineering,» *ACS Omega*, vol. 2, n° 110, pp. 6321-6328, 2017.
- [443] P. G. Alexander, R. Gottardi, H. Lin, T. P. Lozito et R. S. Tuan, «Three-dimensional osteogenic and chondrogenic systems to model osteochondral physiology and degenerative joint diseases,» *Experimental Biology and Medicine*, vol. 239, n° 19, pp. 1080-1095, 2017.

- [444] J. Mccarthy, «Nearly One in Four in U.S. Have Cut Back on Eating Meat,» Gallup, 27 January 2020. [En ligne]. Available: <https://news.gallup.com/poll/282779/nearly-one-four-cut-back-eating-meat.aspx>. [Accès le 15 February 2022].
- [445] C. Bomkamp, S. C. Skaalure, G. F. Fernando, T. Ben-Arye, E. Swartz et E. A. Specht, «Scaffolding Biomaterials for 3D Cultivated Meat: Prospects and Challenges,» *Advance Science - The Good Food Institute*, vol. 9, n° % 12102908, pp. 1-40, 2021.
- [446] «GFI investor survey results - alternative protein,» Good Food institute, 2021.
- [447] B. Balasubramanian, W. Liu et K. Pushparaj, «The Epic of In Vitro Meat Production - A Fiction into Reality,» *Foods*, vol. 10, p. 1395, 2021.
- [448] Q. Cheong, S. Chilukuri et D. Quigley, «Life Sciences,» McKinsey & Company, 31 October 2018. [En ligne]. Available: <https://www.mckinsey.com/industries/life-sciences/our-insights/genetic-testing-opportunities-to-unlock-value-in-precision-medicine>. [Accès le 2022 March 2022].
- [449] «About Us,» Good Meat, 2020. [En ligne]. Available: <https://goodmeat.co>. [Accès le 23 March 2022].